LUMINESCENT SILICON CARBONITRIDE THIN FILMS GROWN USING ECR PECVD: FABRICATION AND CHARACTERIZATION

LUMINESCENT SILICON CARBONITRIDE THIN FILMS GROWN USING ECR PECVD: FABRICATION AND CHARACTERIZATION

By

ZAHRA KHATAMI

B.Sc., M.A.Sc.

A Thesis

Submitted to the School of Graduate Studies

in Partial Fulfillment of the Requirements

for the Degree

Doctor of Philosophy

McMaster University

McMaster University DOCTOR OF PHILOSOPHY (2017) Hamilton, Ontario
(Engineering Physics)

TITLE:	Luminescent Silicon Carbonitride Thin Films Grown using ECR PECVD: Fabrication and Characterization
AUTHOR:	Zahra Khatami , M.A.Sc. (Shahid Behehsti University)
SUPERVISOR:	Professor Peter Mascher
NUMBER OF PAGES:	xx, 260

Abstract

Silicon, the cornerstone semiconductor of microelectronics, has seen growing interest as a low-cost material in photonics. Nanoscience has employed various strategies to overcome its fundamentally inefficient visible light emission such as developing new silicon-based nanostructures and materials. Each of the proposed materials has its own advantages and disadvantages in attempting to reach commercialization. Silicon carbonitride (SiC_xN_y) is a less-studied and multi-functional material with tunable optical features. Despite reports on promising mechanical properties of SiC_xN_y thin films, they have not yet been well explored optically.

This thesis presents the first in-depth analysis of the luminescent properties of SiC_xN_y thin films at a broad range of compositions and temperatures. To better understand this ternary structure, the reported data of the two fairly well studied binary structures was used as a reference. Therefore, three classes of silicon-based materials were produced and explored; SiC_xN_y, SiN_x, and SiC_x. Samples were fabricated using one of the common methods in the semiconductor industry; electron cyclotron resonance plasma enhanced chemical vapour deposition (ECR PECVD). A multitude of characterization techniques were utilized including; optical methods (ultravioletvisible spectroscopy (UVVIS), variable angle spectroscopic ellipsometry (VASE), photoluminescence (PL)) and structural techniques (elastic recoil detection (ERD), Rutherford

backscattering spectrometry (RBS), X-ray photoelectron spectroscopy (XPS), Fourier transform infrared spectroscopy (FTIR), high-resolution transmission electron microscopy (HR-TEM)).

In view of the exploring of emission properties of SiC_xN_y materials, our approach was towards the enhancement of the visible emission by adjusting the film composition and subsequent thermal treatment. First, a systematic study of the influence of carbon on the optical, compositional, and structural properties of SiC_xN_y thin films was carried out. This investigation was followed by an exploration of influence of growth conditions on the visible emission and its connection with the other film properties including hydrogen concentration, microstructure, and composition. In addition, hydrogen diffusion was explored and associated with two featured annealing temperatures.

The key element of this thesis is the comprehensive report on the interdependency of the visible light emission and all optical, structural, and compositional features of SiC_xN_y structures. Unlocking the potential of this ternary and less studied material can appeal to the silicon photonics community to implement it in anti reflection, solar cell, and sensing applications, and in particular as a substitution of SiN_x used in existing microelectronic devices.

Acknowledgements

The completion of this dissertation has been a longer than expected graduate study battle in combination with a host of other life events. Though only my name appears on the cover of this dissertation, a great many people have contributed to its production.

First of all, I have to give my deepest gratitude to my mother, Zibandeh Ghahri Saremi, for the strength and inspiration she has given me in all aspects of my life. My Ph.D. thesis is a little present to appreciate her unlimited integrity, ethics, love, and passion provided to me and all other lucky people surrounding her.

It gives me great pleasure in acknowledging constant support and guidance of my supervisor Prof. Peter Mascher throughout the journey of my graduate studies in a new academic area. He could not be a more understandable, patient, and supporting supervisor who not only guided me through all academic obstacles but also taught me generosity and kindness. He has also generously provided me with the opportunity to attend various international and national conferences and performing any requested experiment. His support does not exclude significant edits of the present thesis, otherwise, I was the only one who would understand the next 250 pages.

I would also like to thank my colleagues from the Prof. Mascher group, both past,

and present, for their various forms of support during my graduate study. Jacek Wojcik initially opened the door of the vacuum world along with all continuous training on the use of PECVD machine. At the top of the list of colleagues is Dr. Patrick Wilson, for his various contributions to the performance of experimental measurements and all the training on X-ray absorption techniques at the Canadian Light Source (CLS) located at the University of Saskatchewan. Kayne Dunn and Ryszard Dabkowski provided advice and help to initiate this project. Giacomo Bosco (exchange student from the University of Campinas) welcomed and helped me tremendously over my 3-month stay in Brazil. I would also like to thank our group members, Bo Mi Lee, Aysegul Abdelal, and Sylwia Lyda for the friendship and sharing their experiences with me. Owen Taggart, Austin Brown, Dan Frisina, and Peihai Lee on several occasions ensured that I could make use of the full 24-hour shift schedule at synchrotron beamlines.

I am also grateful for the contributions from collaborators. The foremost to thank is Prof. Leandro Tessler at the University of Campinas, Brazil, who so freely shared knowledge through informative discussions, while being so willing to provide any SiCN sample grown using reactive RF sputtering system. I would like to extend my gratitude to Prof. Leyla Soleymani for all exceptional encouragements and advice to take steps in my academic career. I would also like to express my gratitude to Prof. Adrian Kitai for excellent advice and guidance along the way and his exciting 3PN4 course on the principle of LED and solar cells (which helped to extend my views from physics to engineering). I gratefully acknowledge Prof. Ayse Turak for the advice on XPS analysis. The last but not least I would like to acknowledge two Mitacs co-op students, Lukas Wolz from the University of Tuebingen located in Germany and Pankul Dhingra from Indian Institute of Technology in Roorkee located in India

(currently a Ph.D. student at the University of Illinois Urbana-Champaign) for the passion and dedication to conduct our summer projects, and all summer students, Cameron Nowikow, Conner Wilson, and Austin Brown for the help with the annealing, TEM sample preparation, and a multitude of characterization techniques. I am also indebted to Dr. Payman Setoodeh for helping me with tackling all grammatical errors for my second paper.

I would like to thank my supervisory committee members Prof. Adrian Kitai and John Preston from the Department of Engineering Physics, and the research engineers: At the Center for Emerging Device Technologies (CEDT) Doris Stevanovic for general assistance in the cleanroom and safety courses, Zhilin Peng for cleanroom training and dicing the carbon plates as well as FIB preparation in the Centre for Advanced Nuclear Systems (CANS), Shahram Tavakoli for his frequent help and discussions on the film growth and vacuum systems (some help was provided with no ask at Tandem Accelerator Building), Jim Garrett from the Brockhouse Institute for Materials Research (BIMR) for assistance with the annealing and preparing custom-made boats, Steve Koprich at McMaster Chemistry and Chemical Biology for Raman measurements, Jim Britten and Victoria Jarvis from the McMaster Analytical X-Ray Diffraction Facility (MAX) for their help with XRD measurements, as well as Fred Pearson, Carmen Andrej, and Andreas Korinek at the Canadian Centre for Electron Microscopy (CCEM) at McMaster University for their valuable insights and assistance with TEM sample preparation and measurements. I would also like to thank all the administrative staff at the Department of Engineering Physics and CEDT such as Marilyn, Linda, Nadine, Fran, Alex, Alexa, and in particular Joanne Squires.

I am also indebted to Prof. Lyudmila Goncharova and Jack Hendriks in the Tandetron Laboratory at Western University (London, Ontario) for their assistance

with RBS and ERD measurements, Mark Biesinger at Surface Science Western for the acquisition and primary analysis of XPS experiments, and the beamline staff and scientists at the PGM, SGM, and SXRMB beamlines at CLS (Tom Regier, Yongfeng Hu, and Lucia Zuin). I would like to thank Martin Gerber and Kevin Boyd at McMaster University for their assistance with the FTIR technique, and Bertha Hui with Raman measurements.

I would like to thank my other family members for their constant support, my father Ghoalhossein Khatami and my siblings, especially my sister, an exceptional researcher, Dr. Fatemeh Khatami who has been my mentor in conducting a research-oriented life.

Last but not least, my especially sincere thanks go to my husband, Prof. Mohsen Mohammadi, whose never-failing sympathy and encouragement made this dissertation possible. He has been unwavering in support, celebrating the high points, and being a comfort in the low points owing to his positive personality. This research has taken me away from him for extended periods of time on a number of occasions for both research and conference trips, where in recent years I left him alone with all the struggles and challenges in a new workplace and city.

This work was funded by the Natural Sciences and Engineering Research Council (NSERC) under the Discovery Grants program. I am thankful to have received the Society of Vacuum Coater Scholarship (2012, 2013), and the Travel Grant (2012) provided by University of Saskatchewan as support for my summer synchrotron training (CLS3 2012). I would like to thank the Vice-Rector Manager of International Relations - VRERI of Unicamp for giving me the opportunity to collaborate with the Institute of Physics “Gleb Wataghin” (IFGW) in Unicamp and for awarding me the scholarship of FAEPEX International 2014.

I dedicate this thesis to the soul of my mother, Zibandeh Ghahri Saremi.

Contents

List of Figures

List of Tables

Notation and abbreviations

CMOS ..... Complementary metal-oxide-semiconductor

CV ..... Capacitance-voltage

ESR ..... Electron spin resonance

ECR PECVD .. Electron cyclotron resonance plasma enhance chemical vapor deposition

EDS ..... Energy dispersive X-ray spectroscopy

ERD ..... Elastic recoil detection

FTIR ..... Fourier transform infrared spectroscopy

HR-TEM ..... High-resolution transmission electron microscopy

ICPCVD ..... Inductively coupled plasma enhance chemical vapor deposition

IR ..... Infrared

I-V ..... Current-voltage

MEMS ..... MicroElectroMechanical system

OES ..... Optical emission spectroscopy

PA-ABD ..... Plasma-assisted atomic beam deposition

PL ..... Photoluminescence

RTA ..... Rapid Thermal Annealing

PzR ..... Piezo-reflectance

QDs ..... Quantum Dots

RBS ..... Rutherford backscattering spectrometry

RC ..... Resistive-capacitive

RE ..... Rare earth

RF ..... Radio frequency

SiC$_x$N$_y$ ..... Silicon Carbonitride

UV-VIS ..... Ultraviolet-visible spectroscopy

VASE ..... Variable angle spectroscopic ellipsometry

XPS ..... X-ray photoelectron spectroscopy

XES ..... X-ray emission spectroscopy

XRD ..... X-ray diffraction

TFT ..... Thin-film-transistor

ncs ..... Nanoclusters

Chapter 1

Introduction

The topic of this thesis is focused on the optical and structural properties of a relatively less studied silicon nanostructure, silicon carbonitride (SiC_xN_y) thin film. The following discussion is on the importance of silicon nanostructures and the motivation for this work. The chapter also contains the outline of the thesis.

1.1 Statement of the Problem

Photonics is one of today's emerging technologies with wide range of applications in our daily life that deals with the generation, guidance, modulation, and detection of light. The particular interest of photonics is in the communication technology where the exponential growth in the information industry and sustained Internet traffic demand higher transmission bandwidth (data rate) [1]. Among all semiconductors, optical interconnections via silicon photonics so far have provided the best solution for the high performance computing and data processing at low-cost due to its well

established and mature technology in microelectronics; the well-known complementary metal−oxide−semiconductor (CMOS) platform. CMOS technology compatible with silicon, over the last forty years, has been widely developed and enabled low cost mass production since silicon is the leading material for nearly all microelectronics. Although the first transistors were designed on germanium [2], the focus turned to silicon due to its high technological advantages including the availability in nature, conductivity manipulation, mechanical robustness, low cost, purity, and in particular, easy manufacturability [3].

The interest in the integration of CMOS technology and photonic components comes from the bottleneck of electronics. Electronic circuits integrated on a chip, normally a silicon chip, mostly consist of transistors (switches and amplifiers made of semiconductor materials) and interconnects (copper wires) [4]. The ongoing demands in switching technology (e.g., computers) and high-speed electronics (e.g., wireless telecommunications) were accompanied by a dramatical increase in the number of transistors as well as their miniaturization. The speed of the electronic circuits suffered from the increased delay time due to the larger resistive-capacitive (RC) delay in the shorter interconnects established based on copper wiring. Microelectronic and telecommunication industries overcame the bottleneck of RC delay by replacing electrical signals with the optical signals (photons) [2] [5]. The utilization of photons in integrated electronic circuits can be achieved through the marriage of electronic and photonic components on a single platform [6].

The demand of the integration of electronics and photonics (opteoelectronics) for one-chip platforms sets a benchmark for silicon on-a-chip production using existing mature semiconductor fabrication techniques. The integration of photonic devices with the electronic components on a CMOS platform is the main challenging part

since silicon fundamentally does not have suitable optical properties required for photonics [1] [6].

Diverse III-V materials have been employed in photonics in contrast to traditional electronics, where silicon is the primary material and only transistors and interconnects are required to be integrated on a chip. Hybrid techniques combine other semiconductors with silicon to realize optical functions such as hybrid light emitting diodes, vertical-cavity surface-emitting lasers, photodetectors, optical micro-electro-mechanical systems, sensors, etc [7]. However, the manufacturing process of hybrid integration is not very cost effective as it is accompanied by a more complex architecture and limitations in the material designs.

Over the past two decades, silicon optical interconnects have been seen as the best technology in terms of communications [1]. Low cost silicon photonics have been the cornerstone of optical fiber in long-distance telecommunication industry at 1.5 μm, but in the short-distance systems within the chip and on circuit boards, we still require copper wiring due to the fundamental silicon deficiency [8]. Beside the use of copper wiring in the short-range distance, the other difficulty arose from huge amount of data carried in a very small volume, which led to more complexity [9]. Using silicon photonics, today a few hundred optoelectronic components are integrated into a single chip, which limits the broadband and high-speed data interconnections. However, some researchers believe that only all-silicon active devices offer a practical path for the advancement of data-communications [10].

Silicon photonics' perspective is to tackle challenges for an electro-optical scheme entirely integrated in a CMOS platform to meet the demands of sustained exponential performance growth in the information industry [11], which would benefit from their inexpensive cost, faster data transferring, and relatively small size. More details on

the history and progress of silicon photonics in the communication technology can be found in an all-inclusive review [12]. In the following subsection, various strategies employed to solve the issue concerning entirely integrated opteoelectronic platform compatible with CMOS are briefly explained.

1.1.1 Silicon-Based Light Sources

Although various optical components, including waveguides, light amplifiers, modulators, photodetectors, and multiplexers have been already developed to a decent level of functionality within silicon photonics technology, a true light emitter monolithically integrated on the silicon chip is still the missing piece. Silicon fundamentally suffers from inefficient light emission properties that cause difficulties in the development of a suitable silicon-based light source [13] [14]. A few approaches have already been demonstrated to enhance the properties of silicon light emission enabling a low-cost CMOS platform for monolithic optoelectronic integrated circuits. These various approaches include silicon Raman lasers, erbium-related light sources, germanium-on-silicon lasers, porous silicon, and silicon nanocrystals [11]. For the first time, in 2004, Boyraz and Jalali [15] developed a pulsed Raman laser in silicon, and one year later, Intel demonstrated the continuous-wave Raman silicon laser [16]. However, these Raman lasers required an external source to be excited making them not fully compatible with on-chip light sources. In a germanium-on-silicon laser, the main barrier comes from a serious mismatch of the operational wavelength with the telecommunication wavelength at 1.5 μm due to the red-shift of germanium emission once it serves as a direct band gap material through the tensile strain process or germanium-tin (GeSn) alloying [11].

The other development is the hybrid integration of gallium arsenide and/or indium phosphide, as two front-runners of III-V semiconductors, onto the silicon substrates. This approach is encountering practical challenges such as bonding process and mechanism, bonding strength, uniformity, wafer surface treatment such as O_2 plasma treatment, and stress distribution, all of each put into question a cost-effective production of hybrid integration [7].

Another approach, involving silicon nanostructures, showed the most ability to solve the major issues, which impede practical implementation of an efficient silicon light source. Bulk silicon is an indirect band gap semiconductor and once the dimensions are shrunk to the nano scale quantum confinement effects significantly enhance the light emission efficiency. In addition, silicon nanocrystals act as sensitizers in both rare earth-doped insulating (silicon dioxide) and amorphous semi-insulating (silicon oxide and nitride) matrices [3] [13]. However, the light emission properties of silicon nanostructures are a challenging perspective since they strongly depend on the composition of the dielectric matrix. The focus of the present thesis is to explore less studied aspects of one of the silicon-based materials, silicon carbonitride (SiC_xN_y), more comprehensively. This study can also be employed to broaden the silicon applications to sectors other than cost-effective high-speed telecommunications and computing.

The market in solar cell technology, to the most part, benefits from the use of silicon-based materials [17]. Silicon has been seeing attention for optical-based sensors, communicating with the sensing target via light, where the focus recently is shifting from electrochemical sensors in the sensing community [18]. The light emission from semiconductor nanoparticles, so-called quantum dots (QDs), has been substituting the conventional laser due to its lower power and prevention of undesired heat.

Two limiting factors of the existing QDs are the low stability of their photoemission and being toxic. Silicon nanostructures, as non-toxic and biodegradable materials appeared to have a more stable emission [19]. Unlocking the potential of silicon through the use of rare earth (RE) elements for biosensors enables the low-cost mass production of disposable lab-on-a-chip devices. As an example, "for ligand-passivated silicon nanocrystals, an internal quantum efficiency reaching 100 %" has been reported [20].

Besides the detection ability of nanostructured silicon for bioimaging, silicon nanocrystals have been reported [21] as ideal candidates in cryptography where data transferring is secured by random and non-readable numbers by a third party. The spontaneous emission in LEDs is statistically a random process that can be used as the source generator of quantum random numbers [21]. In addition to the light emission features for solid-state lighting, displays, and light emitting diodes, imaging, and sensing [22], other optical properties of silicon nanostructures such as refractive index and dielectric function can be employed to guide the light (waveguides) and are widely used in microfluidics and resonators [23].

1.2 Thesis Objectives

Interest in nanostructured silicon oxide, silicon nitride, and silicon carbide has been growing for the development of a silicon-based light source. Each of the proposed silicon-based materials has its own advantages and disadvantages in attempting to reach commercialization, such as those related to the dielectric and/or mechanical properties. SiC_xN_y thin films exhibit a wide and tunable band gap by being combined from the binaries silicon carbide, silicon nitride, and carbonitride (a choice after diamond as a hard material [24]). The significance of SiC_xN_y structures, on one

hand, follows from the fact that their optical, mechanical, and electrical features can be controlled through the adjustments of the relative concentrations of silicon, nitrogen, carbon, and hydrogen in the film layer. On the other hand, establishing a suitable deposition process window for the growth of such a ternary structures with the desired properties requires extra work compared to binary structures.

In contrast to the numerous reports on promising mechanical properties of SiC_xN_y materials in the last 25 years [25], they have not yet been well explored optically [26]. In effect, therefore, the understanding of the optical and luminescence properties of SiC_xN_y structures is lacking. The realization of light emission applications strongly depends on the understanding and control of the film composition. Existing literature on luminescent SiC_xN_y thin films mainly describes samples containing oxygen, i.e., $SiC_xO_zN_y$ structures, wherein oxygen-related bonds are suggested as the sources of the luminescence [27]. In addition, no comparative study has been reported for all three structures, SiC_xN_y, silicon nitride, and silicon carbide thin films.

In this contribution, the first in-depth analysis of the luminescent properties of SiC_xN_y thin films over a broad range of compositions and deposition temperatures is presented. To better understand this ternary structure, the study was extended to the fabrication and investigation of the two fairly well studied binary structures. Therefore, three classes of silicon-based materials were produced and a comparison of stoichiometric N- and C-free, SiC_xN_y thin films is presented as well as an in-depth analysis of structural, optical, and compositional properties. To the author's best knowledge, there exists no comparative study of the visible light emission of silicon carbide, silicon nitride, and SiC_xN_y structures over a wide range of annealing temperatures (400-1200 °C). In view of exploring the emission properties of SiC_xN_y thin films, our approach was towards the enhancement of the visible emission by

adjusting the film composition and subsequent thermal treatment. This study led to the identification of a growth parameters space for the fabrication of SiC_xN_y thin films with intense enough emission to be seen with the naked eye. In parallel, a wide range of experiments were carried out to explain different light emission features observed for different compositions and post-deposition thermal treatments.

In addition, the electron cyclotron resonance plasma enhanced chemical vapor deposition (ECR PECVD) method, similar to other plasma-assisted thin film deposition techniques, allows for the formation of hydrogen-terminated bonds to produce amorphous materials. We showed that hydrogen, incorporated using ECR PECVD, plays a significant role in practical applications and can be controlled via the growth conditions and post-deposition thermal treatment. Little research has been also conducted on the release of hydrogen and the microstructural changes resulting from the thermal treatment of hydrogenated $SiC_xN_yH_z$ thin films [28] [29]. In this thesis we show that the PL, refractive index, and optical band gap of the investigated SiC_xN_y samples strongly varied with the hydrogen content, both in terms of its concentration and dynamics (diffusion). The hydrogen diffusion mechanism was explored and associated with two featured annealing temperatures.

The key element of this thesis is a comprehensive report on the interdependency of the visible light emission and all optical, structural, and compositional features of SiC_xN_y compounds. Unlocking the potential of this ternary and less studied material can appeal to the silicon photonics community to implement it in anti-reflection coating, solar cell, and sensing applications, and in particular as a substitution of silicon nitride used in existing microelectronic devices.

1.3 Academic Achievements

Overall, the results of this thesis have been published in four journal articles and three conference proceedings. The results of side projects have been published in one journal articles and two conference proceedings. They were as well presented at various international, national, and regional conferences that are listed in the following subsections. I had the leading role in all of the accepted and under review contributions except #3 and #6. In addition, I carried out all aspects of the study, including hypothesis development, design of experiments, calibration, sample preparation, measurements, and contributed to drafting and structuring of all manuscripts in this category. Other co-authors assisted with a number of experiments but did contribute to the interpretation of the data and drafting or editing of the manuscripts as they had left academia by the time the articles were developed. This excludes my supervisor, Prof. Mascher, who conceived the project and contributed to both scientific and stylistic edits of these manuscripts as well as significant edits of the present thesis. More details with respect to the content of each individual contribution are as follows:

Although the idea of luminescent SiC_xN_y structure was initiated in a previous masters project [30], where the ICP-CVD system was employed, the parameters to fabricate luminescent SiC_xN_y thin films were not established by the time of the initiation of this thesis. Therefore, first, it was required to calibrate the deposition parameters to find the composition of the SiC_xN_y films that exhibited luminescence. This involves a significant number of film depositions, systematic calibration, maintenance, and troubleshooting of the ECR PECVD system, as well as a multitude of

characterization techniques. We published the first in-depth analysis of the luminescent properties of carbon varying SiC_xN_y thin films in "Thin Solid Films" (#4), and a subsets of the results were presented at numerous meetings and published in two subsequent conference proceedings.

This work then was extended to further material characterization for annealed SiC_xN_y thin films explored in an article in the "Journal of Materials Science" (#2), where the interdependency of hydrogen diffusion and film properties was reported.

Our novel approach to analyze the PL of the SiC_xN_y thin films, which was associated with the PL of silicon carbide and silicon nitride layers was submitted to the "Journal of Luminescence" (#1), which is currently Article In Press.

Contribution #5 is a continuation of our work on the characteristics of SiCN:H layers, where the focus was on the influence of deposition temperatures on the film structure and PL properties. The response to reviewers has been submitted to the "Electrochemical Society Journal of Solid State Science and Technology".

In addition to the aforementioned results presented in this thesis, the role of nitrogen in SiC_xN_y thin films has been also investigated and published in ECS conference proceedings (#8) but has not been included in this thesis because of page limitations. Besides all employed characterization techniques for the present thesis, X-ray absorption spectroscopy was used to analyze the nitrogen varying samples (#8) and carbon varying SiC_xN_y samples doped with rare earth elements (#10). This work involved developing scientific proposals for highly requested beamlines at Canada's national synchrotron facility, Canadian Light Source (CLS), as well as modification of computer codes to handle and analyze data from X-ray absorption spectroscopy. These codes were originally developed by our former group researchers, Dr. Tyler

Rochuk [31] and Dr. Patrick Wilson [32]. Another article will include a comprehensive study of the mechanical and electrical aspects of SiC_xN_y thin films, which is currently under preparation.

The described projects provided me with great expertise in thin film design and material characterization that has been used in a number of other parallel projects over the last years of my Ph.D studies. One project involved a fruitful international collaboration with Unicamp in Campinas, Brazil, where my knowledge of ECR PECVD process parameters to fabricate luminescent SiC_xN_y thin films helped me to quickly fabricate luminescent SiC_xN_y films grown using the reactive radio frequency (RF) sputtering system located at Unicamp. The sputtered SiC_xN_y thin films showed very strong luminescence related to crystalline silicon carbide structures and the results have been presented at EMRS2014 and CCST2015 conferences. A comprehensive set of measurements has been performed on the sputtered SiC_xN_y samples and the results will be drafted in the near future for a journal publication. Besides the sputtered SiC_xN_y thin films, I contributed to the data collection and analysis for the project on terbium doped silicon nitride (Tb-SiN) conducted by this research at McMaster University. The results of this project have been drafted in #6 submitted to "Journal of Luminescence".

The second relevant project is a newly developed unique and highly controllable technique, integrating ECR-PECVD and magnetron sputtering for in-situ doping of RE elements. Through the fabrication of a wide range of compositions of terbium doped silicon-rich silicon oxide (Tb-SRSO) and oxygen rich silicon oxide (Tb-ORSO), we've demonstrated high concentrations of optically active rare earth species in silicon nanostructures offering intense and tunable emission for white light applications and the results of this work are being prepared for the publication in the near future.

This project was a continuation of the a preliminary study of terbium doped silicon dioxide (Tb-SiO_2) thin films grown using this novel technique. The results of this work have been published in the journal of "Surface and Coatings Technology" (#3), where I performed two out of four experiments, contributed to data analysis and interpretation of all four experiments, structured the manuscript and contributed to the analysis and drafting of the discussion sections of the manuscript. The system calibration and sample preparation were carried out by the other internal researchers at the Center for Emerging Device Technologies (CEDT), as well as drafting of the technical aspects of this work.

Finally, by the time of the submission of this thesis, I have been asked to review manuscripts for the journal of "Applied Surface Science", "International Journal of Surface Review and Letters", and "International Conference on Silicon Carbide of Material Research Society (MRS)".

1.3.1 Journal Publications

1. [1] **Z. Khatami**[@], P. R. J. Wilson, J. Wojcik, P. Mascher (2017) On the origin of white light emission from nanostructured silicon carbonitride thin films, *J. Lumin*, In Press. https://doi.org/10.1016/j.jlumin.2017.12.011

2. **Z. Khatami**[@], C. Nowikow, J. Wojcik, P. Mascher (2018) Annealing of silicon carbonitride nanostructured thin films: Interdependency of hydrogen content, optical, and structural properties. *J. Mater. Sci.*, 53(2): 1497-1513. https://doi.org/10.100 7/s10853-017-1576-6

3. *Equal contributing first author.

[1@] indicated the corresponding author

J. Miller*, **Z. Khatami***@, J. Wojcik, J. Bradley, P. Mascher (2017) Integrated ECR-PECVD and magnetron sputtering for rare earth-doped Si-based materials, *Surf. Coat. Technol.*, In Press. doi.org/10.1016/j.surfcoat.2017.08.051

4. **Z. Khatami**@, P. R. J. Wilson, J. Wojcik, P. Mascher (2017) The influence of carbon on the structure and photoluminescence of amorphous silicon carbonitride thin films, *Thin Solid Films*, 622: 110. https://doi.org/10.1016/j.tsf.2016.12.014

Articles submitted to peer-reviewed journals:

5. **Z. Khatami**@, G. B. F. Bosco, J. Wojcik, L. R. Tessler, P. Mascher (2017) Influence of deposition conditions on the characteristics of luminescent silicon carbonitride thin films, *ECS J. Solid State Sci. Technol.*, The response to reviews has been submitted.

6. G. B. F. Bosco@, **Z. Khatami**, J. Wojcik, L. R. Tessler, P. Mascher (2017) Excitation mechanism of Tb^{3+} in a-Si_3N_4:H under sub-gap excitation, Submitted to *J. Lumin* (LUMIN-2017-1905) 1 December 2017.

1.3.2 Conference Proceedings

7. J. Miller@, **Z. Khatami**, J. Wojcik, J. Bradley, P. Mascher (2017) Integrated ECR-PECVD and magnetron sputtering for rare earth-doped Si-based materials, *60th Annual Technical SVC.*

8. **Z. Khatami**@, P. R. J. Wilson, J. Wojcik, P. Mascher (2014) Structural and optical properties of luminescent silicon carbonitride thin films, *ECS Trans.*, 61(5), 97-103. http://ecst.ecsdl.org/cgi/doi/10.1149/06105.0097ecst

9. **Z. Khatami**[@], P. R. J. Wilson, J. Wojcik, P. Mascher (2013) Photoluminescence evolution of silicon carbonitride thin films grown by electron cyclotron resonance plasma enhanced chemical vapour deposition, *56th Annual Technical SVC*, 505/856. http://dx.doi.org/10.14332/svc13.proc.1110

10. **Z. Khatami**[@], P. R. J. Wilson, J. Wojcik, P. Mascher (2013) XANES and XES studies of luminescent silicon carbonitride thin film, *ECS Trans.*, 50(41): 4956. http://ecst.ecsdl.org/cgi/doi/10.1149/05041.0049ecst

11. P. R. J. Wilson[@], **Z. Khatami**, R. Dabkowski, K. Dunn, E. Chelomentsev (2012) XANES and XEOL investigation of cerium and terbium co-doped silicon oxide films, *ECS Trans.*, 45(5), 43-48. http://ecst.ecsdl.org/cgi/doi/10.1149/1.3700408

12. **Z. Khatami**[@], P. R. J. Wilson, K. Dunn, J. Wojcik, and P. Mascher (2012) The Influence of carbon on the structure and photoluminescence of amorphous silicon carbonitride thin films, *ECS Trans.*, 45(5), 153-160. http://ecst.ecsdl.org/cgi/doi/10.1149/1.3700422

1.3.3 Conference Oral Presentations

13. FCSE (2017) Montreal, QC, CA (International).

14. ETCMOS (2016) Montreal, QC, CA (International).

15. ICMCTF (2016) San Diego, CA, US (International).

16. CCST (2015) Sherbrook, SK, CA (National).

17. IFGW Lecture Series (2014) Campinas, SP, BR (Institutional).

18. FCSE (2014) Montreal, QC, CA (International).

19. 225th ECS Meeting, 2014, Orlando, FL, US (International).

20. SVC-2013, Providence, RI, US (International).

21. CS3 (2012) University of Saskatchewan, SK, CA (Institutional).

22. 221th ECS Meeting, Seattle, WA, US (International).

23. Crest Meeting for Women in NES 2012, Hamilton, ON, CA (Institutional).

1.3.4 Posters Presentations

24. [2]Z. Khatami**, G. B. F. Bosco, A. Shah, J. Wojcik, L. R. Tessler, P. Mascher (2014) *EMRS*, Lille, France (International).

25. Z. Khatami**, P. R. J. Wilson, J. Wojcik, and P. Mascher (2012) *Nano Ontario Conference and Workshop*, Waterloo Hamilton, ON (Provincial).

26. P. R. J. Wilson**, Z. Khatami, J. P. Goguen, A. Brown, J. Wojcik, and P. Mascher (2012) *Nano Ontario Conference and Workshop*, Waterloo Hamilton, ON (Provincial).

27. Z. Khatami**, P. R. J. Wilson, J. Wojcik, and P. Mascher (2011) *Nano Ontario Conference and Workshop*, Hamilton, ON (Provincial).

28. P. R. J. Wilson**, Z. Khatami, J. P. Goguen, A. Brown, J. Wojcik, and P. Mascher (2011) *Nano Ontario Conference and Workshop*, McMaster Hamilton, ON (Provincial).

[2]**Indicated the presenter.

1.4 Thesis Outline

Chapter 2 contains background on silicon nanostructures as well as an extensive literature survey of the luminescence properties of SiC_xN_y thin films and some practical applications of these materials.

Chapter 3 provides an overview of the characterization techniques employed to evaluate the material behavior of SiC_xN_y thin films. A brief note on the basics of each technique is given. This chapter mainly concerns the specific parameters and conditions required to be optimized to investigate SiC_xN_y thin film properties.

Chapter 4 gives a description of the ECR PECVD system used to prepare the materials discussed in this thesis. The influence of carbon on SiC_xN_y thin films is developed using the characterization techniques discussed in chapter 3.

Chapter 5 is a continuation of the previous chapter findings on the optimized parameters of the most luminescent sample (a-$SiC_{1.2}N_{0.7}$:$H_{1.4}$) in the post deposition thermal treatment. In addition, the hydrogen dynamics as a function of different annealing temperatures were investigated.

Chapter 6 is devoted a discussion to the underlying PL mechanism of the most luminescent SiC_xN_y thin films; a-$SiC_{1.2}N_{0.7}$:$H_{1.4}$. In general, the samples exhibited a broad luminescence band, covering the visible range with two dominant peaks at $\sim$470 and 550 nm, which appeared "white" to the naked eye.

Chapter 7 provides a summary of the findings on optical, structural, and luminescent characteristics of SiC_xN_y thin films and presents the conclusion of this thesis. It is then finalized with an outlook and suggestions for future research on SiC_xN_y thin films.

Chapter 2

Light Emission from Silicon Nanostructures

Silicon nanostructures so far are the best solution for the implementation of silicon in "all-silicon" photonic devices. In this chapter, the light emission from bulk silicon, efficient emission from quantum-sized silicon structures and its luminescence model, and fairly well-studied silicon-based dielectrics are treated. This chapter concludes with an extended literature review of the light emission from SiC_xN_y thin films and some of their practical applications.

2.1 Electronic Structure of Bulk Silicon

The fundamental drawback regarding the optical functionality of bulk silicon is related to the fact that silicon does not emit efficiently at room temperature. Here, the essential information about indirect band gap structures of silicon and the reason for its inefficient emission are provided and addressed by fundamental topics in quantum

and solid state physics.

In a non-metallic solid, the band gap (E_g) separates the energy band filled with electrons (valence band) from the empty band of electrons (conduction band). This defines a minimum energy required for an electron to move from the top of the valence band to the bottom of the conduction band [33]. The available thermal energy at room temperature is only 25 meV ($E = kT$, where E, k, and T are the energy, Boltzmann constant, and temperature), which is much smaller than the band gap of commonly used semiconductors, e.g. silicon with E_g of 1.1 eV or gallium arsenide with E_g of 1.4 eV. Although, the energy at room temperature is not sufficient to excite an electron from the valence band to the conduction band, still, some electrons are thermally promoted across the band gap at room temperature. The excitation rate is a function of temperature and given by the Boltzmann distribution:

$$Excitation\ Rate = const. \times e^{(-\frac{Energy\ \ Gap}{KT})} \tag{2.1}$$

Although the Boltzmann distribution identifies a low excitation rate for an intrinsic (non-doped) semiconductor at room temperature, a small number of electrons occupy the conduction band [34, 35]. To this end, if an intense light with sufficient energy ($h\nu \geq E_g$) is incident on an intrinsic semiconductor, it can provide the required energy to excite more electrons to the conduction band. The pair of the missing electron in the valence band and the excited electron in the conduction band creates an electron-hole pair. After a certain time (life time) the electron returns back to the valence band to occupy the missing valence-band electron (hole), via light emission, a process called radiative recombination process.

The incidence of light and its subsequent absorption are controlled by two conservation laws; energy and momentum conservation. This means that the energy of the photon should be equal or larger than the band gap energy and the momentum of the photon should be equal to the difference of the quasi-momentum of the initial and final electron states, respectively. The momentum of a photon is generally much smaller in comparison with the dimensions of the crystalline structure (Brillouin zone) and the quasi-momentum of the electron state, i.e. $k_{photon\ of\ visible\ light} = \frac{2\pi}{\lambda} = 10^{-7}\ m^{-1}=$ 0.001 of the value of the wave vector corresponding to the Brillouin zone edge. Ignoring the photon's momentum approximates the momentum conservation law giving no change in momentum of electron state. This implies a direct optical transition occurring vertically in momentum space (k-space) [13]. In a direct bandgap semiconductor such as indium phosphide, the minimum of the conduction band and the maximum of the valence band lie in the same position in k-space, which allows a direct optical transition [34, 36] as shown in Fig. 2.1. In an indirect band structure such as silicon, there is an offset between the minimum of the conduction band and the maximum of the valence band in k-space, which prevents a direct electron-hole recombination. Fig. 2.1 shows the energy-momentum diagram of the silicon band structure. The top of the valence band is located at the Brillouin-zone center, Γ and by E_g of 1.1 eV is separated from the bottom of conduction band, which appears 85% on the way to the zone boundary at the X point in the $\langle 100 \rangle$ direction [36]. The momentum offset between the initial and final electron states preventing a direct electron-hole recombination is required to be compensated during the electron transition process by a third quasiparticle, typically a phonon. Before discussing the effect of the phonon, it is worth mentioning that in Fig. 2.1 another band gap of silicon is also shown; a direct band gap of silicon at the center of the Brillouin zone. As will be discussed

further, this band gap was discovered owing to the observations of (quantum dot) emissions related to the energy states of this band gap, which are higher than the states at the absolute minimum of the conduction band of silicon by ~ 2 eV [37].

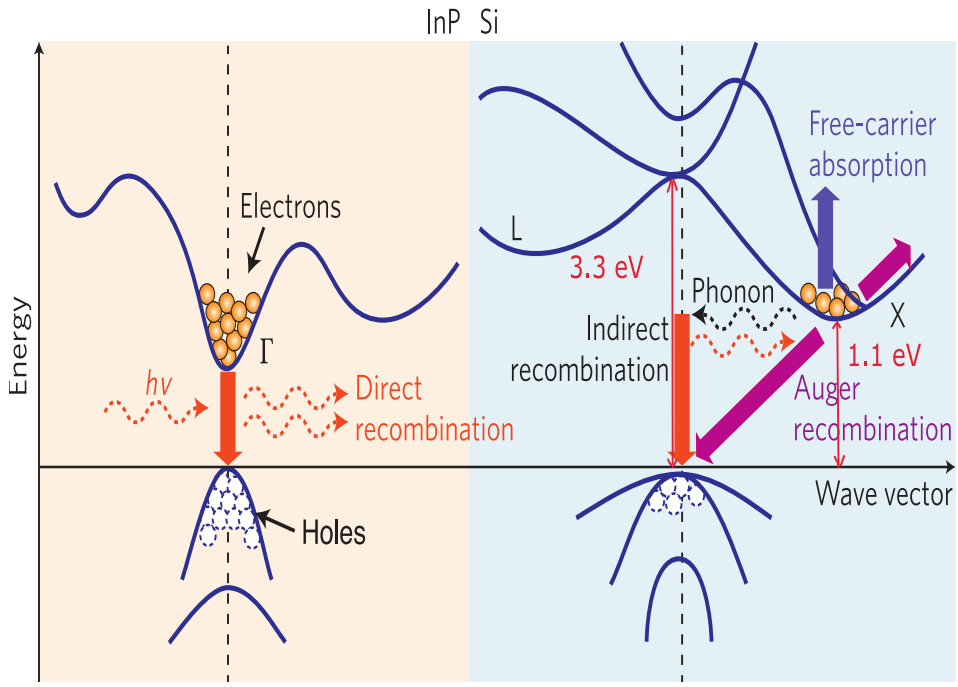

Figure 2.1: **Direct and indirect band gap semiconductors.** A comparison of direct band gap (indium phosphide) and indirect band gap materials (silicon). Some holes occupy the valence band at the Brillouin zone center (the Γ point) and electrons are at the bottom of the conduction band. In silicon, the conduction band is located at 85% of the way toward the X point (the <100> direction). In indium phosphide, the conduction band is positioned at the Γ point so that the electrons and holes have the same momentum and can recombine with no change in the momentum. The direct recombination is very favorable compared to the silicon structure, where a phonon is required to supply the large momentum difference between the holes and electrons. Reprinted (adapted) with permission from [38].

A three-particle process (electron, photon, and phonon) is much less probable than a two-body process (electron and photon) [34]. In an indirect band gap material, the

required assistance of a phonon in the photo-generation process leads to a low radiative recombination rates at room temperature. The lifetime of a radiative transition (τ_r) lies in the range of ms, which is less probable by a factor of 10^{-6} than that of a direct band structure with a lifetime in the range of μs [39] [40]. The drawback of the indirect band gap materials is not the long lifetime for a radiative recombination since lasers using long lifetime recombinations have been already developed [10]. The main issue arises from the occurrence of competing recombination pathways, non-radiative recombinations. Fast nonradiative recombinations with a lifetime of ns limit the radiative recombinations with a lifetime of a few ms [10, 41]. This results in a very low internal quantum efficiency η_{int} on the order of 10^{-3}. Internal quantum efficiency describes the efficiency of a semiconductor to emit light and is given as:

$$\eta_{int} = \frac{W_R}{W_R + W_{NR}} = \frac{1/\tau_r}{1/\tau_r + 1/\tau_{nr}} = \frac{\tau}{\tau_r} \tag{2.2}$$

where W_R and W_{NR} are the radiative and nonradiative probabilities, respectively, and τ is the total lifetime of recombinations [12].

Two other limiting processes become predominant under high-injection conditions desired in a lasing environment. Auger recombination, a three-body transition where more than one carrier is excited as shown by the green arrows in Fig. 2.2. The excess energy of the electron-hole recombination, instead of producing a photon, is transferred to another electron (in either band). The newly excited electron then absorbs the excess energy with a lifetime given by [10, 42]:

$$\tau_A = \frac{1}{C\Delta n^2} \tag{2.3}$$

where C is a constant, which depends on the doping level and Δn is the density

of excess free excited carriers [43]. A higher density of carriers or smaller band gap energy makes the Auger lifetime shorter; e.g. $\tau_A = 10$ ns with $\Delta n = 10^{19}$ cm^{-3} [42]. In addition to Auger recombination, free carrier absorption also decreases the lifetime of nonradiative recombinations. In Fig. 2.2, the orange arrows show the free carrier pathway where the incoming photon is absorbed by an already-excited carrier and intraband transition occurs within a given band [12].

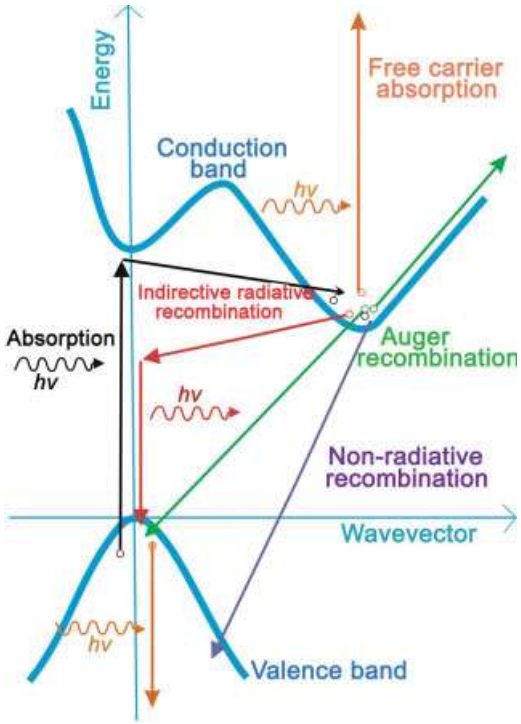

Figure 2.2: **Energy diagram of silicon.** The various arrows indicate the recombination paths for an excited electron; black arrows: indirect absorption; red arrows: indirect radiative recombination with the assistance of a phonon; purple arrow: non-radiative recombination; green arrows: Auger re-combination; orange arrows: free-carrier absorption. Reprinted (adapted) with permission from [12].

Several approaches have been proposed to either increase the probability of radiative recombination or minimize other competing nonradiative recombinations [44].

One strategy aims to suppress nonradiative recombinations by applying thin contacts to high-quality bulk silicon where high doping were localized close to the contact areas [45]; however, the long lifetime of radiative recombination as well as the requirement of surface texturing limit the functionality to serve as an efficient light emitting source [14]. Some methods utilize alloying such as silicon-germanium quantum cascade structures and silicon tin (SiSn) alloys [46], or strain and dislocation-engineering in boron implanted silicon [47]. Another approach is impurity-mediated luminescence achieved by erbium doped silicon nanocrystals [44, 48]. Mostly, the promising strategies to develop a practical silicon light source so far rely on nanostructuring. As an example, experimentally it is evidenced that the maximum contribution of direct optical emission of bulk silicon can be enhanced by a factor of 10^3 in a quantum-confined structure [13]. In the next section, after a brief history of the silicon nanocrystal topic, the most widely accepted hypotheses on the luminescence mechanism, the changes induced by the formation of nanoclusters as well as their influence on the band gap of silicon are explained.

2.2 Low Dimensional Silicon

Historically, the research on silicon nanostructures was actively motivated in 1990 by L. T. Canham at the UK Defense Research Establishment Agency. Canham and coworkers [49] observed visible photoluminescence (PL) from porous silicon associated with the nanostructure and suggested six models describing the origin of the light emission. Although Furukawa and Miyasato [50] for the first time, tuned the light emission from silicon nanocrystals by changing the crystals' size in the range of 2 to 5 nm, they never performed work on the formalization of quantum confinement in

silicon. Nine years after Canham, one of the ideas explaining the luminescence process was developed by P. Fauchet and colleagues who associated the origin of light emission with the surface states in oxidized porous silicon [51, 52]. For the first time, light amplification in silicon nanocrystals embedded in silicon dioxide was demonstrated by an Italian research group led by L. Pavesi [53]. Afterwards, the research on this discovery excessively was followed by numerous researchers and so far the quantum confinement model is the most widely accepted hypothesis explaining the origin of the luminescence from radiative recombination of electrons and holes confined at the nanoscale [44]. In the following subsections, the energy band adjustment induced by quantum confinement effects is discussed, with the focus on indirect band gap materials.

2.2.1 Quantum Confinement

Nanoscience has suggested that scaling down to nano dimensions heavily affects the physical and chemical properties of the bulk materials. To understand the changes in the light emission properties of semiconductors on nanometer scales, one requires knowing the specific character of an exciton [54]. Excitons are quasi-particles forming when an (optically induced) electron leaves a hole in the valence band but remains bound in a pair state by Coulomb's electrostatic attraction. The exciton can dissociate into free carriers, where the radiative recombination of electrons and holes emits light. [54, 55]. The electron and hole of an exciton are bound within a characteristic length called the Bohr exciton radius (a_B) identifying the spatial extent of the exciton in the semiconductor. In addition to this characteristic length, another characteristic of a carrier is its de Broglie wavelength given by the division of Plancks constant

by the momentum of the carrier ($l_b = \hbar/p$). Bohr exciton radius and de Broglie wavelength both are referenced as the exciton size in the bulk.

Quantum confinement is essentially observed once at least one dimension of the crystal approaches (or even reduces to less than) the value of the de Broglie wavelength or Bohr radius of the bulk exciton [56]. In 1981, Van Kampen ascribed this dimension as a limit for the mesoscopic structure, an intermediate scale between micro- and macrostructure. In the mesoscopic regime, according to the directions that the carrier motion is restricted, the structure is classified into three different types including two-dimensional quantum wells/superlattices, one-dimensional quantum wires and zero-dimensional quantum dots (QDs) where the electrons and holes are restricted in one, two, and three dimensions, respectively. Under confinement conditions the spatial overlap of the exciton wave function with each other increases in the constrained direction, which leads to quantized energy levels in that direction [57]. As shown schematically in the top panel of Fig. 2.3, the energy levels become more discrete with further spatial confinement of electron-hole pairs (excitons). In fact, the separation of energy levels results in a higher density of electronic states near the band edges manifested in band gap widening, and subsequently, the photoemission enegy is shifted to the higher energy range of the visible spectrum [58]. The bottom panel of Fig. 2.3 shows the dependence of the luminescence color on the size of QDs embedded in cadmium selenide. Another change induced by the quantum confinement concerns the decrease of the probability of non-radiative recombinations. The spatial confinement of excitons leads to the extension of the wavefunctions, and subsequently, results in the overlap of wavefunctions in momentum space. That can be explained by Heisenberg's uncertainty principle correlating the relationship of the spatial position and momentum of the exciton as follows [58]:

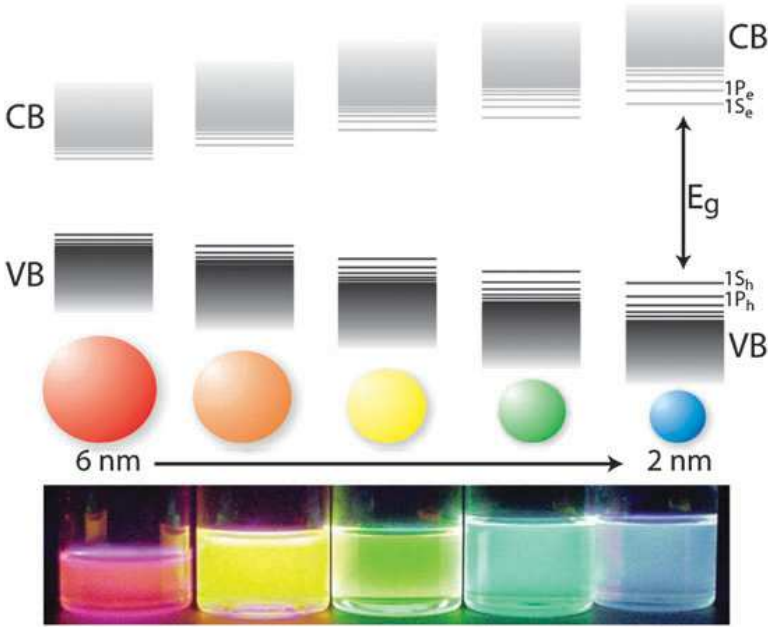

Figure 2.3: **The influence of quantum confinement on energy levels and the associated size-dependent PL emission.** The top panel represents a schematic of discrete energy levels under quantum confinement conditions. The lower panel shows the luminescent color with respect to the size of QDs embedded in colloidal cadmium selenide under UV excitation. Reprinted (adapted) with permission from [59].

$$\Delta x \Delta p_x = \frac{\hbar}{2} \tag{2.4}$$

Therefore, the localization of excitons can break down the momentum conservation law and relaxes the phonon bottleneck in indirect optical transitions. In fact, not needing phonons makes the band structure of indirect band gap semiconductors more direct-like, thereby enhancing the efficiency of the light emission [56]. In the next subsection, the correlation of the energy of confined states with the size of QDs formed within silicon-based compounds is discussed with more theoretical details.

2.2.2 Light Emission from QDs

In the 1980s, QDs were predicted to have a rich structure of various separated energy levels, which was confirmed by a series of experimental works [60]. In the theoretical study of QDs to calculate the band gap energy, Bloch's theory may no longer hold. Bloch's theory describes the propagation of the electrons and holes as Bloch waves under the periodic boundary conditions of a crystal [54]. The confinement of QDs can be viewed as the "particle in a box" model and violates the Bloch theory developed based on an infinite extension of the lattice [61]. For the first time, Bruce applied the effective mass approximation (EMA) to cadmium selenide QDs [62]. He took into account two potentials; the potential corresponding to the attractive Coulomb interaction in the exciton and the spherical potential of confinement due to the presence of QDs. In a quantum confinement situation the exciton cannot be viewed as the quasiparticle, instead, electrons and holes are regarded as single particles in their ground state [56]. Therefore, the confined states are discrete energy states where their dependence on the size of QDs is defined by the so-called Bruce Model as follows [62]:

$$E = \frac{\hbar^2}{2\mu}\frac{\pi^2}{R^2} - 1.786\frac{e^2}{\epsilon R} \tag{2.5}$$

$$\text{where} \quad 1/\mu = 1/m_e^* + 1/m_h^*$$

$\hbar$ is the Dirac constant, ϵ is the semiconductor dielectric constant, e is the electronic charge, μ is the reduced exciton mass, and m_e^* and m_h^* are the effective masses of the electron and hole, respectively. The first (additive) term corresponds to the sum of the energies of each carrier in the ground state. The next (subtractive) term represents the attractive Coulomb interaction and generally is negligible due to the large value of the dielectric constant in the denominator. In fact, the impact of the

surrounding dielectric is to reduce the exciton energy by shielding the electron–hole interactions.

Bruce model (Equ. 2.5) did not take into account the effects of the spatial overlap of the electron and hole, which is more predominant under the strong confinement conditions ($R/a_B \ll 1$) [56]. Kayanuma modified the Bruce model with the addition of an extra term describing the carrier overlap. The spatial correlation of the carriers is mathematically described using a hydrogen-like energy level scheme independent of QD radius. However, instead of the Rydberg energy of atomic hydrogen (E_{Ry}=13.6 eV), the effective pair–state binding energy is given in the exciton form of the Rydberg energy. The effective exciton Rydberg energy is described by [63]:

$$E^*_{Ry} = 13605.8\frac{\mu}{m_0\epsilon^2} \tag{2.6}$$

It can be observed that the equation 2.6 gives an effective Rydberg energy on the order of 1 to 100 meV, which is much smaller than the Rydberg energy of a hydrogen atom. This can be explained by the linear proportionality to the exciton reduced mass, which is much smaller than the masses of unconfined carriers. Another factor making the effective Rydberg energy small is the dielectric constant, which is inversely proportional [55, 64]. The addition of the effective exciton Rydberg energy modifies Equ. 2.5 for the energies of the confined states as follows:

$$E = \frac{\hbar^2}{2\mu}\frac{\pi^2}{R^2} - 1.786\frac{e^2}{\epsilon R} - 0.248E^*_{Ry} \tag{2.7}$$

$$a_B = \frac{4\pi\hbar^2\epsilon_0\epsilon_r}{\mu e^2} \tag{2.8}$$

So that, the lowest gap energy of a QD is given by the so-called modified EMA equation:

$$E_{g(QD)} = E_{g(bulk)} + \frac{\hbar^2}{2\mu}\frac{\pi^2}{R^2} - 1.786\frac{e^2}{\epsilon R} - 0.248E^*_{Ry} \tag{2.9}$$

Equ. 2.9, the so-called modified EMA theory or Bruce model, identifies the band gap energy of the QDs. The inverse relation between the energy gap and the QD size explains the reason of band gap widening which leads to shifting of the emission energy to the higher energy range of the visible spectrum (blue shift) [65], shown in Fig. 2.3. The research presented in this thesis is concerned with the light emission from silicon-based dielectrics. In the following subsections, the subject of the size-dependent band gap energy of silicon nanocrystals is extended. With respect to the terminology used for nanocrystals in the remainder of this thesis, it is noted that QDs and nanocrystals are similar concepts. QDs have been used for both direct and indirect band gap semiconductors while the nanocrystal term commonly has been used to refer to QDs in indirect band gap materials [66].

2.2.3 Silicon Nanocrystals

Mostly, the theoretical calculations have been developed based on the modified EMA theory and semi-empirical tight binding approximations [67]. Delerue calculated the energy gap for silicon nanocrystals embedded in silicon dioxide using a tight-binding model [68]. Delerue's model is plotted in Fig. 2.4 along with a number of other models. He anticipated that a decrease in the size (d) from 7 to 2 nm widens the band gap (E_g) from 1.4 to 2.5 eV corresponding to a blue shift of the PL emission from 900 to 500 nm. Provided the exciton Bohr radius for silicon is 4.9 $\mathring{A}$, the suggested EMA model explaining the luminescent mechanism from silicon nanocrystals embedded in

silicon dioxide was derived the so-called Delerue's model as follows:

$$E_g(d) = E_0 + 3.73/d^{1.39} \tag{2.10}$$

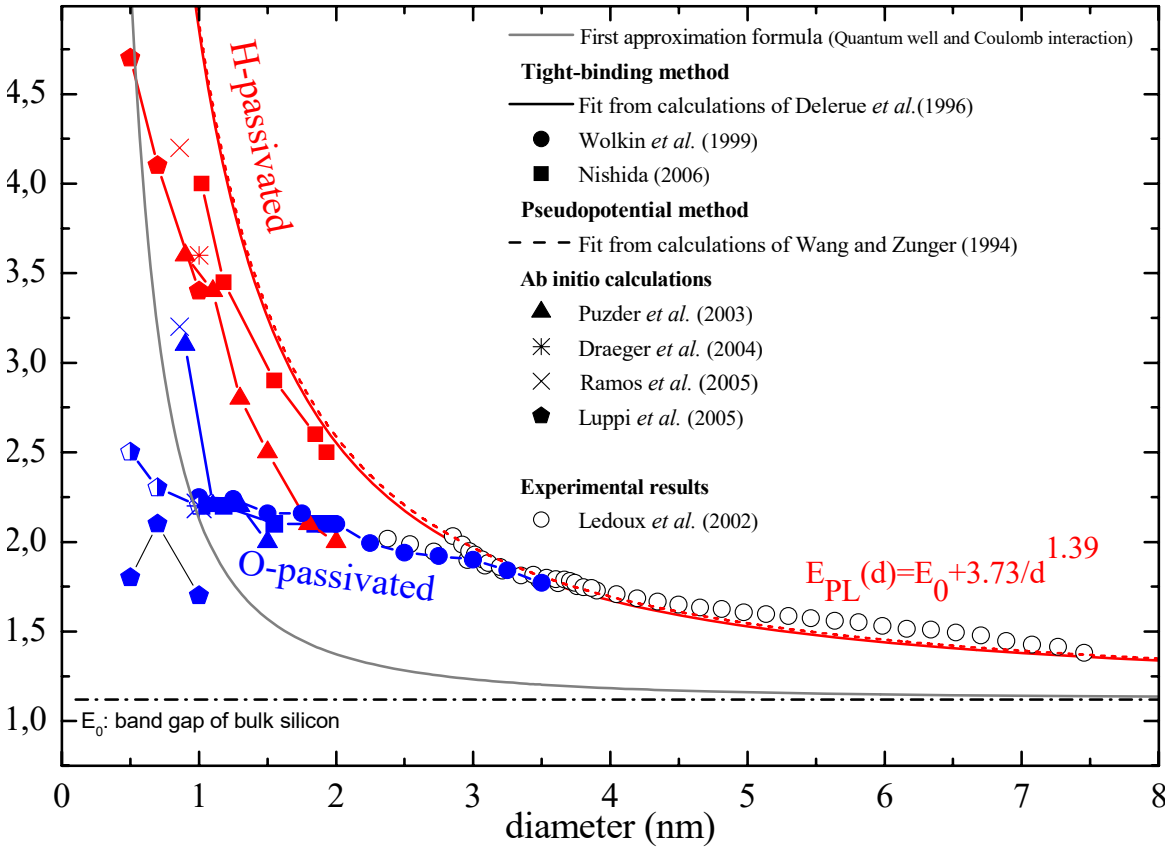

Figure 2.4: **Example of the dependence of PL emission energy on the size of nanocrystals.** The correlation of the average size of the silicon nanocrystals and the PL emission is shown as an inverse power law by Delerue. The correlation of the PL peak energy and silicon nanocrystals passivated with hydrogen and oxygen are shown in red and blue color, respectively. Reprinted (adapted) with permission from [69].

The energy gap of nanocrystals was believed to be directly estimated using the PL measurements. Fig. 2.4 shows that the experimental trends, in general, follow the theoretical calculation performed in Delerue's quantum confinement framework.

However, some discrepancies are observed between the experiment and Delerue's model that impose complementary considerations, in particular, for small sizes of the nanocrystals. One missing factor is found to be associated with the interface states located at the nanocrystal surface [70]. Furthermore, defects at the interface acting as nonradiative centers are detrimental to achieving efficient luminescence from nanocrystals [71]. Another difficulty to predicting the behavior of silicon nanocrystals by EMA theory is related to the properties of the host material. Different compositions of silicon based compounds have different finite potential barriers and polarities greatly affecting the light emission coming from electron–hole pair recombination. In this case, the PL measurement, as one of the well–established and powerful techniques, does not necessarily represent the actual band gap energy. These factors are briefly discussed in the following three paragraphs. Despite numerous studies in this field, still, some questions on the luminescence mechanisms from silicon nanocrystals remain unclear and there is no agreement on a universal model. Later in this chapter, the proposed EMA model for other choices of silicon based materials such as silicon nitride and silicon carbide are explained.

Interface States Fig. 2.4 shows various theoretical calculations of the PL energy as a function of the passivated nanocrystal size. Wolkin reduced the inconsistency from the quantum confinement predictions, due to the surface states, by proposing that the PL of the hydrogen-passivated nanocrystal is independent of the crystal size [72]. The general trend of the calculated PL emission from the quantum confinement model is in good agreement with the experimental PL energy of hydrogen-passivated nanocrystal since hydrogen passivation suppresses the surface defects and improves the PL emission of silicon nanocrystals without changing their size. The

unfilled circles in Fig. 2.4 show the experimental PL data measured for nanocrystals with sizes ranging from 2 and 8 nm where they are in a good agreement with Delerue's model as well as Wolkin's proposed model [67]. In contrast, the effect of oxidation highly depends on the diameter of the crystal since oxygen atoms may form bonds on the surface of small nanocrystals. It is shown that the substitution of the hydrogen atoms by oxygen atoms decreases the PL energy, in particular, for crystal sizes below 3 nm. In Fig. 2.4, the effect of oxidation of already hydrogen passivated crystals is shown in blue circles showing discrepancies from the predictions made by the EMA model. The Si=O covalent bonds form stable states positioned within the mid gap of the nanocrystal where the recombinations occur between the trapped electrons with free holes in the crystals with sizes between 2 and 3 nm, and through trapped excitons for crystals smaller than 2 nm. As a result, approximately, only 30% of nanocrystals embedded in a silicon dioxide matrix are optically active [73].

Passivation In silicon nanocrystals with a size smaller than 3 nm the light emission does not only depend on the nanocrystal size according to the confinement model, due to the increased surface area to volume ratio. Such nanocrystals can be viewed as an interface rather than volume where the surface atoms at the interface between the nanocrystals and host dielectric likely have partially bonded atoms (unsaturated bonds). In general, the unsaturated bonds have higher energy states and create localized states within the band gap acting as trap states for the electron–hole recombination at the interface. They may serve as non-radiative recombination centers to quench the light emission coming from the silicon nanocrystal. The smaller size of the crystals results in a larger surface area to volume ratio, and consequently, a higher non-radiative recombination rate. Although larger nanocrystals have the

advantage of a relatively smaller of surface states, they approach the properties of bulk silicon and hence provide a lower probability to emit. As a solution, the surface passivation either by hydrogen or oxygen was found to enhance the radiative recombination rates for small nanocrystals. The passivation decreases the dangling bond defects serving as the killer centers for the efficient PL from silicon nanocrystals [74]. Surface passivation necessitates alternative explanations taking into account the significant contribution from localized surface states. In addition, the type of the material employed for the surface passivation plays a role, as will be discussed in the following [75].

Potential Barriers The typical surrounding medium of silicon nanocrystals is a dielectric such as silicon dioxide, silicon nitride, and silicon carbide with band gaps of about 8.8 eV [77], 5 eV [78], and 2.4 to 3.2 eV [79], respectively. These band gaps are large enough to support the approximation of an infinite potential barrier required for the particle in a box model. In fact, the potential barrier is the band gap energy difference between the host with relatively large band gap and the silicon nanocrystals with a lower band gap since the confined QDs created by small band gap silicon nanocrystals are sandwiched between two larger band gap host matrix. In reality, the true barrier potentials are not infinite and hence the potential is no longer periodic at the edge of the crystal. The carrier wavefunction can leak and the subsequent wavefunction overlapping with the edge of the crystal brings deviations from the infinite barrier assumption, particularly for sufficiently small nanocrystals. Fig. 2.5 shows that silicon nitride follows the predictions made by the EMA theory better than silicon oxide due to the lower molecular polarity of silicon nitride. The energy levels of silicon nanocrystal in silicon oxide and nitride

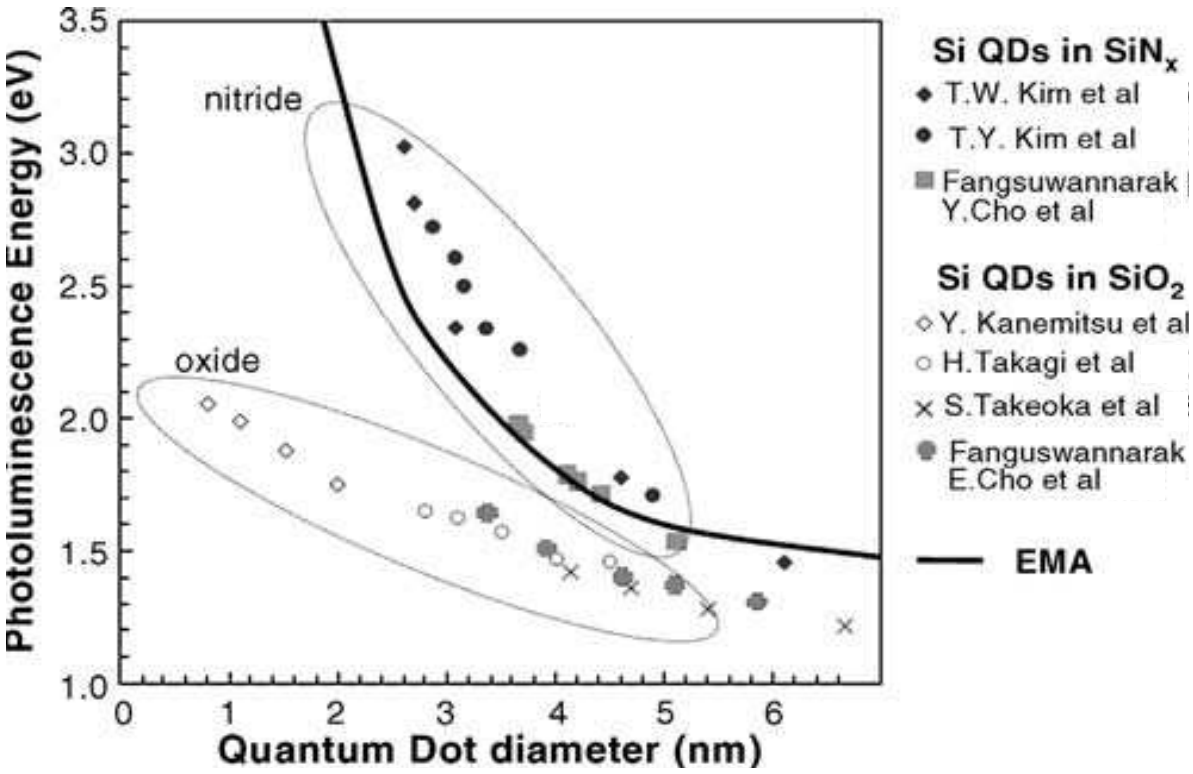

Figure 2.5: **The calculated and measured PL energy of silicon nanocrystals.** The theoretical PL data obtained using EMA theory are compared with the experimental PL data of nanocrystals embedded in silicon (sub)dioxide and silicon nitride host matrices reported by various researchers. Reprinted (adapted) with permission from [76].

are terminated with $-OH$, $-H$, and NH_2 groups, which simulate the oxide matrix, vacuum, and nitride matrix, respectively, in the ab initio modeling. The ab initio calculations using density functional theory (DFT) indicated that the higher polarity between the surrounding matrix and nanocrystal band structure makes the impact of the interface strain stronger than the quantum confinement [80]. Fig. 2.5 reflects how in a 2-nm diameter and OH–terminated nanocrystal, the interface strain reduces the band gap of the nanocrystal. In a less polar matrix such as silicon nitride (and as can be expected for a non-polar one like silicon carbide), the strain effect is not

dominant [76].

Dangling Bonds We discussed that the defects at the interfaces serve as the quenching centers for radiative recombinations in silicon nanocrystals. However, the dangling bonds also can act as the radiative defects and therefore contribute to the visible PL emission, which makes the interpretation of the luminescence from silicon nanocrystals more difficult. Godefroo et al. [81] applied electron spin resonance (ESR) [82] in an attempt to distinguish the origin of the PL emission in the silicon nanocrystals embedded in a silicon oxide matrix. They evaluated the absence or presence of defects through a repetitive process of adding and then removing hydrogen. They verified that defect-related radiative emissions were observed when hydrogen was removed by UV illumination and dangling bonds were no longer passivated. The silicon nanocrystals were small enough so that the effect of the passivation largely influenced the absence or presence of defect-related emission in the system. Fig. 2.6.a shows small nanocrystals (<3 nm) formed within the silicon dioxide matrix and the right panel, Fig. 2.6.b is the schematic of the energy levels of the surface states and highly-localized defects at the interface of silicon and host matrix (SiO_2) [81].

Overall, clearly, the origin of the PL emission of nanocrystals depends on the choice of the host materials. It is also an over-simplification to attribute all of the PL emission to silicon-ncs as explained by Canhams quantum confinement effect and dangling bonds at the interface. In fact, the radiative emission from the defects of the amorphous matrix itself can contribute to the PL spectrum. Now, the very important task is to understand the contributors to the emission process resulting from a combination of the nanocrystals, the interface of nanocrystals and matrix, and the matrix itself. Different silicon-based host structures are further discussed in

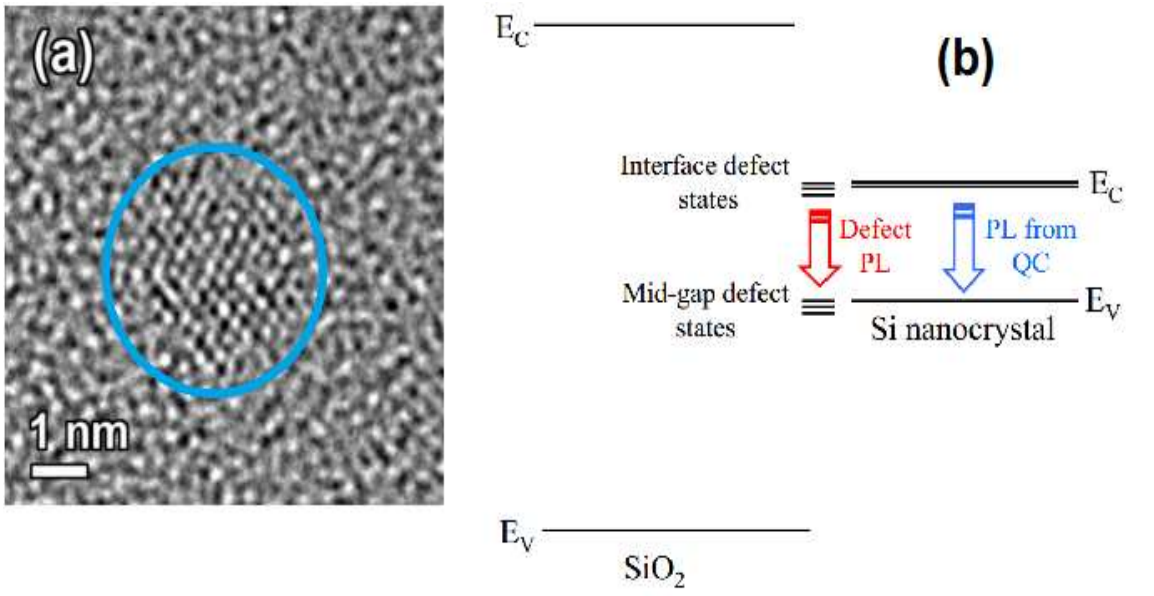

Figure 2.6: **Schematic of defects at the interface of silicon nanocrystals and the host matrix.** (a) TEM image of small nanocrystals (<3 nm) formed within the silicon dioxide matrix and one of them is highlighted by a blue circle; (b) schematic of the energy levels of the surface states and highly-localized defects at the interface of silicon nanocrystals and host matrix (SiO_2). Reprinted (adapted) with permission from [81].

the rest of this chapter.

2.3 Light Emission from Amorphous Dielectrics

It should be noted that in the present thesis, the crystalline structure of the host matrix is not a matter of concern. The goal is to form silicon nanostructures either in the form of crystalline or amorphous nanoclusters (ncs) inside a silicon-based material. The growth of silicon-ncs in a host dielectric is possible in any amorphous host matrix containing excess silicon relative to the stoichiometric requirements (so-called silicon-rich thin films). Before continuing the discussion of the light emission process from

different host materials, some aspects of amorphous materials associated with the light emission properties are introduced in the following subsections.

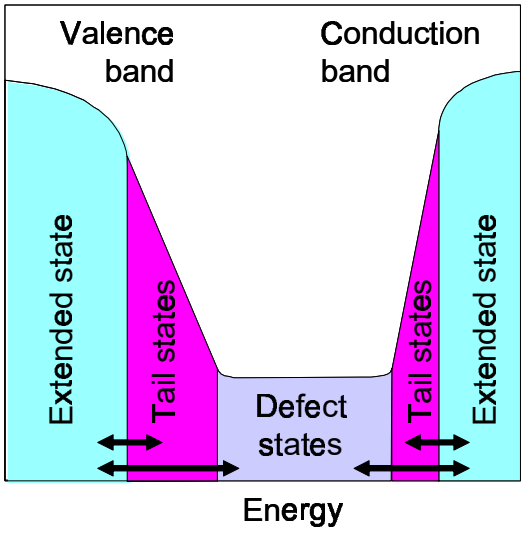

Figure 2.7: **Schematic representation of the density of states in amorphous silicon.** The localized states and defect states within the mobility gap in amorphous silicon are shown. The band tails create the exponential shape of the Urbach energy. Reprinted (adapted) with permission from [83].

2.3.1 Electronic Structure

Amorphous solids are known to have a disordered atomic arrangement. They are better described by a combination of long range disorders and short range orders preserving some characteristics of the crystalline counterparts in the short distance of a few nearest neighbors [84]. A random network model introduced by Zachariasen [85] is used to describe the electronic structure of an amorphous solid as well as its combined short and long range scales. The random network does allow atoms to coordinate with the neighbors in different configurations. Consequently, atoms with

more or fewer bonds than the ideal configuration give a metastable state, which is the specific feature of amorphous silicon-based materials, providing the opportunity to form silicon ncs embedded in silicon rich host matrices. The alternative bonding configurations in a metastable structure are characterized by the angle and length deviations from the ideal bond angles and/or by a different coordination number. In the case of deviations from the ideal angle, the charge distribution in the covalent bonds is strained making the electron and holes localized (bound states). The intrinsic structural defects generated by non-stoichiometric bonding configurations are different from the defects in crystalline solids such as point defects and impurities [86].

Although the number of localized states is large in amorphous materials, some delocalized states are found in a moderately disordered structure forming energy bands similar to crystalline counterparts. In this case, the energy levels of the localized states are positioned near the delocalized states at the band edges (conduction and valence bands). The main difference between the amorphous and crystalline structures is at the band edges where the energy tail of the localized states extends to the delocalized states. The mobility edge is then defined as the energy level that separates the localized states from the extended (non-localized) states [87]. Fig. 2.7 shows a schematic of the localized states as well as the interband gap energy levels of defects for an amorphous structure with a relatively small disorder. It can be observed that the energy states of defects are situated within the band gap showing a more well-defined character in compare to the localized states. Nevertheless, the density of the defect states and in particular the distribution of the band tail states mediate the optical absorption and luminescence. In the following subsections, the mobility gap and its calculations are discussed.

2.3.2 Optical Band Gap

The mobility gap of a disordered amorphous structure is populated by localized states that originate from disordered (strained) bonds and also defects (mainly dangling bonds). Although it is very difficult to precisely measure the mobility gap, it is believed to be associated with the optical gap. The optical gap is a consequence of the fact that the probability of optical transitions between the extended states and localized states is very similar to the direct band-to-band transitions between two extended states. This owes to the less probable and weak optical transitions between the localized states or between one localized and one extended state, which are hard to be observed. The optical transitions are described by the complex dielectric function (ε_1+iε_2 given by transition matrix elements). The imaginary part is associated with the absorption coefficient, which can be measured directly using absorption measurements such as the UV–VIS method and indirectly by variable angle spectroscopic ellipsometry (VASE) [88].

Fig. 2.8 shows a typical transmission spectrum obtained by UV-VIS measurements for one of the amorphous SiC_xN_y samples presented in this thesis as well as the reference corning glass. The noticeable oscillations at longer wavelengths originate from interference due to the internal reflections, depending on the refractive index and the film thickness [89]. The sharp absorption edge just below the band gap of the glass is related to the exciton transitions at the extended states (conduction and valence bands), indicated by dashed lines. The optical absorption spectrum of the amorphous SiC_xN_y (solid lines) shows an exponential curve reflecting the tail of the localized states; a smaller slope indicates a larger degree of structural (compositional) disorders. The bandwidth of the localized states is given by the Urbach energy (E_u),

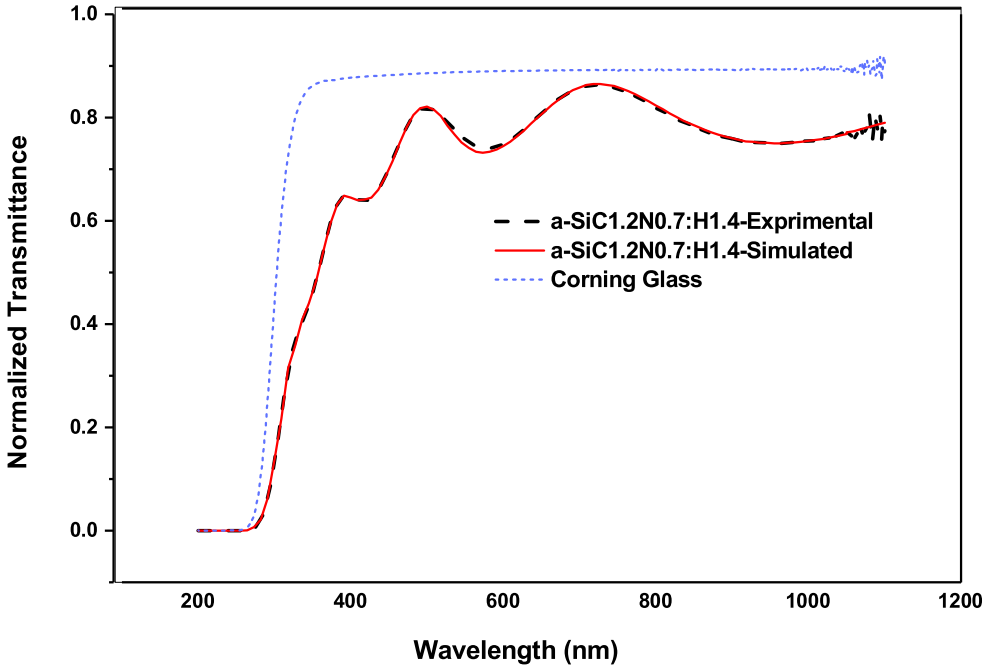

Figure 2.8: **Example of transmittance of amorphous materials.** The slope of the transmission spectra of amorphous SiC_xN_y (solid line) indicates the Urbach tail. The reference corning glass (dotted lines) shows a sharp absorption edge.

which is generally between 100 to 500 meV depending on the level of disorder [90].

Experimentally, the band gap of amorphous semiconductors is quantified using the absorption coefficient (α) given by the transmission measurements followed by employing a proper model. Various models exist to estimate the optical band gap energy from the optical absorption coefficient [91]. The optical band gap (E_{04}) is the energy, where (α) is equal to a standard value of 10^4 cm^{-1}. An alternative definition of the band gap is the Tauc energy gap (E_g), which is typically calculated by extrapolation of the linear Tauc plot showing $\sqrt{\alpha h\upsilon}$ vs the photon energy ($h\nu$) [92] according to Tauc relation as follows:

$$\alpha E = B(E - E_g)^m \tag{2.11}$$

where m is equal to 2 in amorphous silicon based nanostructures with indirect band gaps and B is the constant determined experimentally. Nevertheless, E_{04} was found to be much closer to the effective mobility gap of silicon based compounds given by theoretical suggestions [93]. In this contribution, E_{04} was calculated using both UV–VIS transmission spectroscopy and/or ellipsometry measurements in reflection and transmission modes.

2.3.3 Photoluminescence

The PL spectra of amorphous materials are rather broad compared to the relatively sharp PL peaks observed in crystalline materials. The broadening of the PL spectra originates from the distribution of the band tail and defect states serving as the two sources of radiative recombination in amorphous materials. In the known binary materials such as silicon (sub)dioxides the energy of the PL emission associated with the defects is well established. Fig. 2.9 shows the possible recombination pathways with the corresponding relaxation times in a confined silicon oxide nanostructure. As discussed in subsection 2.1, in the photoabsorption process after a certain time the excited electron recombines with a hole. The exciton-related emission from ncs on silicon (sub)oxide is red and in the timesclae of microseconds (slow), while the defect-related emission from the matrix itself or/and defects at the interface is blue and fast, on the order of nanoseconds [94]. The blue emission is expected not to change with the size of the nanocrystals while the red emission is found to be shifted to the higher energy side of the visible range with smaller size of nanocrystals according to

the discussed EMA model. Fig. 2.9 shows the red and blue photoemission and their corresponding lifetimes along with an extra ultrafast emission related to the quantum confinement in relation to the direct band gap of silicon (the second minimum of the conduction band after the absolute minimum (see Fig. 2.1). It is suggested that the quantum confinement influences the direct band gap in an opposite manner compared to the indirect band gap. Super fast transitions (picoseconds) are generated, where the band gap of silicon ncs narrows, but the associated PL peak of such "hot" transitions is intensified with decreasing ncs size [37]. However, Luo et al. [95] have recently published a correspondence, where the relation between the size of the crystals and the energy band gap of direct transitions was argued using a new method to measure the PL emission of one single silicon nanocrystal. Among all dielectric matrices to embed the silicon ncs, the interface between the ncs and silicon (sub)oxide is one of the most studied interfaces worldwide. The interested reader can find more widely available reference sources to study the defect contribution to the luminescence models of silicon oxide nanostructures [37].

The PL emission observed in the material presented in this thesis indicated that the presence of carbon in the silicon nitride or nitrogen in the silicon carbide structures formed a different chemical structure than that of nitride and carbide submatrices accompanied with different band-tail states and defects. In the next sections, three different common host dielectrics are briefly compared, where the focus is given to the light emission mechanism of the two non-oxidized silicon based matrices (silicon nitride and carbide) to be used for the investigations of SiC_xN_y thin films.

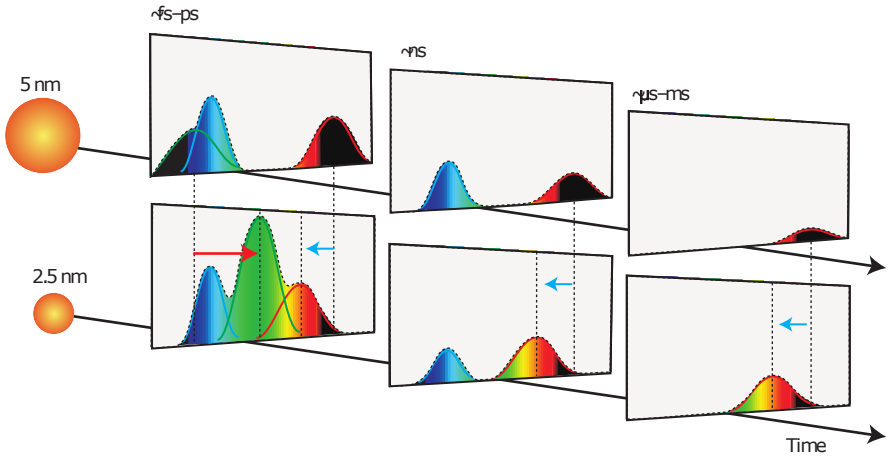

Figure 2.9: **Three luminescence centers in a silicon oxide matrix.** Three types PL emission of nanostructured silicon oxide have been observed so far: Red and slow emission on the order of nanoseconds associated with the indirect transition of silicon ncs; the fast and blue emission originating from the defects at the interface or matrix itself; the "hot" ncs-related emission from the direct band gap of silicon ncs on the timescale of picoseconds shown by green color. Reprinted (adapted) with permission from [94].

2.4 Host Dielectrics for Silicon Nanocrystals

Intensive research has been conducted on the introduction of new materials as the luminescent active layers in silicon-based light sources. The three major candidates to embed the silicon nanocrystals are silicon oxide, silicon nitride [96], and silicon carbide [97]. Silicon dioxide itself is easy to grow thermally and the oxide interface states of silicon ncs are found to be stable and protective to further oxidation in exposure to air. However, other than efficient extraction of light from silicon nanocrystals, the carrier transport needs to be taken into account in the application of silicon in electroluminescenct devices and light emitting sourcesSilicon dioxide itself is easy to grow thermally and the oxide interface states of silicon ncs are found to be stable and

protective to further oxidation in exposure to air. However, other than efficient extraction of light from silicon nanocrystals, the carrier transport needs to be taken into account in the application of silicon in electroluminescent devices and light emitting sources. Fig. 2.10 illustrates the barrier height between the silicon ncs and different host dielectrics. Silicon (sub)dioxide is a good insulator and hence it has the largest barrier height among all typical host dielectrics to form nanocrystals. On the other hand, silicon (sub)dioxide shows low electrical conductivity due to its wide band gap ($E_g \approx 8.8$ eV [77]), which is the major obstacle for this candidate. Alternative candidates such as silicon nitride and silicon carbide have been proposed offering better electrical properties with the advantages of relatively lower band gap compared to silicon oxide. The band gap of silicon nitride ($E_g \approx 5$ eV [78]) and silicon carbide ($E_g \approx$ 2.4-3.2 eV [79]), provides potentially higher conductivity compared to that of silicon dioxide. In the electrical device applications, the carrier requires traveling through dielectrics and the smaller band gap increases the carrier mobility. This means a larger probability for tunneling, and therefore, an increase of the carrier transport.

On the other hand, quantum confinement is effectively obtained by a sufficient height of the potential barrier between the ncs and the host matrix. A lower barrier limits the minimum size of the silicon ncs since the energy levels of smaller silicon ncs likely exceed the lower barriers. This makes the quantum confinement, in principle, not as strong as in silicon oxide materials. In addition, silicon nitride with a lower band gap inherently exhibits high defect densities affecting both the optical and electrical properties [99]. The main issue of silicon carbide with the lowest potential barrier and hence the greatest conductance is the crystallization of the host matrix before the formation of ncs. The complex surface states and defects [100] form a crystalline structure with characteristic length of about 30 nm that makes the quantum

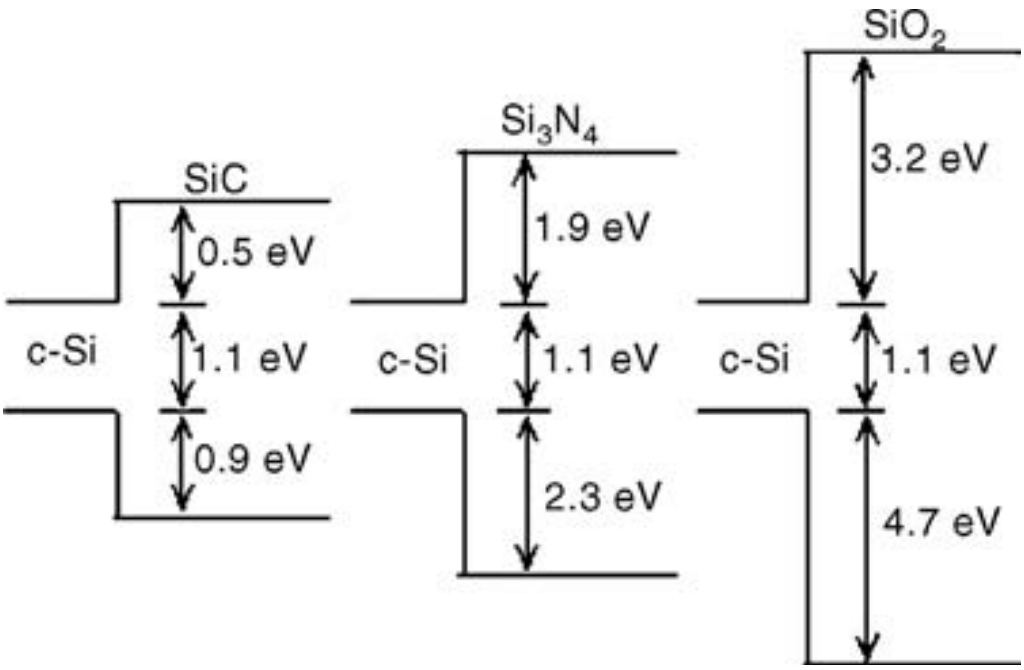

Figure 2.10: **Illustration of silicon ncs in different matrices.** A schematic band diagram and the barrier height for silicon nanocrystlas embedded in silicon dioxide, silicon nitride, and silicon carbide materials. Reprinted (adapted) with permission from [98].

confinement unlikely [101]. By far, the density of interface defects is the lowest in ncs embedded in a high-quality thermal oxide structure [73]; hence, they show the best properties in a studied matrix with the highest quantum yield of 10% [73]. Nevertheless, the efficient extraction of carriers from silicon ncs remains a challenging task to be accomplished and the ultimate solution seems to be the use of a conductive silicon compound [3]. Silicon nitride and silicon carbide can be regarded as better candidates for fabricating devices. In the following, the two non-oxide candidates are compared.

2.4.1 Silicon Nitride

Silicon nitride is an indirect band gap material that has two hexagonal (α and β) and one cubic (c) phases with an indirect band gap reported from 4.5 to 5.3 eV depending on the film composition. In contrast to the discovery of silicon ncs formed within silicon oxide dating back to 1990s, Park et al. [96] in 2000 demonstrated evidence for amorphous ncs formed in a silicon nitride film using PL and optical absorption measurements. One different characteristic of these ncs from the ones formed in silicon oxide was that PL emission could be obtained for untreated samples without the requirement of high-temperature annealing. They attempted to fit the Bruce model using the measured PL data to describe the luminescence of silicon ncs embedded in a silicon nitride matrix and suggested:

$$E(eV) = 1.56 + 2.24/a^2 \tag{2.12}$$

Following this suggestion, they continued to describe the light emission from the crystals or amorphous silicon nanoclusters by modifying the parameters of the proposed model, e.g. E_{bulk} was modified from 1.56 to 1.16 eV in [102] [103]. Later on, Kistner et al. [104] argued that even if the measured PL emission was fitted to the quantum confinement model, it did not necessarily mean that the observed luminescence was related to silicon ncs. They conducted a study on silicon nitride films, where their results could be nicely fitted and interpreted using the EMA theory and Park's modified model. However, transmission electron microscopy (TEM) measurements showed no evidence of silicon ncs. Instead, they could model the luminescence by the band tail emission interpreting the position of the PL band and the corresponding full-width half-maximum. Consequently, the remaining question was whether the

light emission was coming from the embedded silicon ncs or the silicon nitride host matrix itself.

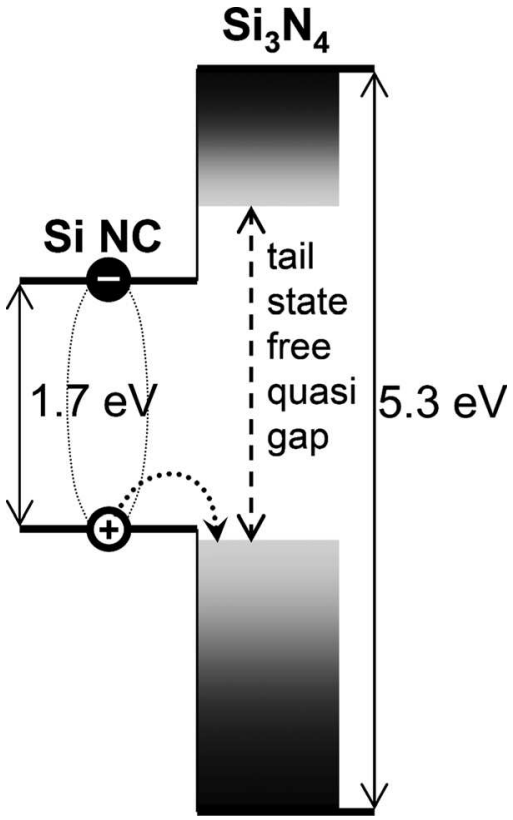

Figure 2.11: **A schematic band diagram of a silicon nc with no dangling bonds in Si_3N_4.** Illustration of a silicon nc with no dangling bonds embedded in Si_3N_4. The dotted arrows show the tail states approach where the extended states of silicon provides the opportunity for the exciton of ncs to lose its hole. If the remaining electron contributes to the Auger recombination, silicon ncs do not contribute to the radiative recombination regardless of the absence of non-radiative defects acting as the quenching center. Reprinted (adapted) with permission from [99].

Later on, Hiller in a collaboration with a large number of researchers [99] studied stoichiometric Si_3N_4 films as a reference sample where the formation of silicon ncs was unlikely. They fabricated alternating layers of Si_3N_4 and silicon rich silicon nitride

layers (superlattices of Si/Si_3N_4) providing a size control of silicon ncs in a range of 2.6 to 5.2 nm [105] [99]. They used the superlattice design since it is not an easy task to predict accurately the size distribution, morphology, surface states, and density of defects for the established process parameters. In a superlattice approach, alternating thin layers of the stoichiometric matrix and silicon-rich matrix are deposited to control the size of silicon ncs [106]. By controlling the size of ncs, the decay time of the PL emission was investigated using measurements concerning various temperatures, times, and excitation sources. Fig. 2.11 shows the suggested tail states approach, where the extended states of silicon provide the opportunity for an exciton of ncs to lose its hole. If the remaining electron contributes to the Auger recombination, silicon ncs do not emit radiatively regardless of the absence of non-radiative surface states and dangling bonds acting as quenching centers. This research group continued to attempt other complementary techniques such as positron annihilation spectroscopy (PAS) to identify the traps between the ncs and multilayers of silicon nitride and silicon oxide annealed at elevated temperatures. The increase of both PL and PAS intensity suggested that the positron trap at the interface does not contribute to the radiative recombination in ncs [107]. In general, this research group recommended to consider the contribution of the host matrix itself to the light emission in the application of particle in the box model to interpret the PL emission from silicon ncs.

Last year, Tsai et al. [108] reported the fabrication of a defect-free amorphous silicon nitride grown using two atomic beams (silicon evaporated beam and N_2-plasma), a method called plasma-assisted atomic beam deposition (PA-ABD). The PA-ABD is capable of removing Si-H and N-H bonds that are generating defect states serving as trap centers for the carriers. The goal of this study was to develop a high-quality defect-free silicon nitride structure for the gate insulators instead of the conventional

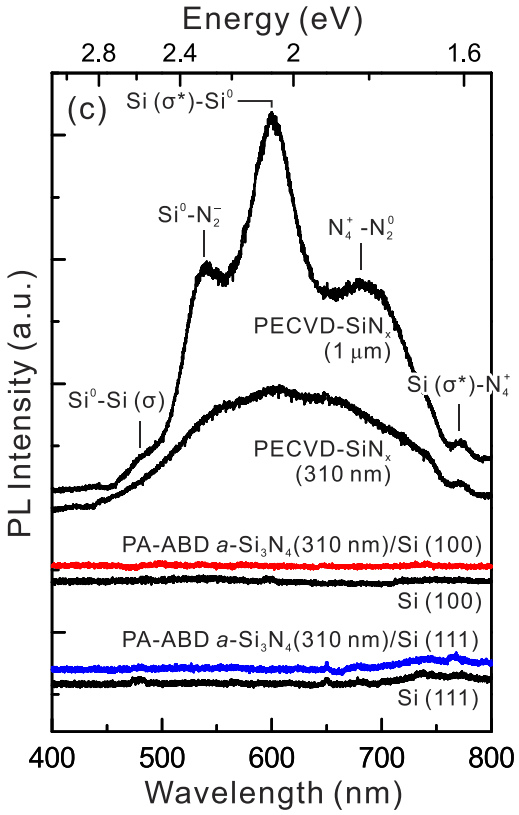

Figure 2.12: **Defect-related PL emission of amorphous Si_3N_4.** The defect-related emission from the non-annealed Si_3N_4 under illumination by a 325 nm laser source is shown and compared with the defect-free samples grown using PA-ABD method. The PL peaks positioned at 2.6, 2.3, 2.1, 1.8, and 1.6 eV are labeled with the corresponding defect for a thick enough sample. Reprinted (adapted) with permission from [108].

silicon oxide. As mentioned earlier, one of the issues with the use of silicon nitride is its large number of defects making moves through the trapping states, while a defect-free silicon nitride is expected to offer large breakdown field and a low leakage current.

The defect-related emission from a Si_3N_4 with no extra silicon can be applied to the subject of this thesis. Tsai and co-workers confirmed the defect levels by comparing the luminescence spectra of Si_3N_4 samples grown by conventional PECVD and the

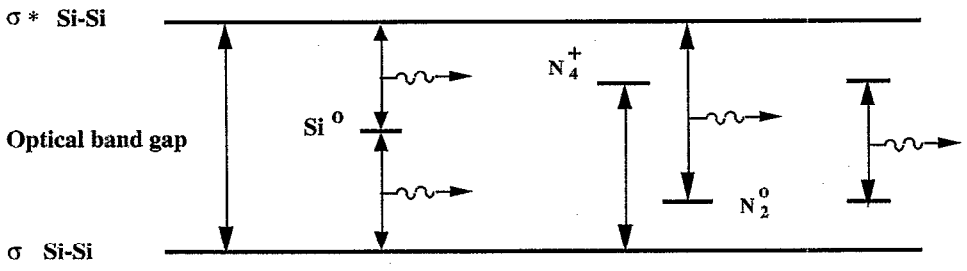

Figure 2.13: **Possible radiative defects in silicon nitride.** A schematic of the possible radiative defect centers is presented for an amorphous Si_3N_4 sample. Reprinted (adapted) with permission from [109].

relatively newly developed method, PA-ABD. Fig. 2.12 shows the defect-related emission from a non-annealed Si_3N_4 sample grown using a PECVD technique and excited by a 325 nm laser source. The PL peaks positioned at 2.6, 2.3, 2.1, 1.8, and 1.6 eV arising from Si^0-Si(σ) and Si^0=N_2, Si(σ^*)^0, N^{4+}-N^{20}, and Si(σ^*)-N^{4+}, respectively, were detected for thick enough samples. The observed peaks were consistent with the calculations performed by Robertson et al. [110]. From a theoretical point of view, Fig. 2.13 shows these interband gap defects related to Si-Si and N-N bonds, and Si and N dangling bonds [109], where the so-called K centers (related to silicon dangling bonds) are the dominant traps for the carriers. Fig. 2.12 shows that a more well-defined shape develops with increasing film thickness for the PL spectrum due to the stronger emission from defects. The room temperature PL spectra for the amorphous Si_3N_4 grown by PA-ABD on silicon (100)(red) and the silicon wafer (100) (black) are shown to verify the absence of the defect-related emission from samples grown using PA-ABS [108].

In summary, the visible emission of amorphous silicon nitride can be explained in terms of defect-related states serving as the radiative recombination centers. Upon

thermal annealing, at the lower temperatures, the PL intensity is improved due to the passivation of non-radiative defects. The PL intensity decreases with annealing at temperatures higher than 1000 °C due to the thermally induced changes, where reduction of the density of dangling bonds suppresses the defect-related emissions. In the silicon-rich silicon nitride, silicon ncs can contribute to the visible luminescence [102], which is enhanced at higher annealing temperatures. A combined visible PL emission from both defect-related states and silicon ncs in silicon nitride has been reported and still, no consensus is achieved to distinguish whether the radiative recombination occurs via quantum confined ncs or via highly localized defects [104].

Silicon Oxynitride Ternary matrices such as silicon oxynitride were attempted to take advantage of silicon nitride defects emitting with higher energies compare to that of silicon oxide in a silicon oxide matrix. Fig. 2.13 shows the energy states of radiative defects in a silicon nitride matrix. In silicon oxynitride compounds, the mixture of nitrogen-related defect states and oxygen-related defects results in extending the PL emission to more of the visible spectrum and an increase in the PL intensity [112] [111]. Similar to the aforementioned PL origin in silicon nitride samples, the PL spectra of silicon oxynitride thin films can be associated with the radiative defect centers related to both silicon oxide and silicon nitride structures as well as silicon ncs. Jou et al [111] implemented this model to amorphous SiO_xN_y thin films fabricated using reactive sputtering in an $Ar+N_2$ plasma with silicon target. Fig. 2.14 shows the decomposition of the PL spectra into five PL sub-bands associated with nitrogen and oxygen-related defects. The following subsection concentrates on the light emission of silicon ncs and defects in silicon carbide thin films. In chapter 6, the approach of deconvolution of the PL spectra and their link to the defects of silicon

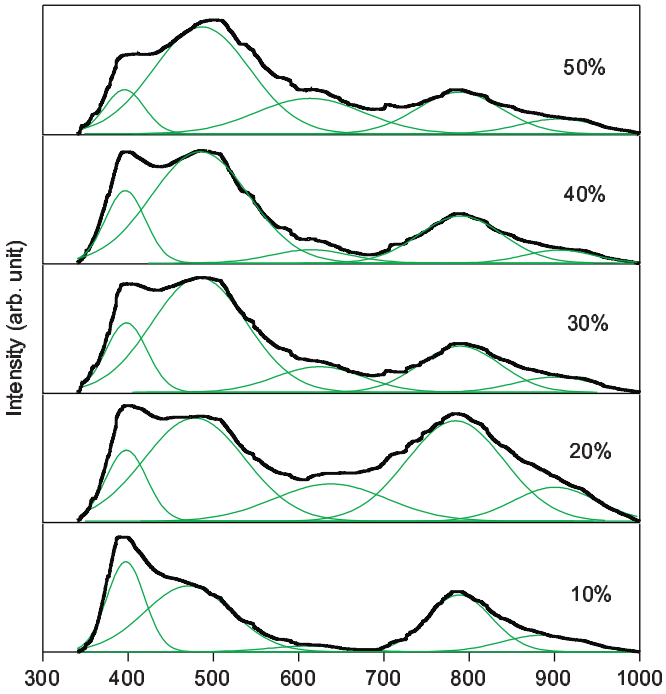

Figure 2.14: **Deconvolution of PL spectra of amorphous SiON.** PL spectra of amorphous SiO_xN_y layers containing various content of nitrogen are measured using a 325 nm excitation source. The percentage indicates the flow ratio of N_2 gas for the samples annealed at 900 °C in a vacuum ambient. Each individual PL peak is deconvoluted into five PL sub-bands and assigned to defect-related emissions. Reprinted (adapted) with permission from [111].

nitride and silicon carbide is taken to interpret the PL emission of the amorphous SiC_xN_y samples presented in this thesis.

2.4.2 Silicon Carbide

Silicon carbide is an indirect band gap material with more than one hundred polytypes - different crystal structures of a given material with varying stacking sequence. Only a few polytypes can be used in electronic devices. The most common polytypes

are listed as 3C-SiC, 4H-SiC, and 6H-SiC with band gaps of 2.3, 3.03, and 3.2 eV, respectively [113].

Although the first traditional diode LED was made of silicon carbide [114], the light emission of silicon carbid is less documented compared to silicon oxide and silicon nitride due to its lower success rate to form ncs. The challenge of silicon carbide nanostructures is to reduce the size of ncs to a few nm and avoid the agglomeration of small ncs [100]. Silicon oxide and to some extent silicon nitride act as the large diffusion barrier, which prevents highly ordered and spherical ncs during the phase separation process [73]. On one hand, silicon carbide with the lowest potential barrier forms likely highly spherical ncs; on the other hand, the smaller barrier provides more coalescence of small ncs so that the large crystals ($\sim$ 30 nm) reach the maximum limit of the quantum confinement.

Wu et al. [115] for the first time demonstrated the experimental evidence for the small size ncs (3C-SiC nanocrystals) formed within porous silicon carbide on the order of 2 to 6 nm that enhanced the luminescence efficiency and shifted the emission to higher energies (2.3 to 2.7 eV). They suggested the following equation as the best fitted model to EMA model explaining the size-dependent energy:

$$E^* = E_g + h^2/8\mu r^2 - 1.8e^2/4\pi\epsilon_0\epsilon r \tag{2.13}$$

where E_g=2.2 eV is the band gap of 3C-SiC. These samples were prepared using electrochemical etching of a polycrystalline 3C-SiC wafer in HF-ethanol (HF: C_2H_5OH 2:1) solution, where following a number of HF etchings the solution was coated on a silicon wafer [115]. Although prior to Wu's work, silicon carbide ncs precipitated in the amorphous silicon carbide layer grown using PECVD was reported to be formed

at annealing temperature of 575 °C, a specific quantum confinement model was not developed [116]. Fig. 2.15.a shows the TEM image of the suspension of porous SiC dripped on a graphite grid demonstrating relatively small spherical nanocrystals distributed separately within the porous silicon carbide background [115]. In contrast to Wu's sample, Fig. 2.15.b illustrates different polytypes of silicon carbide ncs (a mixture of 3C-SiC, 4H and 6H-SiC) distributed closely spaced and randomly in PECVD grown samples [116].

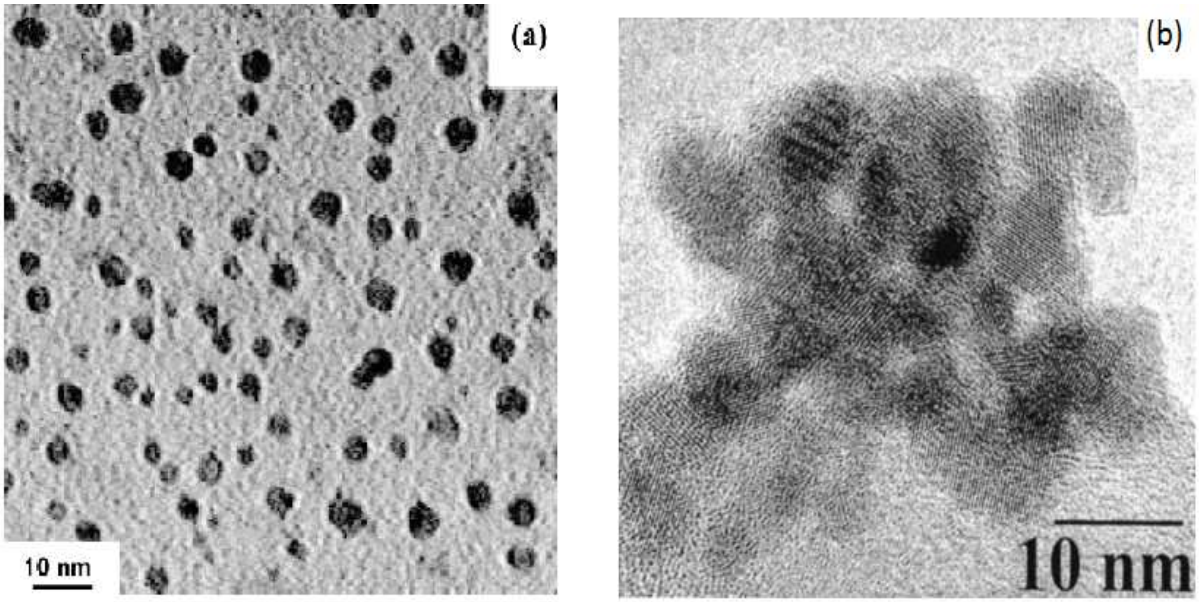

Figure 2.15: **TEM images of silicon carbide ncs.** TEM images indicate the existence of silicon carbide ncs in the amorphous host matrix with; (a) separated distributed ncs obtained using a chemical method [115]; (b) closely packed ncs embedded within the thin films annealed at 575 °C. Reprinted (adapted) with permission from [116].

Generally, the suspension liquid or SiC-polymer techniques are found to keep the small silicon carbide ncs separated and avoid the agglomeration of 30 nm crystals compared to ncs embedded in thin films [117] [118]. Some researchers attempted

to form small ncs within amorphous silicon carbide thin films. Wen et al. [119] demonstrated the formation of silicon ncs inside the hydrogenated silicon rich silicon carbide thin films grown using capacitively coupled (CC)-PECVD in a mixture of SiH_4 and CH_4. As one of the issues observed in the some works concerned with the PL emission from the silicon-based materials, no information on the samples' composition and hydrogen evolution was provided. Nevertheless, the PL spectra of samples excited by a 4 mW HeCd laser at 325 nm was fitted to six sub-bands using Gaussian curves (Fig. 2.16). The origin of four sub-bands was associated with the defects of the amorphous silicon carbide matrix and two PL bands were explained in terms of silicon ncs. The decomposition of individual PL bands is illustrated in Fig. 2.16 and agreed with the reported defects in silicon carbide. It was believed that the intensity of the PL bands related to ncs changed during the annealing process. The shift of the PL peak position to high energy regions of the visible spectrum was assigned to ncs using the quantum confinement model and the decrease in the PL peak intensity was attributed to the defects. Several researchers reported defects in silicon carbide structures. The PL line positioned in the near infrared region is well known as the fingerprint of the silicon vacancy defect, V_{Si} [120]. Castelloto et al. [121] associated the PL bands in the 600-800 nm range with the positively charged carbon antisite-vacancy pair defects, $C_{si}V_c$, the so-called AB lines. ESR and positron annihilation spectroscopy (PAS) experiments identified the AB lines as the dominant defect centers in H-SiC, which exhibit luminescence upon annealing up to 500 °C and in some off-stoichiometries up to 800 °C [122].

Although the luminescence properties of silicon carbide are less explored compared to those of oxide and nitride structures, unlocking the potential of silicon carbide for the use in LED applications is an interesting subject since silicon carbide materials

have been already well-established for harsh-environment applications due to their superior thermal and chemical stability [123] [124]. Recently, Lu et al. [125] fabricated a white light source using a hybrid structure, where 6H-SiC was co-doped with boron and nitrogen and coated with a porous layer by atomic layer deposition (ALD). They took advantage of a combination of the blue/green emission of porous SiC generated from the surface defects and the intrinsic yellow emission from the doped substrates.

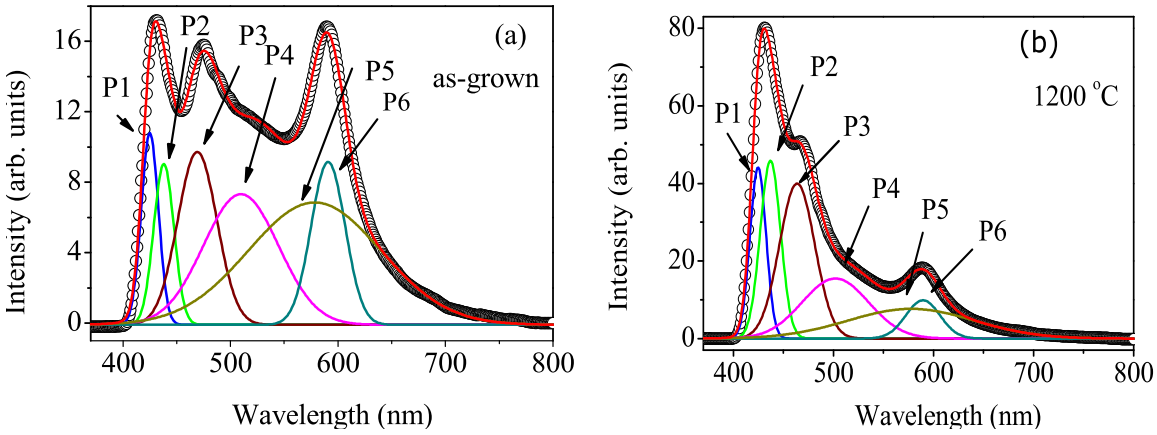

Figure 2.16: **Deconvolution of the PL of silicon carbide.** The deconvolution of PL emission coming from as-deposited and annealed amorphous silicon carbide thin film annealed at 1200 °C. The crystalline silicon carbide and silicon oxide related defects are suggested as the origin of PL emission. Reprinted (adapted) with permission from [119].

Silicon Oxycarbide The ternary material of silicon oxycarbide is attracting interest and one group has been investigating these films intensively [126] [127]. Kassiba et al. quantitatively and numerically studied the emission from fairly large 3C-SiC and 6H-SiC nanoparticles (10 to 25 nm) in a SiOC matrix grown synthesized by CO_2 laser pyrolysis of silane and acetylene. The measured PL spectra were explained in

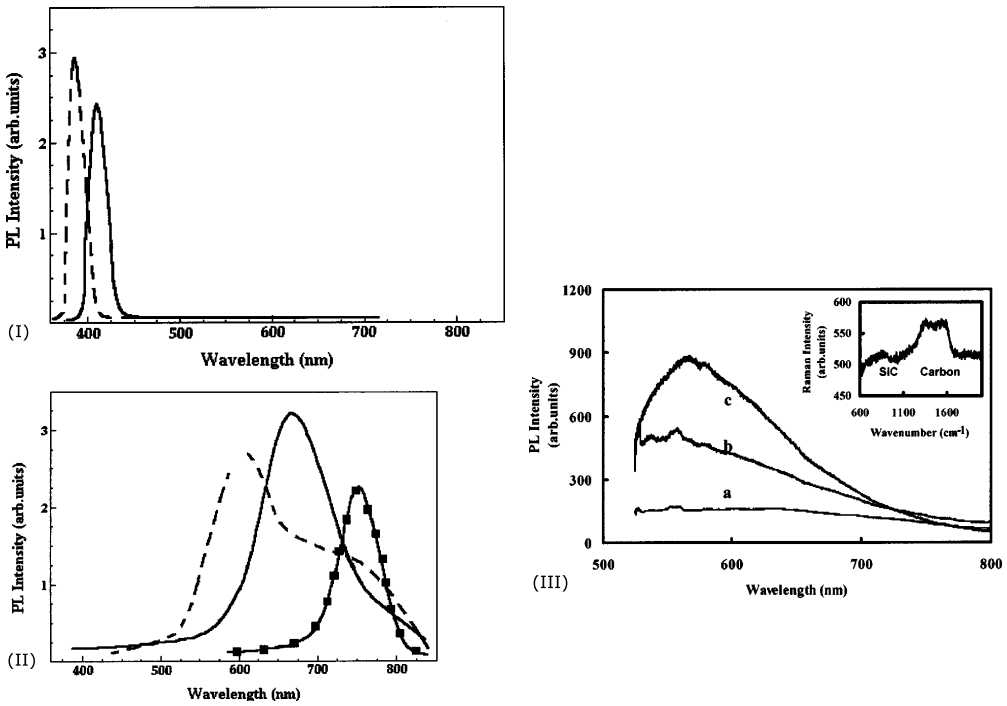

Figure 2.17: **Experimental and calculated PL spectra of SiOC.** I and II show the calculated PL spectra excited by a 337 nm source for crystalline and amorphous SiC clusters; (I) 3C-SiC (solid line) and 6H-SiC (dashed line); (II) amorphous structure (solid line), β-SiC with Si-O bonds (dashed line), and carbon cluster (line with square symbols); (III) measured PL spectra excited with a 514 nm source for (a) as-grown and annealed samples at (b) 440 °C and (c) 970 °C using oxygen ambient. The intensity of (a) and (c) is normalized to (b) by a factor of 1/3 and 1/10, respectively. The inset is the Raman spectrum of the untreated sample showing vibrational bands from carbon and SiC structures [97].

terms of the numerical calculation of the cluster-related and defect-related emissions (carbon and silicon vacancies). The samples were treated in an oxygen ambient and the radiative recombination from carbon clusters and Si-O bonds were suggested to be responsible for the radiative recombination. The calculated PL bands at 410 and 380 nm were assigned to 3C-SiC and 6H-SiC with optical gaps of about 3.02 and 3.26 eV, respectively (Fig. 2.17). Although the band gap of 3C-SiC and 6H-SiC nanoparticles decreased compared to that of bulk, it was attributed to confinement

effect. Nevertheless, this work has been used as one of the references to interpret the luminescent sources of SiOC thin films and some SiC_xN_y samples, where the oxygen contamination was significant that Si-O defects emitted radiatively.

2.5 Silicon Carbonitride

One cannot make a conclusive agreement on balancing the properties of discussed silicon-based compounds and suggest one of these compounds as the best material to be used for the luminescent silicon-based structure since each of them has its own limitations to be commercialized. A relatively new material, SiC_xN_y has shown unique properties inherited from the combined properties of binary substructures and at the same time, by overcoming their limitations [128] [129]. SiC_xN_y is a material, allowing to move from silicon-based structures rich in nitrogen to materials rich in carbon [130]. In the following subsections, a literature review of the luminescent studies on SiC_xN_y thin films is presented, with respect to the latest research developments. The various growth methods to produce thin films of SiC_xN_y are given, and the chapter ends with a discussion of present and future practical applications.

2.5.1 Light Emission from Silicon Carbonitride

Due to less studied optical features of SiC_xN_y thin films, no luminescent model has been suggested to explain the observed emission spectra from this compound. The existing literature on luminescent SiC_xN_y materials includes a limited number of PL studies reported with no further considerations concerning the origin of the light emission. In addition, some researchers discussed most likely sources of luminescence for SiC_xN_y thin films that contained a significant amount of oxygen, which can be

better viewed as SiCON films. Consequently, the Si-O defect-related emission was suggested as one of the contributors to the luminescent centers [27] [131]. Although the origin of the PL emission in a SiCON matrix is not a representative choice to be used for materials presented in this thesis, some of the well-acclaimed reports on SiCON thin films are outlined. Nevertheless, there is still no information available regarding the PL mechanism or any model controlling the PL of SiC_xN_y materials (with negligible oxygen content) in the literature.

We confirmed the amorphous structure of all samples investigated in this thesis by various techniques. The PL emission of such films with negligible oxygen content ($\sim$ 2 to 3 at. %) seemingly can be understood by the explanation of the light emission process in an amorphous material, where the tail state and defect-related transitions are the main contributors. The reason for this assumption can be found in the literature, where the band tail luminescence was assigned not only for amorphous silicon, but also for other amorphous silicon-based structures, see e.g. [132]. Furthermore, Pavesi and co-workers [133] studied extensively the alloying of silicon with nitrogen for a wide range of compositions (SiN_x where $0.15<x<0.52$). They believed that in contrast to amorphous hydrogenated silicon with the dominant, extended band to band transitions, alloying makes the structure more disordered, so that the PL mechanism can be explained in terms of band-tail and/or extra defect-related emission. In chapter 6 we discussed the probable luminescence mechanisms of SiC_xN_y thin films using the reported data of silicon nitride and silicon carbide structures that was discussed in the previous section.

2.5.2 Band Gap of Silicon Carbonitride

One of the interesting features of SiC_xN_y thin films is having a large compositional space allowing for extensive band gap optimization. In fact, the SiC_xN_y matrix has an intermediate band gap between that of stoichiometric SiC (2.4-3.2 eV) [97] and stoichiometric Si_3N_4 (5.0 eV) [96] providing the potential for band gap engineering. Furthermore, the smaller band gap of SiC_xN_y films compared to silicon nitride and silicon oxide structures provides better prospects for electron transports in electroluminescent devices [96].

Chen and co-workers have been one of the pioneers in the fabrication of crystalline SiC_xN_y thin films, who experimentally demonstrated 3.8 eV for the band gap of Si-rich SiC_xN_y crystals [26]. They employed a microwave PECVD at deposition temperatures above 800 °C to fabricate crystalline $Si_{35}C_{26}N_{39}$ thin films and investigated their PL emission and band gap. Its band gap was measured with piezo-reflectance (PzR) spectroscopy determining a direct band gap of about 3.8 eV. It was consistent with the photothermal deflection (PDS) experiments that delivered two absorption edges at 3.8 eV and 3.2 eV. The latter was associated with an indirect band gap and is shown in Fig. 2.18.a by solid lines [26]. However, they were not able to observe any PL emission related to 3.8 eV. The dotted line in Fig. 2.18.a shows an intense broad PL emission centered at 2.8 eV, likely due to the presence of a large number of defects [26]. Chang et al. [134] demonstrated PL emission associated with a 3.8 eV direct band gap in crystalline SiC_xN_y grown using rapid thermal chemical vapor deposition (RTCVD). Fig. 2.18.b shows one of the typical PL spectra showing a sharp PL peak with FWHM of 30 meV (4.1 nm) positioned at 3.77 eV (329 nm). The PL data was used to estimate the band gap for a UV detector. Their research was not

on the visible emission properties of SiC_xN_y materials and their PL mechanism.

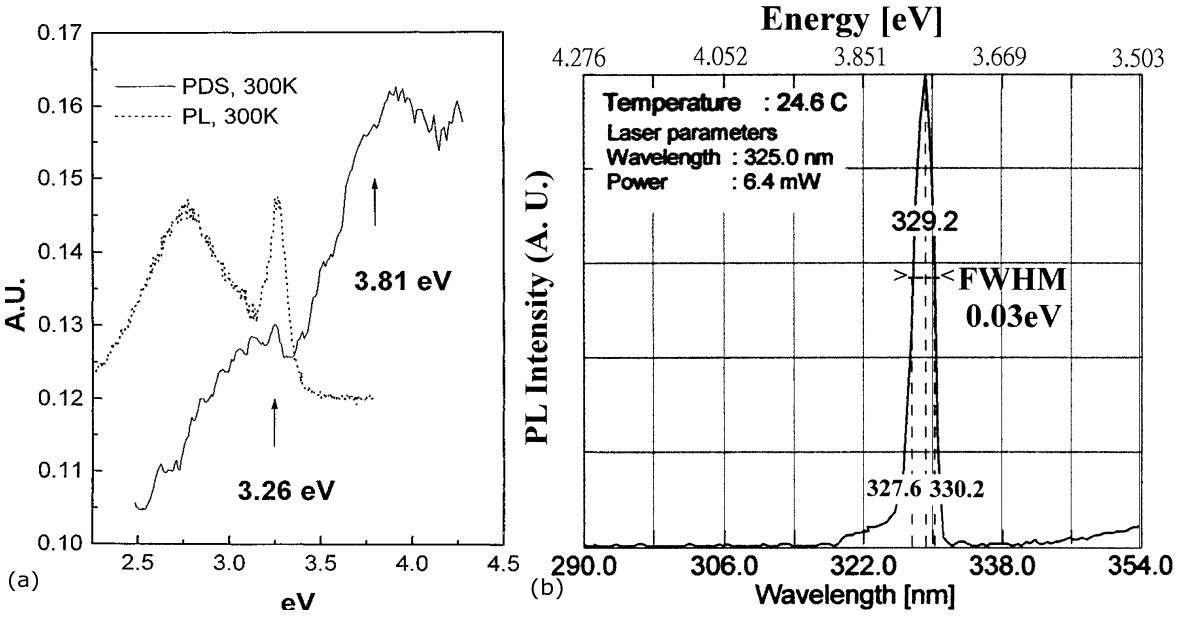

Figure 2.18: **First reported PL of SiC_xN_y.** (a) First reported PL of SiC_xN_y sample and the spectrum of photothermal deflection (PDS) measurements used to evaluate the band gap. Reprinted (adapted) with permission from [26]; (b) The PL spectrum of crystalline SiC_xN_y excited by a He-Cd laser. Reprinted (adapted) with permission from [134].

Later, Chen et al. [135] investigated comprehensively the electronic structure of SiC_xN_y materials using first principles calculations for the first time. Fig. 2.19 shows the band structure calculations of the phases present in SiC_xN_y thin films including α-Si_3N_4, α-Si_2CN_4, α-SiC_2N_4, $\alpha-C_3N_4$ structures, with band gaps of 4.62, 3.5, 3.34, and 3.69 eV, respectively [135]. They verified that the addition of carbon into SiC_xN_y layers increased the concentration of CN bonds as well as SiN bonds. The influence of carbon on the hardness properties of SiC_xN_y was linked to the theoretical calculations and no further discussion of the optical properties was provided.

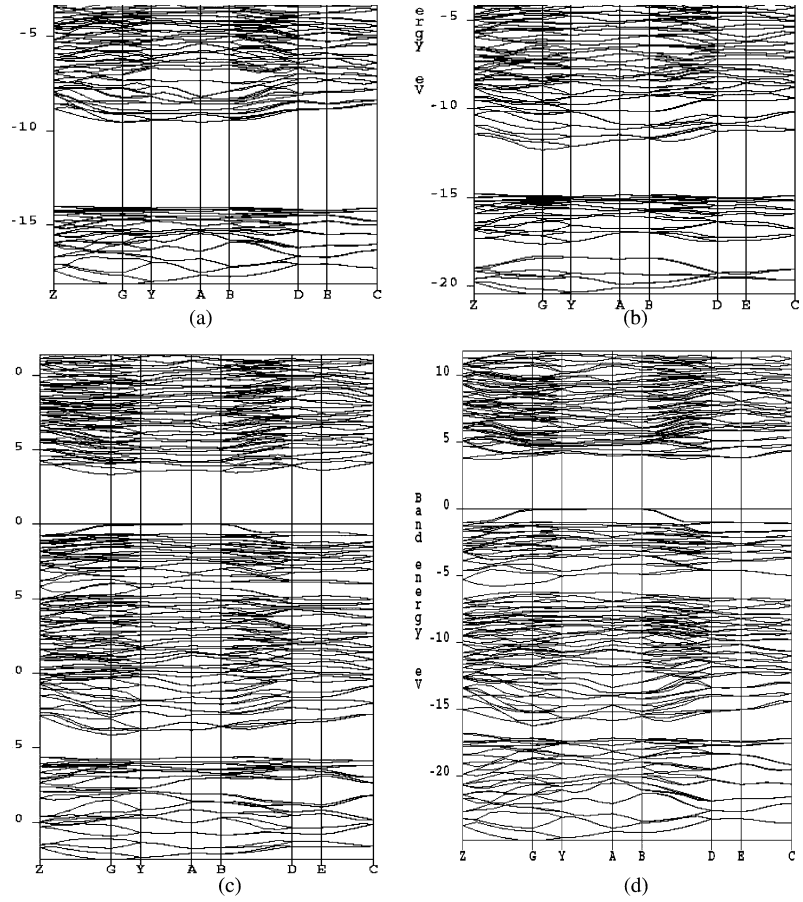

Figure 2.19: **Band structure of SiC_xN_y.** The calculation of the electronic structure of (a) α-Si_3N_4; (b) α-Si_2CN_4; (c) α-SiC_2N_4; (d) αC_3N_4 with band gaps of 4.62, 3.5, 3.34, and 3.69 eV, respectively. Reprinted (adapted) with permission from [135].

2.5.3 Reported Luminescence of Silicon Carbonitride

Ng et al. [27] employed radio frequency (RF) magnetron sputtering with a Si/C composite target in Ar+N_2 gas to fabricate SiC_xN_y thin films. Fig. 2.20 shows the visible PL emission excited using a 514 nm source as a function of different deposition times, which are broaden over the entire visible range. Large silicon carbide ncs were formed and the broad PL peak was assigned to their size distribution. As we explained in the previous section it is difficult to form small silicon carbide ncs due

to their tendency to coalesce. Therefore, with the increase of the deposition time, larger number of silicon carbide nanoparticles agglomerate together. Even though it was assumed that there was no oxygen in these nanostructures (as no oxygen was introduced intentionally during the growth process), significant Si-O bonds were detected in the structural analyses. Subsequently, the luminescent model developed by Kassiba et al. [97] for silicon oxycarbide compounds was employed to describe the PL mechanism. In addition, Ng et al. [27] presented more details concerning the deposition parameters and film composition of these samples, where the oxygen amount increased with the addition of more N_2 gas during the deposition. The oxygen concentration reached 40% in the samples making these samples more like oxygen-rich SiOCN layers.

Du et al. [131] [136] conducted a passivation study on the influence of different gases on the PL emission of samples grown using reactive sputtering with SiC target and Ar+N_2 plasma. The composition of the as-deposited sample was reported as a nitrogen-rich $Si_{27.6}C_{15.8}N_{49.6}O_{6.9}$ (containing low oxygen content) given by the energy-dispersive X-ray spectroscopy (EDS) technique. The samples was subjected to thermal annealing at 1200 °C for 30 minutes with different atmospheres of nitrogen, argon, and hydrogen. Argon annealing was found to induce a phase separation of carbon-rich and silicon-rich clusters while nitrogen was diffused out of the sample. Annealing in nitrogen virtually had no influence on the structure and phases of the sample. Fig. 2.21.a shows the X-ray diffraction (XRD) pattern of hydrogen annealed samples that formed three crystalline phases α-Si_3N_4, β-SiC, and graphite along with an amorphous silicon oxide phase $Si_{37.2}C_{5.8}N_{1.2}O_{55.7}$. Silicon carbide nanocrystals were large enough to be observed in the TEM image while no silicon nitride crystals was detected. Only the sample annealed with in hydrogen gas showed two intense PL

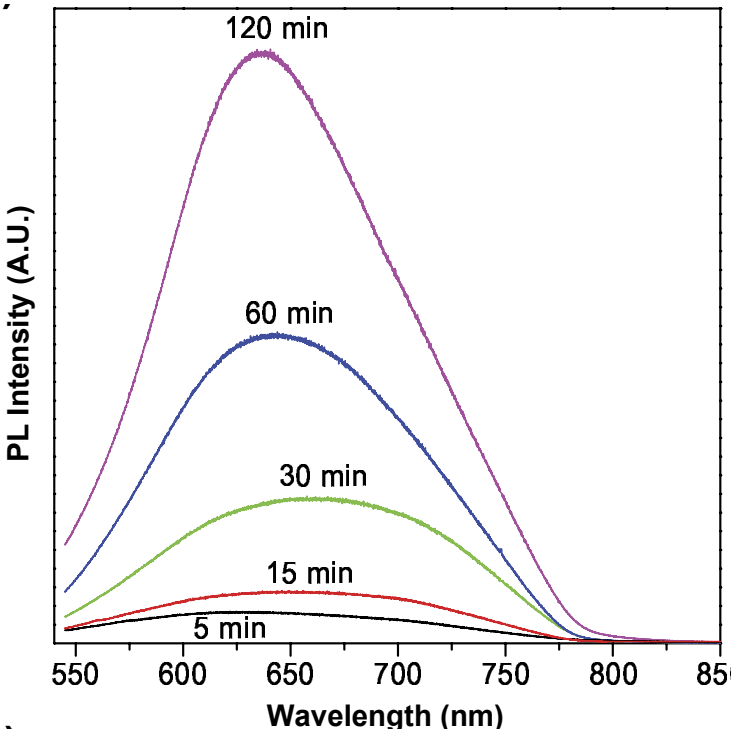

Figure 2.20: **Room temperature PL emission of SiCN films.** Visible PL emission excited using a 514 nm source as a function of deposition time. The origin of the luminescence was assigned to silicon carbide nanocrystals and silicon oxide-related defects. The broadening of the PL emission was associated with coalescence of crystalline silicon carbide nanoparticles with the increase of deposition time. Reprinted (adapted) with permission from [27].

peaks at 355 nm (3.49 eV) and 469 nm (2.64 eV) (Fig. 2.21.b). Si-O defect-related PL was suggested as the source of the first PL peak. The second PL emission was explained in terms of the quantum confinement model for silicon carbon ncs. The authors believed that during the argon and nitrogen annealing, oxygen atoms prevented silicon atoms from bonding with carbon atoms leading to no formation of silicon carbide crystallites. Only hydrogen annealing prevented oxygen atoms to form bonds with silicon carbide nanostructures, which allowed silicon carbon nanocrystal with an

average size of 5 nm formed within an amorphous background of silicon oxide.

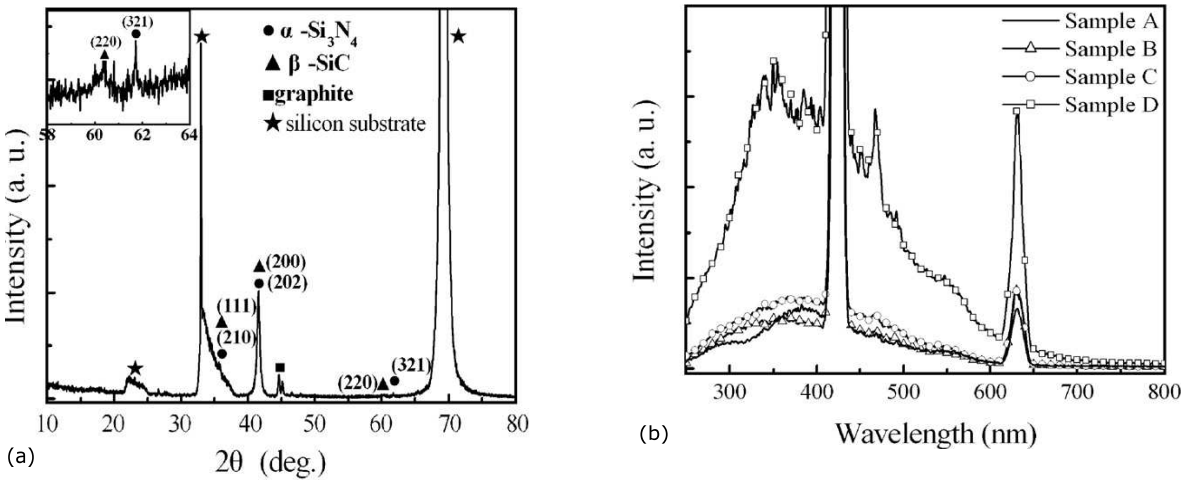

Figure 2.21: **XRD pattern and PL emission of sputtered SiC_xN_y.** $Si_{37.23}C_{5.88}N_{1.23}O_{55.66}$ samples (containing oxygen) annealed for 30 minutes using hydrogen gas; (a) XRD pattern shows the three crystalline phases of graphite, silicon carbide, and silicon nitride; (b) PL spectra excited by a 211 nm excitation source delivers two virtual peaks at 422 and 633 nm due to the frequency multiplication. The PL peaks at 355 nm (3.49 eV) and 469 nm (2.64 eV) were assigned to confined silicon carbide nanocrystals and SiO defects, respectively. B, C, and D are the samples annealed using argon, nitrogen, and hydrogen gas, respectively. Reprinted (adapted) with permission from [131].

Although this study discussed the control of the silicon carbide ncs sizes in an amorphous silicon oxycarbide matrix, it cannot be applied to distinguish the origin of PL emission of SiC_xN_y thin films due to the following two reasons: First, the annealing in nitrogen and argon was reported to induce no influence and phase separation, respectively. However as shown in Fig. 2.21 the PL spectra of all samples have some structure that is intensified in the samples annealed using hydrogen gas. The similarity of the PL emission of an amorphous structure (sample C) and phase separated samples (sample B) with a polycrystalline sample (sample D) has not been taken into account making the reported composition of the phases formed at higher temperatures

questionable. Second, the formation of such oxygen-rich phases leads one to question the initial oxygen level reported for the as-grown sample. The as-grow samples initially contained high level of nitrogen (about 50 at. % of the layer), which gave a possibility that the reported oxygen level was higher than 7 at. %. It is possible that nitrogen and oxygen content were mixed in the EDS analysis, since the fraction of silicon-nitrogen phases in the sample annealed with hydrogen gas was very small and no nitrogen was found for the sample annealed with argon gas. The authors, however, did not discuss this possibility in [131] or other related works [137] [136]. In [137], they applied X-ray photoemission (XPS) to determine the composition of the films where all growth parameters were similar to the samples studied in [131], except for for nitrogen, the concentration of which at was 3 times higher than that of [131], but the sample in [137] contained lower nitrogen and higher oxygen ($Si_{34.7}C_{26.5}N_{25}O_{13.8}$). Overall, Du and coworkers performed compositional analysis using EDS and XPS, which are less accurate compared to other compositional techniques such as RBS employed for the research presented in this thesis. Their samples can be better viewed as SiOCN thin films rather than SiC_xN_y. It is worth mentioning that different gases were tested for our annealed samples and no significant difference was observed for the PL emission. We confirmed that there was no significant reduction of nitrogen for our annealed samples at elevated temperatures using the combined RBS-EDR measurements (chapter 5).

Huran and coworkers shifted their interest from silicon oxynitride to SiC_xN_y thin films using nitrogen ion implantation into silicon carbide to increase the conductivity of silicon nitride thin films [138]. They deposited amorphous SiC_xN_y thin films using PECVD and observed two PL bands positioned in a range from 420 to 470 nm and 500 to 610 nm in the room temperature PL spectrum [139]. The origin of the blue

emission remained in doubt and the second PL band was attributed to the band-band transitions. Then, a study on the influence of deposition temperature on the PL emission of the samples grown using ECR PECVD was conducted. The changes in the PL spectra were assigned to the lower quality of the films due to hydrogen loss and fewer passivated dangling bonds without any discussion of the assigned PL model [140].

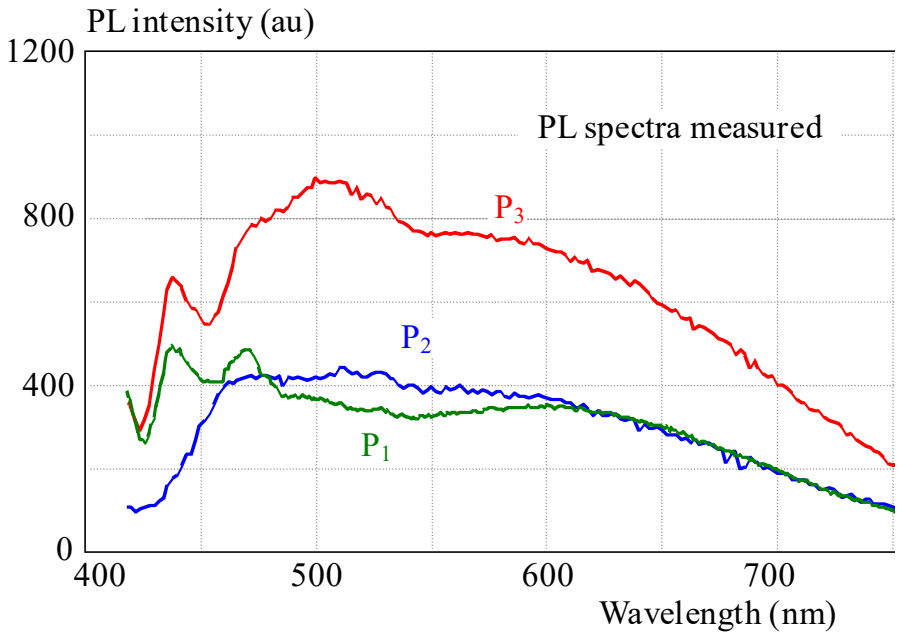

Figure 2.22: **Low temperature PL emission from different SiC_xN_y thin films** PL spectra of as-grown SiC_xN_y thin films deposited using PECVD and measured at 5 K temperature are compared. The P1, P2, and P3 samples were prepared using deposition temperatures of 350, 400, and 450 °C. Reprinted (adapted) with permission from [141].

A year later, Huran and colleagues performed PL measurements close to zero

temperatures (5 K) for three samples grown at three different deposition temperatures, where all samples showed PL bands at 550 and 750 nm as illustrated in Fig. 2.22 [141]. The P1, P2, and P3 samples were prepared using deposition temperatures of 350, 400, and 450 °C containing silicon, carbon, nitrogen, and hydrogen as follows: P1 (30, 25, 25, 24 at. %), P2 (29, 23, 28, 22 at. %), and P3 (30, 22, 30, 20 at. %), respectively. The higher deposition temperature made a third PL peak pronounced at around 610 nm and the intensity of the high energy side of the visible range was enhanced. The authors clarified "in amorphous materials the luminescence originates in the band to band transitions (more precisely, transitions between tails in energy bands) and band (band tail) to discrete level transitions, where discrete levels originate in structural defects. Hence, we assign luminescence bands to these two fundamental transitions" [141] and left the origin of the peak around 450 nm unidentified.

Wu et al. [142] fabricated SiC_xN_y thin films using dual ion beam reactive sputtering at room temperature and different energies. The PL emission excited with a 220 Xe lamp showed two peaks at 410 nm (3.03 eV) and 468 nm (2.64 eV), Fig. 2.23, with virtually unchanged position regardless of the ion beam energy used during the growth process. They assigned the first PL band to the defect related to carbon clusters in the surrounding silicon carbide matrix and the second emission in blue color to sp^2 carbon bonds. The PL model used for the first PL peak had been previously developed for silicon carbo-oxide structures containing no nitrogen. The second PL emission was referenced from [137] as discussed earlier where the samples could be viewed as SiOCN films. Furthermore, no accurate information was provided on the sample composition and the possible source of oxygen was not elaborated.

Ivashchenko et al. [144] fabricated amorphous SiC_xN_y thin films using PECVD

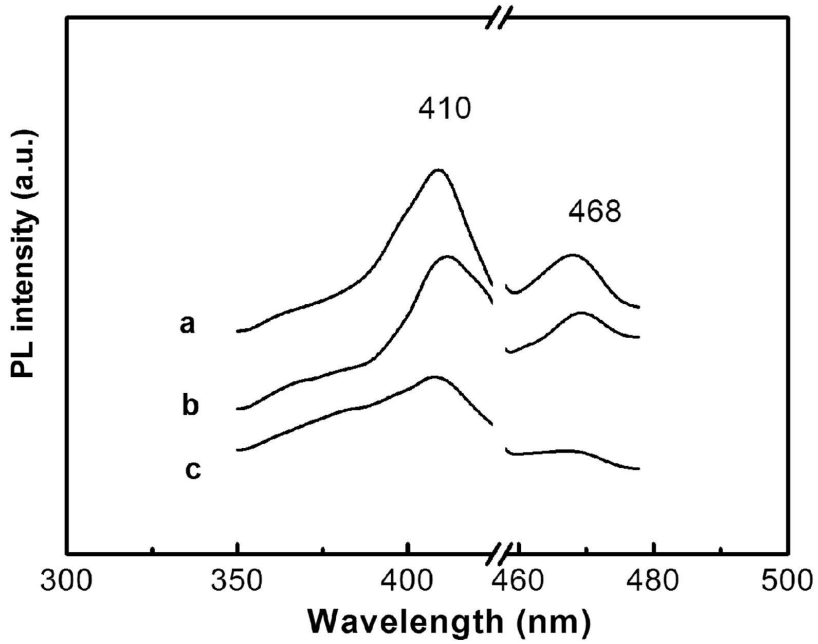

Figure 2.23: **PL emission of SiCN films excited by a 220 nm laser source.** PL emission of SiCN thin films excited by 220 nm Xe lamp shows two peaks at 410 nm and 468 nm for all samples grown using different ion energies. Reprinted (adapted) with permission from [142].

with hexamethyldisilazane (HMDSN) and different nitrogen flow rates at a substrate temperature (T_s) of 450 °C. The structural aspect, PL, and hardness of the films were investigated along with some ab-initio calculations of amorphous SiC_x, SiC_xN_y, SiN_y, and Si_3N_4 [145]. The samples were excited using a Hg lamp with a UV filter ($\lambda \sim 365$ nm), where the PL peaks at 428 to 490 nm and 583 to 594 nm were assigned to a-SiC_xN_y and a-SiC_x, respectively. As shown in Fig. 2.24, nitrogen was found to increase the first PL peak (428 to 490 nm) related to the a-SiC_xN_y network confirming their hypothesis on the origin of emission [144]. In addition, they considered that the photoemission was due to the transitions between the tails in energy bands within a-SiC_x and a-SiC_xN_y. Although the composition of $Si_{0.37}C_{0.37}N_{0.25}$ implied that the film was free of oxygen, the electronic structure of the samples was discussed in terms

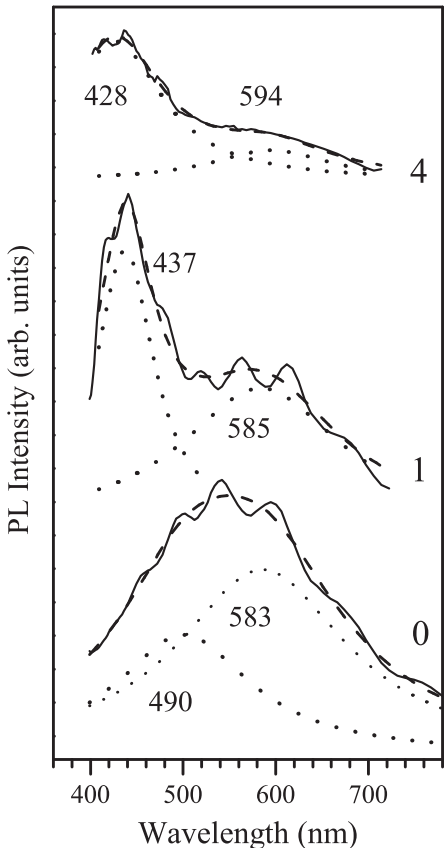

Figure 2.24: **Room temperature PL emission of sputtered SiCN.** PL spectra of SiC_xN_y thin films deposited using different nitrogen flow rates (solid line), excited using a Hg lamp with a UV filter ($\sim$ 365nm). The dotted lines indicate the Gaussian curves fitted to experimental spectra. Reprinted (adapted) with permission from [143].

of oxygen-related bonds. In addition, no discussion was provided on the influence of hydrogen on the band gap states while the PL emission from the defect states was suggested as the luminescent center in conjunction with a PL model developed for silicon oxycarbide thin films [97]. The subsequent articles by Ivashchenko and co-workers (A. Kozak, L.A. Ivashchenko, and O.K. Porada) did not concentrate on any further analysis of the luminescence mechanism and shifted to mechanical studies of SiC_xN_y thin films [146] [147] [148].

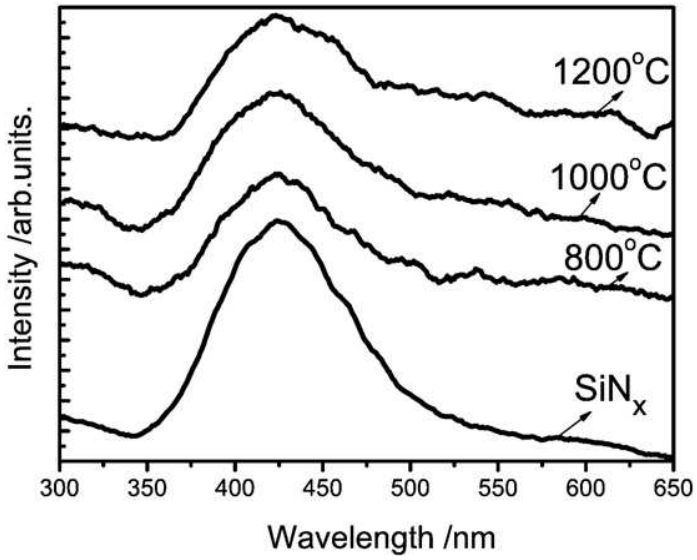

Figure 2.25: **PL emission of carbon-implanted silicon nitride.** PL spectra was measured at 20 K using a UV laser at 197 nm. The amorphous SiN_x and the annealed samples of SiN_x implanted with carbon ions show broad features centered at 420 to 460 nm and 570 to 620 nm. Reprinted (adapted) with permission from [149].

Liu et al. [149] implanted carbon ions into crystalline hydrogenated silicon nitride thin films and measured the PL emission at low temperatures using a UV excitation of 197 nm. The broad PL spectra of as-grown and annealed samples are illustrated in Fig. 2.25 showing that the characteristic Si-N emission at 420 nm (2.95 eV) appeared in both non-implanted and implanted samples. The Gaussian fitting delivered four sub-bands positioned at 420 nm (2.95 eV), 480 nm (2.58 eV), 541 nm (2.29 eV), and 584 nm (2.12 eV). The SiC_xN_y and SiC structures seemed to be responsible for the emissions at 480 nm and 541 nm, respectively.

Bulou et al. [150] [151] studied the influence of carbon and other deposition parameters on SiC_xN_y layers grown using microwave PECVD with HMDSN, N_2, Ar, CH_4 plasmas. Bulou et al. [152] earlier had used in-situ optical emission spectroscopy (OES) to investigate the dominant reactions during the deposition of SiC_xN_y thin

films. Although this research group was involved with the experimental and numerical study of SiOC materials [97], no luminescence from SiC_xN_y compounds was reported. The structural properties of the SiC_xN_y films produced by this group were similar to our SiC_xN_y samples reported in this thesis.

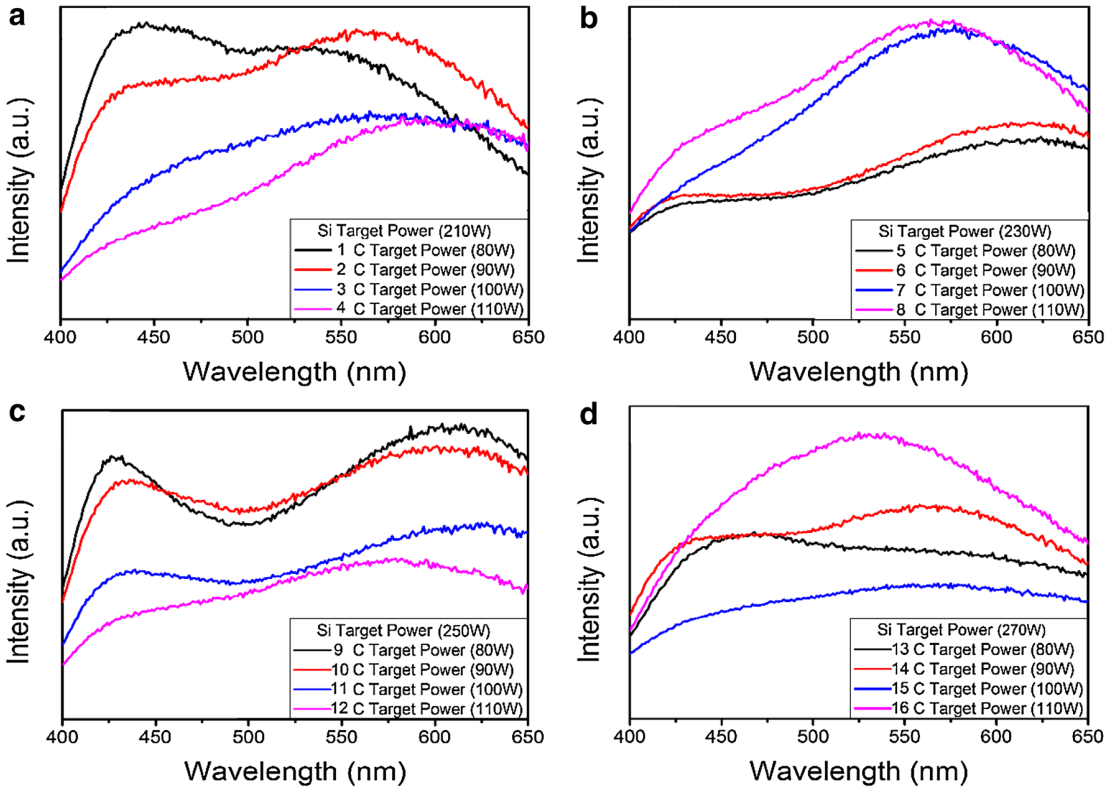

Figure 2.26: **Broad PL emission of SiC_xN_y.** PL spectra excited using a UV laser at 335 nm showed broad features centered at 420 to 460 nm and 570 to 620 nm assigned to carbon clusters and silicon carbide ncs, respectively. With increasing of sputtering power of the carbon target, the intensity of PL peak (around 600 nm) increased due to the shrinkage of silicon carbide ncs size. Reprinted (adapted) with permission from [153].

Recently, Li et al. [153] studied luminescent samples fabricated using reactive magnetron sputtering with an $Ar+N_2$ plasma, where the silicon and carbon content were adjusted by the sputtering power. Fig. 2.26 represents the room temperature

PL spectra excited using a UV laser at 335 nm that showed broad features centered at 420 to 460 nm and 570 to 620 nm assigned to carbon clusters and silicon carbide ncs, respectively. The size of the 3CSiC nanoparticles was estimated to lie between 11 and 18 nm using X-ray diffraction measurements and the Scherrer equation (XRD equation). The authors believed that due to the quantum confinement effect, with sputtering power increase of carbon target the relative intensity of the second PL peak (around 600 nm) to the first peak (around 450 nm) increased due to the enhancement of quantum confinements and shrinkage of silicon carbide ncs size. They employed a silicon oxide structure as a reference for the PL model to assign the PL peak positioned at the lower visible range. Regardless of their interpretation of the quantum confinement model of silicon oxide nanostructures in their SiOCN samples, the role of carbon can be understood. Fig. 2.26 shows that more carbon in the layer made the PL more intense implying the contribution of Si-C structures to the PL emission.

Similar works to the ones mentioned above have been published on PL studies of SiC_xN_y, however, no additional PL mechanism was reported by these authors, see e.g. [154] [155]. In addition, some important contributions concerning the structural properties of thin films were also published without a focus on the luminescent emission, see e.g. [156] [157] [158] [159] [160] [161] [162] [163].

2.5.4 Growth Methods

SiC_xN_y thin films have been produced using several methods including pulsed laser deposition [164] [165], ion beam and reactive magnetron sputtering [27] [142], and various chemical vapor deposition (CVD) techniques such as hot wire CVD [158] and

plasma-enhanced CVD (PECVD) [166]. The growth of SiC_xN_y thin films is not a very easy task due to the possibility of the formation of SiC and SiN phases in the SiC_xN_y network. The methods and conditions of the growth affect the phases formed within the deposited layer. Among the above techniques, plasma-assisted deposition allows the formation of amorphous nitride and carbide at much lower temperatures than those deposited by conventional CVD [141] [167]. High-temperature growth is one of the drawbacks in the production of commercialized devices. Plasma-assisted techniques also provide higher homogeneity of films over the substrate surface, which enhances the formation of the SiC_xN_y phase. ECR PECVD, similar to other plasma-assisted thin film deposition techniques, allows for the formation of Si-H_n ions to produce amorphous materials. The common precursors used in a PECVD method (SiH_4 and CH_4 or C_2H_2) introduce hydrogen, which partly induces the formation of amorphous structures. The extra hydrogen content disorders the bonding structure between silicon and other atoms such as carbon or nitrogen. This can be achieved by breaking the Si-Si bonds in amorphous or crystalline silicon, Si-C bonds in silicon carbide and Si-N bonds in silicon nitride structures [168]. In chapter 5, we experimentally show that the optical properties of the thin films (PL, refractive index, and optical gap) strongly vary with the hydrogen content and diffusion. It is worth mentioning that, in addition to the visible light emission of nanostructured SiC_xN_y materials, which has not been reported in details, little research has been conducted on the release of hydrogen and microstructural changes resulting from the thermal treatment on hydrogenated $SiC_xN_yH_z$ thin films [28] [29].

2.5.5 Applications of Silicon Carbonitride

Besides the potential use of SiC_xN_y materials for light sources, these lumisnencet materials can be used for other applications as will be briefly discussed. These applications have received attention due to superior physical characteristics of SiC_xN_y such as hardness, high thermal stability, oxidation resistance, and corrosion resistance. In fact, SiC_xN_y materials have appeared as an intermediate matrix to meet the demands in hard coating applications. Concurrently, the tunability of their electrical and optical properties has appealed their interest in the field of photonics. Crystalline ceramic SiC_xN_y has been found to be a suitable candidate for high pressure sensors for service temperature ranges above 1400 °C [169]. Returning to the primary intention of this research topic, hydrogenated amorphous SiC_xN_y thin films have attracted the interest of scientists for potential applications in thin film devices. In general, silicon can operate at lower temperatures of hundreds of degree Celsius, which is the major barrier for the application of silicon at high temperatures above 500 °C, where the functionality of MicroElectroMechanical system (MEMS) devices is limited [129].

Since the early 1970s, SiC_xN_y compounds have been of particular interest to research in the ceramic community (Si_3N_4SiC composites) [170], however, in 1996 a break through happened and Riedel et al. [171] reported an amorphous SiC_xN_y compound that featured an oxidation resistance up to 1600 °C owing to the low diffusion coefficient of oxygen in SiC and SiN phases. Following the fabrication of first crystalline SiC_xN_y thin films [26], this ternary material started to receive attention in the attempts to make crystalline carbonitride (C_3N_4) considered as a super hard hypothetical and non-existing compound [172].

In fact, carbon-based thin films do not offer the required properties for current

optical designs [173] and silicon nitride materials have been considered as the basis for several optoelectronic devices [174]. On the other hand, the durability and hardness of silicon nitride structures cannot compete with those of carbon-based hard counterparts such as diamond-like carbon, carbonitride, and silicon carbide compounds [24]. The combination of C_3N_4 and SiN_x structures, therefore, appears as a good strategy to employ the hardness of carbonitride in a more stable silicon-based matrix [175]. This is confirmed by the fact that the hardness of SiC_xN_y thin films exceeds that of silicon carbide and silicon nitride layers [172]. A number of studies show that the addition of carbon to silicon nitride phase yields an increase of hardness and wear resistance. For example, SiC_xN_y structures has appeal to researchers for wear-resistant [176], corrosion-resistant coatings [175], and recently for silicon-based anode materials in lithium ion batteries [177].

The presence of carbon in the silicon nitride matrix, in addition to the enhancement of the mechanical strength, offers advantages over standard silicon nitride thin films as barriers against copper diffusion in low k materials [178]. It already has been well established that in order to reduce the RC delays, the metallization of integrated circuits requires low k dielectrics [179]. The dielectric constant of the conventional silicon nitride barrier is reported as 6.5 to 7.0 and that of porous (hydrogenated) silicon oxycarbide materials is about 2.6, where the incorporation of hydrocarbons decreases the dielectric constant of SiO_2 [180]. SiC_xN_y thin films prepared by radio frequency PECVD at low-temperature showed a dielectric constant between 3.6 and 4.6 [181] [182]. The presence of carbon in the silicon nitride matrix disrupts the interconnectivity of the Si-N-Si network, leading to a lower dielectric constant closer to that of silicon oxycarbide thin films. This was investigated by some researchers for SiC_xN_y and C-rich SiC_xN_y dielectrics instead of conventional silicon nitride [178]. In

2017, a research group from IBM compared the dielectric constants of two different SiC_xN_y thin films with different hydrogen contents fabricated using PECVD and a mixture of NH_3+TSMH gases. The motivation of their work was to develop a second generation robust, low-hydrogen, SiC_xN_y thin film for copper capping [183]. The new SiC_xN_y cap contained a high density of Si-C and Si-N bonds, which showed improvements in oxidation and mechanical properties associated with the copper diffusion barrier functionality.

The other driving force to add carbon into silicon nitride barriers is the mechanical integrity of the interface used in copper interconnect technologies for adhesion purposes. In general, a high dielectric breakdown strength, sufficient mechanical strength, and low leakage are the requirements for a high-quality barrier. The adhesion of the barrier to the copper interconnect is the critical factor in the long-term reliability of the interconnects. In addition, the dielectric breakdown properties of copper interconnects degraded over time due to the presence of moisture and cracking or debonding. Although both silicon carbide and silicon nitride, good candidates for the copper barrier, seemed to show resistance to oxygen and water moisture diffusion, they show debonding and aging due to the diffusion of ambient moisture [184]. This requires a suitable hermetic barrier to avoid the diffusion of moisture and crack growth, debonding, and stress increases. A recent work on optomechanical features of SiC_xN_y thin films reported promising aging properties, which can be applied to an effective barrier and optical MEMS sensors [185].

In addition to copper technology applications of SiC_xN_y thin films, the diffusion of hydrogen at high temperatures is a method to forecast long-term hermeticity of MEMS packaged solutions for end markets [186]. In chapter 5, we will discuss the observed increase of the refractive index at high annealing temperatures, which is an

indication of a lower degree of porosity induced by hydrogen loss and the subsequent increase of compactness and densification [187]. This makes SiC_xN_y thin films more moisture resistant due to the less open porous structure and a more suitable candidate for the fabrication of humidity sensors [188].

Furthermore, such hydrogen-rich thin films potentially have applications in thin film devices as a substitution for silicon nitride. They can be applied to hydrogen passivation of grain boundaries in polysilicon for thin-film-transistors (TFTs) and to decrease the silicon surface recombination in screen-printed silicon solar cells. A silane-free (SiXtron Advanced Materials) PECVD method was applied to fabricate SiC_xN_y thin films for use in anti-reflection (AR) coated solar cells, where the device was compared with the silicon nitride counterpart. Providing the SiC_xN_y anti reflection coating is in its early stages, the efficiency of SiC_xN_y and silicon nitride was virtually equal. The optimization of the film composition and layer thickness of the AR coating highly affects the efficiency of the solar cells requiring further investigations of SiC_xN_y parameters [189]. Fig. 2.27 shows a schematic of a screen-printed solar cell device implying metal contacting in the fabrication process. The annealing at lower temperatures is used in typical passivation processes involving forming gas following aluminum alloying in screen–printed solar cells that are intangible with the detail study of the hydrogen diffusion of this work. Beside the wide range tunability of the refractive index of SiC_xN_y discussed in chapter 4, the results presented in 5 on the hydrogen diffusion mechanism and its connection to two featured stages of annealing open opportunities for a better control of the device quality for screen-printed solar cells.

Another application of SiC_xN_y thin films is in the developments of low-cost UV

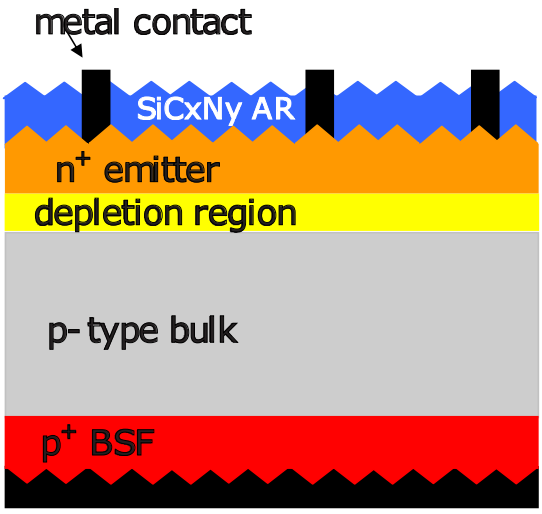

Figure 2.27: **A schematic of a screen printed solar cell.** A schematic of a solar cell coated with SiC_xN_y as the anti-reflection (AR) layer. Reprinted (adapted) with permission from [189].

sensing device, where in addition to efficient light emission, the physical characteristics are also of concern. UV detectors are used in different fields such as biological sensors, solar astronomy, pollution analyzers, and combustion process monitoring. In these applications usually, the ambient temperature is increased due to the absorption of high-energy UV emission requiring a robust and wide band gap material. Most of the conventional UV detectors have been made of group III nitride (GaN, AlN, and InN), which suffer from a low operational temperature as well as high-cost production. Crystalline silicon carbide (4H or 6H-SiC) LEDs with sufficiently stable thermal stability suffer from low efficiency of light emission [190]. Chou et al. [191] reported a UV detector made of a crystalline SiC_xN_y thin films grown on p-type porous silicon using rapid thermal chemical vapor deposition (RTCVD). The photocurrent to dark current ratio of SiC_xN_y was higher than that of silicon carbide on a silicon substrate

or zinc oxide on gallium arsenide substrates. They examined the optoelectronic performance of different UV detectors, where the higher optical current in the UV range at high temperatures suggested a competitive potential of SiC_xN_y to serve as a CMOS compatible UV sensor operated at high temperatures [192] [193] [194].

Chapter 3

Experimental Methodology

The present chapter summarizes the design of the experiments employed for the materials investigated in this thesis. The description of sample preparation and characterization methods are divided into four sections; thin film fabrication and three classes of characterization techniques, i.e. compositional, optical, and structural measurements. Most of the employed techniques are commonly used and also well-established in the theses written by our former group researchers. Therefore, the most attention is paid to the measurement conditions specifically tailored to analyze the obtained results for this project.

3.1 Fabrication of SiCN Thin Films

This section begins by describing the growth method of SiC_xN_y:H_z, SiN_x, and SiC_x thin films discussed in this work. In total four systems have been applied over my Ph.D. and Master's projects. The (two) ECR PECVD and ICP CVD systems are located in Tandem Accelerator building at McMaster University in Hamilton, ON,

Canada and the reactive RF sputtering system is located at the University of Campinas, SP, Brazil. As can be expected, the optical properties of a coated layer tend to vary significantly based on the applied deposition technique. Each individual reactor used for the fabrication of SiC_xN_y:H_z yielded different properties concerning the light emission properties and film composition, with ECR PECVD system producing the most luminescent SiC_xN_y:H_z thin films. The samples grown using ICP-CVD system showed lower PL intensity and a similar amorphous structure to that of ECR-PECVD grown samples, while the sputtered samples showed a different composition and structure. Nitrogen played a significant role in the structure of the sputter samples. Without the use of nitrogen gas during the deposition, no silicon was sputtered from the silicon target, which can be explained by the influence of nitrogen as the reactive gas assisting the increase of the chemical reactions between the target atoms and methane species to form the solid layer on the silicon substrate. The PL intensity of these samples was lower compared to the CVD-grown samples, however, the films contained higher nitrogen content such as $Si_{25}C_{25}N_{39}$ and $Si_{31}C_{26}N_{36}$. In particular, for one of the nitrogen-rich samples with lower silicon content ($Si_{20}C_{33}N_{41}$), the formation of nanoclusters occurred by subjecting the films to high temperature post-deposition annealing. All samples discussed in this work were grown using the ECR PECVD system. The process parameters employed for this system are briefly summarized, followed by the details of the pre- and post-deposition processes as well as samples sets.

3.1.1 Deposition Parameters

It is not intended to discuss the details of the plasma structure, the specific system parameters governing the chemical and electronic characteristics of the produced layers, and the plasma generation in McMaster ECR PECVD system, as details of the excited species and the corresponding plasma characteristics of this system were previously published in [195]. The reader can find more details of the system design in the theses of our former researcher in the group. In 2006, Darren Blakie provided a summary of the ECR PECVD system and its associated physics and chemistry of the deposition process [196]. In 2012, Ryszard Dabkowski produced a comprehensive report on the calibration of the second and more highly automated ECR PECVD system, the so-called Group IV or New ECR PECVD [197]. The design of the ECR PECVD system is located in the Tandem Accelerator Building at McMaster University is can be briefly described as follows:

A load-lock (pre-deposition) chamber is used to minimize the atmospheric contamination. The sample is first transferred to the load lock chamber using a high-speed turbomolecular pump, aiding the load-lock chamber to pump down. Its pressure needs to be below the 10^{-6} Pa before transferring the bare substrate to the main growth chamber. Prior to the deposition, first, the main chamber is evacuated to a base vacuum better than 10^{-7} Pa using an oil diffusion pump backed by a mechanical rotary vane pump. Then, the stage heater is set to the desired deposition temperature, typically in a range between 300 °C to 500 °C. The stoichiometry of the deposited layer can be adjusted by the ratio of the partial pressure of the precursors.

To fabricate SiC_xN_y thin films, silane (SiH_4), methane (CH_4), and nitrogen (N_2) gases are used as the precursors for silicon, carbon, and nitrogen, respectively, and are

fed into the chamber in the form of 30% SiH_4, 10% N_2 in Ar, and pure CH_4 gas. The system was designed to feed N_2 and Ar gases into the plasma region through dispersion holes in a double layer sapphire window. CH_4 and SiH_4 gases are supplied downstream the discharge zone through a separate dispersion ring positioned out of the plasma region close to the substrate. Two dispersion rings provide the opportunity to control better the creation of the species from different gases with different dissociation and activation energy since there is a chance of undesired deposition of CH_4 and SiH_4 on the surrounding chamber walls and dielectric window of the discharge region. Nitrogen gas needs the highest energy to dissociate and the direct interaction with nitrogen molecules can be accomplished by using the energetic of plasma particles in the discharge zone, will be further discussed in section 6.3.

It should be noted that the position of the sample stage is not fixed in this configuration of ERC PECVD. In order to duplicate the samples investigated in this dissertation one needs to adjust the stage in about 15 cm below the plasma cone. Fig. 3.1 shows a close-up of the actual reaction chamber during the deposition where the stage is almost aligned with the shutter position.

The plasma is ignited by N_2-Ar mixture with microwaves at a frequency of 2.45 GHz generated by a magnetron head. In general, the forwarded power for the precursors used to produce SiC_xN_y:H_z thin films is about 510 to 515 W, i.e. the reflected power is in the order of 10 to 15 W. To achieve more uniform and homogeneous samples, stage rotation was used at a rate of 20 rotations per minutes. Setting the microwave power to 500 W, several deposition runs were performed where the total process gas flow rate was varied in the range of 15 to 35 (5%) sccm denoting "cubic centimetres per minute at standard temperature and pressure". For most of the samples, the deposition time generally was optimized to 30 minutes at a nominal

deposition temperature of 350 °C, corresponding to a substrate temperature of approximately 120 °C [198]. The substrate temperature cannot be directly measured due to difficulties of in-situ monitoring, which requires a free port added to the chamber. However, previously the thermal response in ICP PECVD system using the identical heater, sample stage, and PID controller was studied [198]. The intermediate substrate temperatures were found linearly proportional to the heating element's temperature according to the following relation obtained in the initial system calibration.

$$T_{substrate}{}^{\circ}C = 0.3303\ T_{heater}\ {}^{\circ}C + 21.85 \tag{3.1}$$

For this range of stage temperatures, depending on the type of the substrate, as described in subsection 3.2.1, one has to wait between 15 minutes to 1 hour. Given the aforementioned gas sources, a deposition time of 30 minutes results in SiCN samples with thicknesses varying from 180 to 440 nm.

3.2 Sample Sets

Here, the main research objective focuses on understanding the optical properties of $SiC_xN_y{:}H_z$, which requires examining the dependency of the optical and structural film properties on several deposition parameters. The stage heater, deposition time, and the gas flow rates are tailored depending on the goals of the experiments. As such, the specific parameters of each set of samples such as gas partial pressure, deposition temperature, and some post-deposition treatments are assessed in this contribution in the following series of sample sets.

Sample Set_A:

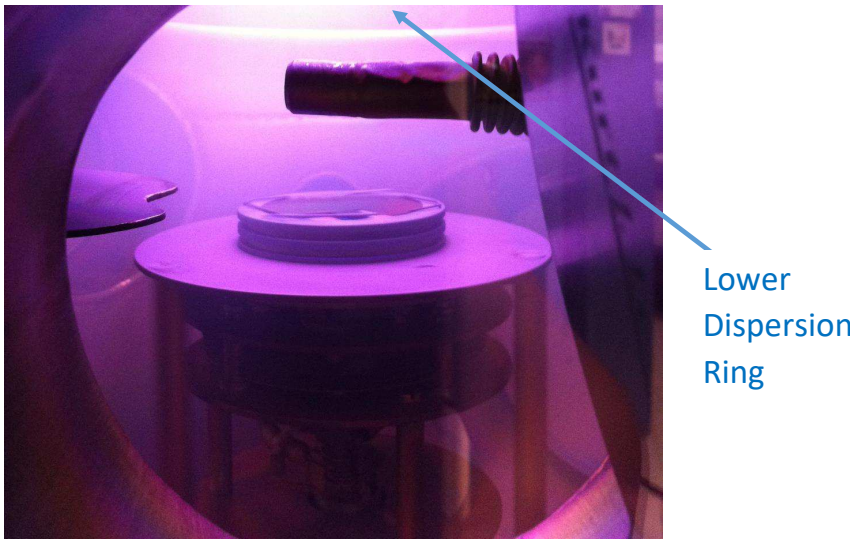

Figure 3.1: **A close-up of the reaction chamber of ECR PECVD.** The position of the sample stage with respect to the lower dispersion ring is shown.

An important sample set for this research includes the thin films with varying carbon content, i.e. CH_4 gas flow rate was varied during the deposition. These samples are discussed in chapter 4 and the influence of Ar dilution during the deposition is also investigated for this set of samples.

Sample Set_B:

These set of samples includes a subset of Set_A which undergo the post-deposition annealing in the quartz tube furnace and are presented in chapter 5. The additional characterization techniques (PL measurements) employed for these samples are discussed in chapter 6.

Sample Set_C:

This set is concerned with the samples grown using different deposition temperatures discussed in the second section of chapter 6.

Unless otherwise specified, for all samples a mixture of 5, 10, 8 sccm (for SiH_4, N_2, and pure CH_4, respectively) were fed into the chamber for a 30-minute deposition with the substrate temperature of 120 °C. For convenience, the specific growth parameter varied with respect to the objective of that study is provided in the corresponding chapter.

3.2.1 Pre-Deposition

Substrates In order to examine the characterization techniques discussed in the following sections, four different type of substrates have been used including n-type c-silicon, un-doped c-silicon, Corning glass 7059, and glassy carbon plate. Mostly, the measurements were performed using a single-polished side antimony (SB)-doped <100> Czochralski silicon wafer with 0.01-0.03 ohm-cm resistivity and 274-304 μm thickness, unless it is stated. The glassy carbon (vitreous carbon) plates have been utilized for RBS techniques. The advantage of the carbon substrate over the commonly used ones (silicon) is providing a more well-distinguished signal from the light elements such as carbon, nitrogen, and oxygen. More details can be found in the description of RBS technique, subsection 3.3.1. The samples grown on Corning 7059 glass substrates of 1x1 cm^2 were used for UV-VIS measurements. For FTIR measurement, a undoped silicon (Double-side polished) wafers with a thickness about 200±25 μm were used to pass the incident light through the film and the substrate layer.

It should be noted that for the depositions using glassy carbon plates and the glass

substrate, one has to wait for 45 minutes, in average, to achieve a uniform coated layer. Typically 15 minutes to 20 minutes is sufficient to avoid any temperature gradient through the silicon substrate. Due to the different thermal coefficient of carbon plates and glass from that of silicon, it takes longer time than the typical waiting time for silicon substrates. In some cases, the coated layers were peeled off from the substrates, in particular, from the carbon substrate when less than 1 hour was heated through the stage heater. In the case of New ECR PECVD, the waiting time is expected to about 30 minutes or more.

Substrates Cleaning Prior to the deposition, the silicon wafers (both single and double side polished) were cleaned with diluted hydrofluoric acid (10:1 H_2O:HF). The other option was the Buffered HF promoting more uniform distribution of the acid on the surface of the silicon wafer and delaying any tissue damages if happened. The procedure started with a UV ozone treatment for 10 minutes to activate surface oxide [199]. The substrate was then etched in the diluted HF for 30 seconds minute (90 minutes for buffered HF 1:10) to remove the native oxide layer and terminate the surface dangling bonds of silicon with hydrogen. Following etching, the substrate was rinsed in running deionized (DI) water to remove the diluted HF and finally dried with nitrogen gas. The procedure was performed right before the sample being transferred into the CVD chamber. The cleaned silicon wafers were carried from the cleaning are to the ECR chamber in a zipper bag fully filled out with nitrogen gas to avoid surface oxide grown naturally on the silicon wafer after a short period of time. The glassy carbon plates were first to cut into 1x1 cm^2 pieces, sufficient for the beam spot of RBS measurements, using a dicing saw machine. Subsequently, they were cleaned with acetone sonication for 10 minutes followed by methanol sonication

for another 10 minutes to remove any residual oil and hydrocarbon contamination.

3.2.2 Post-Deposition

Annealing Silicon-based thin films generally require a driving force provided by post-thermal annealing to agglomerate the excess silicon and form ncs. Commonly, after the deposition, the silicon carbide or silicon nitride dielectric is subjected to post-deposition thermal annealing in a non-oxidizing atmosphere. The ncs are expected to be formed through a phase separation of excess silicon from the dielectric matrix if the temperature is sufficiently high. The required annealing temperature depends on the type of the host dielectric and its potential barrier. In the case of the investigated SiC_xN_y samples, no specific relation has been developed in literature and the details of possible phase separation of a-SiC_xN_y compounds is evaluated discusses in chapter 5 for sample Set_B where the post-deposition thermal annealing was performed at temperatures a wide temperature ranges of 300-1200 °C for 1 hour using N_2 gas.

Purging of quartz tube furnace The quartz tube furnace was purged before the annealing to remove any residual species from the tube walls from the previous experiments. The worth mentioning point is about the purging process and the offset temperature. The purging was performed at about 20 °C above the highest temperature of the annealing. The type of the furnace applied for these samples is Thermolyne 21100 Tube Furnace, 120 V with a maximum operating temperature of 1210 °C. It should be noted that there is an offset between the setpoint and the actual temperature inside the middle of the furnace. For the temperatures close to the limit of the maximum temperature (around 1200 °C), the reading temperature is also different from the setpoint. Fig. 3.2 shows a setpoint of 1180 °C which

reads a maximum of 1600 °C from the actual temperature of 1200 °C read by the thermocouple sitting next to the furnace. Following the purging, the furnace is set to the desired temperature considering the offset. For the lower temperatures, the offset is about 50 °C and the actual calibration is tabulated in Table 3.1. Usually after 2 to 3 hours, depending on the previous temperatures, the samples were placed on a customized boat in the quartz furnace tube, arranged such that the cooling process occurs at the end of the quartz tube with the ambient gas flow passes through the samples. When annealing was completed, the samples were quickly pulled out to the end of the tube, the nitrogen flow rate increased to assist cooling. The samples were taken out once they approached room temperature, usually 20 minutes. This was done in order to avoid contamination of the air during the cooling process.

Figure 3.2: **Offset temperature of quartz tube furnace**. The quartz tube furnace showing the offset between the actual temperature read by thermocouple, setpoint, and read by the furnace.

Table 3.1: The calibration of quartz tube furnace.

Setpoint Temperature °C	280	451	655	855	1062	1160
Read Temperature °C	280	451	655	855	1065	1180
Actual Temperature °C	320	500	700	900	1100	1200

In this study nitrogen (N_2), a mixture of 95 vol. % nitrogen and 5 vol. % hydrogen (%95 N_2+%5 H_2), and argon (Ar) gases were employed for the annealing procedure. The use of different gases during the annealing process was found to have no influence on the PL emission intensity of the SiC_xN_y samples. Fig. 3.3 shows the PL spectra of a sample annealed for 1 h in the quartz tube furnace with flowing of N_2, %95 N_2+%5 H_2, and Ar gases. The shape and intensity of the PL spectra were found to be very similar indicating the hydrogen passivation is unnecessary.

Different annealing procedures One of the important considerations is the annealing procedures. Two different annealing process were tested for the elevated temperatures that no difference in the PL emission of the our SiC_xN_y was observed. In the first method, the samples were annealed directly to the desired temperature while in another procedures first samples were annealed at the lower temperatures such as 400°C, taken out, the furnace set to the higher temperature, and sample is annealed again.

The break down of Si-H bonds are initiated in the temperatures ranging between 300 to 500 °C. In a PECVD grown silicon oxide sample with a ratio of $O/Si < 1$, the precipitation of the silicon ncs happens in one-hour annealing in the range of $800° - 950°$ as follows [76]:

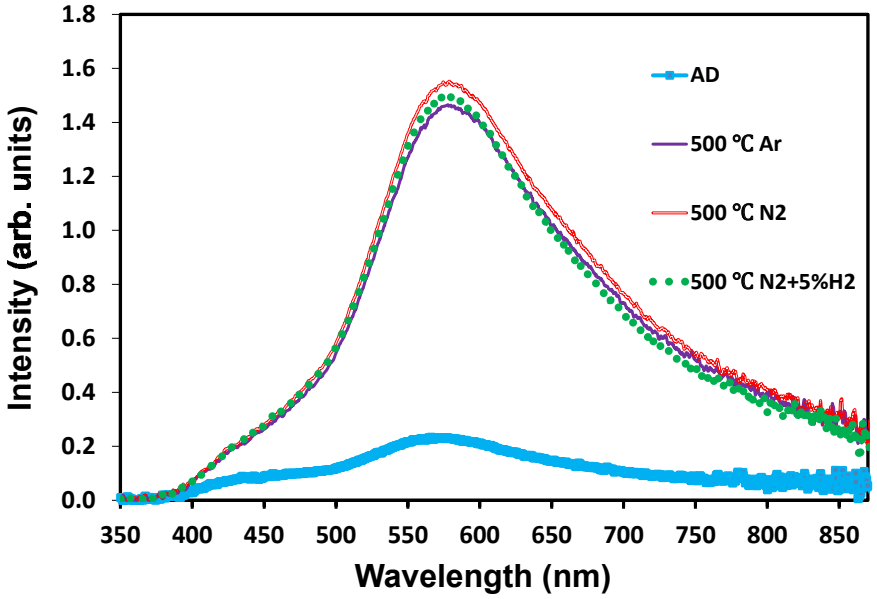

Figure 3.3: **Typical PL spectrum of samples annealed using different gases.** The PL spectrum of samples annealed at 500 °C using different gases is shown. The shape and intensity of the PL spectra were found to be independent of the flowing gas.

$$SiO_x \rightarrow \frac{x}{2}SiO_2 + \frac{x}{2}Si \ , \ where \ 0 < x < 2 \tag{3.2}$$

All excess silicon do not precipitate in the cluster formation, and at the temperature of 1100 $^{\circ}C$ only half of the excess silicon participate in the cluster formation [70, 200]. The point is, silicon is mobile at a higher temperature near 1000°C, while hydrogen can move and diffuse out at lower temperatures. Therefore, the initial low-temperature annealing forces out the excess hydrogen cooperated in the matrix and avoid bubble formation at the elevated annealing temperatures; however, it is

not very clear yet what happens to the remaining hydrogen [76].

Although, no difference was observed for the investigated samples in this project, for the luminescent SiCN thin films grown using sputtering method for the relevant work, the bubbling effect influenced the PL emission. Those samples show very strong emission at 1100 °C with the middle step method. The direct ramping up of the furnace caused the restructuring in the annealed layers in a way that they did not emit any PL at the elevated temperatures. It is recommended to follow the middle step temperature for any samples.

Rapid Thermal Annealing An alternative to annealing in a quartz tube furnace, rapid thermal annealing (RTA), was performed using the Qualiflow Jipelec Jetfirst 100 rapid thermal processor at different temperatures with a ramp rate of 25 °C/s for times ranging from 5 to 1800 seconds in N_2 ambient. This method is not employed for this study due to lower PL intensity of the samples annealed using RTA. A typical example of the PL spectra of SiC_xN_y samples is shown in Fig. 3.4. The PL intensity is quenched on very short time scales which can be explained by different restructuring occurring during the rapid annealing process compared to quartz tube furnace annealing. The interdependency of the SiC_xN_y structure and the PL emission is discussed in chapter 6.

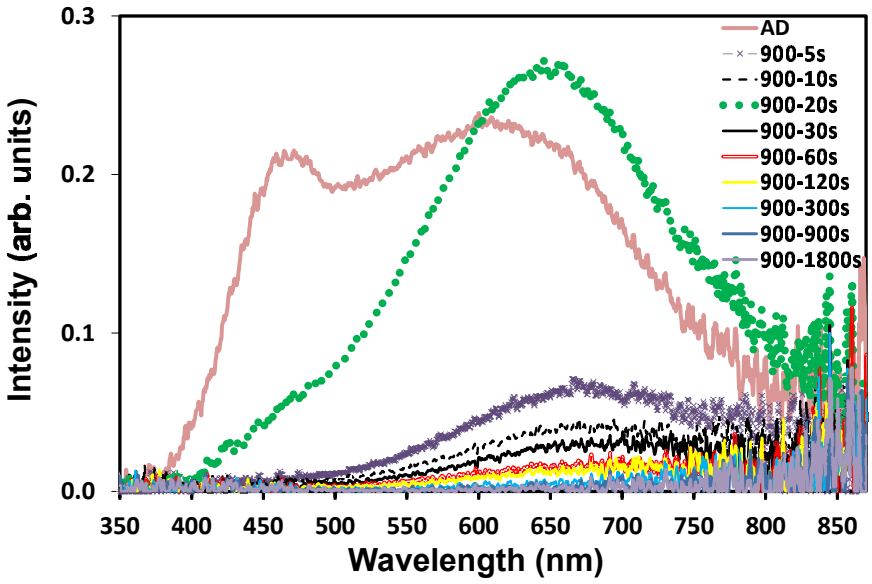

Figure 3.4: **A typical PL spectrum of SiC_xN_y sample annealed using RTA.** The SiC_xN_y sample was annealed at 900 °C in the range of 5 to 1800 seconds using N_2 gas. The PL intensity of samples is low and quenches after five seconds.

3.3 Compositional Characterizations

3.3.1 Rutherford Back Scattering and Elastic Recoil Detection

A combination of Rutherford backscattering spectrometry and elastic recoil detection (RBS-ERD) was applied to determine the absolute composition of the thin films, coupling the advantages of the two measurements. One of the key aspects here is that we consider the hydrogen concentration in the RBS fitting process. The initial concentration of the elements given by RBS data was fed into the ERD simulation, and then RBS spectra were adjusted using the obtained hydrogen content. These techniques do not require elemental standards and are, therefore, more reliable than other compositional experiments [201]. Unfortunately, most research groups do not

tend to used the ERD technique and include the fraction of hydrogen in the layers and thus, could not achieve a proper compositional analysis. If hydrogen is disregarded, the concentration of other elements could be estimated, in particular, because SiC_xN_y materials commonly are grown by precursors containing hydrogen such as CH_4, acetylene (C_2H_2), or ethane (C_2H_6).

RBS is a quantitative and destructive technique directly giving the accurate depth concentration profile of all elements except for hydrogen, which can be determined using the ERD measurement. It is based on the collision and backscattering of a monoenergetic ion beam impinging on a sample, which requires a collimated ion beam of 1-3 MeV energy (typically alpha particle, $4He^{2+}$ ions) be directed onto the sample. The RBS and ERD data sets were collected at the Tandetron Laboratory at Western University (London, Ontario, CA) using 1.8 MeV and 1.6 MeV $4He^{2+}$ ions, respectively. The detectors are placed at 170° (β) and 30° scattering angles, respectively, in Tandetron (CORNELL) geometry and the incident angle (α), is set to 5°. In general, a reference sample of silicon antimony (SiSb) with a known dose of antimony (about 4 x 10^{15} cm^{-2}) implanted in silicon is employed for calibration of the setup.

The backscattered beam is detected with an energy sensitive detector. Once an alpha particle is directed onto the material it scatters back from the sample due to the coulombic repulsion of the target nucleus. A large fraction of the incident ions undergo inelastic collisions and lose their energy through the nucleus interactions. The rest of the incident ions- approximately 10^{-6} of the total number of incident ions- deflect elastically from the sample at different scattering angles [202]. The scattering from each individual atom occurs in a distinguishable and well-understood manner and the energy lost by an ion depends on the nucleus mass of that certain

element. The reverse process is to record the intensity and energy of the scattered ion from an unknown material, which gives the signature of the constituent atoms. The number of scattered particles, Y(E), is recorded as a function of energy (E) in the experimental output of RBS. The measured data can be calculated through computer simulations. The SIMNRA 6.0 software package was used in this work to determine atomic concentrations as a function of film thickness [203]. In fact, the energy scale and yield are converted into a depth scale (thickness) and atomic concentration.

The concentration of the constituent elements can be reported either as the atomic percent or areal density. It should be noted that the processed RBS data gives the absolute atomic concentrations, although not the precise value of the thickness, and hence, not the accurate areal density [204]. The areal density gives the number of atoms per cross-sectional area in the path of the incident beam through the entire film thickness. The layer thickness determined by RBS depends on the ion energy, which can be varied and calibrated according to the sample properties. Applying the exact thickness obtained from variable angle spectroscopic ellipsometry (VASE) with better than 1 nm accuracy (subsection 3.4.3) enables the determination of absolute areal density, and therefore, the film density.

Fig. 3.5 shows an example fit of the SiC_xN_y:H_z sample in Set$-$A grown on a carbon substrate with the spectra of each individual element identified. The panel on the right side of the figure shows the energy calibration and the detector solid angle. More information about this sample can be found in Tables 4.1 and 4.3 where it is labeled as SiCN-08 and R=0.6, respectively.

In some cases, one needs to add the hydrogen fraction to the initial fitting of RBS data. In this case, first, the concentration of hydrogen is excluded from the RBS results. This can be done by dividing each element's fraction (X at. %) by hydrogen

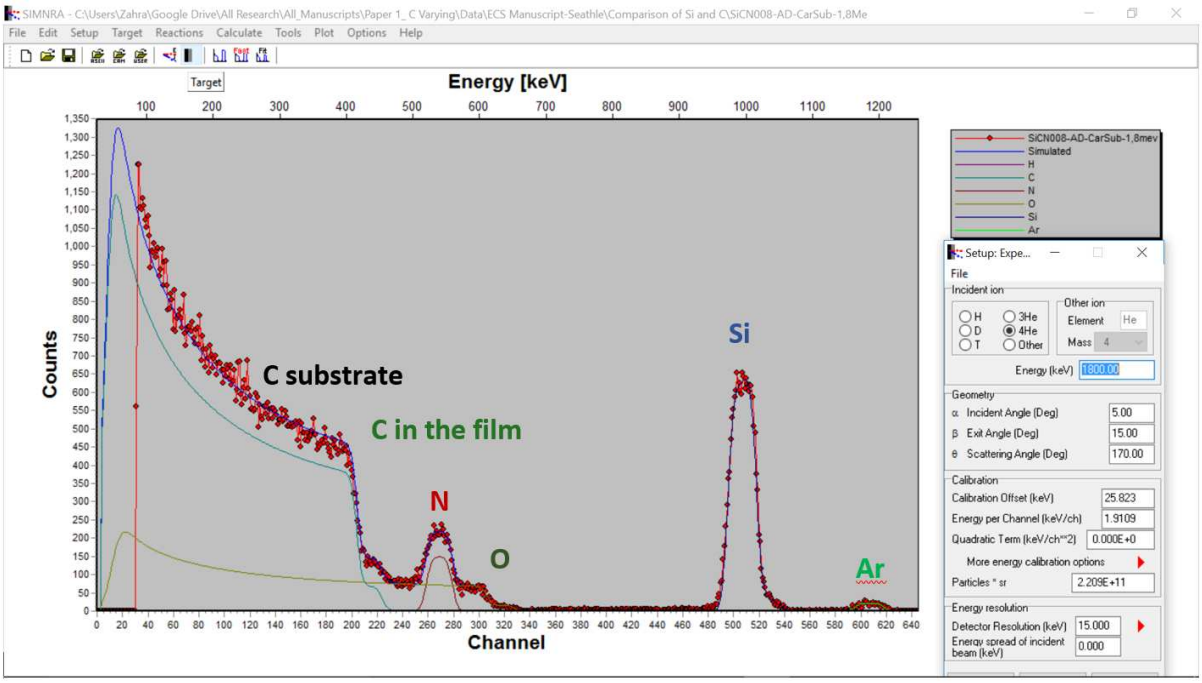

Figure 3.5: **SIMNRA software snapshot**. An snapshot of the SIMNRA software main menu for sample SiCN-08. The x- and y-axes represent the energy scale and the relative signal intensity, respectively. The sample composition is provided in Table 3.2

fraction (H_C at. %) as follows:

$$X'_C = \frac{X_C}{100 - H_C} \tag{3.3}$$

where X'$_C$ is the atomic concentration of the element without considering the hydrogen content. Then the true value of hydrogen given by ERD can be applied in the reverse procedure to obtain the actual concentration of all constituent elements.

Difficulties often occur in obtaining the RBS data of thin films containing lighter elements with relatively close mass numbers on heavy substrates. One of the most efficient solutions to eliminate the interference of the silicon substrate with the SiC_xN_y thin films is the use of a carbon substrate. In addition to the carbon substrate, the

Table 3.2: Example of SiCN composition delivered by the combined RBS-EDR technique.

Element	C [at.%]	N [at.%]	Si [at.%]	O [at.%]	Ar [at.%]	H [at.%]
Atomic Concentration	14.6	24.5	26	1.9	0.3	32.3
Uncertainty	0.9	1.1	0.3	0.1	0.0	1

dual large angle scattering has been used which adds a great deal of time to the fitting calculation. Dual scattering especially is taken into account for the background behind the low energy edge of heavy elements on top of the light elements. In Fig. 3.5 the collection parameters used specifically for sample Set$-A$ are shown.

The accuracy of the fitting generated by SIMNRA program can be estimated by the SIMNRA software as shown in Fig. 3.6. The overall uncertainty of the fitting result is determined by the uncertainties inherent to the RBS measurements.

This error is due to the inherent RBS measurement's uncertainties. To consider the accuracy of the mass density calculation, one needs to apply both the uncertainty of the thickness given by VASE and of the areal density determined by RBS and the subsequent simulated spectrum generated by SIMNRA. Note that the thickness of the layer was determined independently using VASE and the uncertainty of that measurements will be discussed in subsection 3.4.3. The uncertainty given by VASE measurements is the absolute uncertainty which is typically 0.4 nm (this is the maximum uncertainty given by VASE for all investigated samples). The mass density is the division of the areal density over the layer thickness. The addition of their uncertainties can be used to calculate the error of density calculations, not the absolute uncertainty. Considering the relative uncertainties of the thickness and areal

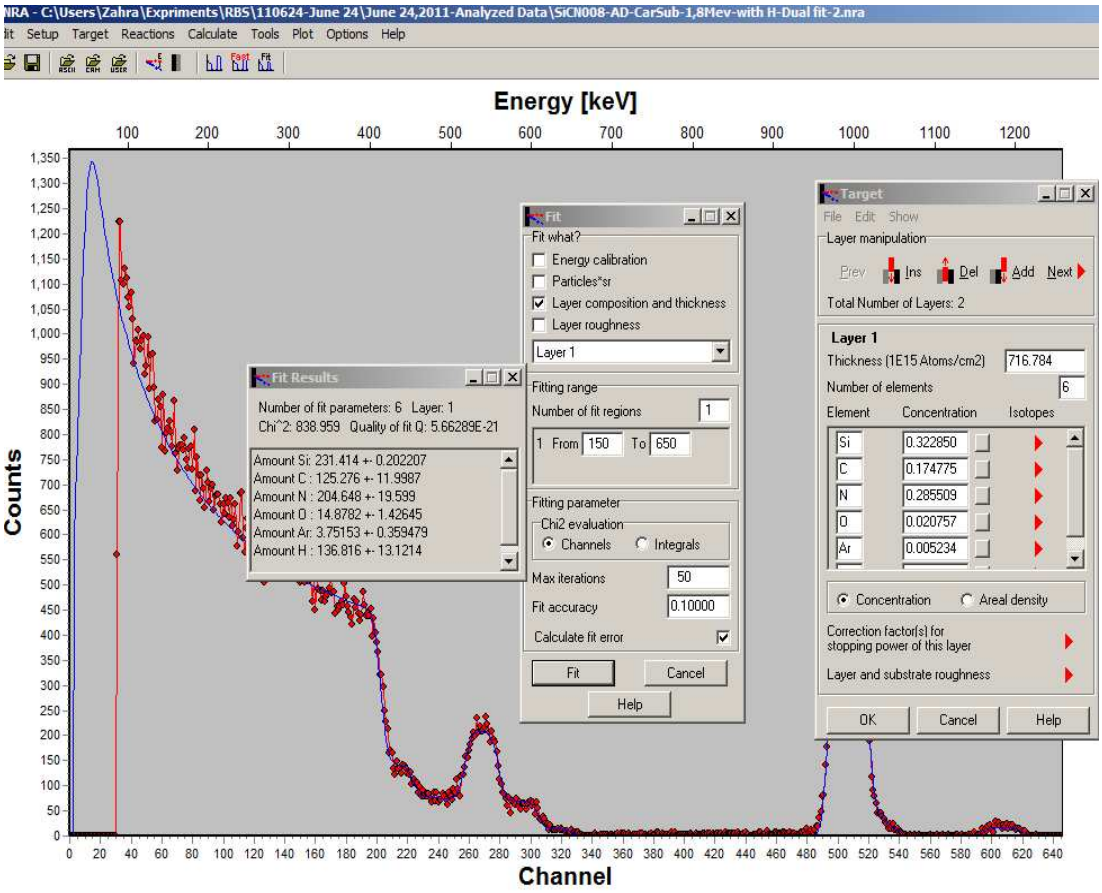

Figure 3.6: **Errors of RBS and ERD using SIMNRA software**. Example of the SIMNRA software main menu showing the panel of the concentration of elements, fitting options, and calculated errors from right to the left of the figure, respectively.

densities, the density of all produced thin films in this study is estimated with an accuracy of about 0.07 g/cm^3.

It should be noted that the mismatch of thermal expansion between the thin films and underlying glassy carbon substrate led to delamination and film cracks during the annealing process. Therefore, samples grown on glassy carbon substrates cannot be used for any thermal treatment that leaves only one choice of the substrates, silicon, the frequently used substrate, see the RBS analysis presented in section 5.1.

3.4 Optical Characterizations

All of the following subsections deal with non-destructive optical techniques with no special measurement environment. Basically, once light hits the sample, it may undergo reflection, absorption, interference, and scattering before it is transmitted. Depending on what kind of these phenomena is monitored different information can be obtained from the material through different spectroscopy designs.

3.4.1 Photoluminescence

PL is a common characterization technique in the study of light emission from thin films. It virtually is the basis of this contribution. The technique is concerned with measurement and interpretation of the emitted light. A photon with energy larger than the bandgap of the sample is absorbed by the sample. The absorbed photon induces a transition of an electron to an excited state and the relaxation back to the initial state. The electron relaxation occurs radiatively and non-radiatively (spontaneous emission and thermal relaxation, respectively).

In this thesis, a 325 nm helium cadmium (He-Cd) laser (E_{exc}= 3.82 eV) was used for PL measurements. The emission intensity is given by the raw PL data (arbitrary units) per wavelength. The PL spectra of different samples, for the most part, are compared with respect to their relative peak intensity and peak positions. This requires calibrating the system using a standard reference for any run to be able to compare the measurements taken over a span of time. In addition, one need to be take into account the power density determined by the actual laser power divided by the effective spot size excited on the sample which is an area of 2.3 mm^2 for this set-up [205]. In 2017, the laser output power and the input power impinging on the

sample were measured to be 2.2∼2.4 and 1.8∼2.0 mW, respectively. The difference between the output and input power can be explained by an estimate of about 10% loss on the mirror reflecting back the laser beam to the sample holder. The original power of the used He-Cd laser model IK3151R-E made by Kimmon Koma company is reported to be 17 mW with an average lifetime of 4500 hrs (gets up to 8000 hrs for some models) and an incident a power of 15 mW on the sample (0.64 W/cm^{-2} is the power density on the sample). The degradation of the gas laser over a long period of time is due to the diffusion of gas out of the laser cavity.

A reference sample of cerium doped silicon oxide with very strong emission has been used to calibrate the optics of the system. Following the calibration of the system using the reference samples, the room-temperature PL profile is collected. First, a background scan is performed in the darkroom and stored by the software to be subtracted automatically. Then the PL signal is recorded using a monochromator with a silicon CCD camera between 350 and 1000 nm and an Ocean Optics Spectrometer. The response of the system is applied to the PL spectrum of SiC_xN_y:H_z, which broadly extends over the visible range. More details regarding the spectrometer and system response used for the correction can be found in reference [206]. For some parts of this research, the PL lines are resolved through a Gaussian fitting into PL subbands. To minimize errors in the decomposition, especially in a broad emission band, the overlapping features of luminescence data require the conversion to energy and consequently, the transposition of the intensity by a factor of λ^2/hc [207]. The recorded room-temperature PL data as a function of wavelength were first converted to energy, smoothed using a Savitzy-Golay function, and then fitted to Gaussian curves using Origin 9.4.1.

3.4.2 UV-VIS Spectroscopy

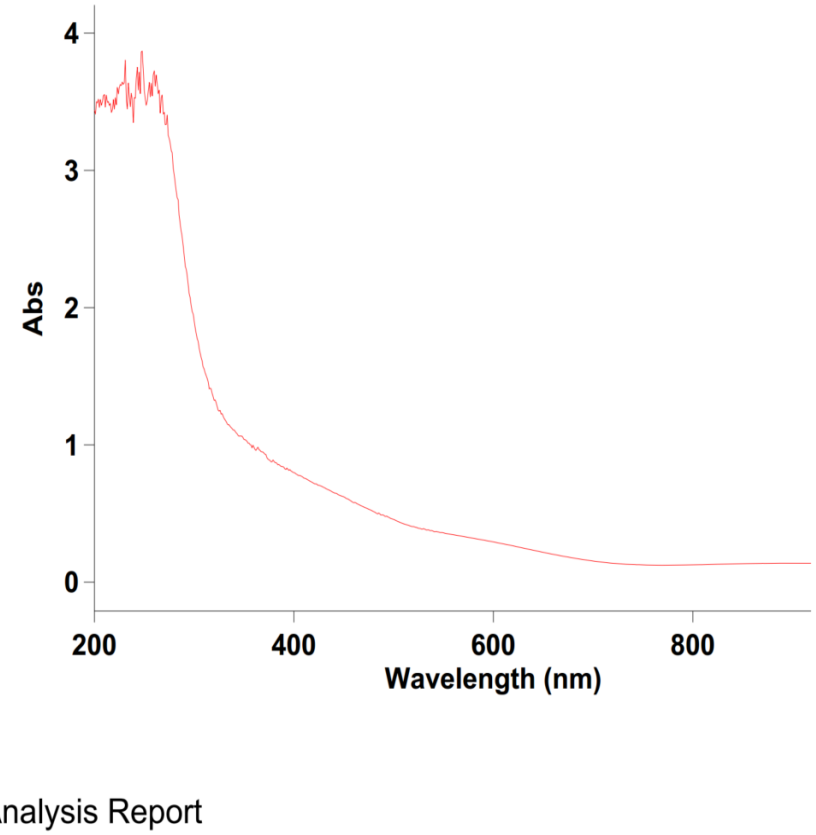

Figure 3.7: **Absorption spectrum.** The absorption spectrum of an amorphous SiC_xN_y sample measured using a UV-VIS spectrometer does not abruptly terminate at the band gap.

The forgoing discussion in subsection 2.3.1 described that although amorphous semiconductors contain a random network, some features of crystalline structures with long-order range can be observed. The short-range order preserves some crystalline properties such as optical band gap (E_{04}). The band gap energy of the investigated samples at room temperature was determined by optical transmission measurements using UV-VIS spectroscopy. The samples grown on Corning 7059 glass substrates of 1x1 cm^2 were used to record the transmittance (or absorptance) spectra using

an Agilent Technologies Carry 50 UV-VIS spectrophotometer located ain the McMaster Chemistry and Chemical Biology Department. This instrument consists of a Xenon Arc lamp with continuous emission from 200 to 1100 nm, a monochromator, a charge coupled device detector and an easy-to-use software. The latter makes the measurements very straightforward and quick. The scan of each sample took about 2 minutes by setting the UV-Vis scan rate of 600 nm/min with intervals of 1 nm. One example of raw data is shown in Fig. 3.7 representing the typical absorptance of amorphous SiC_xN_y thin films with no abrupt termination at the band gap as opposed to crystalline materials [208].

In contrast to the very straightforward measurements of UV-VIS, the determination of the band gap from the raw data of UV-VIS requires analytical calculations. For this project the analytical calculations are performed using a free software, Pointwise Unconstrained Minimization Approach (PUMA)), developed by researchers at the University of Campinas, Brazil. There are no published instructions regarding this software and the information provided on the website of the software can guide the reader how to use it with some real-world examples [209]. PUMA can be used to analyze the absorptance spectrum with no need for additional information of the film thickness and optical constants. The absorption spectrum fitting (ASF) procedure is developed according to underlying physics of this technique, which is based on the absorption of light.

3.4.3 Variable Angle Spectroscopic Ellipsometry

Ellipsometry deals with the reflection of light from the films grown on the absorbing substrates (silicon or carbon) and with the transmission of light passing through a

transparent substrate (glass substrate). In addition, this technique uses the change in light polarization expressed as ellipsometric parameters ψ and Δ for the changes of the amplitude and phase, respectively. In principle, Maxwell's equations are used to determine the relative phase and amplitude of the linearly polarized incident beam and the elliptically polarized beam reflected from the sample. The connection between these two parameters is given by the following equation [210]:

$$tan(\psi).e^{i\Delta} = \varphi = r_p/r_s \tag{3.4}$$

where r_s and r_p are the Fresnel reflection coefficients for normal and parallel components with the incidence plane, respectively. In this work, a J.A. Woollam M-2000U UV-VIS variable angle spectroscopic ellipsometer (VASE) was employed to investigate the thicknesses and optical constants of the films. The ψ and Δ values were obtained through the reflection spectra collected at multiple angles of incidence (55°, 60°, 65°, 70°, and 75°) to confirm the the applied optical model in the range of UVVISNIR (300 _ 1600 nm). The simulation of VASE data using J. A. Woollam's CompleteEASE software package delivers the optical constants (refractive index, n and extinction coefficient, k) along with the thickness of the films [211]. VASE data first was simulated using a Cauchy model assuming a crystalline silicon substrate and a surface roughness layer (with an average thickness of 10 to 15 Ă). A B-Spline model was then added to model the oscillator and follows the experimental trend more closely than the Cauchy model [212]. In fact, the Cauchy model is more appropriate for transparent materials and Tauc-Lorentz is used for absorbing materials. In the carbon varying samples (sample Set_A) the addition of carbon makes the films more semi-transparent which associates applying the model to describe the complex dispersion shapes of optical

constant. More information is very comprehensively are reported in [211].

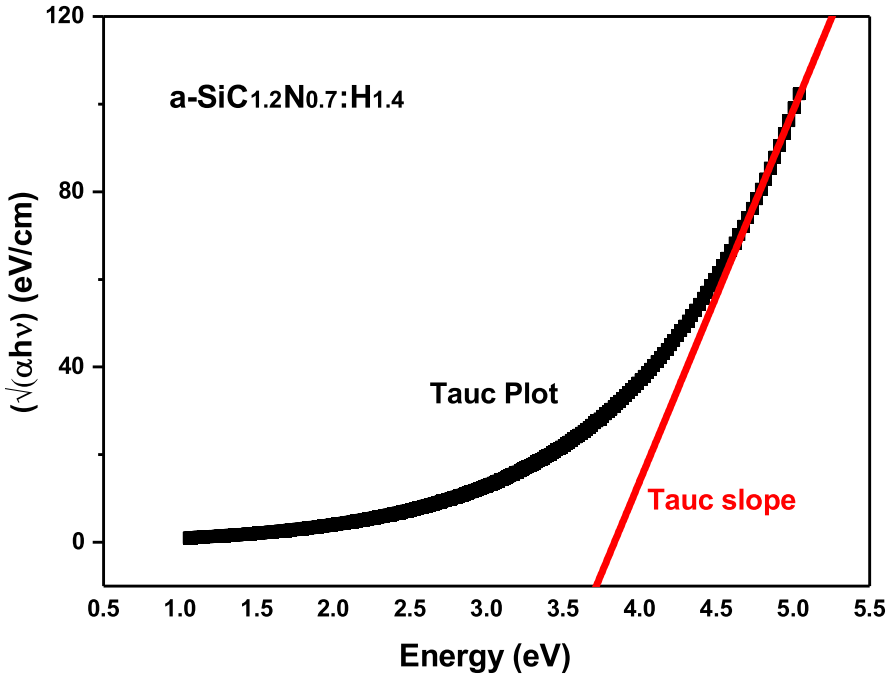

Figure 3.8: **Tauc Plot.** Example of the Tauc plot and the corresponding fit used to determine the optical band gap.

The spectroscopic ellipsometer is capable of measuring further properties such as dispersion of the refractive index and extinction coefficient (k). The extinction coefficient is the imaginary part of the refractive index due to the absorption that enables one to calculate the absorption coefficient (α) in order to estimate the optical band gap according to Tauc's relations, equations 2.11. As extensively discussed in subsection 2.3.2, the optical band gap of amorphous semiconductors can be estimated using their absorption coefficient. In addition, different band gaps depending on a more proper model were discussed in subsection 2.3.2. The optical band gap (E_{04}) defining the energy where (α) is equal to a standard value of 10^4 cm^{-1} was recommended for

amorphous silicon-based thin films [86] [93]. Fig. 3.8 shows an example of one of the as-deposited SiCN samples of Sample Set−B showing the Tauc slope. For all sample sets investigated in this work, excluding sample Set−A, the reflection data are given by VASE method were employed for the calculation of Tauc energy. The band gaps of sample Set−A examined in chapter 4 were obtained using the transmission data given by the UV-VIS technique, which will be further discussed in the following subsection. It should be noted that another choice is to measure the samples grown on glass substrates in the transmission mode of VASE data collection. However, some samples have been measured using both methods and no discrepancy was found between the Tauc energy and optical band gap for the investigated samples in this thesis.

3.5 Structural Characterizations

The electronic structure of the SiC_xN_y samples was determined using XRD, TEM, XPS, and FTIR techniques. All samples were found to be amorphous confirmed by XRD and TEM; two techniques do not deliver any further information of the non-crystalline materials. Spectroscopy method is one of the techniques sensitive to the chemical structure of any material, amorphous or crystalline [54]. Mostly two spectroscopic methods are extended to facilitate the electronic structural analyses of the thin films investigated in this contribution; XPS and FTIR are concerned with the emission and transmission of the incident light, respectively.

High-resolution transmission electron microscopy High-resolution transmission electron microscopy (HR-TEM) images of film cross-sections were captured

using the FEI Titan 80-300 Cryo-in situ and JEOL 2010F microscopes at the Canadian Center for Electron Microscopy (CCEM) located at McMaster University. The procedure of HR-TEM sample preparation started with bonding two SiCN slices in the center of silicon bars with a fast-curing epoxy. After polishing and ultrasonic cutting, two circular samples were produced to which Moly ring was attached, followed by dimple grinding and ion milling.

X-ray Diffraction X-ray diffraction is based on the constructive interference of diffracted of the X-ray beam. XRD identifies the inter-layer spacings of atoms in the crystal structure using the Bragg reflections associated with the crystal structure. The investigated SiC_xN_y samples were also examined by 2D Powder X-ray diffraction (XRD) using a Bruker D8 Davinci X-ray diffractometer with the monochromatized Cu-K_a line located McMaster Analytical X-Ray Diffraction Facility (MAX). The system includes a Bruker Smart6000 CCD area detector, Bruker 3-circle D8 goniometer, Rigaku RU200 Cu-Ka rotating anode, Gebel cross-coupled parallel focusing mirrors, and Fixed Chi at 54.8°. The scans were at a fixed incident angle of 2° with a frame exposure of 300s in a distance of 16.74 cm from the detector (power setting of 90 mA, 50 kV). Samples showed no specific ring or point in a large bump in the 2D patterns collected using a diffractometer equipped with a 2D or area detector, instead, the scattering in certain directions of crystallographic orientation of crystalline materials is identified by the intense peak in 2D pattern [213].

3.5.1 X-ray Photoelectron Spectroscopy

X-ray Photoelectron Spectroscopy (XPS) or Electron Spectroscopy measurements is known as one of the standard routines for the identification of chemical states of

elements in an amorphous material. This surface-sensitive analytical technique can be regarded as a semi-quantitative method for determining both the film composition and electronic state information of the surface region (about 7 to 10 nm). The underlying process is upon irradiating a sample with X-ray beam exciting the core electrons in lowest energy level. A transition of core level occurs at a specific binding energy that can uniquely give the characteristic of the bounding states of the core electrons. An electron energy analyzer measures the kinetic energy (KE) and the number of electrons emitted from the sample surface versus binding energy (the energy of electrons before leaving the atom). The peak intensity is related to the number of photo-ejected electrons versus time and identifies the amount of the elements by calculating the respective contribution of each peak area (Survey scans). The film composition in this research accurately was investigated using RBS technique (subsection 3.3.1). For the most part, the peak positions and relative intensities of the PS spectra were found favorable for this study. The peak position is the element specific given by the binding energy (BE) of the electrons that can be identified from the recode kinetic energy by:

$$h\nu = KE + BE + \phi \tag{3.5}$$

where h is the Planck constant (6.62 x 10^{-34} J s), ν is the frequency (Hz) of the X-ray energy and ϕ is the spectrometer work function (about a few eV). A monochromatic source of radiation is Al K_a X-ray excitation with 15 mA current and 14 keV energy (hν). The calibration of the system included the work function and spectrometer dispersion. The instrument work function was calibrated to give a binding energy (BE) of 83.96 eV for the Au $4f_7/2$ line of metallic gold. The spectrometer dispersion

was adjusted to provide a BE of 932.62 eV for the Cu $2p_3/2$ line of metallic copper. Survey scans were carried out with an analysis area of 300 x 700 microns and a pass energy of 160 eV. High-resolution scans were then performed with an analysis area of 300 x 700 microns and a pass energy of 20 eV. The measurements were conducted in an ultra-high vacuum. Generally, the photoemitted electrons have low kinetic energy, which requires a high vacuum environment to avoid interference from gas phase collisions (10^{-9} Torr). The obtained spectra were analyzed using CasaXPS software version 2.3.14 and for some samples, Origin 9.1 was employed.

For SiC_xN_y samples presented here, the C 1s, N 1s, Si 2p, and O 1s core level spectra were recorded. Due to the challenges of Ar^+ pre-sputter cleaning of insulating materials [204], as an alternative, the surface of the XPS samples was cleaned with buffered hydrofluoric acid (BHF) for 30 seconds to remove the surface oxide layer and documentation. The complex and different C 1s peak shapes compared to the standard carbon reference in the measured samples made necessary a charge correction of the spectra to the sharp N 1s peak set to 397.8 eV instead of charge correction normally done with respect to the C-C/C-H peak set to 284.8 eV. The N 1s peak was found unchanged and hence could act as a reliable internal reference. This approach likely increased the uncertainties in the exact binding energies for all spectra to ± 0.5 eV [204]. Prior to the core level fitting, a Shirley background correction was applied to reproduce the secondary electron background. For all core levels, the fitting process was guided through peak shapes of a Gaussian (Y%) Lorentzian (X%) mix accounting for the instrumental resolution and lifetime broadening, respectively. This profile is defined in CasaXPS as GL(X) wherein lines with large natural line-widths, such as C 1s, N 1s, and Si 2p, are better fitted with a GL(30) line-shape compared to the other choices of X [214]. For both the C 1s and Si 2p spectra, all peaks were

constrained to have equal FWHM. The C-O/C-OH and C-Si peaks were constrained to be 1.5 eV above and from 1 to 1.5 eV below the C-C/C-H peak, respectively. The Si-O_x peak was constrained to lie between 103.0 and 103.5 eV, while the Si-N peak was constrained to lie between 101.6 and 101.9 eV and the Si-C peak was set at 101.1 eV. In each individual set of sample in this thesis the XPS data is individually analyzed using the binding energies corresponding to the various peaks are published in [215] [216] [217] [218] [219], however, the identification of some features is common for all samples demonstrated in the following.

3.5.2 XPS Peak Assignments

For SiC_xN_y materials, the assignment of peak at 284.7 eV depends on the relative concentration of nitrogen to carbon. At low concentrations of nitrogen, it has been assigned to the C-C peak for sp^3 bonded carbon in a diamond-like matrix; at higher nitrogen concentrations, it has been ascribed to the C-C peak for sp^2bonded carbon in a graphite phase in SiC_xN_y matrix [216] [217]. However, in our earlier study of the influence of carbon on these bonds in a-SiCN:H films, the assignment of the peak at 284.7 eV to C–C/C–H bonds rather than C-N bonds was confirmed [220], showing that at least a major contribution to this peak can be assigned to the C-C bond. It is noted that no peak was resolved at 287.0 eV (Csp^3 bonded to one nitrogen neighbor) or at 288.0 eV (Csp^3 bonded to two nitrogen neighbors) [221]. The observed peak at 286.3 eV can be attributed to C≡N (C(sp)-N) bonds due to no contribution of N–sp^2C bonds in the N 1s spectra and the presence of the C≡N stretching mode at 2100∼2200 cm^{-1} in FTIR absorption spectra. The identification of the feature positioned at 286.3 eV is also not straightforward, since it can be assigned to both

C≡N and C-O bonds. In the investigated samples, the peak at 286.3 eV is attributed to the C≡N bond rather than C-O bond due to the negligible oxygen contamination in the samples. This peak appears in the as-deposited sample even though it does not contain any oxygen, decreases in the sample annealed at 500 °C, and has disappeared after annealing at 1200 °C. All samples were HF etched before XPS measurements, hence, the presence of the strongest feature at 286.3 eV in the as-deposited sample is not associated with the surface oxide contamination. The association of this feature with the C≡N bond is also supported by the observed trend of the C≡N feature at 398.9 eV in the N 1s edge and a feature at ∼2200 cm^{-1} in FTIR absorption upon annealing [216]. Also, as will be demonstrated in the next subsection, IR absorption shows no significant oxide feature for the as-deposited sample and the one annealed at 500° C.

3.5.3 Fourier Transform Infrared Spectroscopy

The term "Infrared" generally indicates 0.7-1000 μm of the electromagnetic radiation and includes three subregions of Far, Mid, and Near IR radiations. In $SiC_xN_yH_z$, most of the chemical bonds formed between silicon, nitrogen, carbon, and hydrogen are mid infrared-active, which refers to the wavelength between 2.5 and 25 μm (wavenumber of 4000 to 400 cm^{-1}). Therefore, the nature and the concentration of chemical bonds commonly are determined through the use of FTIR spectroscopy. This technique is extended to study either reflection or transmission data. For the presented contribution, a Bruker Vertex 80v vacuum infrared spectrometer with a resolution of 4 cm_{-1} was used to record the spectra of the transmitted light from

samples. To remove the chemical bonds of air constituents, the data of measurements in absorption modes were taken in vacuum at a pressure below 3 mTorr. This FTIR spectrometer (and any other modern and fast-scan spectrometer) is a modified Michelson interferometer. The hearth of this system is a simple optical device called interferometer consisting of two mutually perpendicular plane mirrors, KBR beam splitter, DTGS KBR detector, and a compensating plate [222]. The split beam is reflected off from a fixed and a moving mirror. Due to the path difference, the signals coming from two mirrors interfere with each other and produce a signal called interferogram. The interferogram simultaneously encodes all information about every frequency arrived from source. The decoding of the intensity versus each inducing frequency is accomplished mathematically by Fourier Transformation [223].

Different FTIR spectra for a set of samples, for the most part, are compared in terms of peak intensities and peak positions. To interpret each individual spectrum first a baseline subtracted is carried out. A piece of the uncoated double side polished wafer was used to measure the baseline transmission spectrum of the background of each spectrum. The baseline subtraction and normalization were performed using either a Bruker OPUS 6.5 software package or ohmic software. The further date manipulation proceeds by deconvolution of the absorption spectra into Gaussian peaks using the "fit multiple peak Gaussian function" of ORIGIN 9.4 software. The areas under the Gaussian peaks were taken into account for the determination of bond densities. The bond density between two atomic species of X and Y is denoted by X-Y and calculated using the following equation, wherein κ is the proportionality constant, a is the absorption coefficient, and ω is the wavenumber,

$$X - Y = \kappa \int \frac{\alpha(\omega)}{\omega} d\omega \tag{3.6}$$

The use of a Gaussian fit allowed us to simplified this equation to,

$$X - Y = \kappa/\omega \int \alpha(\omega) d\omega \tag{3.7}$$

The integral corresponds to the integrated intensity of the Gaussian peak. Hence, the multiplication of the known values of κ and the calculated area of each Gaussian peak, centered at ω, gives the density of chemical bonds. The bond density of a certain chemical bond is the sum of densities of that specific bond obtained at different positions in the IR spectrum. The density at any individual peak is given by the product of the proportionality constant and the area under that band. Due to the limited number of studies in the literature on SiC_xN_y:H_z materials, the infrared absorption modes were assigned with the help from reported absorption modes of submatrices; i.e., CN and silicon-based materials such as SiN_x, SiC_x, and SiO_x. Additionally, in the literature, the measurement performed in the atmosphere pressure show a high level of "noise"-background coming from carbon dioxide and moisture in the region between 1300-2000 cm^{-1} spectral range.

3.5.4 FTIR Peak Assignments

In order to analyze IR, the strong band was numerically deconvoluted using five Gaussian absorption peaks with the best residual (the difference between the experimental and fitted spectra) [224]. A summary of the infrared vibrational modes detected in SiC_xN_y:H_z films and the corresponding κ-values are presented in Table 3.3. Furthermore, the presence of hydrogen in the structure of a-$SiC_xN_yH_z$, introduced using PECVD processes, complicates the bond assignment of IR absorption modes compared to non-hydrogenated SiC_xN_y films grown using alternative techniques such as

sputtering [128]. Peter et al. [160] reported discrepancies of about 150 cm^{-1} in the peak positions of Si-C and Si-N absorption modes. Hydrogen bonding also alters the approximate positions of the absorption bands; red-shifting the stretching modes and blue-shifting the bending modes [225].

Table 3.3: Literature assignments of IR absorption peaks.

Bond	Frequency (cm^{-1})	Proportionality Constants (cm^{-2})	Reported
Si-O	∼420	-	[160] [226]
Si-N	∼470	2×10^{19}	[227] [228]
Si-H	∼640	1.6×10^{19}	[229]
Si-C	∼800	2.1×10^{19}	[230] [231]
Si-N	∼790	2×10^{19}	[226]
Si-N	∼940	2×10^{19}	[226]
C-N	∼1000-1060	8×10^{19}	[232]
Si-C	∼1030	3×10^{19}	[229] [232]
Si-O	∼1060	-	[232] [228]
N-H	∼1180	2×10^{19}	[227] [228]
Si-C	∼ 1250	2.2×10^{19}	[230] [231]
C-N/C=N	∼1350	8×10^{19}	[128]
C=C/C=N	∼1450	9×10^{19}	[233]
C-C/C=C	∼1590	1.1×10^{20}	[234] [128]
C-C/C=C/C=N/C-N	∼1850	0.9×10^{19}	[235]
Si-H	∼2100-2200	1.4×10^{20}	[226] [231]
C≡N	∼2100-2200	1.1×10^{20}	[234]
C-H	∼2800-2900	1.7×10^{21}	[230] [231]
N-H	∼3300	1×10^{20}	[227] [226]

Chapter 4

Carbon Varying Silicon Carbonitride

[1]The objective of this chapter is to demonstrate that the PL emission of a-SiC_xN_y:H_z thin films can be tubed by adjusting the composition of the samples. The focus is put here to enhancing the luminescence properties of as-deposited a-$SiN_{1.3}$:$H_{0.3}$ thin films by addition of carbon. A systematic study of the influence of carbon incorporation on the optical, compositional, and structural properties of a-SiC_xN_y:H_z were developed.

[1]The results presented in this chapter have been previously published in one journal article and two conference proceedings as follows:

- **Z. Khatami**, P. R. J. Wilson, J. Wojcik, P. Mascher (2017) The influence of carbon on the structure and photoluminescence of amorphous silicon carbonitride thin films, *Thin Solid Films*, 622: 110. https://doi.org/10.1016/j.tsf.2016.12.014
- **Z. Khatami**, P. R. J. Wilson, J. Wojcik, P. Mascher (2013) Photoluminescence evolution of silicon carbonitride thin films grown by electron cyclotron resonance plasma enhanced chemical vapour deposition, *56th Annual Technical SVC*, 505/856. http://dx.doi.org/10.14332/svc13.proc.1110
- **Z. Khatami**, P. R. J. Wilson, K. Dunn, J. Wojcik, and P. Mascher (2012) The Influence of carbon on the structure and photoluminescence of amorphous silicon carbonitride thin films, *ECS Trans*, 45(5), 153-160. http://ecst.ecsdl.org/cgi/doi/10.11 49/1.3700422

The results of different characterization techniques is presented in three sections. In the final section the link of the chemical and structural properties with the PL properties is explored and the optimal conditions with respect to the most luminescent sample are reported. The results have been previously published in two conference proceedings and one journal article [236] [237] [220].

4.1 Growth of Initial Set of Samples

In general, a ternary structure composed of silicon, nitrogen, and carbon is more challenging to study compared to binary structures, i.e. silicon carbide or silicon nitride. To start the project first one of the constituent elements (carbon) was chosen as the variable and the other two elements (silicon and nitrogen) were kept unchanged. To perform the study of the influence of carbon incorporation, stoichiometric $SiN_{1.3}$:$H_{0.3}$ was used as the reference sample and then the CH_4 gas flow rate was adjusted from 0 ($SiN_{1.3}$:$H_{0.3}$) to 20 (5%) cubic centimeters per minute at standard temperature and pressure (sccm), while the gas flow rates of SiH_4 and N_2 were held constant at 5 and 10 sccm, respectively. It should be noted that, following a number of depositions, the precursor flows were adjusted to 5 and 4 sccm (for silicon and carbon sources) and 5 and 10 sccm (for silicon and nitrogen sources) to produce the stoichiometric SiC (N-free SiC_xN_y:H_z) and Si_3N_4 (C-free SiC_xN_y:H_z) reference samples, respectively. The details of the growth parameters of these films are summarized in Table 4.1 showing only a certain subset of the samples that have been fabricated to find the parameters of stoichiometric silicon carbide samples.

In the initial set of experiments, it was found that the deposition time was an

issue. Silicon nitride samples grown using any deposition time longer than 30 minutes cracked immediately following their removal from the deposition chamber. A deposition time of 30 minutes resulted in silicon nitride layers with the a thickness of 170 mm,see subsection (4.3.2), which showed no stress issues. Note, once CH_4 is introduced in the deposition process, it is possible to grow silicon carbonitride layers using any longer deposition times. However, to keep the consistency of the growth parameters for all samples, the deposition time of 30 minutes was used in the course of this work. There was also no need to grow thicker films for the choice of the characterization methods. The analysis of the stress presented in the silicon nitride layers was not in the scope of this project. The interested reader would find a comprehensive study of various silicon-based structures in a master project performed by another researcher in our group, O. Taggart [238].

In Table 4.1, the recorded RF power is the desired RF power (500 W) plus the reflected power. For this set of sample no Ar gas compensation was used to minimize the variables in different samples. SiH_4, CH_4, and N_2 gases were used as precursors for silicon, carbon, and nitrogen, respectively, and were fed into the chamber in the form of 30% SiH_4 in Ar, 10% N_2 in Ar, and pure CH_4. Setting the microwave power to 500 W, several deposition runs were performed where the total process gas flow rate was varied in the range of 15 to 35 (5%) sccm. Deposition times of 30 minutes resulted in films with thicknesses varying from 180 to 440 nm (subsection 4.3.2). The deposition process was conducted using a stage heater temperature of 350 °C, corresponding to a substrate temperature of approximately 120 °C. To achieve more uniform and homogeneous samples, stage rotation was used at a rate of 20 rotations per minutes.

It worth mentioning that, all luminescent samples presented in this chapter are as-deposited samples with amorphous structure. XRD and HR-TEM revealed no

Table 4.1: Deposition parameters of carbon varying SiCN samples.

Sample	CH_4 [sccm]	N_2\ Ar [sccm]	SiH_4\ Ar [sccm]	P_{CH_4} [mTorr]	P_{N_2} [mTorr]	P_{SiH_4} [mTorr]	Dep. Time [min]	Heater Temp. $^\circ$ C	RF Power [W]
SiCN-08	2	10	5	0.09	0.81	0.43	30	350	512
SiCN-09	4	10	5	0.11	0.82	0.43	30	350	513
SiCN-10	6	10	5	0.17	0.81	0.43	30	350	520
SiCN-11	8	10	5	0.22	0.81	0.43	30	350	524
SiCN-12	0	10	5	0.0	0.81	0.43	30	350	510
SiCN-14	4	10	6	0.11	0.81	0.43	30	350	516
SiCN-17	12	10	5	0.3	0.78	0.43	30	350	521
SiCN-18	16	10	5	0.41	0.81	0.43	30	350	520
SiCN-19	20	10	5	0.54	0.81	0.43	30	350	521

crystalline phases in the as-deposited layer.

4.2 Film Composition

The samples used in RBS measurements were grown on the carbon substrates as opposed to the commonly used substrate, silicon, in most of the similar studies. The practical reason for using a carbon glassy plate was concerned the increase of the accuracy of the RBS technique. The SiC_xN_y matrix contains light elements such as carbon and nitrogen. In subsection 3.3.1 the physics behind of the RBS method was described wherein a typical spectrum of a thick substrate was highlighted. In our produced layer, the thickness of the film and substrate are in the order on 100-300 nm and a few μm, respectively. The RBS spectra of samples deposited on glassy carbon substrates gave well separated carbon and nitrogen peaks. The carbon and nitrogen peaks cannot, however, be accurately distinguished in the SiC_xN_y matrix deposited on the silicon substrate (Fig. 4.1.b). The carbon and nitrogen spectral overlap may be understood in two ways; 1) being next to each other in the periodic table with close atomic masses, and 2) the interference from the silicon substrate may cause difficulties in distinguishing the spectral signature of lighter elements. Therefore, the compositions of all thin films in this set, deposited with different CH_4 gas flow rates, were determined using glassy carbon substrates.

4.2.1 Different Substrates

A representative RBS spectrum for a sample containing atomic concentrations of 25.4 ± 0.3 at.% silicon, 17.5 ± 1.1 at.% nitrogen, 32.2 ± 1.0 at.% carbon, and 22.8 ± 0.9 at.% hydrogen grown on two different substrates, carbon and silicon, is shown

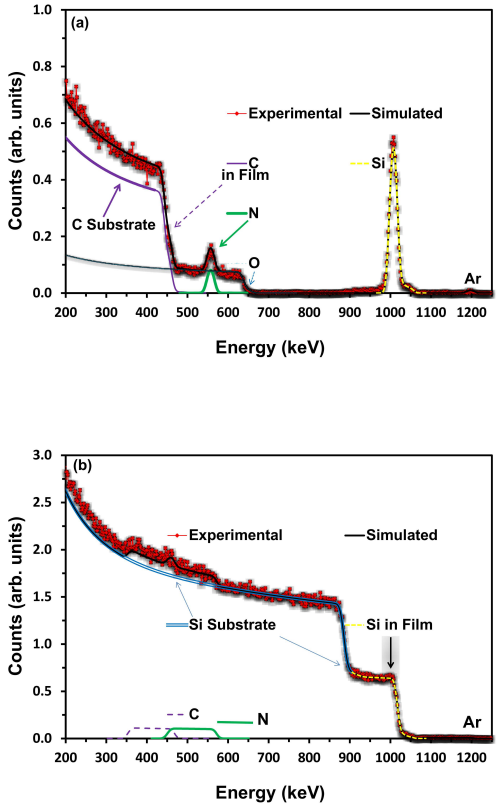

Figure 4.1: **Comparison of carbon and silicon substrates.** Experimental (red dots) and simulated (black line) RBS spectra obtained for a SiC_xN_y:H_z sample grown on (a) carbon substrate and (b) silicon substrate with the composition presented in Table 4.2. The signals from carbon, nitrogen, and silicon can be clearly distinguished when using the carbon substrate.

in Figs. 4.1.a and b, respectively. The experimental data (red dots) and the fitted data (solid black line) are plotted and the spectral contribution from each element is depicted and labeled. To avoid the influence of differences in the process parameters, both samples were prepared simultaneously under the same experimental conditions. Results of the combined RBS and ERD measurements of SiC_xN_y:H_z samples deposited on two different substrates are provided in Table 4.2. The initial concentration of the elements given by RBS data was fed into the ERD simulation, and then RBS spectra

were adjusted using the obtained hydrogen content. In some cases, one needs to add the hydrogen fraction to the initial fitting of RBS data. In this case, first the concentration of hydrogen is excluded from the RBS results, see subsection 3.3.1 for more details. Then the true value of hydrogen given by ERD can be applied in the reverse procedure to obtain the actual concentration of all constituent elements. The concentration of the constituent elements is reported by atomic percent. Table 4.2 also shows that the use of a silicon substrate resulted in relatively larger uncertainties for carbon and nitrogen in comparison with using a carbon substrate.

Table 4.2: **Comparison of carbon and silicon substrates.** Composition analysis given by combined RBS-ERD of a-SiC_xN_y:H_z thin films deposited with a CH_4 gas flow of 8 sccm.

Substrate	H [at.%]	C [at.%]	N [at.%]	O [at.%]	Si [at.%]	Ar [at.%]
Silicon	23.5±1.0	26.9±8.5	19.6±2.5	Not detected	29.7±0.3	0.3± 0.0
Carbon	22.8±0.9	32.2±1.0	17.5±1.1	1.8±0.1	25.4±0.3	0.3±0.0

It can be observed that the spectrum of a film on a carbon substrate showed a small amount of oxygen while this peak was lower than the noise level when using a silicon substrate. The oxygen containing residuals, i.e., water vapors, oxygen, and carbon oxides, adsorbed to the chamber wall can be considered as the sources of the excess oxygen impurities. The apparent silicon atomic fraction in the film deposited on the silicon substrate was higher than in the one deposited on the carbon substrate. This is as a result of the overlapping of the silicon spectra of the film with the silicon substrate signal. In the case of argon, being heavier than silicon, its atomic fraction measured on both substrates was the same.

4.2.2 RBS of Carbon Varying SiCN

The summary of the compositional analysis of as-deposited SiCN films fabricated on carbon substrates with different CH_4 gas flow rate is provided in Fig. 4.2. The key aspects of the approach applied for the compositional analysis were the use of carbon substrates for RBS and using RBS and ERD simultaneously. The small error bars shown in Fig. 4.2 confirm that this approach leads to highly accurate results. The analysis showed film compositions varying from stoichiometric Si_3N_4 (CH_4=0 sccm) to C-rich SiCN (CH_4=20 sccm) films. Argon and oxygen concentrations varied between 1 and 3 at.% regardless of the precursors used in the deposition process. By adding a small amount (2 sccm) of CH_4 gas into the gas mixture, the carbon content reached 14.6 at.%. The carbon concentration steadily increased to a value of around 41.6 at.% in the most C-rich sample (CH_4=20 sccm)and remained practically unchanged with further increase of the CH_4 flow rate. Nitrogen and silicon concentrations both decreased, with silicon decreasing less compared to nitrogen, which is clearly shown in Fig. 4.3. This relates to the reaction of carbon and nitrogen in the deposition process where N_2 is more reactive with carbon components than SiH_4 gas-derived species. Previous in-situ plasma analysis showed that the CN and HCN emission lines were found to be the major components present in the plasma [152]. The presence of C-N species in the plasma led to the less formation of C-N bonds in the growing layer and explained the nitrogen deficiency in the SiCN samples.

4.2.3 ERD of Carbon Varying SiCN

The result of the ERD analysis is also presented in Fig. 4.2, providing a measure of the hydrogen fraction of up to 35.7 $\pm$ 1.0 at.% in SiCN films, both bonded and

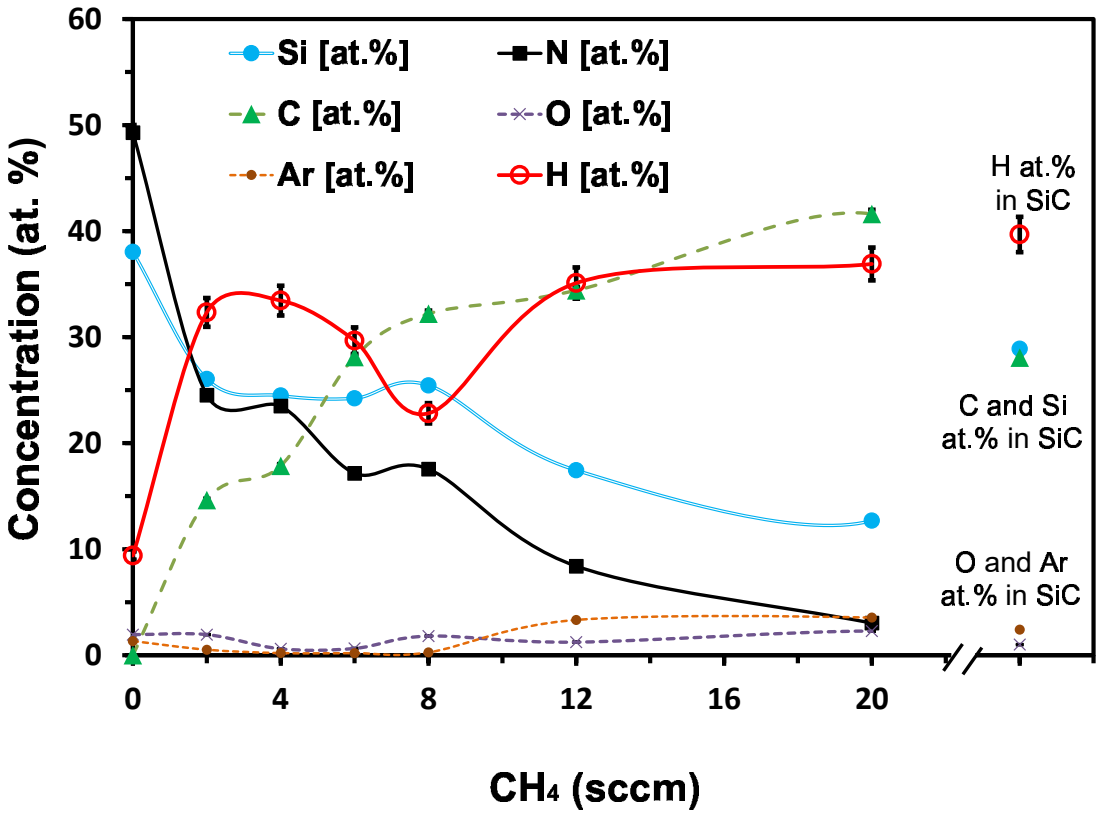

Figure 4.2: **Elemental composition of carbon varying SiCN films.** Elemental composition analysis using RBS and ERD of SiCN samples as a function of CH_4 gas flow rate. The small error bars of RBS results (C, N, and Si) are depicted. The error bars of about 1 at.% are calculated for hydrogen in ERD analysis.

un-bonded. These results were used as an input for the RBS fitting process to obtain compositional information for the other elements in the film. The hydrogen content was greatly increased by introducing a small amount of carbon into the SiN matrix. Because of the dissociation of CH_4 in the deposition process, large concentrations of hydrogen remained in the films, reaching up to 32.3 at.% for the sample grown using a CH_4 gas flow of 2 sccm. Increasing the CH_4 gas flow rate from 2 to 8 sccm resulted in a reduction of the hydrogen concentration, despite the introduction of more hydrogen in the deposition process. The reduction of the hydrogen concentration is

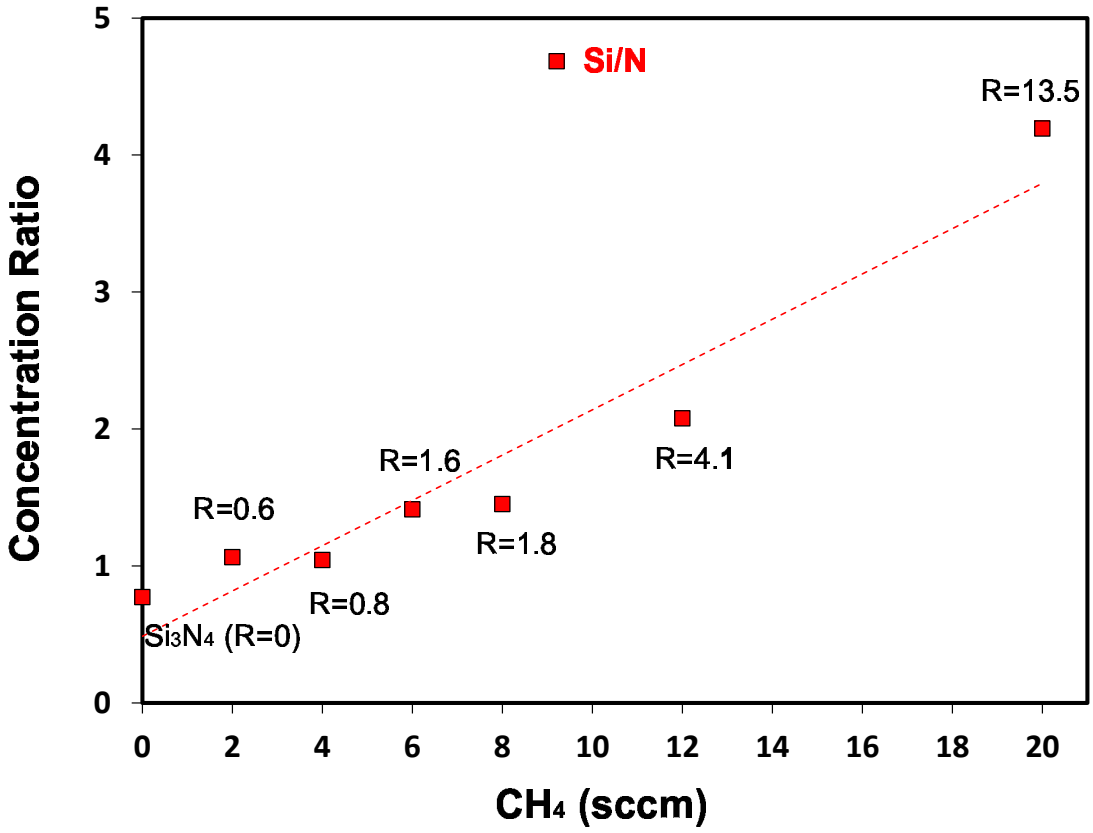

Figure 4.3: **Ratio of silicon to nitrogen.** Atomic concentration ratio of silicon to nitrogen as a function of CH_4 gas flow rate. The linear trend is included to show the increase and is not intended to represent a model.

due to more incorporation of carbon in the films. This leads to more carbon bond formation (observations made by XPS and FTIR, to be discussed later in subsection 4.4) leaving less opportunity for the formation of hydrogen bonds; i.e., an increase in the formation of Si-C bonding which is stronger compared to the C–H bond in the SiC_xN_y:H_z matrix. Further increase of the CH_4 gas flow rate from 8 to 20 sccm led to an increase of hydrogen in SiCN films to about 35 at.%. This can be attributed to continuous reduction of nitrogen in the film, which provides more opportunities for hydrogen to form bonds with carbon and silicon. The hydrogen concentration

reached 40.8 at.% in the stoichiometric SiC film (grown using SiH_4=5 and CH_4=4 sccm). The comparison of stoichiometric SiC with the counterpart SiC_xN_y:H_z (grown using SiH_4=5, CH_4=4, and N_2=10 sccm), indicated that the hydrogen concentration decreased from 40.8 to 33.4 at.% with the introduction of N_2 in to the gas mixture.

By using RBS results, in the following sections, the samples are identified by the carbon-to-nitrogen concentration ratio in the film which is described by the parameter R=C/N. Table 4.3 shows the film composition (in atomic percentage) and corresponding gas flow rates used for each individual sample. Only CH_4 gas flow rate is reported as N_2 and SiH_4 were kept unchanged at 10 and 5 sccm, respectively.

Table 4.3: **Composition analysis of carbon varying SiCN films.** Film composition (at.%) determined by RBS of the film deposited on a carbon substrate using different methane flow rates.

CH_4 (sccm)	0	2	4	6	8	12	20	4
R=C/N	0	0.59	0.78	1.64	1.83	4.09	13.5	SiC
H	9.4	32.3	33.4	29.7	22.8	35.1	36.9	39.8
C	0	14.6	17.8	28.1	32.2	34.4	41.6	36.7
N	49.3	24.5	23.5	17.1	17.5	8.3	3.0	0
Si	38.0	26.0	24.4	24.2	25.4	17.4	12.7	22

4.3 Optical Properties

The optical properties of the films were analyzed using UV-VIS spectroscopy, VASE, and PL in the visible range. The results of VASE do not directly deliver the refractive index, thickness, and absorption coefficient. VASE data first was simulated using a

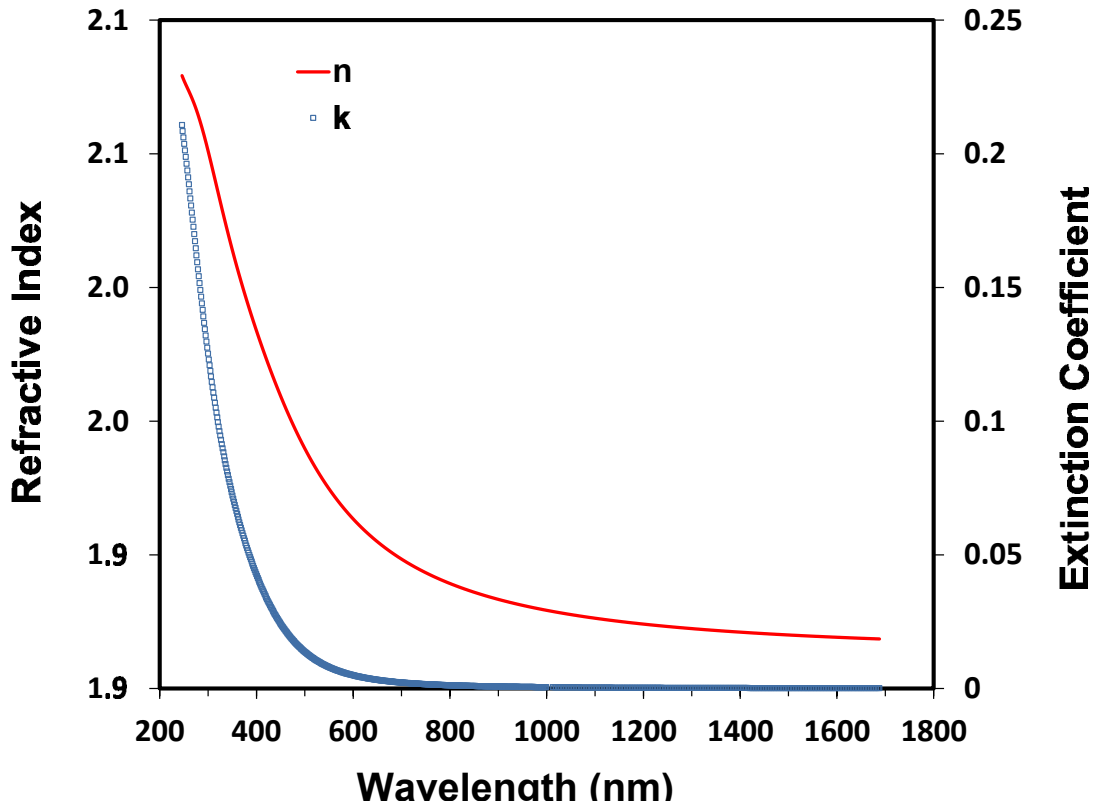

Figure 4.4: **Optical properties of SiCN with R=0.4.** The refractive index and extinction coefficient of a sample with R=0.4.

Cauchy model assuming a crystalline silicon substrate and a surface roughness layer (with an average thickness of 10∼15 Å). A B-Spline model was then added; this model follows the experimental trend more closely than the Cauchy model [212]. The resulting refractive index and extinction coefficient of a sample deposited using R=0.4 is plotted in Fig. 4.4. The small value of the extinction coefficient (k) indicates no significant absorption in the visible region for all samples (10^{-2}). This did not change significantly with the increase of carbon in the matrix which suggests that the SiCN layer is a good candidate as a transparent material in display applications.

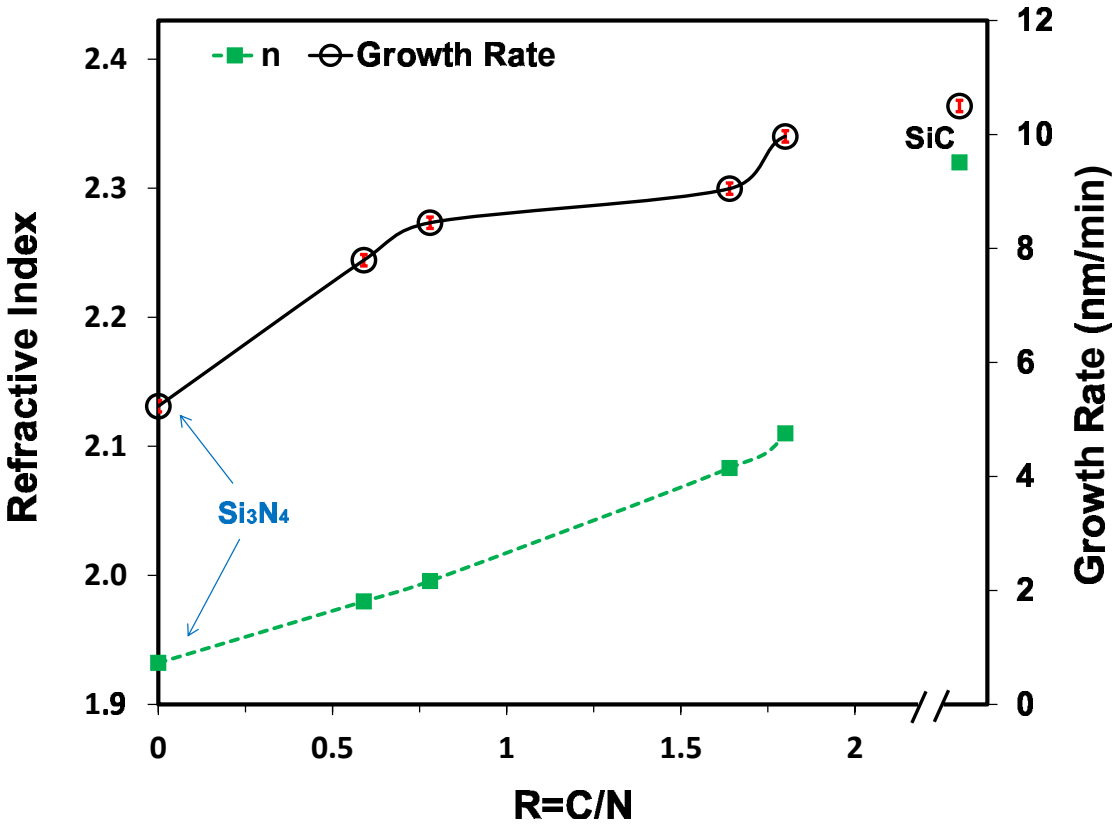

Figure 4.5: **Refractive index and growth rate of carbon varying SiCN films.** Variation of the refractive index (at 632.8 nm) and growth rate with different R-values (R is the carbon-to-nitrogen ratio). R-value cannot be defined for silicon carbide represented a separate data. The error bars are shown with the red signs.

4.3.1 Refractive Index of Carbon Varying SiCN

The refractive indices of films with different compositions are plotted as a function of carbon to nitrogen concentration ratio in Fig. 4.5. An increase in refractive index was observed from 1.90 to 2.12, corresponding to film stoichiometries between C-free (Si_3N_4) and C-rich SiCN films, respectively. These values lie in the range of refractive indices of stoichiometric Si_3N_4 (n=1.90) and stoichiometric SiC (n=2.28) confirming the presence of both Si–C and Si–N networks [157]. The obtained values of refractive indices in our stoichiometric Si_3N_4 and SiC samples were slightly smaller than those of

Si_3N_4 and SiC synthesized using CVD, reported as 2.0 and 2.6, respectively [239] [240]; likely due to the presence of a large amount of hydrogen incorporated during the low-temperature growth [241]. Based on the Lorentz-Lorenz equation, the refractive index depends on both the variation of the chemical composition and the density of the films, being correlated parameters [242]. In our samples, by the introduction of carbon to SiN matrix, the chemical composition changed which led to larger refractive indices due to the higher Si-C density (see XPS results later in subsection 4.4). In addition, the density of the films decreased and the refractive index increased in less dense layers [243].

4.3.2 Growth Rates of Carbon Varying SiCN

The growth rate was estimated from the thickness determined by the VASE measurements with an uncertainty of ±3.5 Å. Fig. 4.5 shows a non-linear increase of the growth rate as a function of carbon to nitrogen concentration ratio. Kuo et al. [167] showed that the effect of reactant gases on the growth rate is significant at the lower deposition temperature of 380 °C. In our case, the increase of CH_4 flow from 0 to 8 sccm (R=1.8) at a substrate temperature of 120 °C led to 1.7X higher growth rate. However, the observed trend of the growth rate is in contrast to the results reported in [150]. This could be due to the difference in the density of the produced films. According to the calculations of the film density from RBS and VASE results (not shown here), our films appeared to be less dense than the ones described in [150], likely because of the relatively high concentration of hydrogen.

4.3.3 Optical Band Gap of Carbon Varying SiCN

Fig. 4.6 shows the optical transmission spectra of SiCN thin films with varying carbon concentrations. The noticeable oscillations at longer wavelengths originate from interference due to the internal reflections, depending on the refractive index and the film thickness [89]. The average optical transmittance was found to be as high as 85% in the visible spectrum range indicating highly transparent films. The transmittance decreased as the CH_4 gas flow rate increased in the deposition process and films with higher carbon content were produced. The optical absorption edge was then calculated from the transmission data using PUMA software [209].

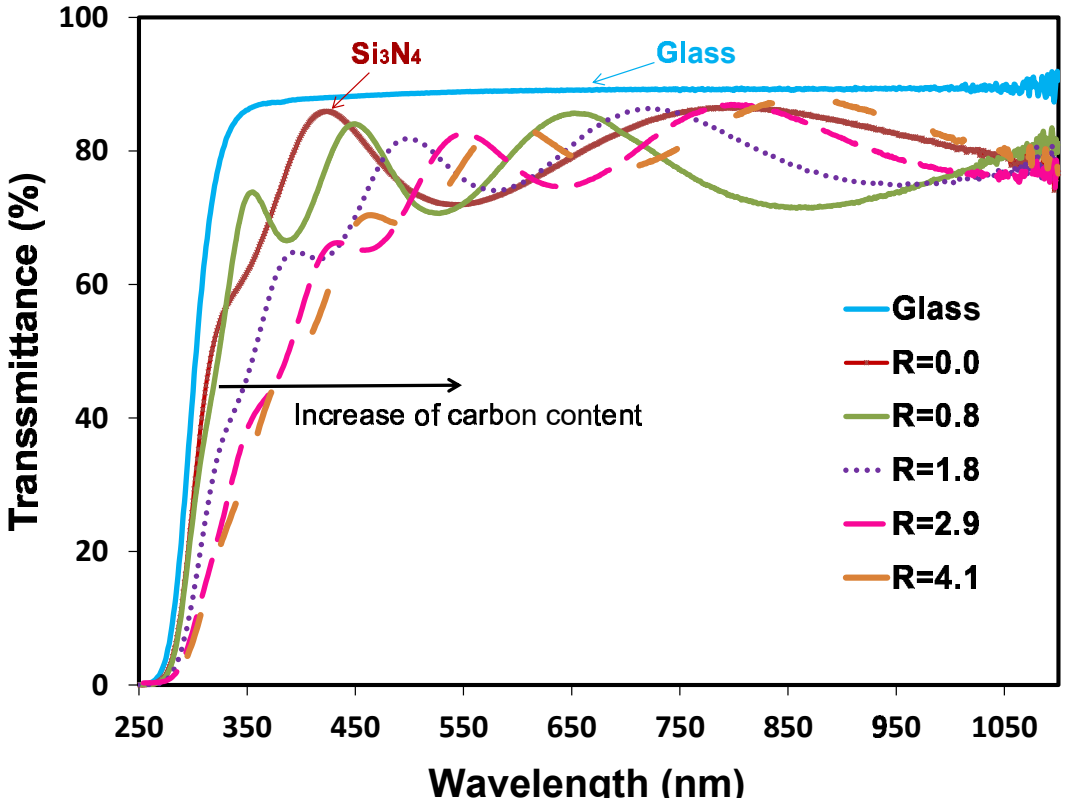

Figure 4.6: **Transmission spectra of carbon varying SiCN films.** The variation of the transmission spectra of carbon varying SiCN thin films is plotted.

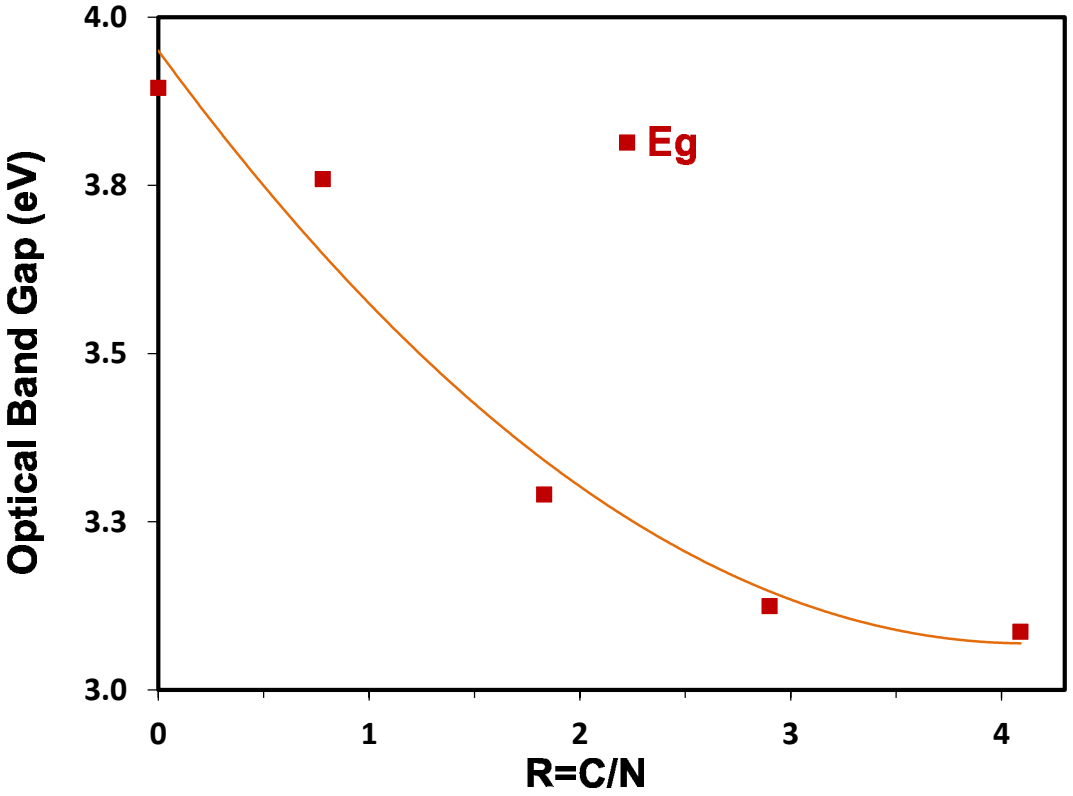

Figure 4.7: **Optical band gap of carbon varying SiCN thin films.** The optical band gap of SiCN thin films with varying carbon concentrations is plotted. The trend is included to show the decrease and is not intended to represent a model.

Fig. 4.7 shows a decrease of the band gap energy from 3.83 to 3.08 eV for films synthesized with R=0 to R=4.1, respectively. The experimental band gap of stoichiometric Si_3N_4 is reported to be about 5.01 eV [78], which is somewhat larger than 4.3 eV obtained by density functional theory calculations [244]. The band gap energy of SiN films with no carbon could not be determined on Corning glass due to the lower band gap energy of glass. The optical band gap of SiC is reported to lie in the range of 2.6 to 3.05 eV depending on different polytypes [245]. Therefore, the slight incorporation of carbon into the SiN matrix lowered the energy gap to values smaller than 3.8 eV. The band gap reduction steadily continued as the CH_4 gas flow rate was

increased further. The band gap narrowing may be ascribed to the formation of Si–C bonds due to the creation of electronic localized states as observed in XPS analysis (subsection 4.4) [164]. In addition, ERD results (subsection 4.2.3) showed that the hydrogen concentration decreased, which would lead to a narrowing of the band gap due to the increase of the dangling bond density [187].

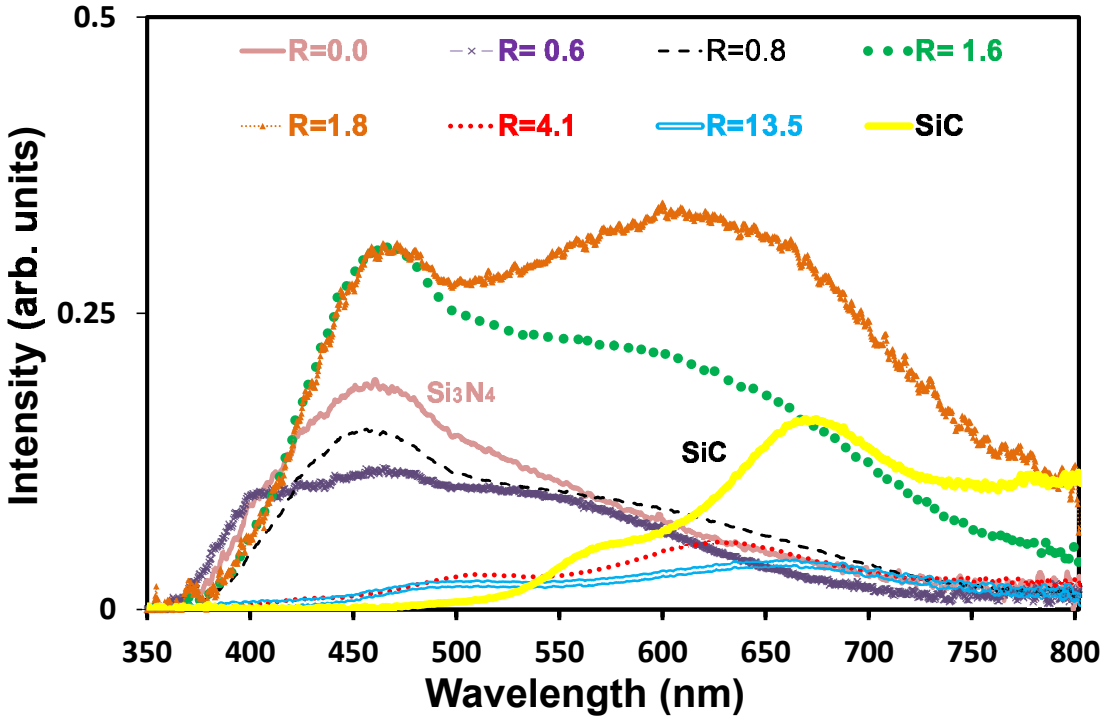

Figure 4.8: **PL of carbon varying SiCN films.** PL spectra excited by 325 nm He-Cd laser as a function of wavelength for SiCN thin films with varying carbon concentrations.

4.3.4 PL of Carbon Varying SiCN

Under excitation by a 325 nm HeCd laser source, the PL spectra of as-deposited samples were measured (Fig. 4.8) In general, the PL emission, ranging from 350 to

800 nm, is broadened in the SiCN matrix in comparison with PL peaks of both SiC and SiN. The broadening likely originates from the structural disorder, which increases the width of the localized states (called "antiparallel band-edge fluctuations") [132]. The first peak position at 475 nm (2.61 eV) remained unchanged regardless of the presence of carbon in the matrix; however, it decreased in C-rich SiCN (R=13.5) and vanished in SiC samples. This peak could be assigned to the recombination processes at silicon dangling bonds in a-SiN thin films [132] [110]. With an increase of the carbon content, the center of the second (main) PL peak shifted towards longer wavelengths, from 550 to 660 nm (2.25-1.87 eV). As shown in Fig. 4.7, the band gap energy decreased with increasing the carbon content, resulting in a redshift of the main PL peak at 550 nm. The PL spectrum of a stoichiometric SiC (N-free) film showed two main peaks and one small peak at 550, 650, and 780 nm (2.25, 1.90, and 1.58 eV), respectively. According to the theoretical PL calculations explained in chapter 2, these peaks were attributed to carbon in the β-SiC configuration, a-SiC, and carbon clusters, respectively. Both C-rich SiCN (R=13.5) and stoichiometric SiC samples showed a peak position at 650 nm, attributed to a-SiC clusters. Most likely the redshift of the second (main) peak in SiCN films, observed after the introduction of carbon to SiN films, is related to the formation of SiC clusters.

Fig. 4.9 illustrates the dependence of the emission intensity on the ratio of carbon to nitrogen content in the layer. First, by introducing carbon into the SiN matrix the PL intensity decreased for R=0.6 (C=14.6 at.%) and R=0.8 (C=17.8 at.%) samples. It then gradually increased with the further increase of CH_4 flow. The most luminescent SiCN film was obtained for R=1.8 (C= 32.2 at.%) deposited using a CH_4 gas flow of 8 sccm. No significant enhancement of PL intensity was observed with the further increases of the CH_4 gas flow rate up to 12 and 20 sccm which produced

samples with R=4.1 (C=34.4 at.%) and R=13.5 (C=41.6 at.%), respectively. In fact, the maximum PL intensity did not vary significantly for any R-value higher than R=4.1. SiN and SiC samples exhibited lower PL intensity which indicated that the intensity of the PL can be optimized by an appropriate ratio of carbon and nitrogen in the matrix.

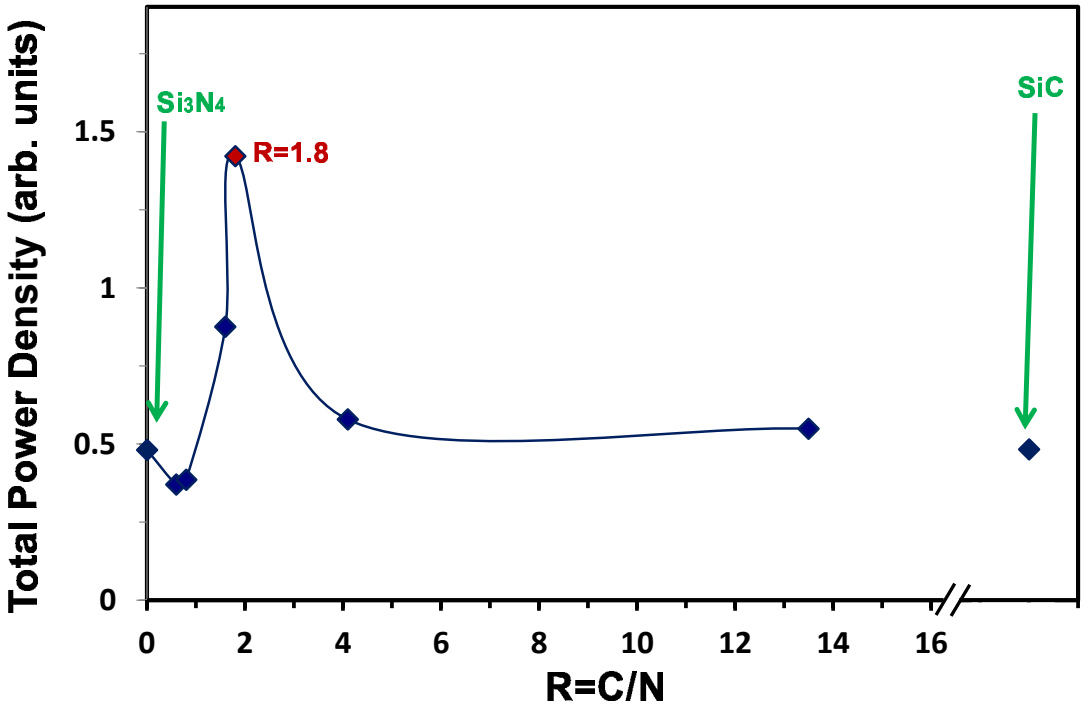

Figure 4.9: **Total power emission of carbon varying SiCN films.** The total power emission of carbon varying SiCN samples as a function of R is plotted.

Hydrogen passivation was performed by the use of 95%N_2 +5% H_2 instead of pure N_2 as the ambient gas in the annealing process. The temperature evolution of the PL spectra following the annealing process has been discussed in reference [246]. The PL intensity was similar for both passivated and non-passivated or C-rich and less C-rich samples. Thus, the hydrogen passivation was found to have no effect on

the PL emission intensity from C-containing samples, which deviates from results reported for Si-rich SiN films [247]. This difference likely is related to the use of CH_4 as the reactant gas during the growth. As ERD in subsection 4.2.3 showed, CH_4 introduced high concentrations of hydrogen in the film. Ma et al. showed that the PL improved by the use of NH_3 gas as the nitrogen source in the deposition process instead of N_2 gas [247]. Their SiN samples were prepared using NH_3 contained significant hydrogen concentrations and the PL improved at the lower temperatures, where the out-diffusion of hydrogen did not occur and hydrogen remained in the film.

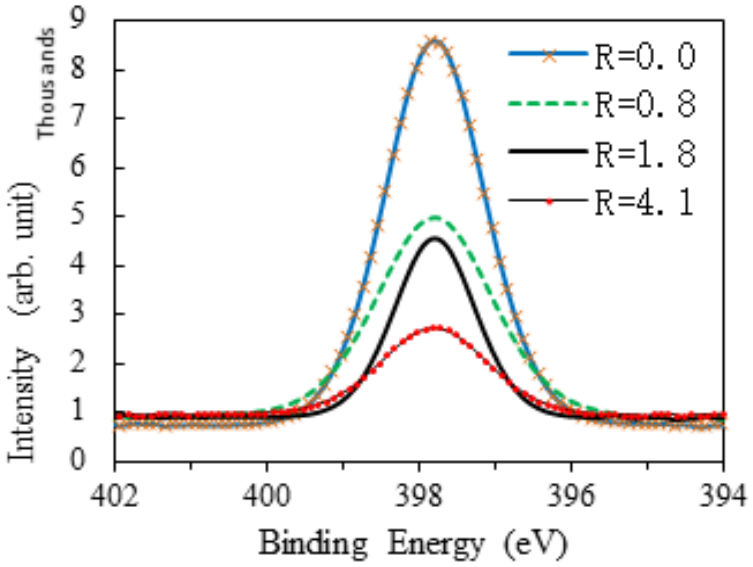

Figure 4.10: **N 1s spectra of carbon varying SiCN films.** XPS spectra of the N 1s of SiCN thin films with different carbon content.

4.4 XPS of Carbon Varying SiCN

XPS was used to study the effect of carbon incorporation on the electronic restructuring of SiCN films at the C 1s, N 1s, Si 2p, and O 1s edges. The instrument work

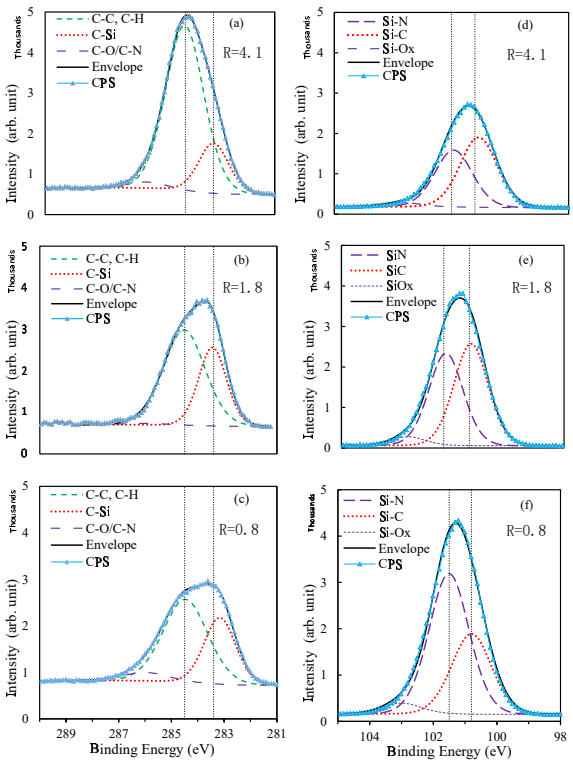

Figure 4.11: **XPS spectra of carbon varying SiCN films.** XPS spectra of the (a-c) C 1s and (d-f) Si 2p peaks of SiCN thin films with different carbon content. R is the carbon-to-nitrogen ratio (top: highest carbon concentration; bottom: lowest carbon concentration). Solid lines show the measured data. Dashed lines represent the peak positions of specific peaks obtained from deconvolution of the (a-c) C 1s and (d-f) Si 2p contributions.

function was discussed in subsection 3.5.1. We observed one negligible O 1s peak at 532.6 eV for all samples, likely due to the small amount of oxygen contamination. Low oxygen contamination in the film was mentioned in RBS results on the carbon substrate (subsection 4.2); however, the surfaces oxide layer was removed by HF treatment. Fig. 4.10 shows that the N 1s spectrum consisted of one peak centered at 397.8 eV in all C-free and C-containing films, which remained with no shift. The peak at 397.8 eV identified the N-Si bonds, which showed the only higher amount in Si_3N_4 (R=0) and a decrease as the carbon content increased in the film. No N-sp^3C

at 398 eV and N–sp^2C bonds at 400 eV was detected. The assignment of the N 1s components was adopted from the general agreement of the presence of nitrogen in a mixed and non-fixed environment [221] [218].

Figs. 4.11. a, b, c show the C 1s core level spectra for three as-deposited samples with various carbon concentrations (prepared with different CH_4 gas flow rates). The deconvolution of the C 1s spectra yielded three peaks centred at 283.4 eV (C-Si), 284.8 eV (C–C and/or C–H), and 286.2 eV (C–O and/or C–N), with no feature at 289.0 eV (C=O) as was expected from the low oxygen content [215]. There was also no peak at 287.0 eV (associated with the Csp^3 bonded to one N neighbour) or at 288.0 eV (Csp^3 bonded to two N neighbours) [221]. A small peak at 286.2 eV showed the identity of the C–N bond rather than the C–O bond. The contribution of the C–O bond can be ignored due to the negligible O 1s peak and the low oxygen contamination. The peak at 286.2 eV remained nearly unchanged regardless of the carbon concentration and only showed slightly higher intensity in the low-carbon content film (R=0.8) with an nitrogen content of 23.5 at.%. The type of carbon and nitrogen bond was identified as the C≡N triple bond at 286.3 eV and the trigonal sp^2C–N bond at 286.5 eV [218]. Most likely, the observed peak at 286.2 eV can be attributed to C≡N triple bonds due to no contribution of N–sp^2C bonds in the N 1s spectra and the presence of the C≡N stretching mode at 2100∼2200 cm^{-1} in the IR spectrum (subsection 4.5).

The peak at 284.8 eV has been attributed to C–C, C–H, and C–N bonds. The assignment of this component depends on the concentration of N. At low concentrations of N, this binding energy was assigned to the C–C peak for sp^3 bonded C in a diamond-like matrix; at higher nitrogen concentrations, it was ascribed to the C–C peak for sp^2 bonded C in a graphite phase in SiCN matrix [216] [217]. The lack of XPS experimental data of SiCN in the literature necessitated exercising caution in

the assignment of N 1s and C 1s to definite chemical states. Other authors associated the peak at 284.8 eV with Csp^2 bonded to either carbon or nitrogen in CN materials [221] [216]. However, in the produced SiCN films, we assigned the peak at 284.8 eV to C–C/C–H bonds rather than C–N bond for two reasons; First, the lower concentration of nitrogen in R=4.1 implied that the higher intensity of this peak could not be attributed to C–N bonds and can be linked to both graphite formation (sp^2C) and more formation of hydrocarbon (C–H) bonds; ERD and RBS (subsection 4.2) showed a higher concentration of hydrogen and carbon in sample R=4.1. In addition, the feature at 286.2 eV did not change from sample R=1.8 to sample R=4.1, indicating no further changes in C–N bonds.

Adding carbon into the SiN matrix resulted in the formation of C–Si bonds 283.4 eV. The left vertical line in Figs. 4.11. a, b, and c. shows that increasing the R-values (R=C/N) from R=0.8 (C= 17.8 at.%) to R=1.8 (C= 32.2 at.%) led to the rise of the C–Si bond relative integrated intensity (the amount defined as the ratio of the band area to its envelope area). With the further increase of the carbon content to R=4.1 (34.4 at.%.), the amount of C–Si bonds became smaller compared to sample R=1.8, whereas the amount of C-C bonds continuously increased from R=0.8 to R=1.8 and then from R=1.8 to R=4.1. It should be noted that R=4.1 contained the highest carbon content wherein no more carbon could be incorporated in the layer with the rise of CH_4 gas flow rate in the growth process. The added carbonaceous components made the carbon 1s of R=1.4 more complicated. The observed decrease in C–Si bond was likely due to the increase in the other carbon containing species at the surface. Therefore, the data of Si 2p was used to report the trend of Si–C bond. Figs. 4.11. a, d, e, and f show the Si 2p peak containing a mix of carbide, nitride, and oxide bonds positioned at 100.8, 101.5, and 103.0 eV, respectively. With increasing CH_4

gas flow rate in the deposition (increasing the carbon content in the produced films as a result), the amount of Si–N bond gradually decreased. The amount of the Si–C bond increased significantly from R=0.8 (C= 17.8 at.%) to R=1.8 (C= 32.2 at.%) and with the further rise in the carbon content to R=4.1 (34.4 at.%.), the amount of Si–C appeared unchanged (slightly increases $\sim$ 1% of the relative integrated area).

With correlation to the PL behavior of these films, the relatively large density of Si–C bonds and lower amount of C–C bonds could be found in the most luminescent sample with R=1.8. This sample showed more intense PL emission than R=4.1 (Fig. 4.8) which contained a higher C–C content and a similar amount of Si–C to that observed in R=1.8. This yields an optimal relative concentration of constituent elements (Si, N, C, and H) to produce the highly luminescent SiCN thin film. It is noted that Chen et al. [26] did not observe considerable Si–C peaks at either carbon 1s or Si 2p edges in their crystalline SiCN films. They suggested the existence of a Si-C-N phase with a hexagonal crystalline structure similar to SiN, where Si atoms were partially substituted by carbon atoms, with nitrogen as a bridge. However, in our amorphous samples, most likely due to the low concentration of nitrogen, carbon was favored to make bonds with silicon rather than nitrogen, as we verified both by XPS and FTIR results. The low concentration of nitrogen led to the formation of amorphous phases of SiC and SiN in the produced SiCN thin films.

4.5 FTIR of Carbon Varying SiCN

The transmission spectra of as-deposited samples with different carbon contents (Fig. 4.12) includes a dominant peak in the range of 600 to 1200 cm^{-1} and several individual peaks. The assignment of the absorption peaks is provided in Table 3.3 using data

from section 3.3. The ternary structure of SiCN includes many possible absorption bands making the peak assignment a not clearly resolved matter [160]. In addition, the reported data from different growth methods, and the use of polymer data are also sources of discrepancies [248]; for example, Peter et al. [160] mentioned discrepancies of about 150 cm^{-1} in the peak positions of Si–C and Si–N bonds.

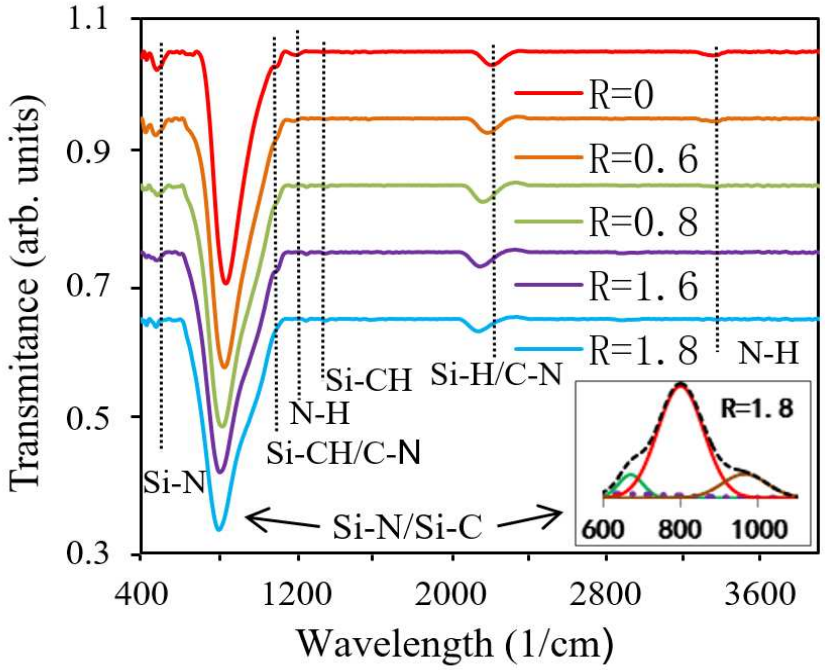

Figure 4.12: **FTIR spectra of carbon varying SiCN films.** Representative infrared transmittance spectra for SiCN thin films with various carbon contents. The inset depicts the deconvolution in the wavenumber range of 600–1200 cm^{-1} of the sample deposited with R=1.8. Dashed lines represent the position of the main peaks.

The very first peak at 420 cm^{-1} (Si–O–Si stretching) did not depend on the carbon concentration in the film, as could be expected from the low and constant O concentrations in the layer. The Si–N symmetric stretching mode (470 cm^{-1}) is weakened in the SiCN sample (R=1.8), indicating a decrease in the number of Si–N bonds. The dominant broad absorption area is centered near 820 cm^{-1} and is a

superposition of the Si–N stretching mode (near 900 cm^{-1}), the Si-N local distorted stretching mode (at about 790 cm^{-1}), and the N–Si_3 asymmetric stretching mode (850 cm^{-1}) [227]. The deconvolution of the main envelope ranging from 600 to 1200 cm^{-1} was approximated using three Gaussian curves to magnify the effect of restructuring occurring by the carbon introduction to the SiN matrix. The inset in Fig. 4.12 shows an example of deconvoluted FTIR spectra of the sample with R=1.8. Incorporation of CH_4 into the growth process resulted in changes both in the shape and intensity of the main peak due to the enhanced structural disorder of the Si–C bonds. The broadening towards the lower wavenumbers could be accounted by the increase in the intensity of the characteristic stretching vibration of Si–C bonds centered at 800 cm^{-1}. The widening of the main peak toward larger wavenumbers could be attributed to both the C–N wagging and Si–CH_x bending modes occurring at about 1030 cm^{-1}. After increasing the carbon content, another remarkable feature was the decrease in the intensity of the main peak showing further evidence of reduction of the Si-N bonds in the favor of the formation of Si–C modes positioned at 800 cm^{-1}.

The position of this peak shifted towards lower wavenumbers by 94 cm^{-1} and slightly decreased by increasing the carbon to nitrogen concentration ratio (R-value) from 0 to 1.8. The presence of sp-bonded N at 2100$\sim$2200 cm^{-1} was strongly correlated with the C–N contribution to C 1s at around 286.5 eV [218] [216]. The observed decrease in the C–N stretching mode was in agreement with the decrease of C–N bond at 286.2 eV from the sample with R=0.8 to sample with R=1.8 (section 4.2 and Figs. 4.11.a and b).

N–H bonds at 1190 and 3300 cm^{-1} completely disappeared after incorporation of carbon to the SiN matrix, as can expected from the significant decrease of nitrogen concentration. An absorption band at 650–660 cm^{-1} was also observed but could not

be attributed to any bonds in SiCN films. Peter et al. [160] reported this peak in a list of non-published absorption peaks obtained using optical modeling of a vacuum/a-SiCN:H/monocrystalline Si/vacuum structure.

The addition of carbon to the SiN matrix led to the formation of a small amount of C–N and C≡N with a significant increase of the Si–C bond density. Carbon prefers to form bonds with silicon rather than nitrogen. All of the observed changes likely originate from the formation of Si–C and C–N bonds resulting in the observed decrease in the intensity of Si–N and N–H peaks in the FTIR spectra SiCN matrix. This is indicative of the decrease of nitrogen incorporation in films, as verified by the lower nitrogen concentrations obtained using RBS (Fig. 4.2).

Chapter 5

Annealing of Silicon Carbonitrides

[1]The thermal annealing behavior of the sample exhibiting the strongest luminescence (a-$SiC_{1.2}N_{0.7}$:$H_{1.4}$) is the main focus of this chapter. The hydrogen diffusion in such a metastable thin film is discussed in terms of the post-deposition annealing and is reviewed quantitatively employing two different experimental techniques; ERD and FTIR. Then the interdependency of the optical, structural, and compositional features determined by a multitude of characterization techniques is addressed. In particular, hydrogen (and hydrogen desorption) is one of the key determinants of the film properties, as discussed in section 2.5. In the present chapter, the link between the thermally induced changes of the film properties and hydrogen diffusion in such films is also highlighted. The content of this chapter has been published in one conference

[1]The content of this chapter has been published in one journal article and one conference proceedings as follows:

- **Z. Khatami**, C. Nowikow, J. Wojcik, P. Mascher (2018) Annealing of silicon carbonitride nanostructured thin films: Interdependency of hydrogen content, optical, and structural properties. *J. Mater. Sci.*, 53(2): 1497-1513. https://doi.org/10.1007/s10853-017-1576-6
- **Z. Khatami**, P. R. J. Wilson, J. Wojcik, P. Mascher (2014) Structural and optical properties of luminescent silicon carbonitride thin films, *ECS Trans.*, 61(5), 97-103. http://ecst.ecsdl.org/cgi/doi/10.1149/06105.0097ecst

proceeding [249] and one journal article [250].

5.1 Fabrication of Annealed SiCN

The precise stoichiometry of a-$SiC_{1.2}N_{0.7}$:$H_{1.4}$ sample was obtained in via the proper adjustment of the carbon content of a series of a-SiC_xN_y:H_z thin films, as was described in the previous chapter. The precursors of 30% SiH_4 in Ar, 10% N_2 in Ar, and pure CH_4 were fed into the deposition chamber with gas flow rates of 5, 10, and 8 ($\pm$5%) sccm, respectively. A nanolayer with a thickness of 230 nm was deposited in 30 minutes at a nominal deposition temperature of 350 °C, corresponding to a substrate temperature of approximately 120 °C. To study the thermal annealing behavior of a-SiC_xN_y materials, post-deposition, the as-deposited a-$SiC_{1.2}N_{0.7}$:$H_{1.4}$ sample were cleaved and subsequently subjected to the thermal annealing in a quartz tube furnace using ambient gases of pure N_2 and 95% N_2 + 5% H_2 for one hour at temperatures (T_a) ranging from 300 to 1200 °C in 100 °C increments. To minimize contamination by the atmosphere; all samples were allowed to cool to room temperature in N_2 gas before extraction from the tube furnace.

For the temperature studies, the thin films deposited on substrates of n-type silicon were used for all measurements except an un-doped silicon substrate that was employed for FTIR measurements. As described in subsection 3.3.1 the use of carbon substrates is one the most efficient solutions to avoid the overlapping signal of the silicon substrate with the signal of silicon and lighter elements of SiC_xN_y thin films. However, in our study of the evolution of the composition as a function of post-deposition thermal annealing, films grown on silicon substrates were used instead of carbon substrates. The mismatch of thermal expansion between the thin films and

underlying glassy carbon substrate led to delamination and film cracks during the annealing procedure, in particular at the elevated temperatures.

5.2 Film Properties of Annealed SiCN

5.2.1 Film Composition

Fig. 5.1 shows an RBS spectrum of a-$SiC_{0.8}N_{0.5}$:$H_{0.08}$. This sample is the annealed a-$SiC_{1.2}N_{0.7}$:$H_{1.4}$) at 1200 °C for 1 hour. It is grown on silicon substrate, so that, the RBS spectrum is superimposed on the background signal of the thick silicon substrate. The fit generated by the SIMNRA program is plotted by the black line. The spectrum is composed of constituent elements, for which the partially fitted spectra are plotted separately along with the corrected areal density. The corrected areal densities (atoms/cm^2) are calculated by the multiplication of the true thickness obtained from VASE analysis and concentrations measured using RBS.

The combined RBS-ERD analysis was performed for the as-deposited a-$SiC_{1.2}N_{0.7}$:$H_{1.4}$ sample, and the ones annealed at 500, 900, and 1200 °C. The atomic percent of all constituent elements, including hydrogen, given by the combined RBS-ERD method is presented in Fig. 5.2. The summary of the concentration of each constituent element, reported in atomic percent at.%, is provided in Table 5.1. The corrected areal densities are also listed in Table 5.1 along with the corresponding estimated accuracy given by the SIMNRA program, which is related to the inherent RBS measurement's uncertainties.

The result of the ERD analysis (Fig. 5.2) provides the concentration of both bonded and unbonded hydrogen, while, as will be discussed in subsection 5.2.5, the

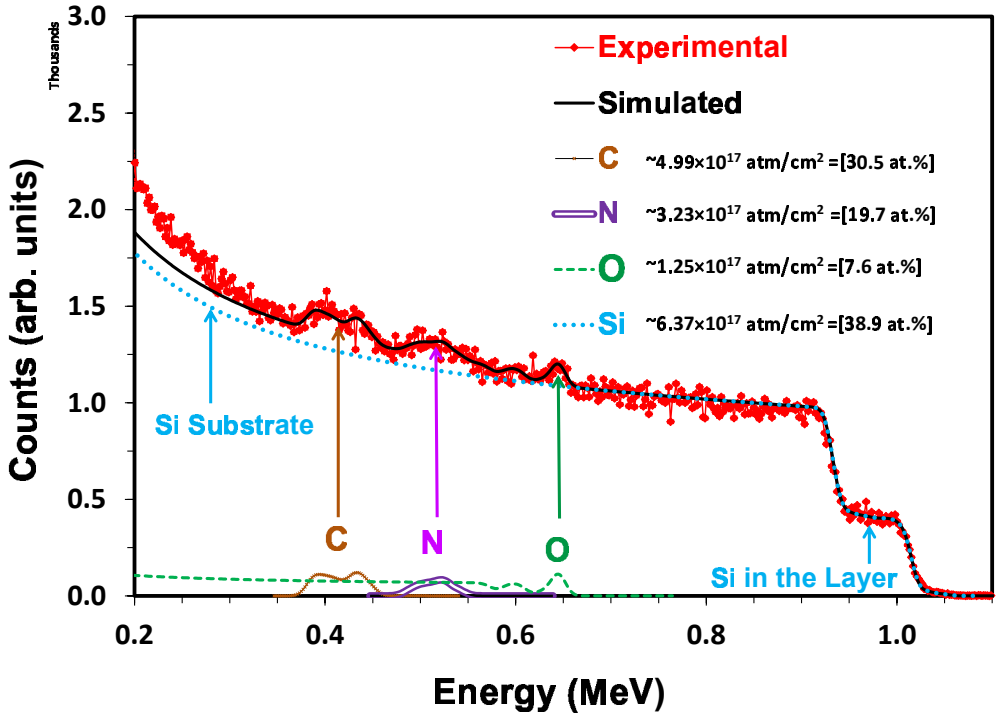

Figure 5.1: **Composition and density of annealed SiCN films.** RBS spectrum of hydrogenated a-$SiC_{1.2}N_{0.7}$:$H_{1.4}$ annealed at 1200 °C. The annealing produced a sample with the composition of $SiC_{0.8}N_{0.5}$:$H_{0.08}$). The experimental data (red dots), fitted data (solid black line), and partial fitted spectra of each element are presented. The carbon and oxygen signals indicate a non-uniform distribution through the layer upon thermal annealing.

IR absorption data only deliver the density of bonded hydrogen. Therefore, only the ERD results are considered only to report the hydrogen density in the layer at various annealing temperatures. Due to the dissociation of CH_4 gas during the growth process, and the applied plasma assisted CVD method, a large concentration of hydrogen (32±2 at.%) appears in the as-deposited a-$SiC_{1.2}N_{0.7}$:$H_{1.4}$) thin film. Upon thermal annealing, taking into account the uncertainties presented in a-$SiC_{1.2}N_{0.7}$:$H_{1.4}$), the hydrogen concentration is virtually unchanged for temperatures below 500 °C ($T_a <$ 500 °C). The hydrogen content rapidly decreases for annealing temperatures up to

T_a=900 °C. After this annealing step, the hydrogen content reaches values close to the ERD detection limit (2 at.%) indicating that virtually all hydrogen is depleted from the film layer.

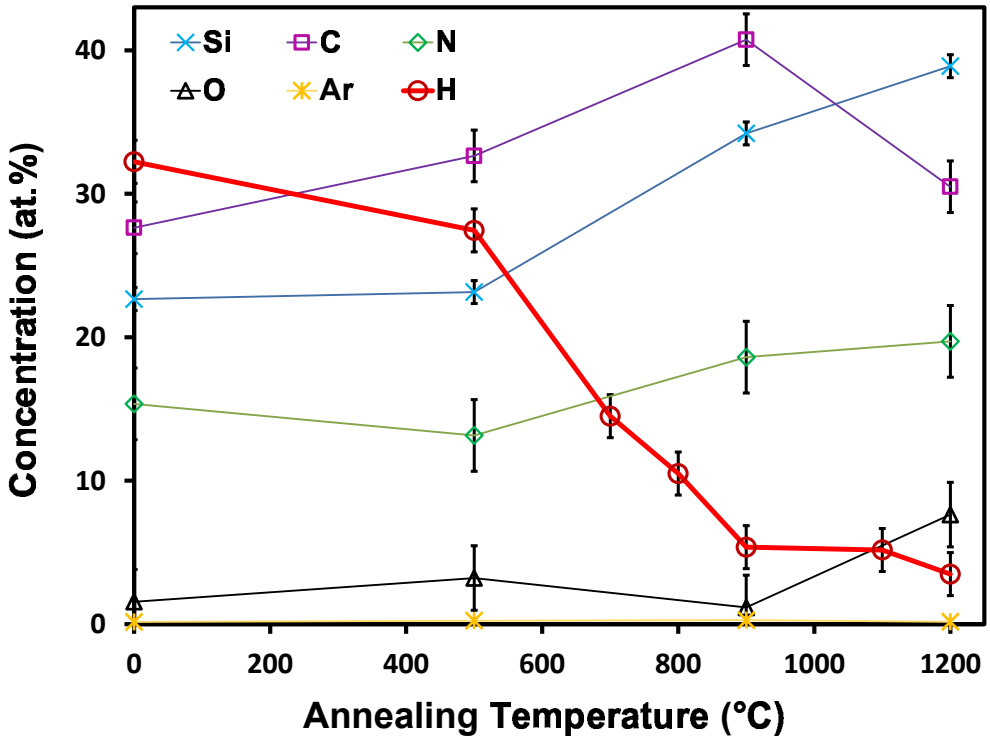

Figure 5.2: **Summary of combined RBS-ERD analysis.** The composition of hydrogenated a-SiC_xN_y films containing (initially) high hydrogen content as a function of annealing temperature. The hydrogen content rapidly decreases after annealing at temperatures above 500 °C.

Fig. 5.2 shows that higher annealing temperatures yield a remarkable increase in the concentration of silicon and a weaker one for that of nitrogen. The carbon concentration first increases up to T_a=900 °C and then decreases with further increase of T_a to 1200 °C. Oxygen contamination is low and nearly remains constant over the thermal annealing range, except at T_a=1200 °C. It is noted that the unit of the elemental concentration is given by the atomic percentages (at.%) showing the

relative contribution of the corresponding elements in the layer; therefore, an increase in the elemental concentration does not mean necessary that there is an increase in the actual amount of carbon, nitrogen, and silicon. In fact, the significant hydrogen loss that occurs during annealing leads to the increase of the atomic percentage of the other elements. Fig. 5.1 confirms the formation of carbon clusters and oxide features at T_a=1200 °C through the non-uniform distribution of carbon and oxygen. The peak widths of the carbon and oxygen signals are not symmetrically distributed through the film depth, while those of silicon and nitrogen are virtually symmetric. The double-peaked carbon signal is an indication of carbon clusters (of graphite-like structure) formed in the inner layers of the film. This is in good agreement with the XPS results of the sample annealed at 1200 °C showing only the C-C feature at the C 1s core level (subsection 5.2.4). The high energy side of the oxygen peak in Fig. 5.1, corresponding to the top layer of the film, represents the surface oxide. The narrow width of the oxygen peak agrees with a thickness of the oxide layer of 32 nm observed in the HRTEM image (Fig. 5.3).

The mass density of the annealed samples is calculated from the combined RBS-ERD and VASE results, as described in 3.3.1. The values of mass density along with the corresponding uncertainties are listed in Table 5.1. The untreated a-$SiC_{1.2}N_{0.7}$:$H_{1.4}$ sample, containing 32 at.% H, shows a density of 2.05 g/cm^3 which increases to 3.05 g/cm^3 in the sample annealed at 1200 °C containing only 3 at.% H (a-$SiC_{0.8}N_{0.5}$:$H_{0.08}$). Moreover, the densities of the as-deposited a-$SiN_{1.3}$:$H_{0.3}$ and a-SiC:$H_{1.3}$ films were analyzed as the reference samples and matched the published values for hydrogenated material grown by PECVD processes [251]. We obtained density values (hydrogen contents) of 2.3 g/cm^3 (9 at.%) and 1.9 g/cm^3 (39 at.%) for a-$SiN_{1.3}$:$H_{0.3}$ and a-SiC:$H_{1.3}$, respectively. It should be noted that the thickness of the layer and the

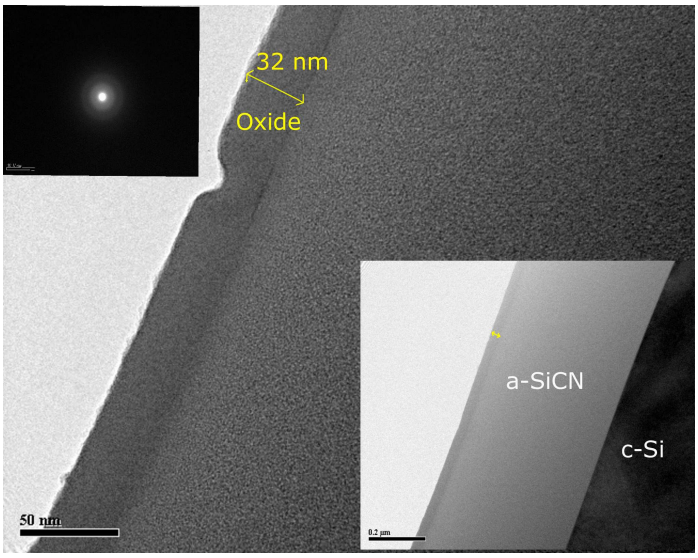

Figure 5.3: **HRTEM of SiCN samples annealed at 1200 °C.**The magnified HRTEM cross sectional image with a corresponding SAED pattern taken from the a-$SiC_{1.2}N_{0.7}$:$H_{1.4}$ annealed at 1200 °C. The line highlighted by the yellow color shows the thickness of the oxide layer formed after annealing at 1200 °C for 1 h. The inset at the bottom is the lower magnification image of the a-$SiC_{1.2}N_{0.7}$:$H_{1.4}$ deposited on the silicon substrate, in which the surface oxide layer is still observed. The inset on the top is the diffraction pattern confirming the amorphous structure of the a-$SiC_{1.2}N_{0.7}$:$H_{1.4}$.

relevant error are determined independently using VASE as will be discussed in 5.2.2. The accuracy of the film density can be evaluated using the sum of the relative accuracies of atomic concentration and the thickness measurements. The details of mass density calculation has been discussed already in subsection 3.3.1 according to the basic rules of uncertainty calculation [252]. The typical relative uncertainty of the mass density of this set of samples is estimated from 2 to 6 %, which gives a maxim of 0.07 g/cm^3 for the absolute uncertainty of film densities.

Table 5.1: The elemental composition and density of annealed a-$SiC_{1.2}N_{0.7}$:$H_{1.4}$ thin films and as-deposited SiC:$H_{1.3}$ and a-$SiN_{1.3}$:$H_{0.3}$ thin films.

Sample	([Si]± 0.8) at.%	([C]± 2.5) at.%	([N]± 1.8) at.%	([H]± 2.0) at.%	([Si] ±0.2) x10^{17} at.%	([C] ±0.5) x10^{17} at.%	([N] ±0.4) x10^{17} at.%	([H] ±0.4) x10^{17} at.%	Film Density (±0.07) g/cm^3
AD-SiCN	22.7	28	15	32	5.2	6.4	3.5	7.5	2.05
SiCN-500°C	23.2	33	13	28	5.2	7.3	3.0	6.2	2.09
SiCN-900°C	34.2	41	19	6	6.1	7.3	3.3	1.0	2.90
SiCN-1200°C	38.9	30	20	3	6.4	4.9	3.2	0.6	3.13
AD-SiN	38.4	0	49	9	5.0	0	6.4	1.2	2.35
AD-SiC	28.3	29.4	0	39	9.1	14.5	0	15	1.93

5.2.2 Optical Properties

The thermally induced changes in the refractive index (n), thickness (d), and optical band gap (E_{04}) of the annealed $SiC_{1.2}N_{0.7}$:$H_{1.4}$ thin films are listed in Table 5.2. The values of these properties refer to a wavelength of 632.8 nm; as-deposited $SiN_{1.3}$:$H_{0.3}$ and SiC:$H_{1.3}$ films are also calculated as a reference. The obtained refractive index values of the investigated stoichiometric a-$SiN_{1.3}$:$H_{0.3}$ and SiC:$H_{1.3}$ films (1.9 and 2.3) are slightly smaller than those of a-Si_4N_3 and SiC synthesized using CVD techniques, reported as 2.0 and 2.6, respectively [239] [240]. This can be expected due to the presence of a large amount of H incorporated during the low temperature PECVD processes. The as-deposited a-$SiC_{1.2}N_{0.7}$:$H_{1.4}$ sample has a refractive index of 2.1 and

a thickness of 263 nm. Annealing was found to shrink the layer by 0.2, 1.3, 1.8, 2.5, 2.5, 8.0, 6.2, and 7.3 %, respectively, in any 100 °C increment from 300 to 1200 °C.

It has been extensively discussed in subsection 2.3.2 that the short-range structural orders present in amorphous materials introduce localized states into the band gap. The Urbach energy and calculation of optical band gap (E_{04}) were explained in subsection 2.3.2. Here, E_{04} of all three classes of material is determined using VASE data and the results of fitting which delivers the values of the extinction coefficient. As the matrix evolves from $SiN_{1.3}$:$H_{0.3}$ to a-$SiC_{1.2}N_{0.7}$:$H_{1.4}$ the band gap narrows from 3.9 to 3.6 eV. Table 5.2 the energy gaps and the corresponding E_u is listed for a-$SiN_{1.3}$:$H_{0.3}$ and SiC:$H_{1.3}$ as well as the as-deposited a-$SiC_{1.2}N_{0.7}$:$H_{1.4}$ sample. It also shows the estimated values of the optical band gaps of annealed a-$SiC_{1.2}N_{0.7}$:$H_{1.4}$ which lie in the range of 0.5 to 3.6 eV. The as-deposited a-$SiC_{1.2}N_{0.7}$:$H_{1.4}$ sample has the maximum E_{04} with a value of 3.6 eV, which is red-shifted to lower energy upon annealing. The first band gap narrowing happens at T_a=500 °C (first annealing stage), and sharper narrowing occurs at 900 °C (second annealing stage). Beyond annealing at this temperature the bandgap is shifted slightly to higher energies, while the mid band gap states (E_u) show the opposite behaviour.

5.2.3 Nanostructure

Fig. 5.3 is the cross-sectional HRTEM image and the corresponding selected-area electron diffraction (SAED) pattern taken from the a-$SiC_{1.2}N_{0.7}$:$H_{1.4}$ sample annealed at 1200 °C for 1 h. As determined from RBS-ERD

The line highlighted by the yellow color shows the thickness of 32 nm for the oxide layer formed on the surface of the film following annealing at 1200 °C. In the inset

Table 5.2: The optical band gap, Urbach energy, thickness, and refractive indices of annealed a-$SiC_{1.2}N_{0.7}$:$H_{1.4}$ thin films and as-deposited SiC:$H_{1.3}$ and a-$SiN_{1.3}$:$H_{0.3}$ thin films.

Temperature (°C)	E_{04}±0.1 (eV)	E_u (eV)	d±0.4 (nm)	n@λ=623.8 (nm)
AD-$SiC_{1.2}N_{0.7}H_{1.4}$	3.6	0.28	263.1	2.08
300	3.5	0.29	262.7	2.08
400	3.5	0.30	259.3	2.08
500	3.5	0.49	254.7	2.08
600	2.7	0.50	248.3	2.08
700	1.5	0.89	242.1	2.10
900	0.5	1.24	222.8	2.22
1100	0.8	0.94	209.0	2.59
1200	1.0	0.71	193.7	2.69
AD-$SiN_{1.3}H_{0.3}$	3.9	0.25	138.7	1.9
AD-$SiCH_{1.3}$	3.0	0.3	363.6	2.3

of Fig. 5.3 is shown the image of the $SiC_{0.8}N_{0.5}$:$H_{0.08}$ single layer on the crystalline silicon substrate, in which the surface oxide layer is still observed using the lower magnification. The HRTEM image identifies a purely amorphous nanostructure of the $SiC_{0.8}N_{0.5}$:$H_{0.08}$ film layer. The SAED pattern also does not reveal any contrast, which clearly confirms that the $SiC_{0.8}N_{0.5}$:$H_{0.08}$ sample does not contain any crystalline regions. The structural analysis of amorphous thin films is challenging and in this work is performed using the two methods discussed in the following subsections.

5.2.4 XPS

In Fig. 5.4 are shown the spectra of O 1s, N 1s, Si 2p, and C 1s core levels revealing the electronic restructuring of a-$SiC_{1.2}N_{0.7}$:$H_{1.4}$ as a result of thermal treatment. In the O 1s spectra of the as-deposited sample and the one annealed at 500 °C, only one weak peak was resolved at 532.6 eV, see top panel of Fig. 5.4. This negligible O 1s peak can be expected due to low oxygen contamination in the film, as previously discussed in connection with the RBS results (see subsection 5.2.1). Fig. 5.4 also shows the formation of a new oxide feature after annealing at 1200 °C in a dry purge N_2 environment. This dominant oxide feature on the surface formed despite one-minute HF etching to remove the surface oxide layer with a thickness of about 30 nm (Fig. 5.3), prior to the XPS measurement. This etching time was chosen by considering the reported typical dilute HF (1:10 of H_2O + HF (49 %)) etch rate of 24 nm/min at room temperature for a thermally grown silicon dioxide [253]. It can be inferred that the HF etching rate of the formed oxide-based layer is much less than the standard etching rate of a thermally grown oxide layer. Thus, it appears that an oxide-based layer with a composition and density different from thermal stoichiometric silicon dioxide is formed on the surface of a-$SiC_{1.2}N_{0.7}$:$H_{1.4}$ during the thermal treatment at T_a=1200 °C. The potential sources of oxygen could be contamination of the N_2 source or/and the reactions of the dangling bonds, created as a consequence of annealing, with atmospheric oxygen.

The N 1s core level spectra in the bottom panel of Fig. 5.4 show the features of the N-Si bond at 397.8 eV (dotted lines) and N=C bond at 398.9 eV (connected symbols) in the as-deposited sample, while the sample annealed at 500 °C can be fitted only to one single peak centered at 397.8 eV, identifying the N-Si bond. No peak at the N 1s

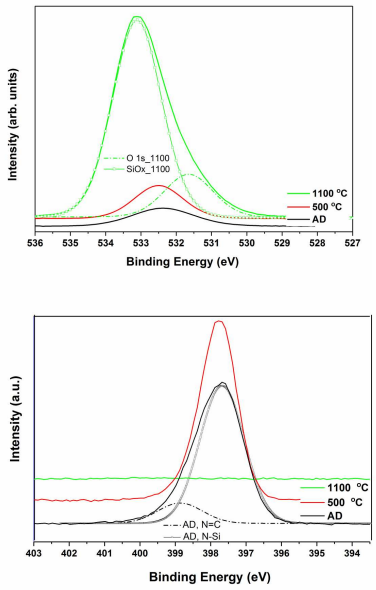

Figure 5.4: **The O 1s and N 1s core levels of annealed SiCN films.** XPS data showing the O 1s and N 1s spectral lines of a-$SiC_{1.2}N_{0.7}$:$H_{1.4}$. Offset was added and the legends were ordered from the bottom to the top; (top panel) the O1s core level signal is weak except after annealing at 1200 °C where two peaks were resolved due to the presence of a surface oxide, (bottom panel) N 1s core level of the AD sample shows the feature of N-Si at 397.8 eV (dotted lines) and N=C at 398.9 eV (connected symbols) while the sample annealed at 500 °C was fitted to only one individual peak centered at 398.8 eV and the sample annealed at 1200 °C showed no signal).

core level is detected in the sample annealed at 1200 °C. The absence of N-Si bonds at 1200 °C agrees with the disappearance of the Si-N feature at the Si 2p core level shown in Fig. 5.5. Figs. 5.5 and 5.6 show the XPS spectra of the Si 2p and C 1s core levels, respectively, where three main peaks are resolved in each spectrum. Prior to thermal annealing, the as-deposited film at room temperature exhibits the Si-C bond at both Si 2p (101.1 eV) and C 1s (283.5 eV), the Si-N bond (101.8 eV), and a small oxide feature of Si-O at Si 2p (103.0 eV), and the C=N bond at the C 1s (286.3 eV) edges. Annealing at 500 °C results in a reduction of the integrated intensity of the Si-N bond at the Si 2p edge with an increase of the Si-C signal at both Si 2p and C

1s core levels, and the disappearance of the C=N peak (286.3 eV) at the C 1s edge. The sample annealed at 1200 °C barely shows any signal of the Si-C and Si-N bonds, which is an indicator of Si-N and Si-C bond breaking, well in agreement with the observation in the IR absorption modes of sample annealed at 1200 °C (see Fig. 5.7). The Si-O peak at the Si 2p edge and the C-C peak at the C 1s edge are the main features resolved after annealing at 1200 °C, due to the formation of the dominant surface oxide and carbon clustering in the inner layer, respectively.

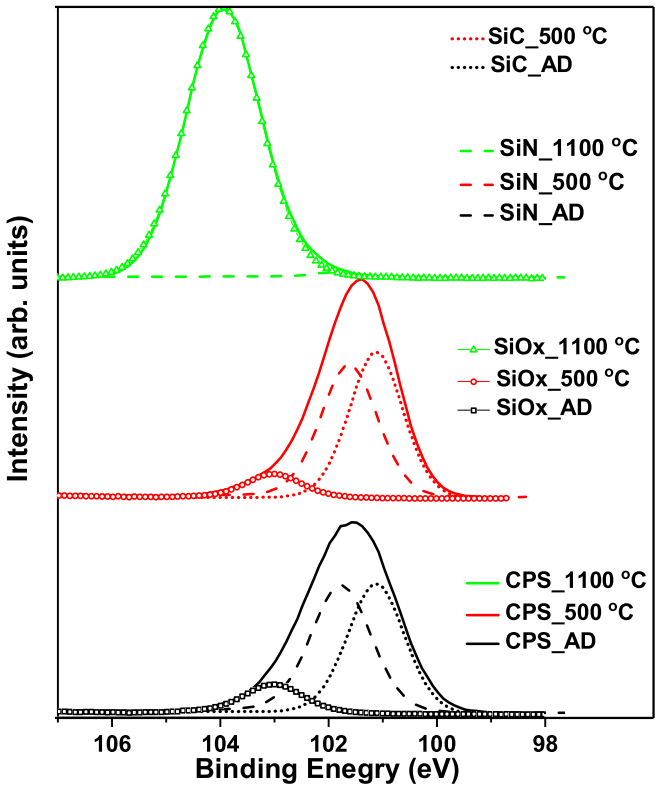

Figure 5.5: **The thermal evolution of the Si 2p core level of annealed SiCN films.** XPS data showing the Si 2p spectral lines (solid lines) and their fits for a-$SiC_{1.2}N_{0.7}$:$H_{1.4}$, AD, and annealed at 500 and 1100 °C. The Si-C bond at 101.1 eV (labelled with a dotted line), Si-N at 101.8 eV (dashed lines), and Si-O at 103 eV (connected symbols) were resolved.

It is noted that no peak was resolved at 287.0 eV (Csp^3 bonded to one nitrogen

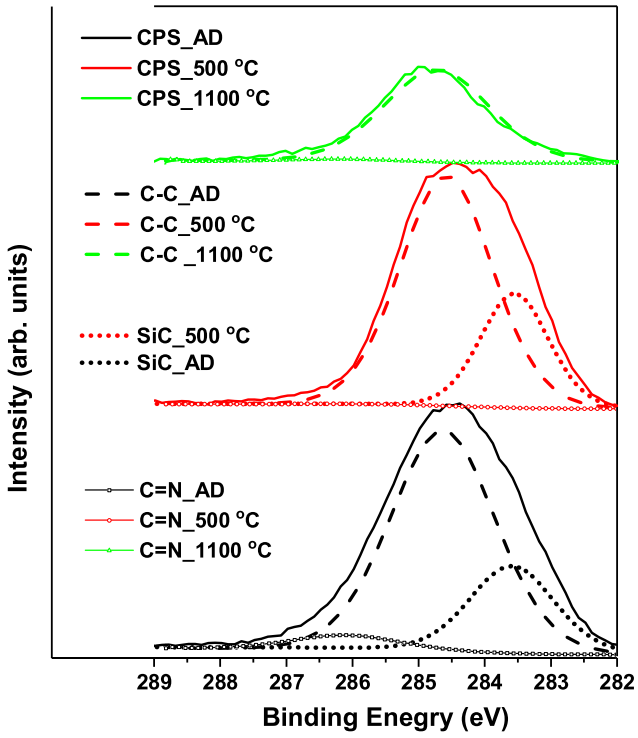

Figure 5.6: **The thermal evolution of the C 1s core level of annealed SiCN films.** XPS data showing the C 1s spectral lines (solid lines) and their fits for a-$SiC_{1.2}N_{0.7}$:$H_{1.4}$, AD, and annealed at 500 and 1100 °C. The C-Si bond at 283.5 eV (dotted line), C-C at 284.7 eV (dashed lines) and C=N at 286.3 eV (connected symbols) were resolved. Upon annealing at 500 °C, the intensity of the Si-C bond increases and the N=C bond disappears, and then, with further annealing to 1100 °C, Si-N and Si-C peaks disappear and only the C-C bond is dominant along with a surface oxide feature.

neighbour) or at 288.0 eV (Csp^3 bonded to two nitrogen neighbours) [254]. The observed peak at 286.3 eV can be attributed to C=N (C(sp)-N) bonds due to no contribution of N-sp^2C bonds in the N 1s spectra and the presence of the C=N stretching mode at 2100 $\sim$ 2200 cm^{-1} in FTIR absorption spectra (Figs. 5.7 and 5.8). Moreover, the assignment of the peak at 284.7 eV in SiC_xN_y materials depends on the relative concentration of nitrogen to carbon. At low concentrations of nitrogen, it has been assigned to the C-C peak for sp^3 bonded carbon in a diamond-like matrix; at

higher nitrogen concentrations, it has been ascribed to the C-C peak for sp^2 bonded carbon in a graphite phase in SiC_xN_y matrix [216] [255]. However, in our earlier study of the influence of carbon on these peaks in a-SiC_xN_y:H_z thin films [220], the assignment of the peak at 284.7 eV to C-C/C-H bonds rather than C-N bonds was confirmed (for details see subsection 3.5.1), showing that at least a major contribution to this peak can be assigned to the C-C bond. The identification of the feature positioned at 286.3 eV is also not straightforward, since it can be assigned to both C=N and C-O bonds. In the investigated samples, the peak at 286.3 eV is attributed to the C=N bond rather than C-O bond due to the negligible oxygen contamination in the samples. This peak appears in the as-deposited sample even though it does not contain any oxygen, decreases in the sample annealed at 500 °C, and has disappeared after annealing at 1200 °C. All samples were HF etched before XPS measurements, hence, the presence of the strongest feature at 286.3 eV in the as-deposited sample is not associated with the surface oxide contamination. The association of this feature with C=N bond is also supported by the observed trend of the C=N feature at 398.9 eV in the N 1s edge and a feature at about 2200 cm^{-1} in FTIR absorption upon annealing [216]. Also, as will be demonstrated in the next subsection, IR absorption shows no significant oxide feature for the as-deposited sample and the one annealed at 500 °C.

The information from all core level spectra can be summarized as a decrease of the concentrations of Si-N, C-C, and C=N bonds and an increase of the density of Si-C bonds from as-deposited to 500 °C. With increased annealing temperature, eventually only the Si-O and C-C features could be observed at T_a=1200 °C. The intensity of C-N or C=N bonds was below the detection limit of XPS measurements. We thus consider the C-N and C=N bonds using IR absorption data as will be further

discussed in the following subsection.

5.2.5 Infrared Absorption

The presence of hydrogen in the structure of a-$SiC_{1.2}N_{0.7}$:$H_{1.4}$, introduced by the PECVD process, complicates the bond assignment of IR absorption modes compared to non-hydrogenated SiC_xN_y films grown using alternative techniques such as sputtering [128]. Peter et al. [160] reported discrepancies of about 150 cm^{-1} in the peak positions of Si-C and Si-N absorption modes. Hydrogen bonding also alters the approximate positions of the absorption bands; red-shifting the stretching modes and blue-shifting the bending modes [256]. In Fig. 5.7 the mid-infrared absorption spectra of the as-deposited and several annealed a-$SiC_{1.2}N_{0.7}$:$H_{1.4}$ samples are presented, baseline-subtracted and normalized to the film thickness. Figs. 5.8 and 5.9 present the densities of the chemical bonds calculated using the proportionality constant κ, discussed in subsection 3.5.3. The absorption modes of IR spectra plotted in Fig. 5.7 are discussed in five spectral sub-regions, starting from the lower wavenumber, as below:

(i) The first region in Fig. 5.7, from 400 to 600 cm^{-1}, does not overlap with the main strong absorption band. Fig. 5.8 shows that the density of Si-N bonds (460 cm^{-1}) remains virtually unchanged over a wide range of annealing temperatures; however, it completely disappears after annealing in excess of 900 °C (second stage of annealing) when the Si-O-Si stretching mode (420 cm^{-1}) starts to grow. As expected from the low oxygen contamination in the film, the signal of Si-O at 420 cm^{-1} is weak at annealing temperatures below 1000 °C.

(ii) The strong double-peak in the range of 600-1300 cm^{-1} is a superposition of

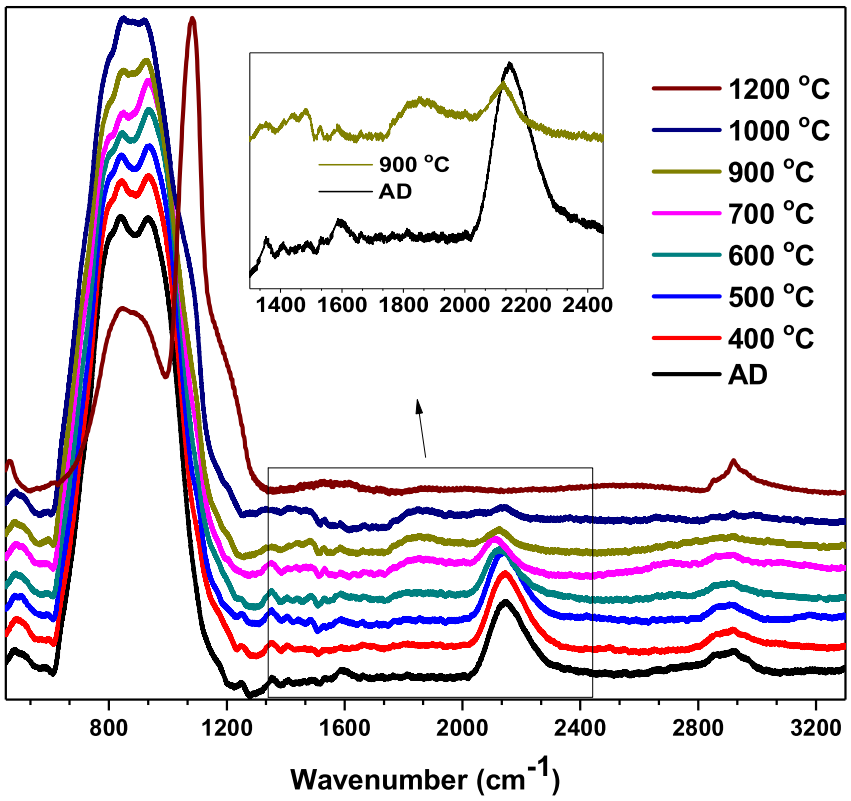

Figure 5.7: **The thermal evolution of FTIR absorption spectra of SiCN films.** Fourier transform infrared (FTIR) absorption spectra of a-$SiC_{1.2}N_{0.7}$:$H_{1.4}$ as a function of thermal annealing. In the inset, the third region of IR absorption band of two different samples is magnified.

690, 770, 835, 940, 1060, 1190, and 1240 cm^{-1} peaks (the symmetric and the asymmetric stretching modes of Si-H, Si-N, Si-C/Si-O, Si-N, C-N/Si-CH/Si-O, Si-O, and Si-CH_n, respectively). The broadness of this strong band, representing a less defined molecular structure in the film [257], remains unchanged upon annealing. In contrast, the relative intensity of the peaks changes (the one located at higher energies first increases and then decreases). This can be explained by the deconvolution of this region allowing one to understand the

changes of each absorption mode during annealing. The spectrum from 600 to about 1200 nm can be decomposed to five bands (690, 770, 835, 940, and 1060 cm^{-1}). The changes of the absorption mode at 835 cm^{-1} are responsible for the observed thermally induced changes of the relative peak intensities. This peak is an overlap of the absorption modes of Si-O and Si-C, making it difficult to assign the observed changes in detail. The vibrational modes of Si-C at 1240 cm^{-1} and Si-O at 1190 cm^{-1}, having no overlap with any other bands in IR absorption spectrum, can help to further explore the changes of the peak at 835 cm^{-1}. Its initial increase after annealing at 500 °C and subsequent decrease after annealing at 900 °C is correlated with the Si-C bond, since the respective vibrational mode at 1240 cm^{-1} (Si-CH_n) increases up to T_a=500 °C, then gradually decreases, and eventually disappears at T_a=900 °C (second stage of annealing). In subsection 5.2.4, a similar behavior was observed at the C 1s and Si 2p core levels showing the increase of the concentration of Si-C bonds at T_a= 500 °C and its vanishing at higher temperatures. Therefore, the reason for the re-increase of the 835 cm^{-1} peak after annealing at 900 °C can be explained by the initiation of Si-O bonds. This is supported by changes of the counterpart Si-O bond at 1190 cm^{-1} starting to develop at about T_a=1000 °C. The Si-O bond at 1060 cm^{-1} was also present as a separate peak; however, we did not consider this band as a separate Si-O bond due to the presence of Si-CH_x bending modes around 1030 cm^{-1}. In addition, this peak can be assigned to C-N wagging modes. However, this is one of the strong and individual bonds observed in IR spectra of $SiCH_{1.3}$, which allows us to assign the peak around 1030 cm^{-1} to the Si-CH_x bond rather than the C-N bond. The contributions of all absorption modes of Si-CH_x and Si-O around 1060 cm^{-1} can explain why the peak labeled as 1060 cm^{-1} in Fig. 5.8

is detectable at lower annealing temperatures, despite the absence of significant oxide bonds. Therefore, in the density calculation of Si-O and Si-CH_x bonds in $SiC_{1.2}N_{0.7}$:$H_{1.4}$ films, Fig. 5.8, this peak can be ignored. Two additional lines were resolved in the decomposition of this strong region of interest the Si-N bonds at 940 and 770 cm^{-1}. They show virtually no change after annealing up to about 1000 °C and disappear after annealing at 1200 °C (similar thermal behavior was observed for the Si-N bond at 470 cm^{-1} in region (i)).

(iii) The third spectral region is considered to lie between 1300 and 2000 cm^{-1} and contains features at 1350, 1480, 1590, and 1850 cm^{-1} related to carbon bonded to other carbon or nitrogen atoms. These features are weak, however, the integrated intensity of them is still measurable. The IR spectra of two samples are shown in the inset of Fig. 5.7 and these features are labeled. The first peak in this region at 1350 cm^{-1} is assigned to C-N/C=N bonds, and remains nearly constant from AD to 700 °C. As the annealing proceeds to 900 °C, it starts to decrease rapidly, and after annealing at 1200 °C, it is no longer detectable. The peaks at 1450 and 1480 cm^{-1} are related to the C=C/C=N vibration modes. They show a continuous increase by the increases of annealing temperature up to 700 °C and a decrease upon annealing to 900 °C, beyond 1000 °C disappear. This behavior is similar to what is observed for the IR band at 1850 cm^{-1} and is discussed in the following. The next feature at 1590 cm^{-1}, generally associated with both C=C and N-H bonds, first decreases gradually from as-deposited up to T_a=900 °C and then increases sharply from 1000 to 1200 °C. The decrease is related to the breaking of N-H bonds (not C=C bonds), as will be discussed in (iv), the respective N-H bond, positioned at higher energies

(3300 cm^{-1}) disappears below T_a=900 °C. The increase of this peak at annealing temperatures beyond 900 °C is assigned to the increase of the concentration of C=C bonds (observed at the C 1s edge of the XPS data). At higher energies, there are multiple peaks due to the carbon and nitrogen bonds centered at 1850 cm^{-1} and broadened between 1750 and 1950 cm^{-1} (such as 1769, 1812, 1894, 1920, and 1960 cm^{-1}). All of these vibrational bonds are labelled as "1850" in Fig. 5.8, which increases noticeably from as-deposited to 700 °C, then slightly decreases from 700 to 900 °C, and sharply increases in excess of 900 °C. The increase between the as-deposited sample and the one annealed at 700 °C can be assigned to the increase of C-N/C=N bonds and the slight decrease beyond 700 °C is possibly related to the breaking of C-N and C=N bonds (as observed at 1350 cm^{-1}). The sharp increase can be attributed to the C=C/C-C bonds (graphite phase formation) in agreement with the discussed enhancement of C=C/C-C bonds at 1590 cm^{-1} and C-C bonds observed at the C 1s core level. The last feature at this region is the N-H bond (around 1600 cm^{-1}), which cannot be obtained separately and taken into account for the N-H bond density calculation due to the poor separation of C-N and N-H absorption peaks [235]. In most cases, the overlap of the CN and C=N absorption modes made it difficult to distinguish them [235].

(iv) The next spectral region lies between 2000 and 2500 cm^{-1} with the predominant peak around 2135 cm^{-1}. The assignment of this peak in a-$SiC_{1.2}N_{0.7}$:$H_{1.4}$ was made difficult due to the overlaps of stretching modes of Si-H_n and C=N. As the annealing temperature increases, this peak appears to weaken and it also slightly shifts to lower wavenumbers and then remains virtually constant to T_a=1000

°C. In the previous chapter studying different compositions of a-$SiC_xN_yH_z$ films, the presence of the C=N bond at 2135 cm^{-1} was confirmed by a red-shift of 94 cm^{-1} with a slight decrease in the intensity of this band following the increase of the carbon content in the film from 0 to about 30 at.%. In effect, therefore, the increase of the intensity of this peak accompanied with a red-shift at the higher annealing temperatures is related to the formation of C=N bonds, while the reduction of the intensity of this peak below 700 °C was caused by the breaking of Si-H bonds. This agrees with the observed reduction of the stretching mode of Si-H at the 640 cm^{-1} band, discussed in (i).

(v) From the features in the region beyond 2500 cm^{-1}, it can be inferred that hydrogen is bonded to carbon and nitrogen, in addition to silicon. This region is characterized by several other bonds due to hydrogen in different atomic configurations; including the stretching modes of C-H from 2500 to 3000 cm^{-1} and NH bonds from 3000 to 3400 cm^{-1}. The peak observed at 2900 cm^{-1} (an overlap of C-H and C-N bonds) is weakened upon annealing, as expected from H desorption, but persists to T_a=1000 °C. This is the stretching mode of C-N/C=N, obscured by the stronger signal of C-H, which becomes detectable following the breaking of C-H bonds at the elevated temperatures. The intensity of the other two weak peaks at about 3050 and 3150 cm^{-1}, related to N-H bonds, first increases slightly upon annealing up to 500 °C and then gradually decreases, disappearing after annealing at 900 °C. Such behavior has been reported similarly for the N-H bonds in SiON, SiO, and SiON samples [258]. The sample annealed at 1200 °C shows no hydrogen bonds and only new features at 3700 and 3500 cm^{-1}, corresponding to SiO-H, which appears due to

the oxygen contamination and formation of a surface oxide layer after annealing at T_a=1200 °C, as indicated in the TEM image (Fig. 5.3). The low oxygen content allows us to ignore the density of O-H bonds in the calculation of the hydrogen bond density. The effect of the overlaps of O-H observed at the higher annealing temperatures and N-H absorption modes at about 3400 cm^{-1} makes it impossible to follow in detail the evolution of the 3400 cm^{-1} peak during the annealing process. Therefore, in the calculation of N-H bond densities, only a peak centered at 3370 cm^{-1} is taken into account.

5.3 Discussion of Thermal Evolution

On the basis of the results described above, we identified T_a=500 °C and T_a=900 °C as two key annealing temperatures, where significant changes to the film properties occurred, as presented in Fig. 5.10. We consider these temperatures as the first and second annealing stages, respectively. Fig. 5.10 shows that hydrogen starts to effuse from the film above 500 °C (first stage of annealing) and is entirely depleted at T_a=900 °C (second stage of annealing). The optical band gap is stable up to the first stage and gradually narrows to the second stage, where band gap widening is observed. The refractive index remains virtually constant all the way up to the second stage and it increases subsequently. Thermal annealing leads to layer densification, and the largest shrinking of the film thickness occurs at the second stage. In addition, the electronic configuration of the film showed significant changes in both stages of annealing.

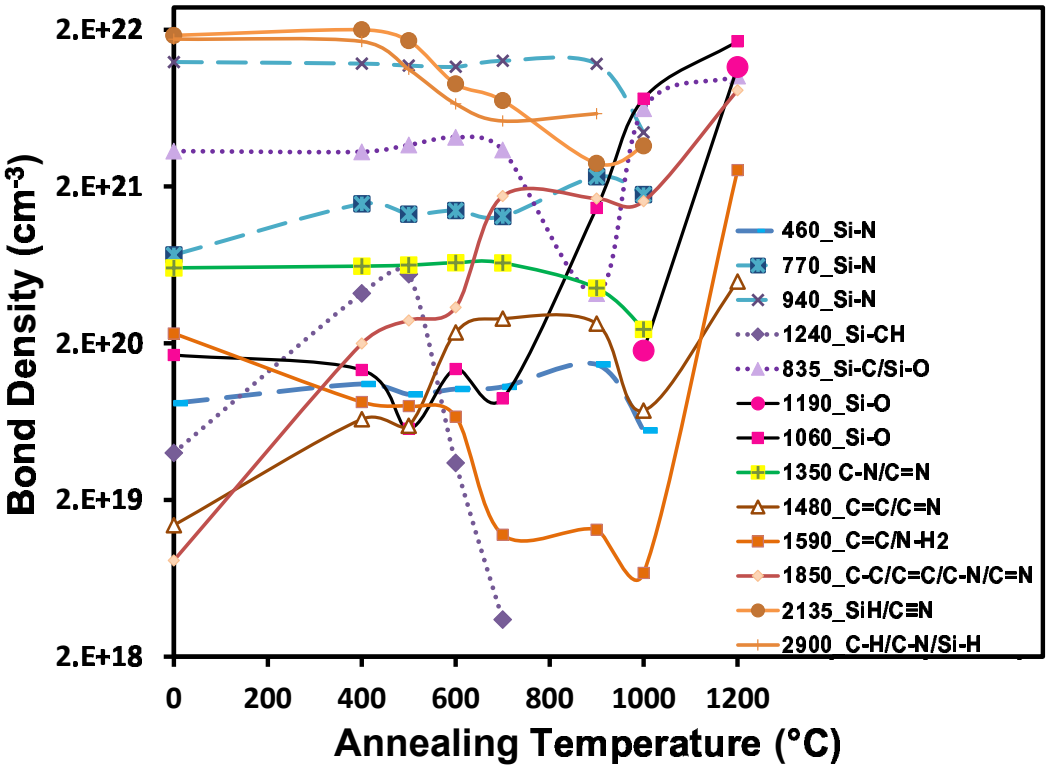

Figure 5.8: **The thermal evolution of all non-hydrogen bond densities.**The densities of all non-hydrogen containing chemical bonds in a-$SiC_{1.2}N_{0.7}$:$H_{1.4}$, plotted as a function of the annealing temperature.

5.3.1 Microstructure

The combination of XPS and FTIR absorption shows the significant changes of the electronic configurations at the two stages of the annealing process. The density of the H-terminated bonds (Si-H, N-H, and possibly C-H) and Si-C bond increases in the first annealing stage, decreases with further annealing to 700 °C, and then disappears completely at the second stage. In contrast, the Si-N bond is virtually unchanged before the second stage (XPS shows a negligible decrease) and then fades

out at 1000 °C. The carbon-nitrogen triple bond (C=N, sp hybridization) decreases at the first stage and become undetectable in XPS spectra, while a weak signal is still measurable in IR absorption spectra up to the second annealing stage. This feature shows a sharper decrease at the second annealing stage and vanishes at 1200 °C. The carbon-nitrogen single bond (C-N, sp^3 hybridization) and carbon-nitrogen double bond (C=N, sp^2 hybridization) show a different behaviour, which can be expected from their higher bond strength compared to C=N bonds. The C-N and C=N bonds are virtually constant up to the second stage of annealing, persist up to T_a=1000 °C, and are not detectable after annealing at T_a=1200 °C. This can be expected from the stable phases of carbonitrides (N=C-C=N and N-C) which break down to CN radicals following any heat exposure above 1000 °C [172]. The weakening of the intensity of C-N/C=N bonds after the second annealing stage is associated with the formation of C-C/C=C bonds. They sharply increase from 1000 to 1200 °C, where only graphite and silicon oxide phases are observed, in accordance with the HRTEM and RBS results. TEM imaging (Fig. 5.3) delivered an oxide feature with a thickness of 32 nm, while carbon clustering was inferred from XPS and FTIR structural analyses as well as the non-uniform distribution of carbon in RBS spectra (Fig. 5.1).

5.3.2 Hydrogen Diffusion

To explore more closely the link between the chemical bonds and overall hydrogen content, the densities of all hydrogen bonds are shown separately in Fig. 5.9. The stability of Si-H, N-H, and C-H bonds up to the first stage of annealing can explain the nearly constant hydrogen content given by the ERD analysis subsection 5.2.1. In addition, the concentration of N-H bonds increases at T_a=400 °C, which lets us infer

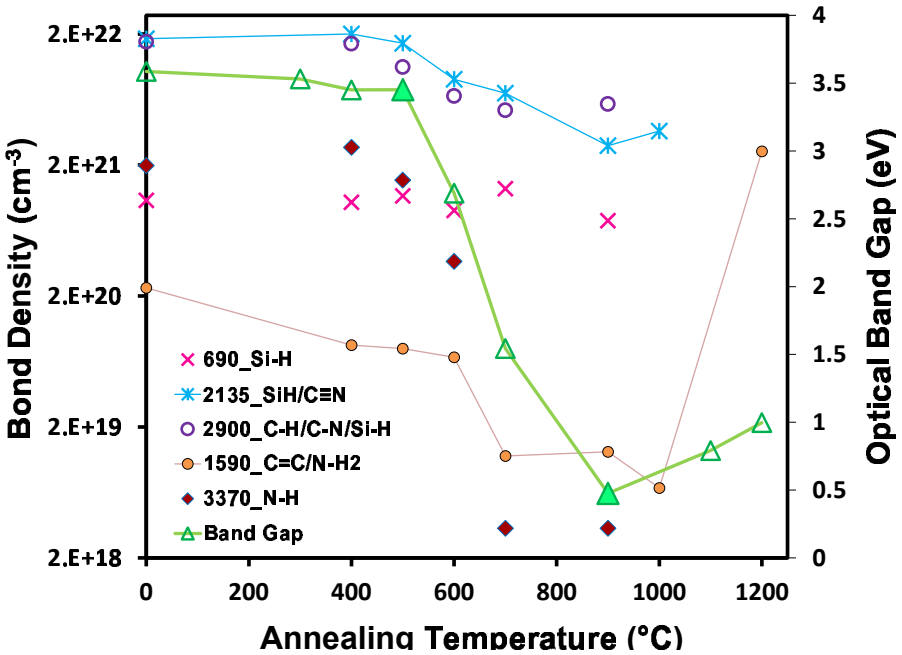

Figure 5.9: **Correlation of the hydrogen bond density and optical band gap at different annealing temperatures.** The density of hydrogen bonds (Si-H, N-H, and C-H) in a-$SiC_{1.2}N_{0.7}$:$H_{1.4}$ and the optical band gap as a function of thermal annealing. The two main stages of the annealing are highlighted by the filled mark in the optical band gap plot (500 and 900 °C). The IR absorption modes which are an overlap of H-terminated and non-H bonds are shown using the line and symbols. The H-terminated bonds are shown by symbols. These bonds start to decrease after the first annealing stage and disappear at the second annealing stage.

that the energy provided via this annealing temperature increases the attachment of un-bonded hydrogen to dangling bonds of nitrogen and possibly silicon. This also agrees with the slight decrease of the Si-N bond density, as demonstrated by XPS data in Figs. 5.4 and 5.5. As the temperature further increases to 500 °C, a slight hydrogen loss is observed coinciding with the formation of more Si-C bonds (Fig. 5.8). The dehydrogenation of Si-H and C-H bonds leads to an increased coordination of silicon with carbon atoms in accordance with the observation made by XPS and

FTIR analyses. The resultant dissociated hydrogen at T_a=500 °C remains in the film due to the smaller diffusion coefficient of hydrogen at lower temperatures. It is noted that the diffusion model explaining the activation energy and transport of hydrogen in a-SiC_xN_y thin films is not well explored. However, a similar submatrix, CVD grown Si_3N_4, was used to estimate the diffusion coefficient showing exponential dependence on inverse temperature. As an example, the diffusion coefficient of hydrogen in a-$SiN_{1.3}$:$H_{0.3}$ films changes from 10^{-17} (corresponding to only 4 nm diffusion length [99]) to 5x10^{-14} between 700 to 1000 °C [259]. Also, the increase in T_a makes the film layer thinner and provides the required energy to break Si-H, N-H, and C-H bonds. This can explain the observed significant hydrogen effusion with the further increase of T_a to 700 °C, wherein the hydrogen content is reduced to less than half of its initial value (12.2 at.%). As the annealing proceeds to the second stage, i.e. T_a=900 °C, the hydrogen content in the film further decreased to about 6 at.%, in agreement with the reported temperature required for effective loss of hydrogen in Si_3N_4 films [260]. As indicated in Fig. 5.10, the most pronounced shrinking of the $SiC_{1.2}N_{0.7}$:$H_{1.4}$ layer was also observed at this annealing stage. The combination of the increased hydrogen escape and the decrease of the film thickness leads to the densification of the a-$SiC_{1.2}N_{0.7}$:$H_{1.4}$ film from 2.09 g/cm^3 (untreated) to 2.90 g/cm^3 upon annealing from 500 to 900 °C (Table 5.2). Above this stage, the hydrogen concentration decreases to 3 at.% at 1200 °C, which is close to the detection limit of the ERD technique. The density of the film increases to 3.05 g/cm^3 which is not affected by hydrogen content and can be explained by the changes of the electronic structure of the film due to the formation of the Si-O and C-C bonds, i.e., the formation of graphite and oxide phases discussed in subsection 5.2.1.

5.3.3 Refractive Index

Variations of the hydrogen content and the electronic configuration of the film allows for the tuning of the refractive index of the film. We observe a strong inverse (direct) relationship between the hydrogen content (film density) and refractive index, as shown in Fig. 5.10. The refractive index of the annealed films remains constant at around 2.1 up to the first annealing stage, and it slightly changes (by 0.2) from the first to the second stage of annealing. After this stage, where the main depletion of hydrogen from the films occurs (T_a= 900 °C), the refractive index increases rapidly and reaches 2.7 at 1200 °C. As explained by the Lorentz-Lorenz equation, its value depends on both the variation of the atomic configuration and the density of the films, being correlated parameters [243]. The loss of hydrogen and the subsequent increase of the film density is responsible for the small increase of refractive index below the second annealing stage [261]. The observed high index region after this stage is due to the evolution of the film morphology, accompanied by the increase of graphite-like phases at the expense of carbon bonded to nitrogen atoms. This has a more profound influence on the refractive index of the films compared to the film densification (due to hydrogen loss) and the electronic restructuring during the annealing process at the lower temperatures.

5.3.4 Optical Band Gap

Fig. 5.9 shows the correlation of the optical band gap (E_{04}) with the thermally induced changes of the hydrogen bonds confirming that the variations of the hydrogen content and film restructuring both lead to the evolution of the optical band gap at two stages of annealing. After the first stage, the E_{04} gap narrows by about 2 eV, while after

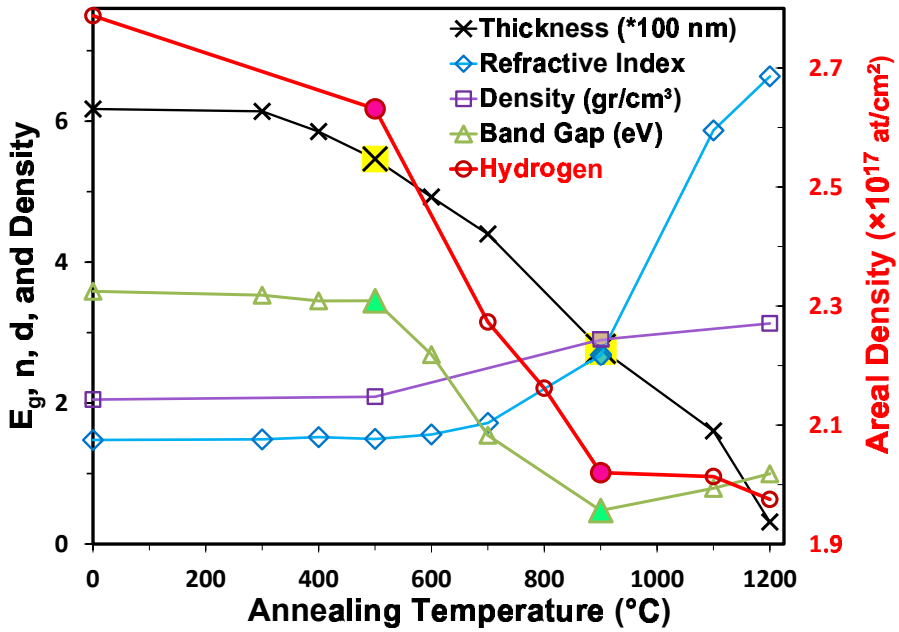

Figure 5.10: **The refractive index, optical band gap, mass density, and thickness of annealed SiCN films.** The refractive index, optical band gap, mass density, and thickness of a-$SiC_{1.2}N_{0.7}$:$H_{1.4}$ film containing (initially) high hydrogen content as a function of annealing temperature. Also shown is the hydrogen areal density. The two annealing stages (500 and 900 °C) are highlighted by the filled symbols. The left-hand vertical axis illustrates the values of the refractive index, optical band gap, mass density, and thickness of the film, while the right-hand axis provides absolute values of the hydrogen areal density.

the second stage, a slight widening is observed from 0.5 to 1 eV at 1200 °C. The E_{04} gap for the as-deposited a-$SiC_{1.2}N_{0.7}$:$H_{1.4}$ sample has the maximum value of 3.6 eV, which exhibits negligible narrowing up to the first annealing stage and then a more pronounced narrowing after this stage. The combination of hydrogen loss along with the breaking of the chemical bonds is responsible for this sharp band gap narrowing from the first to the second stage of annealing and affects the E_{04} gap in two ways: First, dangling bonds are created as a result of the breaking of H-terminated (Si-H,

N-H, and C-H) bonds in the annealing process. It is well known that the passivation of the dangling bonds and defects increases the E_{04} gap so that the hydrogen loss from the film consequently increases the localized mid band gap states (E_u) in the band structure, leading to the decrease of E_{04} (Table 5.2). A similar trend was observed by an other research group [261]. Second, the rearrangement of the film atomic structure induced by non-H bonds reduces the E_{04} gap. Among all these bonds, the Si-C bond appears to have the greatest influence on the band gap narrowing because its density rapidly decreases at T_a=700 °C, the E_{04} gap red-shifts by about 1 eV at T_a=900 °C, where the Si-C bonds completely disappear, yet Si-N bonds persist to T_a=1000 °C. After the second stage of annealing, the hydrogen has no profound influence on the thermally induced changes of E_{04}, which increases from 0.5 eV at 900 °C to 1.0 eV at 1200 °C. The Si-N and Si-C bonds are not detectable in this range of temperatures and the breaking of these bonds have already influenced E_{04} at lower annealing temperatures. Such band gap widening can be explained by the formation of C-C and Si-O bonds, the only two noticeable bonds at T_a=1200 °C. The partial graphitization occurs through the gradual substitution of Si-N, C=N, C=N and, C-N bonds by C=C or C-C strong bonds.

Chapter 6

Origin of the Light Emission from Silicon Carbonitride

[1] The work demonstrated in this chapter is a continuation of chapter 5 to discuss the probable luminescence mechanisms of $SiC_xN_y:H_z$ thin films. To better understand this ternary and complex system, the reported data of the two fairly well studied binary structures are used as a reference. Therefore, the effects of thermal annealing on the visible luminescence of three classes of materials were explored; $SiC:H_{1.3}$, and $SiN_{1.3}:H_{0.3}$, and a-$SiC_{1.2}N_{0.7}:H_{1.4}$. The choice of a-$SiC_{1.2}N_{0.7}:H_{1.4}$ is discussed in

[1]The results present in this chapter are published on-line in one peer reviewed journal as well as one conference proceeding and have been submitted to a peer reviewed journal as follows:

- **Z. Khatami**, P. R. J. Wilson, J. Wojcik, P. Mascher (2017) On the origin of white light emission from nanostructured silicon carbonitride thin films, *J. Lumin*, In Press. https://doi.org/10.1016/j.jlumin.2017.12.011
- **Z. Khatami**, G. B. F. Bosco, J. Wojcik, L. R. Tessler, P. Mascher (2017) Influence of deposition conditions on the characteristics of luminescent silicon carbonitride thin films, *ECS J. Solid State Sci. Technol.*, The response to reviews has been submitted.
- **Z. Khatami**, P. R. J. Wilson, J. Wojcik, P. Mascher (2013) XANES and XES studies of luminescent silicon carbonitride thin film, *ECS Trans.*, 50(41): 4956. http://ecst.ecsdl.org/cgi/doi/10.1149/05041.0049ecst

chapter 4 where the film composition was tuned with respect to the optical properties of SiC_xN_y thin films. The results of this chapter have been published in one peer reviewed journal [262] and one conference proceeding [263].

6.1 PL as a Function of Annealing Temperature

6.1.1 PL Deconvolution

The room-temperature PL spectra of the samples were measured between 350 and 1000 nm using a 325 nm He-Cd laser (E_{exc}= 3.82 eV) with an optical power of 5 mW exciting an area of 2.3 mm^2. The room-temperature PL profiles broadly extend over the visible range. A closer assessment of the visible luminescence can be achieved by reproducing PL spectra using energy conversion and Gaussian curve fitting. The PL of samples are resolved through Gaussian fitting into four PL subbands. To minimize errors in the decomposition, especially in a broad emission band, the overlapping features of luminescence data require the conversion to energy and consequently, the transposition of the intensity by a factor of λ^2/hc [207]. The recorded room-temperature PL data as a function of wavelength were first converted to energy, smoothed using a Savitzy-Golay function, and then fitted to Gaussian curves using Origin 9.4.1.

Existing literature on the PL mechanism of SiC_xN_y films reported on films containing oxygen, i.e., $SiO_xC_yN_z$ structures [264] [136], wherein oxygen related bonds are suggested as the sources of the luminescence. The understanding of the origin of PL of SiC_xN_y structures is lacking [27] [141]. In this chapter, the origin of the luminescence in a-$SiC_{1.2}N_{0.7}$:$H_{1.4}$ is investigated using the correlation with the sources of

the luminescence observed in submatrices of SiC:$H_{1.3}$ and $SiN_{1.3}$:$H_{0.3}$ thin films. The thermally induced changes of the PL of hydrogenated amorphous N-SiC_xN_y, C-free SiC_xN_y, and $SiC_{1.2}N_{0.7}$:$H_{1.4}$ samples is explored.

Choice of Samples

In chapter 4, it was observed that SiCN samples exhibited a broad luminescence band, covering the visible range with two dominant peaks at ∼470 and 550 nm, which appeared "white" to the naked eye. Further more, our findings in chapter 4 showed that the intensity of the PL emission of a-$SiC_{1.2}N_{0.7}$:$H_{1.4}$ was higher than that of the binary matrices. $SiC_{1.2}N_{0.7}$:$H_{1.4}$ is also the sample emitting the most intense PL among all investigated SiC_xN_y:H_z samples.

The as-deposited samples subsequently were annealed between 400 and 1200 °C for 1h in a nitrogen atmosphere in a quartz tube furnace. The structural and compositional properties as well as hydrogen diffusion were explored (chapter 5). Some of the results are summarized for the three samples presented in this chapter. The as-grown a-$SiC_{1.2}N_{0.7}$:$H_{1.4}$, SiC:$H_{1.3}$, and $SiN_{1.3}$:$H_{0.3}$ thin films were 263, 364, and 139 nm thick with optical band gaps of 3.6, 3.9, and 3.0 eV, respectively, and contained 32, 40, and 9 at.% H (Table 6.1). In Fig. 6.1, the Si 2p core levels of annealed a-$SiC_{1.2}N_{0.7}$:$H_{1.4}$ films with the corresponding chemical bonds are shown. Fig. 6.2 shows the mid-infrared absorption spectra of the as-deposited and several annealed $SiC_{1.2}N_{0.7}$:$H_{1.4}$ samples, along with a-$SiN_{1.3}H_{0.3}$ and a-SiC:$H_{1.3}$ references, baseline-subtracted and normalized to the film thickness. Later in the chapter the results of XPS and FTIR will be used after analyzing the thermal evolution of PL.

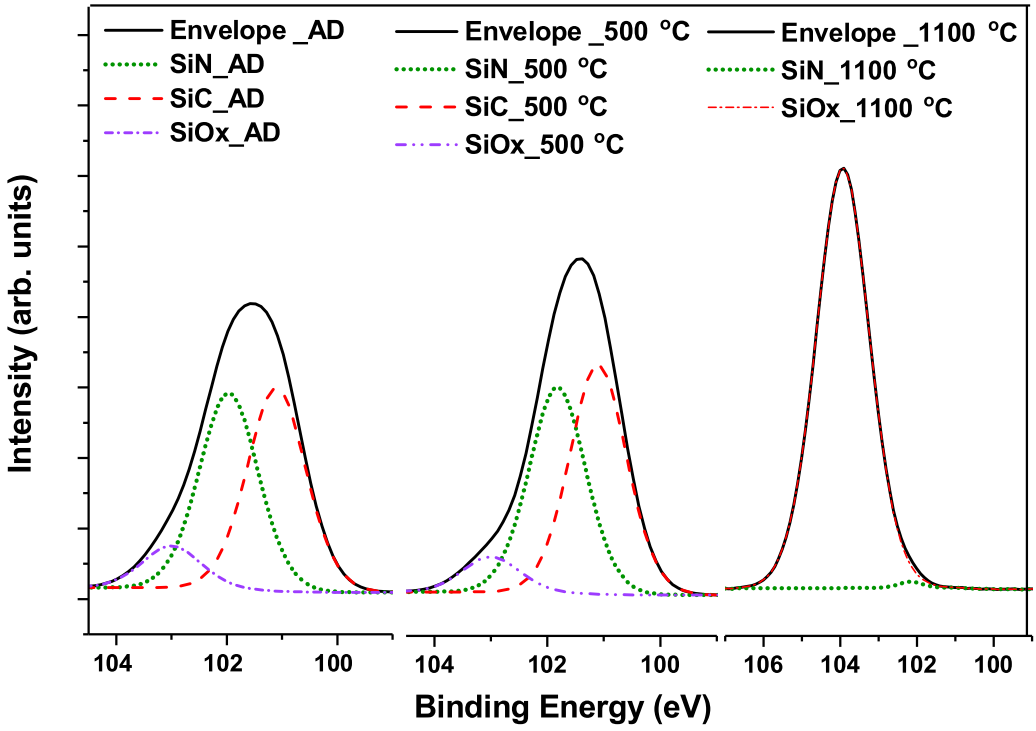

Figure 6.1: **XPS Si 2p of annealed a-$SiC_{1.2}N_{0.7}$:$H_{1.4}$.** Comparison of Si 2p core levels of the annealed a-$SiC_{1.2}N_{0.7}$:$H_{1.4}$ films with the corresponding chemical bonds. The relative concentration of Si-C to Si-N bonds is higher at 500 °C. The small signal of the Si-N bond is, still, detected at higher temperatures while the Si-C feature entirely disappears.

6.1.2 PL of Annealed SiCN

Fig. 6.3 shows PL spectra of untreated a-$SiC_{1.2}N_{0.7}$:$H_{1.4}$ and thermally annealed samples covering the entire visible range. The broadening of the PL originates from the long-range structural disorders present in the amorphous materials introducing localized states into the band gap ("antiparallel band-edge fluctuations") [132]. The width of the band tail due to the localized states is indicated by the Urbach energy (E_u) given in Table 6.1. Upon annealing to 500 and 900 °C, E_u increases while the

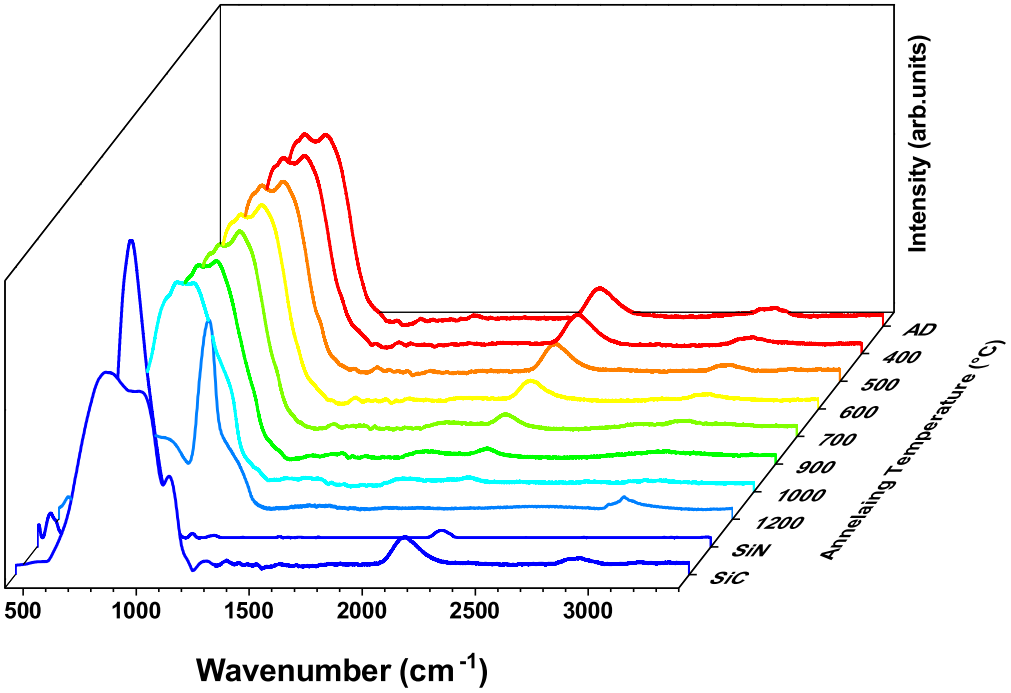

Figure 6.2: **FTIR of a-SiC$_{1.2}$N$_{0.7}$:H$_{1.4}$, a-SiN$_{1.3}$H$_{0.3}$, and a-SiC:H$_{1.3}$.** Infrared absorption spectra of a-SiC$_{1.2}$N$_{0.7}$:H$_{1.4}$ as a function of annealing temperature are shown along with a-SiN$_{1.3}$H$_{0.3}$ and a-SiC:H$_{1.3}$ reference samples.

optical band gap (E_{04}) narrows from 3.6 to 2.7 eV and from 2.7 to 0.5 eV, respectively. ERD measurements show that the majority of the hydrogen content effuses beyond annealing at 500 °C and is entirely depleted at 900 °C. The hydrogen desorption from the film layer results in an increase of unsaturated bonds. This leads to an increase of the mid-gap states in the band structure (an increase of E_u), and in turn, a decrease of the E_{04} gap.

Fig. 6.3 shows that the PL intensity increases upon annealing and reaches a maximum at 500 °C, degrades after 500 °C, with no emission at 900 °C and beyond. Hence, the optimum temperature for the post-deposition annealing is determined

Table 6.1: The optical properties of annealed a-$SiC_{1.2}N_{0.7}$:$H_{1.4}$ films.

Annealing Temperature (°C)	E_{04} (±0.2 eV)	E_u (eV)	D (±0.4 nm)	n (λ=632.8 nm)
AD-SiCN	3.6	0.28	232.7	2.08
400	3.5	0.30	226.3	2.08
500	3.5	0.49	224.7	2.08
600	2.7	0.50	218.3	2.08
700	1.5	0.89	212.1	2.10
900	0.5	1.24	192.8	2.22

to be 500 °C, where the highest concentration of the hydrogen-terminated bonds is observed in IR spectra [250]. The camera photo of the observed bright luminescence at 500 °C is shown in Fig. 6.4 along with the corresponding chromaticity diagram (CIE 1931). The emission, with a correlated colour temperature of T_c=4200 K, is positioned at x=0.381 and y=0.389 in the chromaticity diagram, which is very close to the values of "white" light, usually associated with a weighted sum of the three primary colors giving the value of x=0.33 and y=0.33 [96].

An example of an emission spectrum of a sample annealed at 500 °C, consisting of four superimposed line-shapes is presented in Fig. 6.5. Shown in Fig. 6.6 are the integrated intensities of each line-shape of the corresponding PL spectrum of a-$SiC_{1.2}N_{0.7}$:$H_{1.4}$ in Fig. 6.3, denoted as P_1, P_2, P_3, and P_4, which are centered at 2.6 eV (475 nm), 2.2 eV (565 nm), 1.8 eV (670 nm), and ∼1.4 eV (850 nm), respectively. The peak positions of the resolved line-shapes and their full widths at half maximum (FWHMs) are listed in Table 6.2. Upon annealing the two dominant PL peaks (P_2 and P_3) red-shift by 0.2 eV, with a decrease of their FWHMs. The slight red-shift of the PL bands agrees with the observed optical band gap narrowing and can be

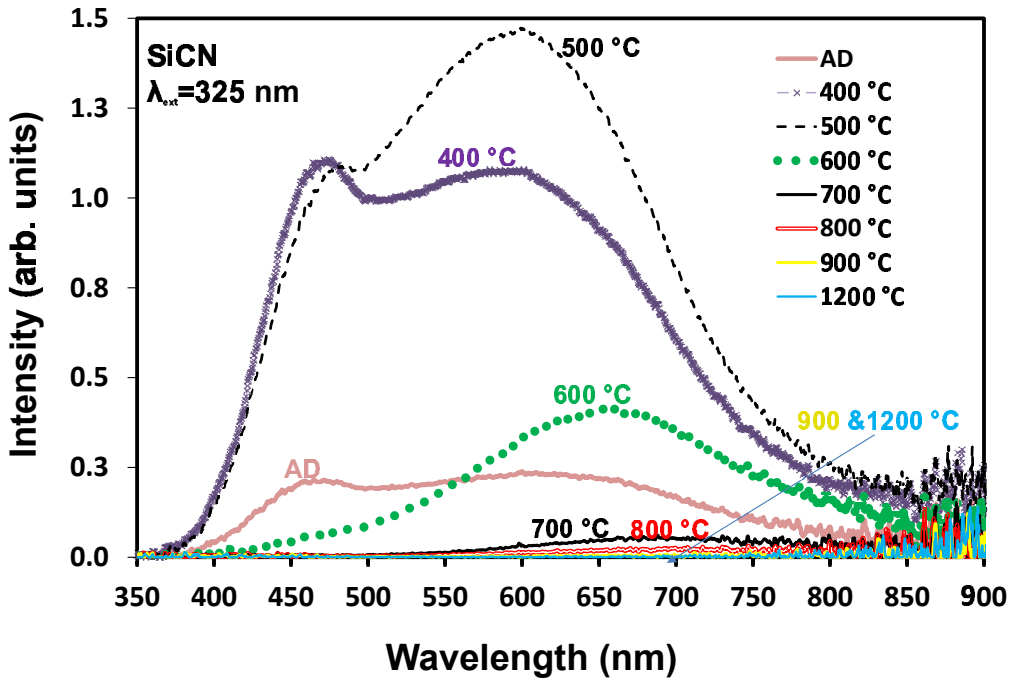

Figure 6.3: **PL of annealed a-$SiC_{1.2}N_{0.7}$:$H_{1.4}$.** The room-temperature PL spectra of a-$SiC_{1.2}N_{0.7}$:$H_{1.4}$ annealed at 400 to 1200° C for 1 h in N_2 are shown. The intensity of the emission reached a maximum at 500 °C.

primarily attributed to changes of Si-C bond concentrations in accordance with XPS and FTIR analyses (Figs. 6.1 and 6.2).

The band tail states created by the short-range disorders are generally regarded as the luminescence centers in silicon-based amorphous materials, however, the localized defects can also play a role in the luminescence process as was extensively discussed in chapter 2. Consequently, the PL emission from a-SiC_xN_y can be explained by the band-to-tail and/or tail-to-tail transitions [27]. However, the PL mechanism and corresponding transitions in a-SiC_xN_y structures lacks detailed investigation [141]. We utilized the reported luminescence centers of two fairly well-studied submatrices, SiC [121] and Si_3N_4 [265], to identify the possible origin of the PL bands resolved

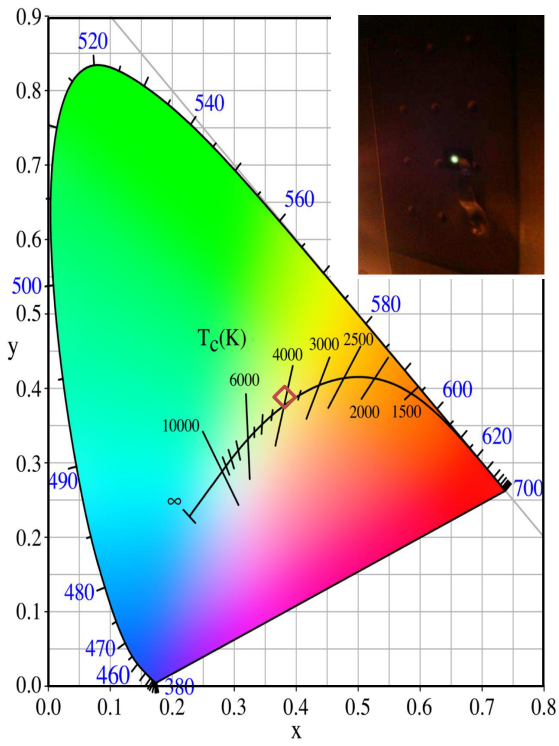

Figure 6.4: **CIE digram of annealed a-SiC$_{1.2}$N$_{0.7}$:H$_{1.4}$.** The inset shows the camera photo of the observed visible luminescence a-SiC$_{1.2}$N$_{0.7}$:H$_{1.4}$ annealed at 500 °C. That gives a color coordinate with x=0.381 and y=389 in CIE 1931 chromaticity diagram and a correlated colour temperature of T_c = 4200 K.

within the PL profile of a-SiC$_{1.2}$N$_{0.7}$:H$_{1.4}$. Figs. 6.7 and 6.8 show the thermally induced changes of the PL spectra of SiC:H$_{1.3}$ (N-free SiC$_x$N$_y$) and SiN$_{1.3}$:H$_{0.3}$ (C-free SiC$_x$N$_y$), respectively. Figs. 6.7 and 6.8 indicate that PL emission of a-SiC$_{1.2}$N$_{0.7}$:H$_{1.4}$ samples compared to that of N- and C-free SiC$_x$N$_y$ films changes in two ways: The intensity increases by about 1.5 and 1.25 orders of magnitude and the FWHM changes by 2 and 0.8 times, respectively.

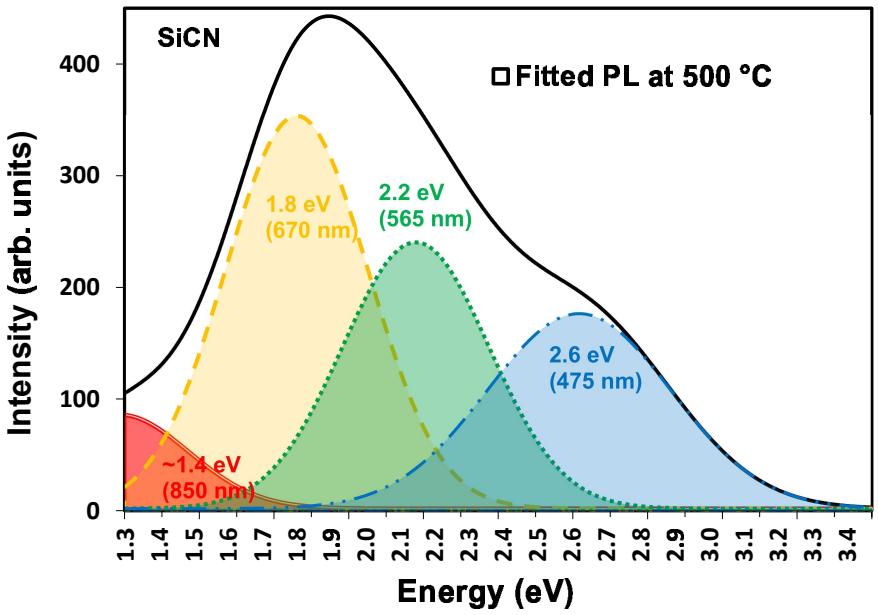

Figure 6.5: **Deconvoluted PL of annealed a-$SiC_{1.2}N_{0.7}$:$H_{1.4}$.** The a-$SiC_{1.2}N_{0.7}$:$H_{1.4}$ film annealed at 500 °C is decomposed into 4-line shapes. The color lines were obtained by Gauss fitting.

6.1.3 PL of SiC

All non-annealed and annealed SiC:$H_{1.3}$ samples exhibit strong PL emission at wavelengths in the 500 to 900 nm range (Fig. 6.7), which are deconvoluted into five PL bands, as shown in the inset of Fig. 6.9. These five PL bands are labeled as P_3, P_{3-2}, P_4, P_5, and P_6 and their changes at different annealing temperatures are presented in Fig. 6.9. Two of the lines are denoted by P_3 and P_{3-2}, since they are positioned in the region of the P_3 band observed in the PL of SiC:$H_{1.3}$. The P_4 line, located in the near infrared, showed a thermal evolution similar to the P_4 line of a-$SiC_{1.2}N_{0.7}$:$H_{1.4}$. PL lines at 2.0 eV (P_3, 610 nm), 1.8 eV (P_{3-2}, 670 nm), and 1.4 eV (P_4, ∼900 nm) are attributed to the silicon carbide structure. The two lines at 1.7 eV (P_5, 730 nm) and 1.6 eV (P_6, 758 nm) are related to carbon clusters in

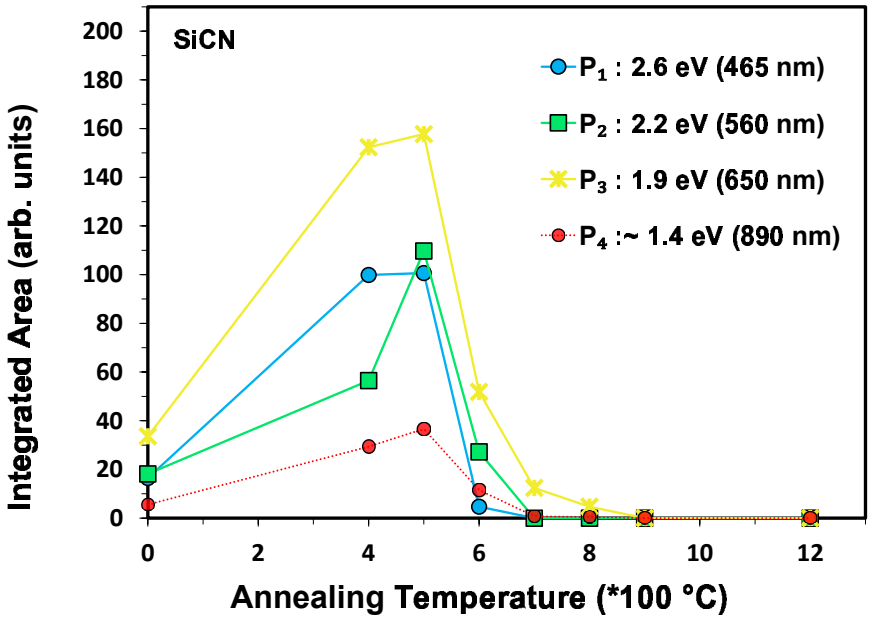

Figure 6.6: **Integrated PL intensities of annealed a-SiC$_{1.2}$N$_{0.7}$:H$_{1.4}$.** The dependence of the integrated PL intensities of each line shape on the annealing temperatures.

amorphous silicon carbide according to the theoretical PL calculations performed by Kassiba et al. [97]. These two peaks, arising from carbon clustering, are not observed in the PL of a-SiC$_{1.2}$N$_{0.7}$:H$_{1.4}$, guiding our interest to investigating the thermal behavior of the three remaining bands of SiC:H$_{1.3}$; i.e. P$_3$, P$_{3-2}$, and P$_4$ represented by symbols connected with solid lines in Fig. 6.9. The P$_4$ line, positioned in the near infrared region, is well known as the fingerprint of the silicon vacancy defect, V_{Si}, in crystalline SiC [120]. The P$_3$ and P$_{3-2}$ bands show a thermal behavior similar to the counterpart band (P$_3$) in a-SiC$_{1.2}$N$_{0.7}$:H$_{1.4}$. Castelloto et al. [121] associated the PL bands in the 600–800 nm range with the positively charged carbon antisite-vacancy pair defects, $C_{si}V_c$. Consequently, in our SiC:H$_{1.3}$samples, P$_3$ at 670 nm and P$_{3-2}$ at 610 nm can be assigned to $C_{si}V_c$ defects (the so-called AB lines). ESR and PAS

Table 6.2: **PL peak positions and FWHM of PL sub-bands of a-$SiC_{1.2}N_{0.7}$:$H_{1.4}$** The peak positions of the resolved PL lines and corresponding FWHMs of the a-$SiC_{1.2}N_{0.7}$:$H_{1.4}$ films along with the maximum uncertainty obtained for each individual peak.

Annealing Temp. (°C)	P_1 (eV) ±0.05	P_2 (eV) ±0.01	P_3 (eV) ±0.01	P_4 (eV) ±0.01	$FWHM_1$ (eV) ±0.09	$FWHM_2$ (eV) ±0.01	$FWHM_3$ (eV) ±0.02	$FWHM_4$ (eV) ±0.08
AD-SiCN	2.67	2.22	1.85	1.43	0.43	0.41	0.44	0.17
400	2.63	2.25	1.92	1.41	0.57	0.29	0.36	0.05
500	2.59	2.16	1.88	1.46	0.45	0.41	0.39	0.19
600	2.56	2.09	1.80	1.51	0.41	0.32	0.36	0.54
700	-	-	1.72	1.48	0	0	0.50	0.19
800	-	-	1.72	1.50	0	0	0.48	0.15
900	-	-	-	-	0	0	0	0

experiments identified the AB lines as the dominant defect centers in H-SiC, which exhibit luminescence upon annealing up to 500 °C and in some off-stoichiometries up to 800 °C [122].

The reported data on the defect-related emissions of crystalline SiC can be used regardless of the polytype configuration and the excitation energy used to identify those defects [122]. Although none of our investigated samples showed any crystalline structure, the origin of the PL bands still can be understood using common crystalline SiC polytypes (6H-SiC, 3C-SiC, and 4H-SiC). The short-scale order in amorphous materials preserves electronic properties of the crystalline state such as energy bands. Our SiC:$H_{1.3}$ samples can be assumed to have a configuration similar to wurtzite SiC (H-SiC) structures. The band gap of SiC:$H_{1.3}$ (3.06 eV) is much closer to the values of 2.8-3.0 eV for 6H-SiC and 3.2-3.3 eV for 2H-SiC structures rather than the value

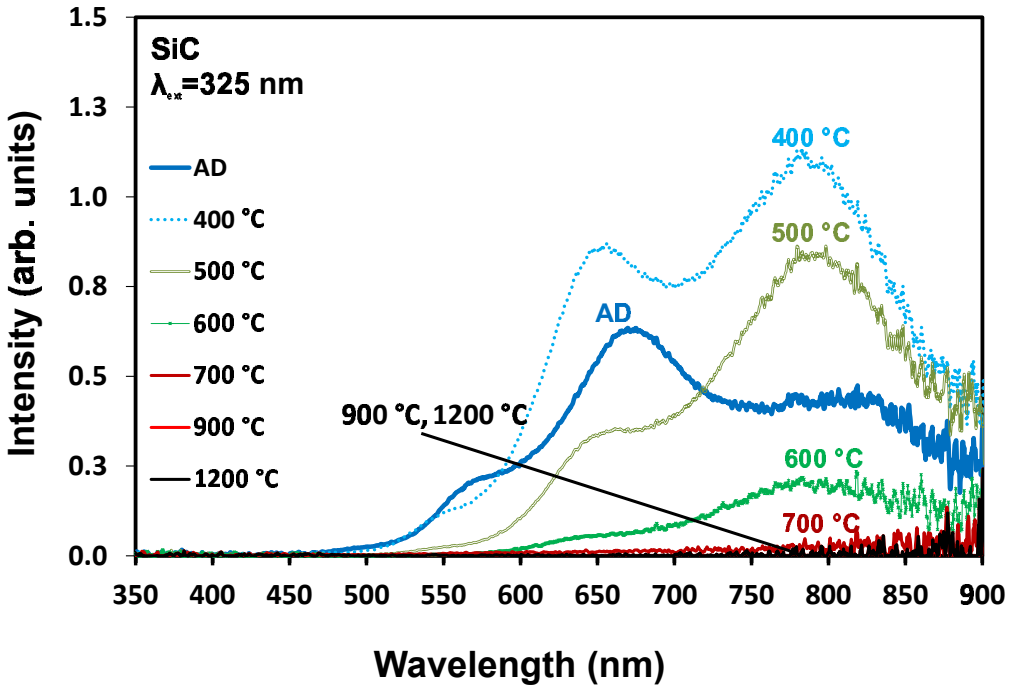

Figure 6.7: **PL of annealed a-SiC:$H_{1.3}$.** The change of room-temperature PL spectra for a-SiC:$H_{1.3}$ films annealed at 400-1200° C for 1 h in N_2.

of 2.4 eV reported for the band gap of the cubic 3C-SiC. Most likely, the properties of our SiC:$H_{1.3}$ samples are closer to the most stable polymorphic, 6H-SiC, due to the identical values of the band gap. Moreover, Fauch et al. [120] reported 6H-SiC as the polytype of SiC to have the highest intensity of the P_4 line, which is one of the resolved PL lines of SiC:$H_{1.3}$ at 1.43 eV. Therefore, the P_3 and P_{3-2} lines of SiC:$H_{1.3}$ in Fig. 6.9 persist up to temperature annealing of 500 °C and are aligned with the AB lines, the two characteristics in carbon vacancy defects in wurtzite SiC (H-SiC).

6.1.4 PL of SiN

The PL of $SiN_{1.3}$:$H_{0.3}$ is plotted in Fig. 6.8 showing that non-annealed and annealed samples emit differently, which contrasts with the observed PL of both SiC:$H_{1.3}$ and

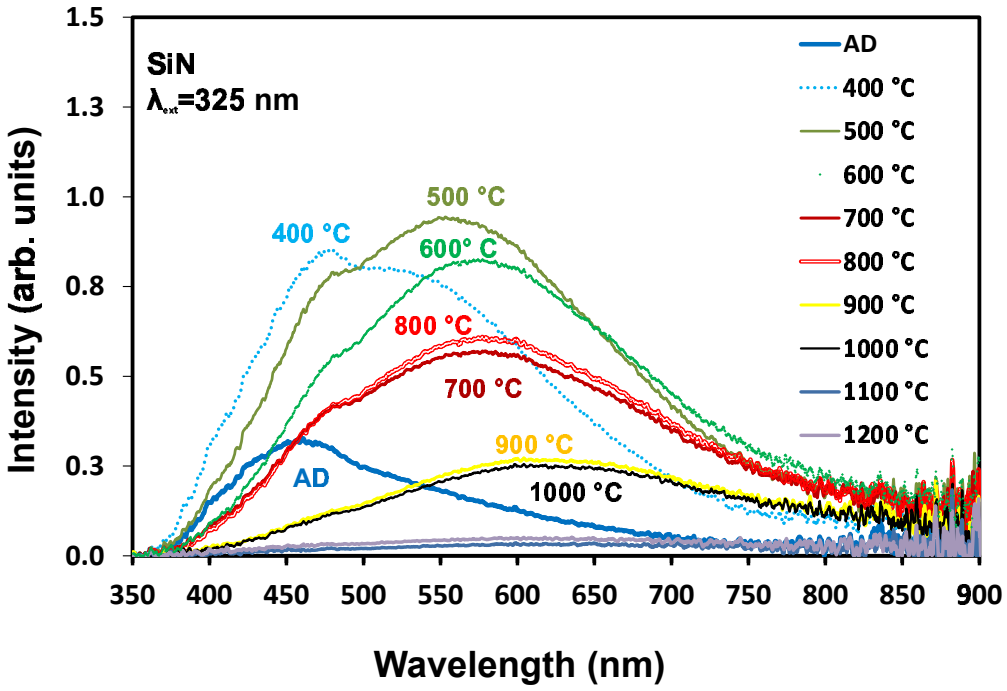

Figure 6.8: **PL of annealed a-SiN$_{1.3}$H$_{0.3}$.** The change of room-temperature PL spectra for a-SiN$_{1.3}$H$_{0.3}$ annealed at 400-1200 ° C for 1 h in N$_2$.

a-SiC$_{1.2}$N$_{0.7}$:H$_{1.4}$ films. Within the PL profile of the non-annealed SiN$_{1.3}$:H$_{0.3}$, only two PL bands are deconvoluted and are positioned at 2.6 and 2.3 eV, arising from Si^0-Si(σ) and Si^0=N$_2$, respectively, in agreement with published reports [108]. As soon as the SiN$_{1.3}$:H$_{0.3}$ layer is exposed to heat, phase separation occurs and only the emission at 2.6 eV remains, the line at 2.3 eV vanishes, and two new emission lines at 2.1 and 1.7 eV appear. Accordingly, the three resolved PL bands in the annealed SiN$_{1.3}$:H$_{0.3}$ samples are denoted as P$_1$, P$_2$, and P$_7$. P$_1$ and P$_2$ lines are resolved in the PL of a-SiC$_{1.2}$N$_{0.7}$:H$_{1.4}$ and are labelled similarly while the last line (P$_7$) is not observed. The changes of P$_1$ and P$_2$ bands are represented by symbols connected with solid lines and the P$_7$ band is represented by scatter symbols in Fig. 6.10. The blue-green emission from the P$_1$ line at 2.1 eV (475 nm) has been mainly attributed to metastable anion

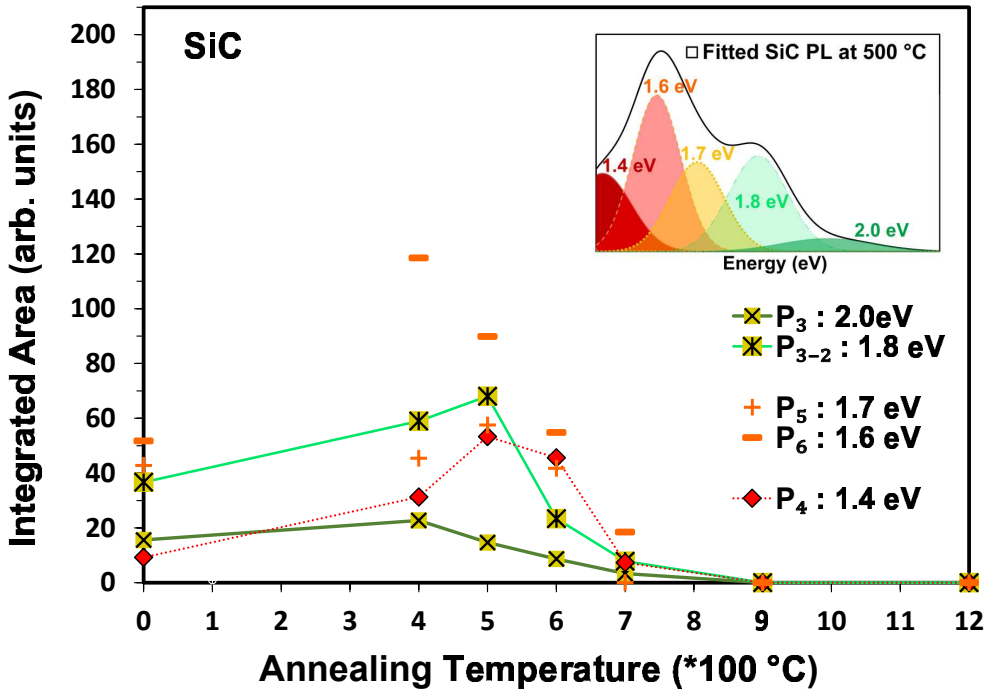

Figure 6.9: **The integrated area intensity of the decomposed PL peaks of a-SiC:$H_{1.3}$.** The integrated area intensity of the decomposed PL peaks as a function of annealing temperature for a-SiC:$H_{1.3}$ samples. The PL peaks presented by symbols connected with solid lines are like peaks observed in PL spectra of annealed a-$SiC_{1.2}N_{0.7}$:$H_{1.4}$ films. The inset is an example of the decomposed peaks of the fitted PL spectrum.

N radicals [265]. The P_2 band coming from the nitride-related dangling bonds such as N_3≡Si, K-centers [110], act as radiative centers emitting with an energy of 2.1 eV (600 nm) and lose PL emission after annealing at 1000 °C. The P_7 line is the only one among all PL bands observed from SiC:$H_{1.3}$, $SiN_{1.3}$:$H_{0.3}$, and a-$SiC_{1.2}N_{0.7}$:$H_{1.4}$ that persist after annealing at 1000 °C and significantly intensifies after annealing at 1200 °C. Earlier studies ascribed the luminescence of this line to quantum confinement with the evidence of fully nitride-embedded silicon nanocrystals [266]. However, it is not universally agreed to relate this line to SiN itself or fully nitride-embedded silicon

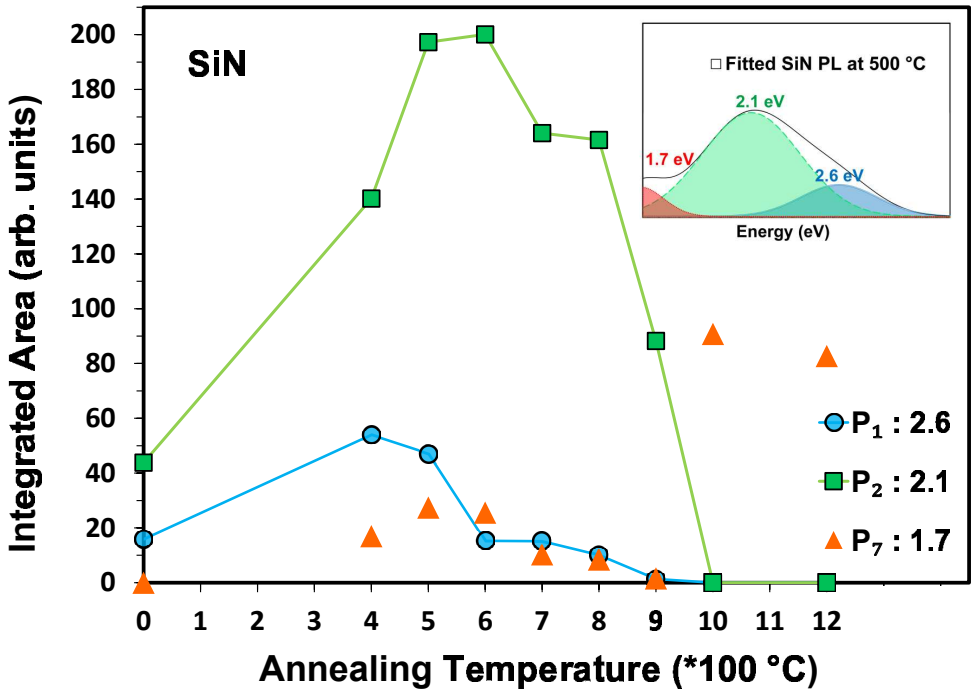

Figure 6.10: **The integrated area intensity of the decomposed PL peaks of a-$SiN_{1.3}H_{0.3}$.** The integrated area intensity of the decomposed PL peaks as a function of annealing temperature for a-$SiN_{1.3}H_{0.3}$ samples. The PL peaks presented by symbols connected with solid lines are like peaks observed in PL spectra of annealed a-$SiC_{1.2}N_{0.7}$:$H_{1.4}$ films. The inset is an example of the decomposed peaks of the fitted PL spectrum.

nanocrystals, for which no comprehensive calculation of the energy range has been reported [99].

6.2 Origin of PL Emission from Silicon Carbonitride

The origin of the resolved PL bands of a-$SiC_{1.2}N_{0.7}$:$H_{1.4}$ (Fig. 6.6) can be explored by combining the discussed PL bands of SiC:$H_{1.3}$ and a-$SiN_{1.3}$:$H_{0.3}$ (Figs. 6.9 and6.10).

Starting from the low energy side of the PL profile of a-$SiC_{1.2}N_{0.7}$:$H_{1.4}$, the P_4 band is positioned and changes similarly to the P_4 line ascribed to silicon vacancies, observed in both SiC:$H_{1.3}$ and $SiN_{1.3}$:$H_{0.3}$ samples. However, we disregard the changes of this PL band due to the low signal level and the noise beyond ∼800 nm coming from the lower sensitivity of the CCD camera in this detection range. On the other hand, the P_2 and P_3 lines show considerable enhancement up to 500 °C. The P_3 band at 1.8 eV (675 nm), coming from AB-lines in SiC:$H_{1.3}$, was not resolved in $SiN_{1.3}$:$H_{0.3}$. The enhancement of the P_3 band at 500 °C is likely due to more attachments of silicon to carbon atoms, supported by IR absorption and XPS data. The P_3 line decays gradually and is completely quenched after annealing at 800 °C, well in agreement with the reported thermal behavior of the AB-lines [121]. The P_2 band at 2.2 eV (565 nm), arising from nitride related defects, was observed in PL profiles of $SiN_{1.3}$:$H_{0.3}$ and shows similar changes, except that the temperature of "annealing out" is 600 °C, which is lower than that of $SiN_{1.3}$:$H_{0.3}$ (<1000 °C) as demonstrated in Fig. 6.10. This could be explained by the structural disorders imposed by the presence of carbide bonds in the silicon nitride structure leading to the "annealing out" of the P_2 emission at lower annealing temperatures. P_1 at 2.6 eV (475 nm) is observed only in the PL profile of $SiN_{1.3}$:$H_{0.3}$, but not in SiC:$H_{1.3}$, and is assigned to the transitions between gap states in silicon dangling bonds, the so-called K-centres. In contrast to the stability up to 900 °C of the P_1 line in $SiN_{1.3}$:$H_{0.3}$, the P_1 line of a-$SiC_{1.2}N_{0.7}$:$H_{1.4}$ remains optically active only up to 600 °C. However, the intensity of P_1 resolved in a-$SiC_{1.2}N_{0.7}$:$H_{1.4}$ annealed at 500 °C is about 50% higher than that of $SiN_{1.3}$:$H_{0.3}$, given that initially the intensity of P_1 is equal for un-treated both films. Likely, the carbon bridge in the $SiN_{1.3}$:$H_{0.3}$ matrix could have caused a change of the activation energy of silicon vacancies, making those defects less stable in the a-$SiC_{1.2}N_{0.7}$:$H_{1.4}$ structure.

The interdependency of carbon and nitrogen in the a-$SiC_{1.2}N_{0.7}$:$H_{1.4}$ films make the K-centers vanish at lower annealing temperatures and the AB lines to stay optically active at higher temperatures. Moreover, the presence of nitrogen in a-$SiC_{1.2}N_{0.7}$:$H_{1.4}$ films leads to quenching of the emission from carbon clusters (related to the P_5 and P_6 bands observed in SiC:$H_{1.3}$).

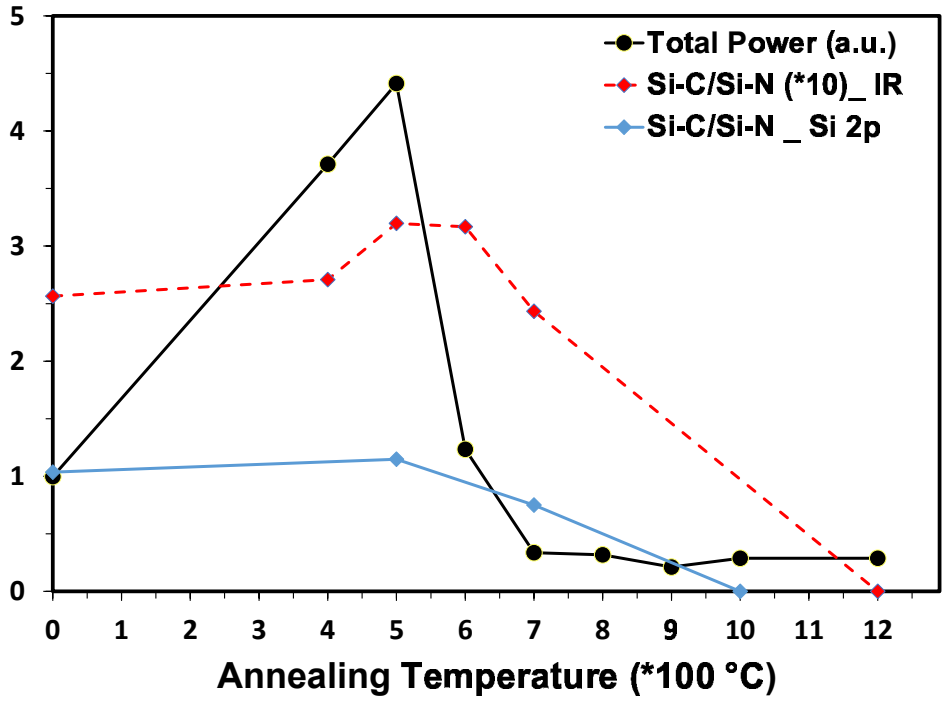

Figure 6.11: **Relation of total PL emission power and Si-C and Si-N bonds.** Correlation between the total PL emission power and the ratio of Si-C/Si-N bonds for different annealed a-$SiC_{1.2}N_{0.7}$:$H_{1.4}$ films. The intensity of PL increases with the relative increase of Si-C bonds.

Fig. 6.1 shows that the largest relative density of Si-C to Si-N bonds at the Si 2p core level is observed at 500 °C, where the strongest PL emission is observed. Further annealing leads to a decrease and eventually breaking, of Si-C bonds, while the weak signal of Si-N bond still can be detected at higher temperatures. FTIR results

(Fig. 6.2), in agreement with XPS analyses, shows that the Si-N bonds are virtually constant up to 900 °C (within the uncertainty of FTIR measurements), while Si-C bonds increase up to 500 °C and decreases beyond 700 °C. This suggests that the Si-N bonds show less change during the annealing compared to the Si-C configurations. In Fig. 6.11, the total PL intensity at various annealing temperatures is plotted along with the relative ratio of the decomposed Si 2p peaks corresponding to Si-C to Si-N bonds and relative concentration of Si-C to Si-N bonds in IR spectra. The intensity of PL increases with the relative increase of Si-C bonds indicating a stronger correlation of the PL emission with the changes of Si-C bonding configurations. In addition, the major PL emission of a-$SiC_{1.2}N_{0.7}$:$H_{1.4}$ films are primarily due to the P_3 band and secondarily, the P_2 band. The P_3 emission is related only to radiative carbon defect centers of SiC:$H_{1.3}$ implying that AB-lines (carbon vacancies) could play a significant role in the visible luminescence of a-$SiC_{1.2}N_{0.7}$:$H_{1.4}$ films. Previously, for as-grown a-SiC_xN_y:H_z films with different carbon content, the most luminescent a-SiC_xN_y:H_z composition was closely correlated with the highest density of Si-C bonds [220]. Therefore, the light emission from a-SiC_xN_y:H_z films likely can be optimized via the adjustment of the Si-C bond configurations during the annealing process.

6.3 Influence of the Substrate Temperature

To explore the influence of substrate temperature, the stage temperature (denoted as the deposition temperatures, T_d) was varied from 300 to 450 °C, in 50 °C increments, corresponding to substrate temperatures (denoted as T_s) of 120, 137, 154, and 170 °C, respectively. The substrate temperature was found to be linearly proportional to the heating element's temperature according to the relation 3.1. Therefore, four

a-$SiC_xN_yH_z$ samples (SiCN-300, SiCN-350, SiCN-400, and SiCN-450) were grown using identical parameters except for the deposition temperature that was kept at 300, 350, 400, and 450 °C, respectively. Gas flow rates of 5, 10, and 8 (±5%) sccm were used for 30% SiH_4 diluted in Ar, 10% N_2 diluted in Ar, and pure CH_4 with the corresponding partial pressures of 0.42, 0.8, and 0.23 mTorr, respectively. The samples are labeled accordingly in Table 6.3 showing the heater temperature used for each sample. It should be noted that the ECR PECVD system employed in this study is designed to feed N_2 and Ar gases into the plasma region and supply CH_4 and SiH_4 gases downstream from the discharge zone through a dispersion ring positioned out of the plasma region close to the substrate.

6.3.1 Composition of SiCN with Different T_s

The combined RBS-ERD results show that the substrate temperature strongly affects the film composition. Fig. 6.12 shows the variation of the concentration of all constituent elements of a-SiC_xN_y:H_Z samples (including hydrogen) as a function of the deposition temperature with the corresponding experimental uncertainties. The small uncertainties are related to the use of a glassy carbon (vitreous carbon) substrate, which has an RBS signal at lower energy than the light elements in the SiC_xN_y:H_z layer, in contrast to the commonly used silicon substrate. The values of the atomic concentrations listed in Table 6.3 indicate that an increase of T_d from 300 to 400 °C (T_s from 120 to 154 °C) decreases the nitrogen concentration by about 25% of its initial value, silicon is virtually constant, and the carbon content increases by about 75%. At T_d=450 °C (T_s=170 °C) the concentration of silicon and nitrogen reduce drastically and the film becomes carbon rich. The hydrogen concentration decreases

from 38 to 12 at.% when increasing T_d from 300 to 450 °C (T_s from 120 to 154 °C). The substrate temperature affects the migration of the species on the surface and their reactions [267]. The observed changes of the film composition can be explained by the increase of the reactivity of CH_4 with higher substrate temperature, leading to a larger fraction of free radicals and fewer hydrocarbons. As a result, carbon is the main element substituting hydrogen in the coating layer, while nitrogen slightly decreases. The density of the samples is provided in Table 6.3 and was calculated using the atomic concentration obtained from the combined RBS-ERD measurements and the thickness given by VASE. The film density increases when T_d increases from 300 to 400 °C (T_s from 120 to 154 °C), which is related to the loss of hydrogen (and subsequent thinner layers) and incorporation of a significant amount of carbon into the film. In sample SiCN-450, in contrast to the continual hydrogen loss, the film density decreases to 1.85 gr/cm^3, due to the abrupt decrease of the silicon content.

6.3.2 Structural Analyses of SiCN with Different T_s

Fig. 6.13 presents the C 1s and Si 2p photoemission spectra and the corresponding fits of the SiCN-350 and SiCN-400 samples, where SiCN-400 (deposited at T_s = 154 °C) is presented by the solid lines. The C 1s core levels are characterized by two main peaks at 283.5 and 284.7 eV assigned to C-Si and C-C bonds and a smaller shoulder at 286.2 eV attributed to C-N bonds. The Si 2p spectra contain a mix of Si-C, Si-N, and Si-O bonds positioned at 101.1, 102.0, and 103.0 eV, respectively. The presence of insignificant amounts of oxygen is due to the slight oxygen contamination in the film and the post-deposition exposure of the sample to air after performing the HF treatment.

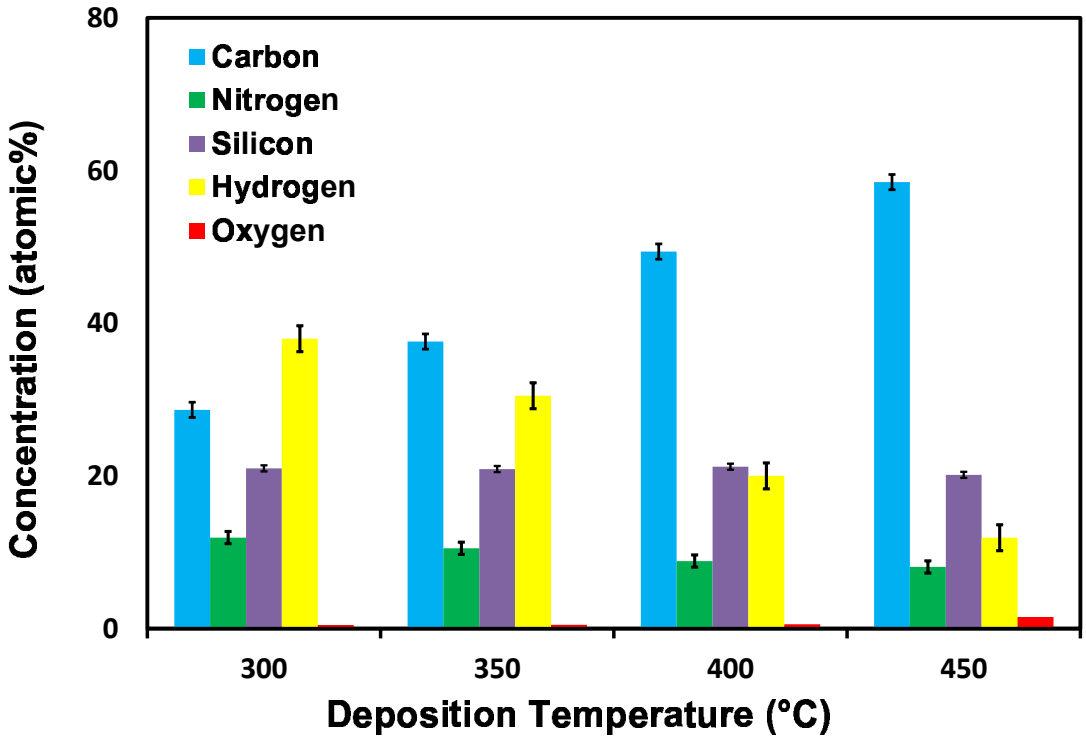

Figure 6.12: **Composition vs substrate temperature.** The concentration of constituent elements of a-SiC_xN_y:H_z films as a function of deposition temperature (T_d). With an increase of T_d from 300 to 400 °C; the concentration of hydrogen and nitrogen decreases, the carbon content increases, and the silicon content is virtually constant. At T_d=450 °C, the concentrations of silicon and nitrogen decrease drastically and the film becomes strongly carbon rich.

An increase in the substrate temperature leads to an increase of Si-C and C-N bond densities and a decrease in the concentrations of C-C and Si-N bonds. In agreement with RBS results (subsection 3.1), the higher reactivity of CH_4 at higher temperatures generates more free radicals to form carbon-related bonds such as C-N and Si-C. The decrease of the Si-N bond density can be expected from the lower nitrogen concentration in the film layer.

The IR absorption spectra of samples grown at 300, 400, and 450 °C (corresponding to T_s=120, 154, and 170 °C) are normalized to the sample grown at the lowest

Table 6.3: The atomic concentrations of carbon, nitrogen, silicon, and hydrogen along with the mass density determined by combined RBS-ERD. The refractive index and thickness were determined using VASE. For all samples, a 30-minute deposition with a mixture 5, 10, and 8 sccm of SiH_4/Ar, N_2/Ar, and CH_4, respectively, were used.

Sample	T_d (°C)	[H]±1.8 (at.%)	[C]±1.0 (at.%)	[N]±0.8 (at.%)	[Si]±0.4 (at.%)	d±0.4 (nm)	n (λ= 632.8 nm)	Density (±0.07 g/cm^3)
SiCN-300	300	38	28	12	21	381	1.95	1.88
SiCN-350	350	32	37	10	21	361	1.99	2.00
SiCN-400	400	20	49	9	21	322	2.04	2.20
SiCN-450	450	12	57	9	20	289	2.08	1.85
Ar-SiCN-350	350	20	48	12	19	424	1.98	2.93

deposition temperature (T_d=300 °C). The evolution of the film bond structure by varying T_d is particularly significant in the three regions of the IR spectrum shown in Fig. 6.14. The first change is observed at a peak positioned at 1100 cm^{-1} (Fig. 6.14.a), with the second region of interest located at 1700 cm^{-1} (Fig. 6.14.b). Both can be assigned to carbon-nitrogen configurations [250]. In most cases, the overlap of the C-N and C=N absorption modes makes it difficult to distinguish them [235]. We attribute the enhancement of these two peaks to the formation of more C-N/C=N bonds at higher T_d, which was also observed by Tomasella et al. [268]. Fig. 6.14.c shows the spectra in a third region, between 1900 and 2200 cm^{-1}, which is an overlap of Si-H stretching modes and the C≡N stretching vibration at around 2100–2200 cm^{-1}. A larger density of Si-H bonds is observed at lower substrate temperatures

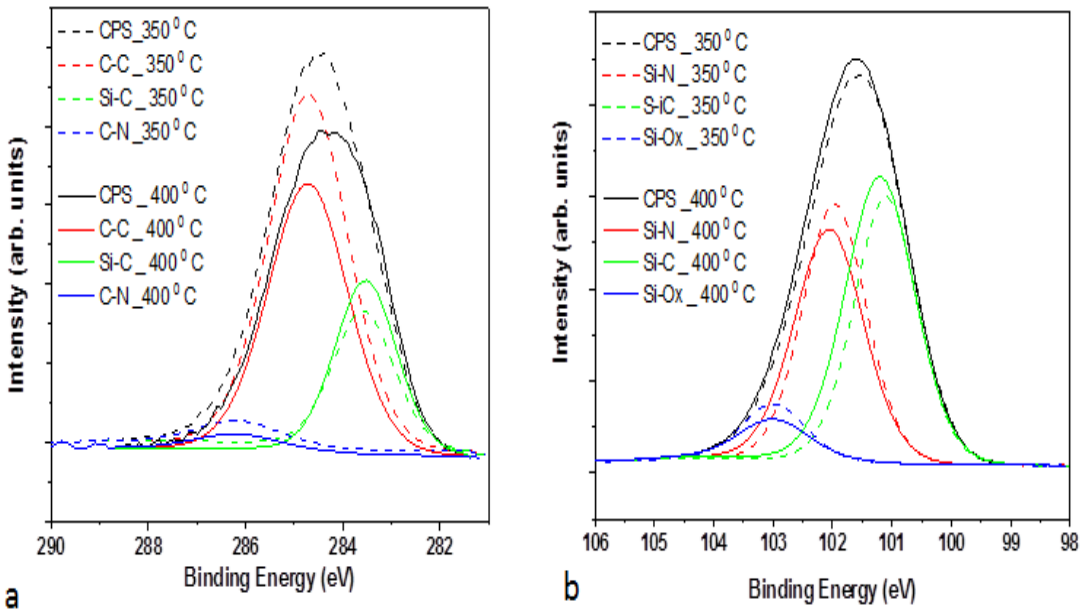

Figure 6.13: **XPS spectra vs substrate temperature.** The photoemission spectra and the corresponding fits of a-SiC_xN_y:H_z thin films for the core levels of (a) C 1s and (b) Si 2p. The samples grown at higher deposition temperatures are presented by solid lines.

due to the higher hydrogen content in the films. The increase in the substrate temperature makes the contribution of the C≡N bond around 2200 cm^{-1} significantly larger. The combination of the changes of the Si-H and C-N bonds with the variation of substrate temperature leads to the observed shift to larger wavenumbers at higher temperatures. The evolution of the bonding configuration given by IR absorption can be explained by the cross-linking of C to N atoms due to the increase of the carbon content and hydrogen loss at higher temperatures, in agreement with the discussed XPS analysis (Fig. 6.13) showing a larger density of carbon bonded to nitrogen at higher temperatures. It is noted that the changes of the Si-N and Si-C bonds were analyzed only using XPS measurements and their IR results are disregarded due to the large overlap of their IR bands.

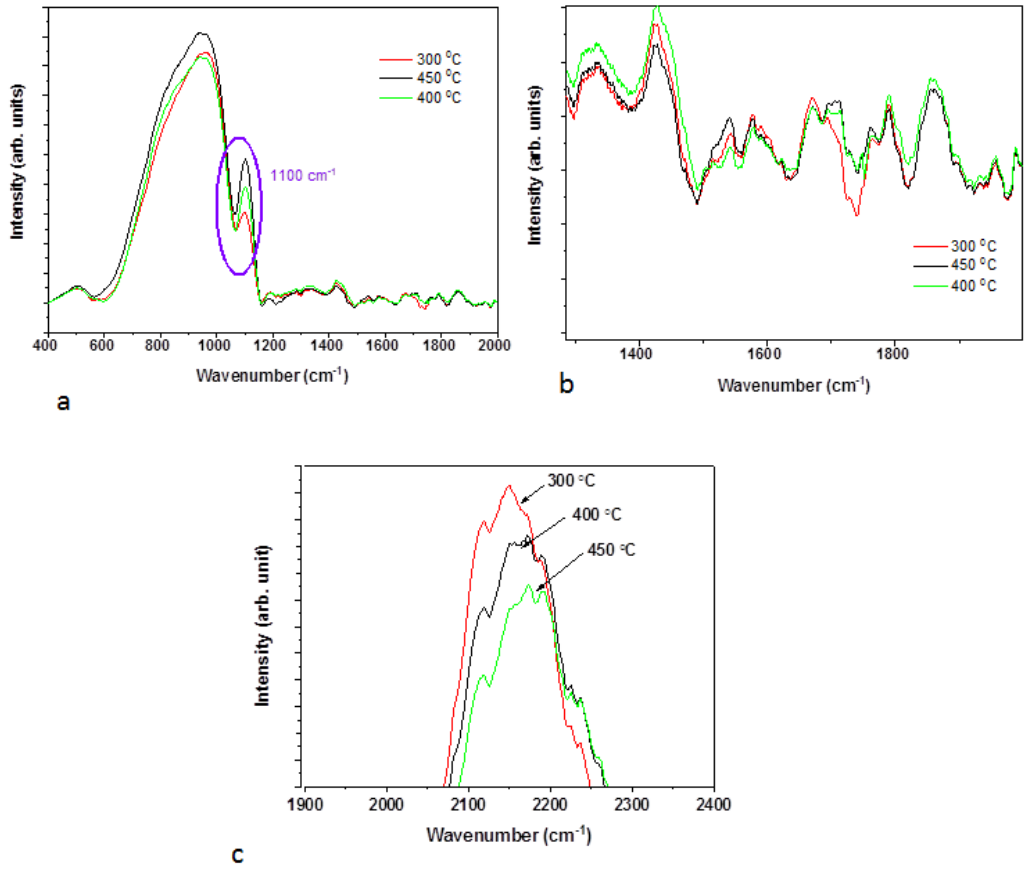

Figure 6.14: **IR absorption vs substrate temperature.** FTIR spectra of a-SiC_xN_y:H_z thin films grown at different deposition temperatures. Three specific area of interest are shown.

6.3.3 Optical Properties of SiCN with Different T_s

The values of the optical band gap related to the localized states were determined from the absorption coefficient (deduced from VASE simulations). Fig. 6.15 shows the variation of the optical band gap along with the other parameters determined directly from VASE simulations, i.e. refractive index and growth rate, as a function of the deposition temperature. It can be observed that higher temperatures result in optical gap widening, an increase of the refractive index, and thinner layers.

The increase of the substrate temperature by 50 °C (T_d by 150 °C) results in a decrease of growth rate from 126 to 96 nm/min due to the incorporation of less hydrogen into the film (24% film shrinkage). The refractive index, which is related to the polarization response of a material, increases with substrate temperature. According to Lorentz-Lorenz equation, two correlated quantities, the density of the film and chemical configurations, affect the polarization [243]. Higher temperature induces changes in both the film mass density and microstructure through the larger density of carbon bonds in the SiC_xN_y:H_z layer as a direct result of the hydrogen loss and higher carbon content in agreement with previously report on the substrate temperature of silicon carbide films grown using PECDV [116].

The values of the optical gap provided in Table 6.4 indicate an increase of 0.3 eV with an increase of substrate temperature by 50 °C (T_d by 150 °C), which is a result of the competition between the hydrogen loss and formation of carbon-related bonds. It is well known that lower hydrogen content increases the localized mid-band gap states in the band structure, and in turn, the optical band gap narrows. On the other hand, the rearrangement of the film atomic structure, observed by XPS (Fig. 6.13) and FTIR (Fig. 6.14), induces a higher concentration of Si-C and C-N bonds leading to optical band gap widening. It is well known that lower hydrogen content increases the localized mid-band gap states in the band structure, and in turn, the optical band gap narrows. Apparently, the evolution of structure has a more profound effect on the changes of the optical band gap compared to the hydrogen loss.

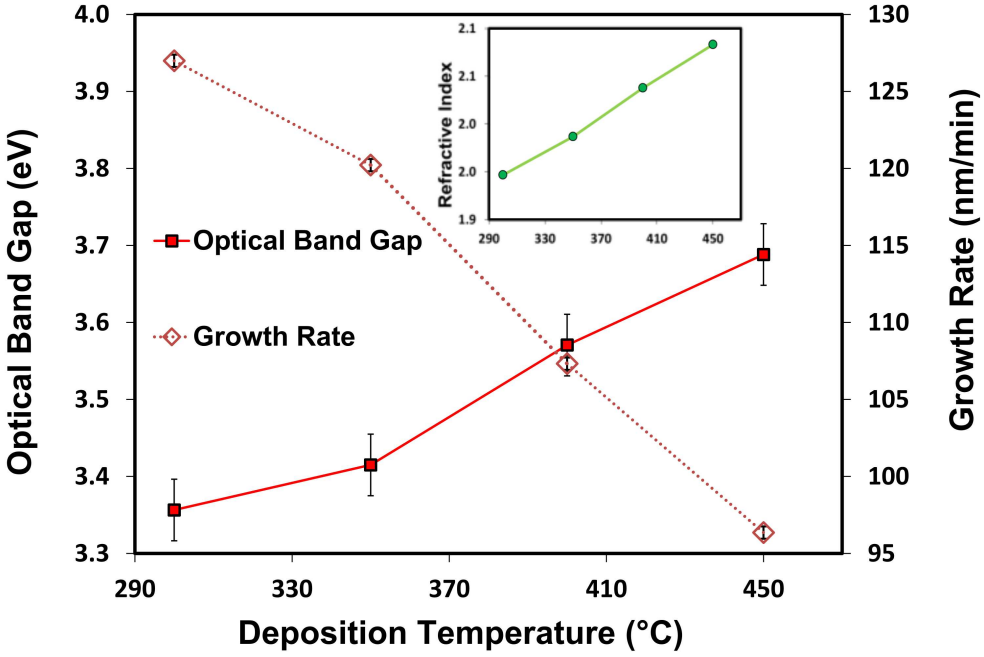

Figure 6.15: **Optical band gap and growth rate vs substrate temperature.** Variation of the optical band gap (E_{04}) and growth rate as a function of the deposition temperature along with the corresponding uncertainties. The inset shows the refractive index of the samples grown at different deposition temperatures.

6.4 PL as a Function of T_s

As discussed above, the increase of the growth temperature leads to layer densification and film shrinkage. The difference in the layer thickness of the samples grown at different temperatures makes it necessary to normalize the PL spectrum of each sample to the corresponding thickness. Fig. 6.16 shows the PL emission profile under excitation using a 325 nm laser source of different SiC_xN_y:H_z thin films as a function of wavelength. Fig. 6.17 shows the PL sepctra of these samples normalized to the film thickness. In fact, the thickness of the samples studied in this thesis does not

affect the PL intensity of the samples since their thicknesses are close to each other (see Table 6.3). The normalized samples show a similar ratio of the PL intensity observed for non-normalized samples (Fig. 6.16). Nevertheless, the intensity and the full width at half maximum (FWHM) of the PL profiles increase due to the enhancement of the low energy tail of the PL spectra with higher substrate temperature. To quantitatively understand the changes of the overall luminescent color, the chromaticity coordinates were calculated from the PL emission spectra. Fig. 6.18 shows the chromaticity coordinates of SiC_xN_y:H_z thin films with the corresponding deposition temperatures labeled in the CIE 1931 chromaticity diagram. The values are listed in Table 6.4. With the increase of substrate temperature of 50 °C (T_d=150 °C), the emission color changes from orange to yellow and is accompanied by an increase of the total emission power by a factor of 6.2 (Fig. 6.19). In general all samples show a very broad PL spectrum covering the whole visible range. The energy of the centroid of PL spectra increases when the band gap increases at higher temperatures. It can be observed that the energy of the PL spectra increases when the band gap increases at higher temperatures.

Fig. 6.20 shows thermal evolution of PL of SiC_xN_y samples grown using different substrate temperatures. The samples are annealed between 400 to 1200 °C for 1 h in N_2 ambient and the corresponding deposition temperatures are indicated. The PL band positioned at lower energy side of the visible range is enhanced with higher deposition temperatures due to the formation of more Si-C bonds. It can observed that the most luminescent sample is achieved at the deposition temperature of 350 °C.

To explore the details of the PL evolution, the deconvoluted PL spectra of each sample are shown in Fig. 6.21, delivering four PL bands as P_1, P_2, P_3, and P_4 located

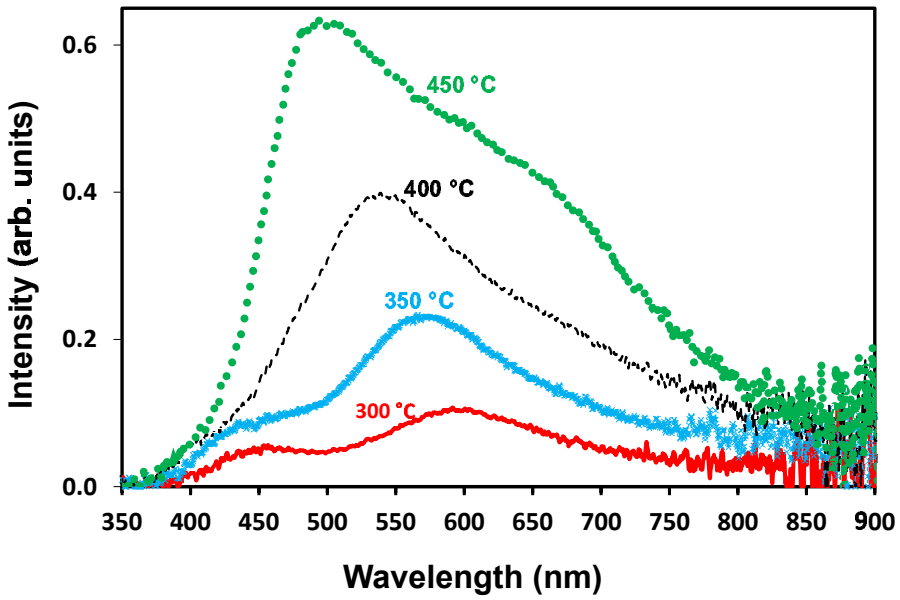

Figure 6.16: **PL of as-deposited samples vs substrate temperature.** The PL spectra excited using a 325 nm laser source of as-deposited SiC_xN_y:H_z thin films as a function of deposition temperature.

at $\sim$ 2.6 eV (475 nm), 2.2 eV (565 nm), 1.8 eV (675 nm), and 1.4 eV (850 nm). Fig. 6.21 shows that by an increase of T_d from 300 to 350 °C, the P_2 band at 2.2 eV and the P_3 band at 1.8 eV become far more intense. Further increase of T_d from 350 to 400 °C results in the smaller contributions of the P_2 band and a gradual increase of the P_3 band, while the P_1 band at 2.6 eV remains virtually unchanged. Even further increasing T_d to 450 °C induces more significant changes in the P_3 band, which intensifies by a factor of 9 and blue shifts to 1.79 ev (688 nm) from 1.62 eV (765 nm) for SiCN-300.

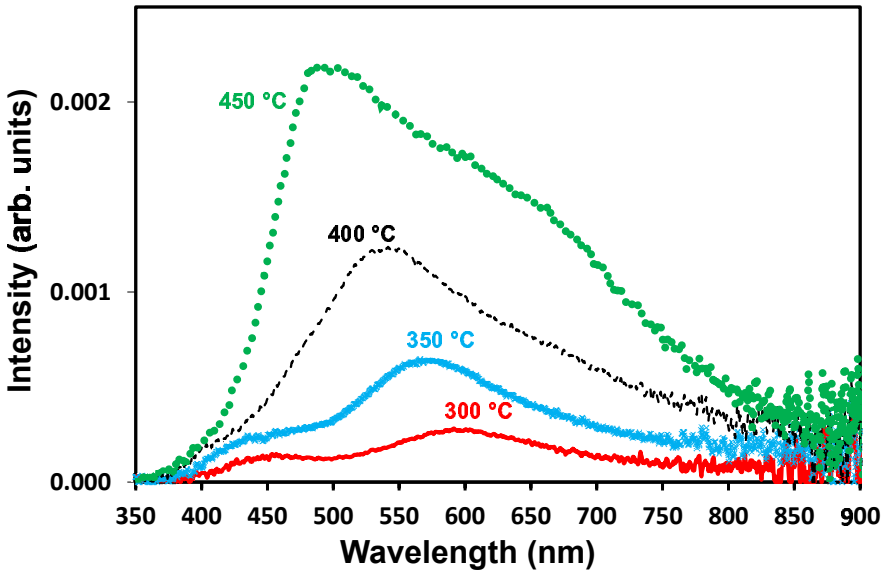

Figure 6.17: **The PL spectra of as-deposited samples normalized to the film thickness.** The PL spectra of as-deposited SiC_xN_y:H_z thin films are normalized to the film thickness.

6.5 Discussion of T_s

The dissociation rate of SiH_4 is comparable with that of common carbon sources used in CVD techniques such as C_2H_2 and C_2H_6. More stable gases such as (CH_4) require higher thermal energy to be dissociated [269]. The combination of the substrate temperature of about 300 °C and the energetic reactants coming from plasma more likely allows breaking of Si-H bonds (3.6 eV) originating from SiH_4 than C-H bond (4.3 eV) from CH_4. Furthermore, the sticking coefficient of carbon based radicals is much lower than that of silicon-based species [270]. The increase of the substrate temperature is in such a way that makes CH_4 species more chemically active with SiH_4 species. Ctvrtlik et al. [28] reported that the interatomic interactions between the carbon, silicon, and nitrogen increases with the higher deposition temperature leading

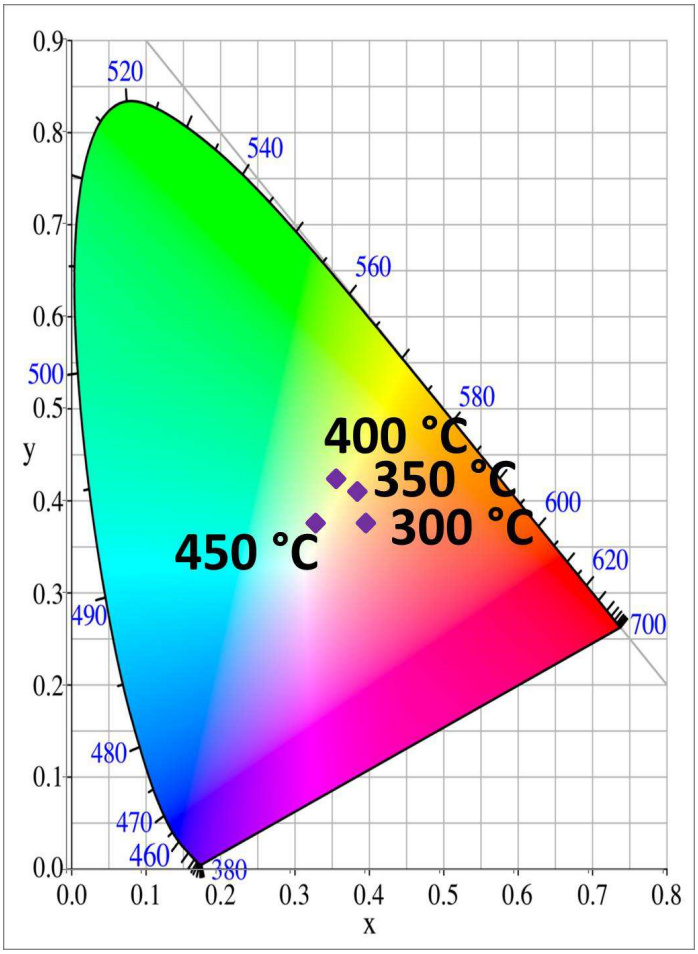

Figure 6.18: **CIE 1931 chromaticity diagram of as-deposited samples.** The chromaticity coordinates labeled in the CIE 1931 chromaticity diagram for as-grown samples grown using different deposition temperatures is shown.

to less formation of carbon clusters. Compositional analyses verified that more carbon was incorporated into the growing layer as a result of the higher activation of CH_4. A decrease of hydrogen and nitrogen at higher substrate temperatures and a significant increase of carbon in the resultant films were observed.

The reasons for the low hydrogen content at higher temperatures are twofold: First, the incomplete dissociation of CH_4 at such low substrate temperatures causes some hydrogen atoms to remain bonded to carbon atoms in the chemical species

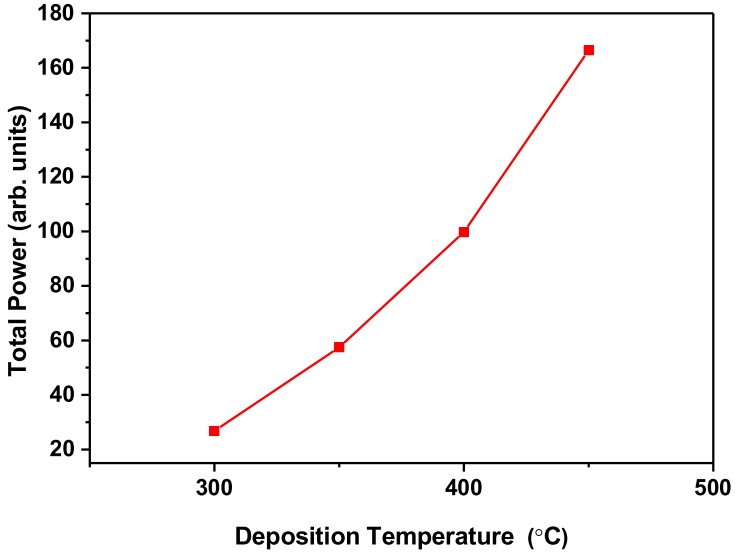

Figure 6.19: **Total emission power of PL of as-grown samples vs deposition temperature.** Total emission power of PL of as-grown samples vs substrate temperature indicates a strong increase with the deposition temperature.

reaching the growing surface. This incorporates more hydrogen into the film layer in the form of hydrocarbon bonds. Second, at higher temperatures, weak hydrogen-terminated bonds are less stable leading to hydrogen desorption from the growing surface. Consequently, with the increase of temperature, carbon is the element substituting hydrogen in the layer, while nitrogen decreases.

From a structural point of view, IR absorption verified the increase of the representative bonds of CN/C=N at 1100 and 1700 cm^{-1} with higher deposition temperature. The increase of C-N and C=N bonds, despite the presence of a smaller amount of nitrogen in the film, can be explained by the changes of hydrogen cyanide (HCN) and CN at higher substrate temperatures. These two emission lines were found to be the major components in the gas mixture, which lead to the relatively low concentration of C-N bonds in CVD grown thin films [152]. Higher reactivity of CH_4 at higher

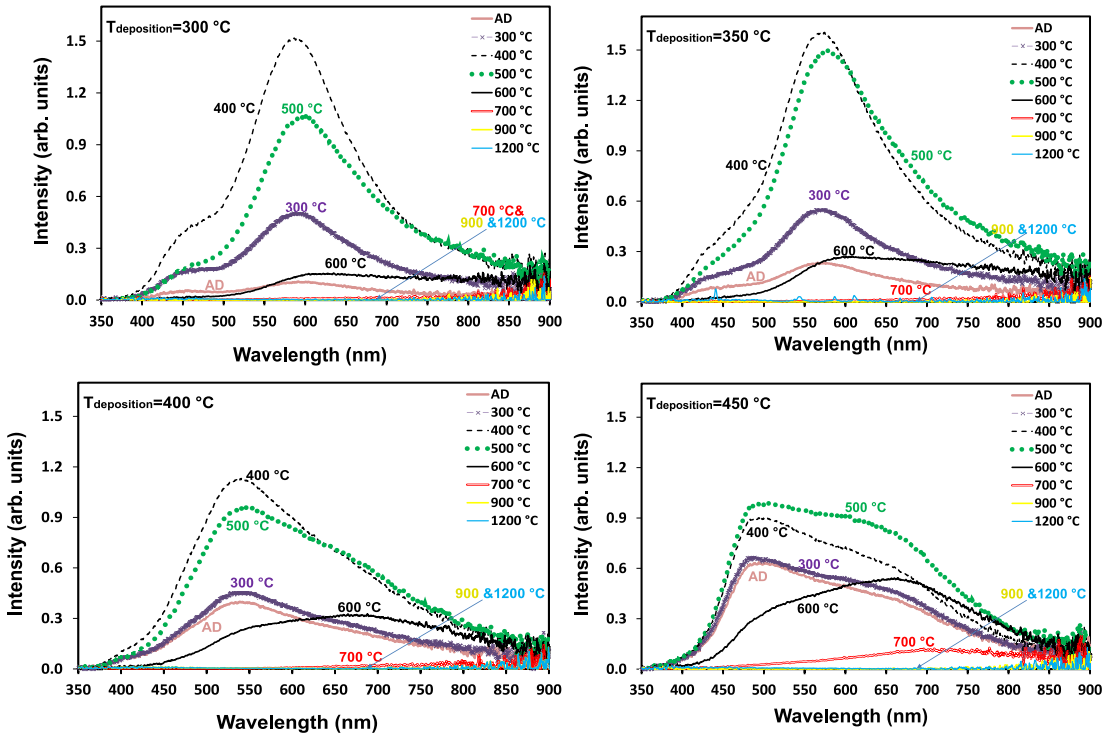

Figure 6.20: **Thermal evolution of PL of SiC_xN_y samples grown using different substrate temperatures.** The PL spectrum of a-SiC_xN_y:H_z samples excited using 325 nm laser source. The samples are annealed between 400 to 1200 °C for 1 h in N_2 ambient and the corresponding deposition temperatures are indicated. The PL band positioned at lower energy side of the visible range is enhanced with higher deposition temperatures due to the formation of more Si-C bonds.

substrate temperature yields less formation of hydrogen cyanide, HCN, providing the opportunity for the formation of C-N bonds in the film.

The increase of Si-C bonds and a decrease of Si-N bonds in the film grown using higher substrate temperatures can be also correlated to the higher chemical activity of CH_4 with SiH_4 radicals to form Si-C related bonds. This provides more attachment of carbon to silicon in the growing film decreasing the opportunity of nitrogen atoms to be bonded to silicon. Moreover, the Si-C bonds increase by the connection of silicon and carbon dangling bonds generated by the hydrogen desorption on the surface of

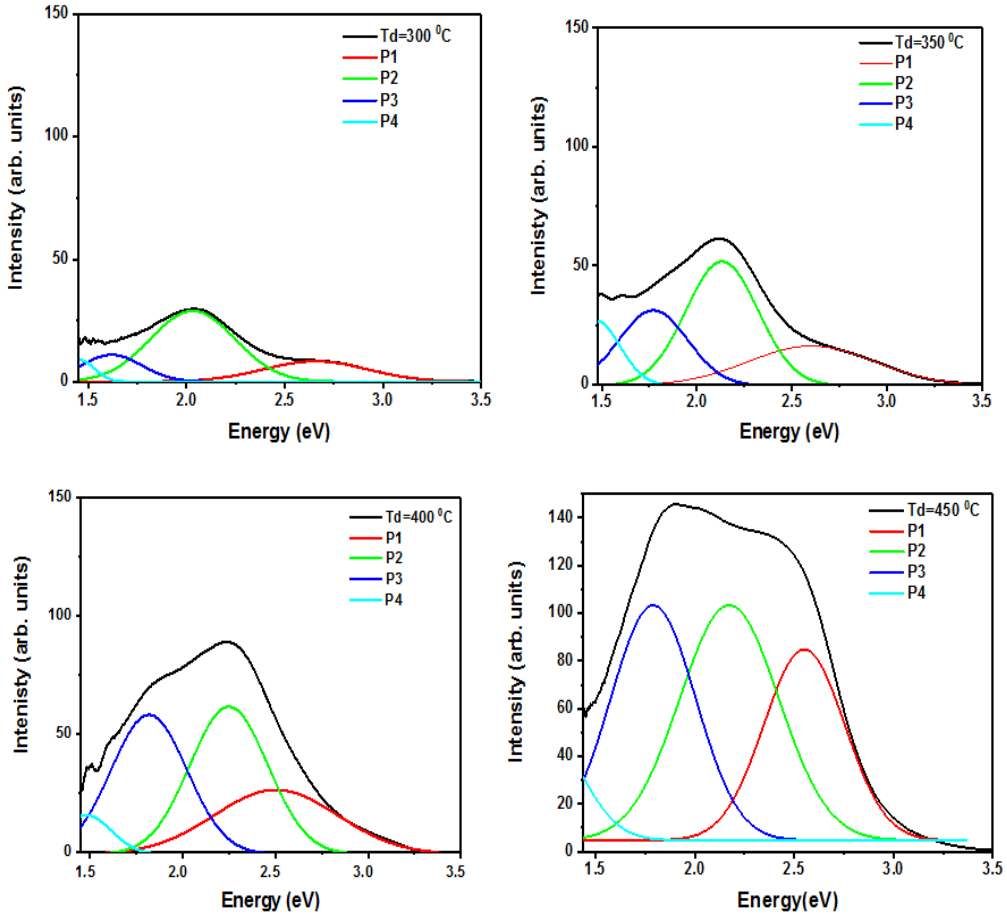

Figure 6.21: **PL deconvolution of samples grown using different substrate temperatures.** The deconvolution of PL spectra excited using a 325 nm laser source of as-deposited SiC_xN_y:H_z thin films for different deposition temperatures.

the film.

Therefore, the higher reactivity of CH_4 at higher temperatures not only promotes the incorporation of more carbon in the layer but also reduces the amount of hydrogen-terminated bonds in the film, providing more cross-linking of carbon atoms in the resultant film. All induced changes in the optical band gap, layer density, and refractive index are correlated with the described process of hydrogen loss, changes of film stoichiometry, and larger density of carbon-related configurations.

Table 6.4: The optical band gap (E_{04}), the position of PL subbands, and color coordinates of SiC_xN_y:H_z thin films, grown at different temperatures using otherwise identical deposition parameters.

Sample	E_{04} $\pm$0.05 (eV)	P_1 (eV)	P_2 (eV)	P_3 (eV)	P_4 (eV)	Color-Coordinates (x, y)	P_2/P_1	P_3/P_2	P_3/P_1
SiCN-300	3.36	2.66	2.60	2.55	2.50	(0.51, 0.46)	2.8	0.3	0.8
SiCN-350	3.42	2.03	2.13	2.17	2.25	(0.46, 0.50)	1.8	0.6	1.0
SiCN-400	3.57	1.62	1.76	1.79	1.82	(0.43, 0.51)	1.4	0.9	1.3
SiCN-450	3.68	1.46	1.46	1.42	1.47	(0.42, 0.53)	1.5	0.9	1.3

We took into account the characterization results described above, for the interpretation of the changes of PL properties as a function of the substrate temperature. Huran et al. [141] reported a similar PL reduction with the deposition temperature, while no details on the underlying mechanism for the changes in both shape and intensity of the PL emission were discussed. In our investigated samples, the PL peak position and intensity follow the increase of the optical gap. This indicates that the observed PL is due to the radiative recombination of carriers in defects and/or localized states at the band tails of the amorphous alloys. Furthermore, because the luminescence is intense enough to be seen with the naked eye, the probability of non-radiative recombination in a deep defect is small due to the very small mobility of carriers in the band tails [271]. In samples with smaller bandgap, the luminescence intensity is smaller because of the increased probability of the carriers reaching a

non-radiative recombination center [272].

We further explored these mechanisms by studying the variations of constituent PL bands obtained through the deconvolution of PL emission spectra as shown in Fig. 6.21 and listed in Table 6.4. It should be noted that the overlapping features of PL bands make it possible to increase the contribution of a certain band due to the increase of other bands even if that band has not been changed. Therefore, a comparison of the relative integrated intensities of all bands in the PL spectra of a certain sample is a more reliable way to study the evolution of PL bands in different samples. The relative integrated intensities of each PL band calculated for each individual spectrum, i.e. P_2/P_1, P_3/P_2, and P_3/P_1 are provided in Table 2. The integrated intensity of the P_3 band relative to all other bands increases with temperature, while the relative intensities of P_3/P_2 and P_2/P_1 decreases, implying that the contribution of the P_2 band decreases at higher deposition temperatures.

The intensity of the P_4 line, ascribed to silicon vacancies, is disregard due to the low signal level and the noise beyond ∼800 nm coming from the lower sensitivity of the CCD camera in this detection range. The origin of the P_3 band at ∼1.8 eV (675 nm) is associated with the carbon vacancy defects ($C_{si}V_c$), the so-called AB lines. The systematic increase of the P_3 band suggests that more radiative carbon vacancy defects formed when the deposition temperature is increased, in particular from 300 to 400 °C. As shown in the inset of Fig. 6.18 the luminescence color change through orange to yellow as the deposition temperature increases in agreement with the increase of relative intensity of green to blue PL emission (P_3/P_1). The increase of the P_3 band at higher temperatures can be expected from the aforementioned structural and compositional discussions where the presence of more carbon in the film leads to a larger density of carbon bonds (Si-C and C-N bonds) and consequently

the increase of carbon-related emissions. The P_2 band at 2.2 eV (565 nm) arises from nitride related states while the P_1 band at 2.6 eV (475 nm) is assigned to the transitions between gap states in silicon dangling bonds (more likely back bonded to nitrogen atoms), the so-called K-centers. The decrease of the P_2 band increasing the deposition temperatures can be explained by the lower content of nitrogen, as verified by XPS and RBS discussions.

6.6 Argon Dilution

To investigate the effect of Ar gas flow, sample AR-SiCN-350 was fabricated using deposition parameters similar to those used for R=1.8, except for an extra 5 sccm of Ar gas which corresponds to a partial pressure of 0.4 mTorr.

Ar dilution significantly decreases the hydrogen content from 32 to 20 at. %, where the carbon content increases significantly (see Table 6.3). In fact, the composition of Ar-SiCN-350 sample is very close to that of SiCN-400 sample grown without Ar dilution except for the presence of lower silicon and larger nitrogen concentration in Ar-SiCN-350. The PL emission of Ar-SiCN-350 is illustrated in Fig. 6.22 and can be compared with that of SiCN-350 and SiCN-400 presented in Fig. 6.21. The addition of Ar enhances the PL in the higher energy range in analogy to changes observed in the PL spectrum with the increase of 50 °C of T_d from SiCN-350 to SiCN-400. The addition of Ar enhances the contribution of the P_3 band in analogy to P_3 enhancement observed with the increase of 50 °C from SiCN-350 to SiCN-400. However, the integrated intensity of the P_2 band of Ar-SiCN-350 (nitrogen-related defects) is higher than that of SiCN-350 and SiCN-400 samples. This can be explained by the higher concentration of nitrogen in the Ar-SiCN-350 sample.

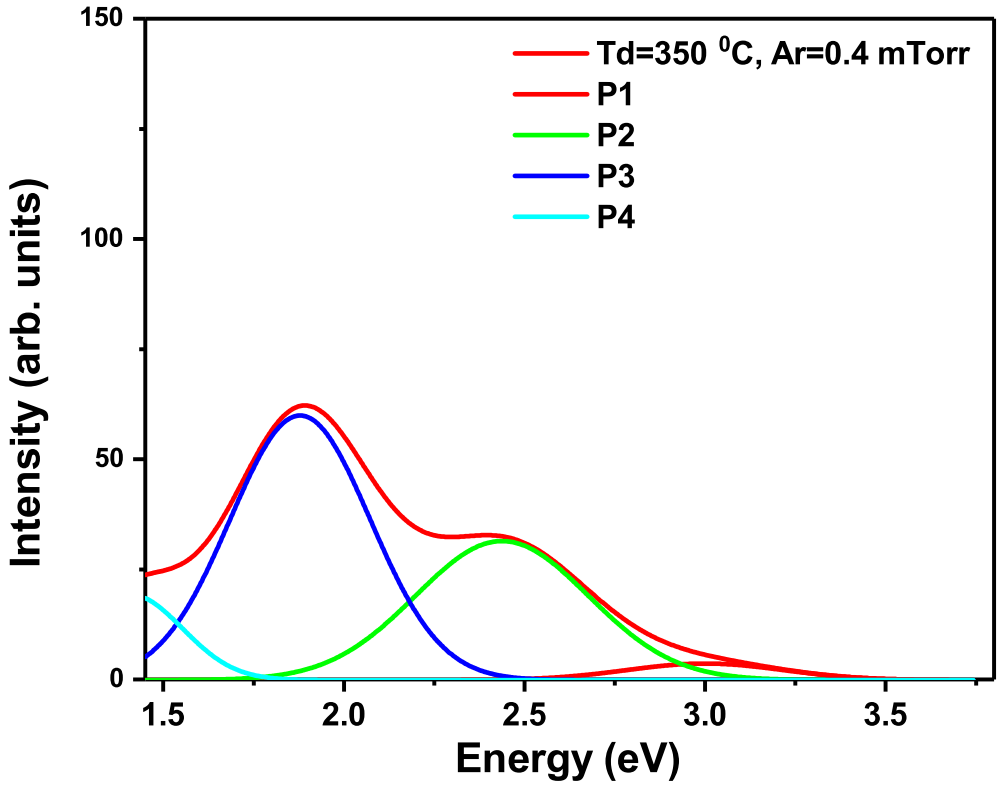

Figure 6.22: **Influence of argon dilution on the PL emission.** The deconvolution of PL emission of as-deposited a-$Si_{19}C_{48}N_{12}$:H_{20} thin film grown using 5 sccm of Ar (0.4 mTorr).

The addition of Ar gas changes the plasma chemistry and the dissociation rate of precursors which affect consequently the film composition and bonding states of the elements in the growing layer [273]. In the presence of more energetic Ar ions, CH_4 (with higher activation energy) is decomposed more effectively explaining the significant increase of carbon content in the resultant film (see Table 6.3). This is in agreement with other studies indicating a higher conversion rate of CH_4 with the addition of rare gases such as Ar [274].

It can be inferred that Ar dilution influences the film properties in analogy to the

increase of the deposition temperature by 50 °C (T_s by 15 °C). Both SiCN-400 and Ar-SiCN-350 samples showed higher carbon and lower hydrogen contents compared to the SiCN-350 sample. The hydrogen loss with Ar dilution was previously reported by other researchers [275]. The only difference between SiCN-400 and Ar-SiCN-350 is the higher nitrogen and lower silicon content in SiCN-400. This can be explained by high activation of strongly bonded N_2 in the plasma containing more Ar gas [276], which makes the amount of available N_2 species larger than the amount of N_2 species in the SiCN-400 sample grown with no Ar dilution. In SiCN-400 a decrease in the density of Si-N bonds and nitrogen content was observed due to the competition of constant N_2 species with the increasing number of reactants generating from CH_4. In the fabrication of Ar-SiCN-350 sample, the N_2 radicals created in the plasma cone impacted the gas phase chemical reactions and the species arriving at the surface that ultimately leads to the incorporation of more nitrogen and less silicon in the film. This explains the changes in the PL emission where the enhancement of the P_2 band assigned to the nitrogen-related defects in the film.

Chapter 7

Conclusions and Suggestions for Future Work

7.1 Conclusions

The research presented in this thesis is a first examination of luminescent silicon carbonitride thin films within a broad range of composition, process parameters, and thermal treatment. The most important findings derived from employing a multitude of experimental characterization techniques are summarized as follows in two main categories:

A: Film Properties

1. Stoichiometric Si_3N_4 and SiC: The process parameters to fabricate stoichiometric amorphous Si_3N_4 and SiC using ECR PECVD in a mixture of CH_4, N_2, and SiH_4 gases were determined in parallel with those necessary for fabricating various compositions of SiC_xN_y samples.

2. Comparison of SiC_xN_y, Si_3N_4, and SiC: A comprehensive comparison of the refractive index, mass density, and band gap of stoichiometric Si_3N_4 and SiC with SiC_xN_y was performed that can be used for band gap engineering and anti-reflection coatings.

3. Influence of carbon on the film structure: A systematic study of carbon-free to highly carbon-rich (∼50% of the film) SiC_xN_y samples was performed. The addition of carbon into SiN_y resulted in the expected increase of carbon and decrease in both silicon and nitrogen concentrations. Carbon preferred to make bonds with silicon, where the bridging of carbon between the interconnectivity of silicon and nitrogen bonds in Si_3N_4 was found a difficult task. Our SiC_xN_y samples did not show a dominant network of Si-C-N and can be regarded as an intermediate phase of Si-N, Si-C, and a small amount of Si-C-N phases. The formation of Si-C bonds appeared to be saturated in the most luminescent sample with C=32 at.%. Further addition of carbon (carbon-rich samples) did not change the amount of Si-C bonds significantly, while the C concentration increased and in effect, therefore, more C-H and C-C bonds were formed.

4. Film composition: One of the key elements of this study was the compositional analysis where the use of carbon substrates for RBS measurements delivered low uncertainty and combined RBS and ERD was employed simultaneously. A reliable and highly accurate compositional analysis is a necessary component to understanding a less-studied structure.

5. Band gap: Carbon addition to Si_3N_4 samples, the increase of the deposition temperature, and Ar dilution narrowed the band gap, which can be explained by the formation of Si-C bonds and reduction of Si-N bonds. In the case of Ar

dilution and an increase of substrate temperature, the rate of increase of the band gap was lower due to the opposite effect of another contributing factor, hydrogen loss.

6. Refractive index: The addition of carbon to Si_3N_4 increases the refractive index from 1.9 to 2.1, however, due to the high amount of hydrogen the refractive index remained very close to Si_3N_4 matrices. Higher deposition temperatures and Ar dilution also increased the refractive index.

7. Thermal annealing: The as-deposited SiC_xN_y samples were highly metastable systems and in the study of thermal annealing in a wide range of temperatures from 300 to 1200 °C, two featured temperatures were found at T_a=500 °C and 900 °C. The H desorption and the restructuring of the chemical bonds affected the film modifications and each of them took a dominant role depending on the annealing stage.

8. Hydrogen content: All produced SiC_xN_y thin films were amorphous with relatively high concentrations of hydrogen (about 30 at.%). The introduction of methane in the deposition process increased the hydrogen content in the resultant Si_3N_4 layer from 10% to about 30% in SiC_xN_y films. The hydrogen level is controlled through the substrate temperature and post-deposition thermal treatment and was quantitatively analyzed. The increase of the deposition temperature by 150 °C reduced the hydrogen content from 38 to 12 at.%. The lowest hydrogen content was obtained at the highest deposition temperature of 450 °C.

9. Hydrogen diffusion: The hydrogen density remained virtually constant at the

first annealing stage, likely due to the stability of Si-H, N-H, and possibly C-H bonds. In addition, the N-H bond density increased at T_a=400 °C, due to the attachment of un-bonded hydrogen to the dangling bonds of nitrogen. At T_a=500 °C, the formation of more Si-C bonds led to hydrogen release from the layer through the cross-linking between C-H and Si-H bonds. At T_a=700 °C nearly all H bonds were broken ([H] = 12.2 at.%); however, a combination of the lower hydrogen diffusion along with thicker layers at the moderate annealing temperatures delayed the complete depletion of hydrogen to the second stage of annealing at T_a=900 °C ([H] = 6 at.%).

10. Film structure vs temperature: The partial graphitization of the film structure is accompanied by the thermally induced changes of the chemical bonds during the annealing process, i.e. the formation of a graphite phase at the expense of C-N/C=N bond breaking. The Si-N bonds appeared to be the more stable bonds than Si-C and C-N/C=N bonds. The increase of the substrate temperature also increased the density of Si-C and C-N/C=N bonds. We believe that the structure of SiC_xN_y is similar to Si-N structure likely due to the incorporation of large density of hydrocarbon (C-H) bonds into the growing layer, higher substrate temperatures led to hydrogen loss which in turn increased the Si-C bonds in the film.

11. Thermally induced changes in the band gap: In relation to hydrogen desorption, band gap narrowing was observed from the first stage to the second stage of annealing. After the second stage, the E_{04} gap widened due to the film restructuring and the formation of a graphite-like phase.

12. Thermal evolution of refractive index: According to the microstructure analyses

and hydrogen density calculations, the variations (loss) of hydrogen content played the main role in the changes of the refractive index at lower annealing temperatures. The refractive index significantly increased from 2.1 to 2.6 after the second stage of annealing due to the graphite phase formation.

13. Film thickness: The addition of carbon made a thicker and ess dense layer that can be expected from the high hydrogen content. During the annealing process, the strongest shrinkage of the film layer occurred after the second annealing stage, i.e., 900 °C due to full hydrogen depletion.

14. Argon dilution: The addition of argon to the plasma affected the film properties in analogy to the increase of 50 °C for the deposition temperature.

B. PL Studies

1. Hydrogenated amorphous, N-free SiC_xN_y, C-free SiC_xN_y, SiC_xN_y samples were explored to provide a comparative study of the visible light emission of these three matrices over a wide range of annealing temperatures. Si_3N_4 and SiC samples exhibited lower PL intensity compared to that of SiC_xN_y samples.

2. The origin of PL emission of as-grown and thermally treated Si_3N_4 and SiC samples was studied using the existing models reported for amorphous silicon nitride and silicon carbide compounds.

3. The relative concentration of carbon to nitrogen of the most luminescent sample was obtained as 1.8. Therefore, this work led to the identification of optimized processing parameters for the growth of highly luminescent a-SiC_xN_y films.

4. The most luminescent samples had a composition of a-$SiC_{1.2}N_{0.7}$:$H_{1.4}$ at the annealing temperature of 500 °C with a deposition temperature of 350 °C.

5. In carbon varying samples, an intermediate carbon-rich sample (a-$SiC_{1.2}N_{0.7}$:$H_{1.4}$) showed the most intense PL and its density of Si-C bonds was largest among all samples. For some reason, the carbon-rich sample did not have the highest density of Si-C bonds, further addition of carbon to the most luminescent sample did not change the Si-C bonds whereas C-C and C-H bonds kept increasing.

6. The Si-C structure plays the key role in enhancing the SiC_xN_y emission as it was evidenced experimentally using the changes of the film structure in relation to the annealing studies, film composition, and substrate temperature. In the thermal annealing studies, PL showed a strong correlation with the thermally induced changes of the Si-C bond densities compared to fewer changes of more stable Si-N bonds. The most luminescent sample contained the largest density of Si-C bonds and also fewer C-C bonds compared to the C-rich sample. Higher substrate temperatures led to the loss of hydrogen, incorporation of more carbon in the film, and larger density of Si-C leading to the changes of the PL emission of the second peak around 550 nm.

7. In general, the room-temperature PL of SiC_xN_y samples exhibited a broad luminescence band, covering the visible range with two dominant peaks at ∼470 and 550 nm, which appeared "white" to the naked eye. We believe that the nitride-related states are responsible for the first PL peak and the second PL peak is associated with the carbide structure according to the following evidence:

    - The first peak at 475 nm remained unchanged regardless of carbon presence in the SiN_x matrix and the amount of carbon in SiC_xN_y films. The possible transitions were assigned to the recombination processes at silicon dangling

bonds in the nitride structure (K centers, a standard Si_3N_4 defect) as observed in SiN film.

- The addition of C to the Si_3N_4 matrix led to band gap narrowing and a shift of the center of the second (main) peak at 550 nm to the lower energy range of the visible spectrum. This redshift occurred with the formation of Si-C bonds.
- We further investigated the origin of the luminescence of a-$SiC_{1.2}N_{0.7}$:$H_{1.4}$ using the correlation with the sources of the luminescence observed in submatrices of SiC:$H_{1.3}$ and $SiN_{1.3}$:$H_{0.3}$ thin films.
- We believe that the structure of SiCN is similar to Si-N structure likely due to the incorporation of large CH- concentrations into the film, higher substrate temperature led to hydrogen loss which in turn increases the concentration of Si-C bonds in the film. Subsequently, the second PL peak in the lower energy range (∼550 to 600) was found to be more intense, in agreement with the carbon-related PL emission for this peak.

In summary, the PL of a-SiC_xN_y:H_z was bright enough to be seen by the naked eye. The alloying of silicon nitride with carbon or silicon carbide with nitrogen introduced disorders in the amorphous a-SiC_xN_y:H_z in such a way that a more intense PL of a-SiC_xN_y:H_z was observed in compared to that of the silicon carbide and silicon nitride films. The PL peak positioned at higher energy was associated with the silicon nitride-related structure and silicon carbide submatrix appeareded to be responsible for lower energy PL peaks. A more intense PL of a-SiC_xN_y:H_z can be explained by the radiative luminescence centers (band tails states and/or defects) in a-SiC_xN_y:H_z acting differently than the commonly observed ones in submatrices such

as AB lines (carbon-related defects) and K-centers (silicon dangling bond back bonded to nitrogen atoms) in a-SiC and a-SiN thin films, respectively. In particular, a variety of experiments confirmed the strong correlation of the visible PL emission with the Si-C bond configuration, which suggested possible optimization of the luminescence of a-SiC_xN_y:H_z via the adjustment of Si-C the bonds.

7.2 Future Work

This fundamental work clearly constitutes a first attempt to identify the origin of light emission from SiC_xN_y thin films. The interdependency of the PL emission with the film structure and composition was evaluated along with the influence of the processing parameters on these properties. The key findings of the present thesis deliver a foundation to be used for further research as follows:

Material Characterization To obtain further evidence of the origin of PL emission, a number of complementary approaches can be taken. A very effective tool to provide a detailed insight with respect to the luminescent centers would be time-resolved PL spectroscopy. The PL decay time gives information on the radiative relaxation processes of the luminescent defects and allows for the determination of the dominant process, whether it is related to silicon carbide or silicon nitride phases. The PL behavior can be further investigated by low-temperature PL measurements. Furthermore, the results of different excitation sources (PL excitation) can be used to correlate the intensity of the PL emission with the energy of the excitation source.

Further material characterization can be achieved by synchrotron-based measurements such as X-ray absorption and X-ray emission spectroscopy delivering information on the electronic structure of the conduction and valence band, respectively. Some preliminary measurements have been already performed and the formation of Si-Si bonds at lower annealing temperatures was observed up to 500 °C (this is in agreement with FTIR results discussed in chapter 5). In connection with the hydrogen studies, XAS and XES will reveal a complete picture of the film structure and its thermal evolution.

Processing Parameters Given that the material behavior of these thin films is highly affected by the growth technique, a comparison of different deposition systems is suggested. Some set of samples already have been grown using ICP-PECVD and magnetron sputtering techniques using similar partial pressure of gases used to grow the set of carbon varying samples presented in this thesis. ICP-grown samples contained a higher nitrogen content compared to ECR PECVD grown samples and crystalline structures were formed in the annealed sputtered samples, where an intense PL emission was observed allowing for a substantial extension to studies at elevated temperatures.

In general, the incorporation of carbon into the Si_3N_4 lattice is a difficult task and SiN_x phase remained in films annealed at elevated temperatures. In comparison with other works that reported crystalline and high-quality SiC_xN_y thin films with a large density of Si-C-N networks the nitrogen content in our films was lower. In addition, in the ECR PECVD employed system for this study, stable N_2 molecules are dissociated in the plasma cone, where the incorporation of more nitrogen in the film can be achieved through Ar dilution and the increase of the plasma power (the

power of the ECR PECVD system possibly can be increased to 800 W). Another suggestion is to use NH_3 gas instead of N_2 gas as the nitrogen source. The strong double-bond of N_2 is hard to be dissociated, while in the ammonia (NH_3) molecule one nitrogen atom is bonded to three hydrogen atoms in a trigonal pyramidal shape, making the dissociation energy of the NH_3 gas to about half of that of N_2 gas.

Furthermore, the increase of incorporation of nitrogen to form a higher density of Si-C-N networks should be accompanied by using a less hydrogenated carbon source since our finding confirmed that the Si-C structure played a significant role in the enhancement of the PL emission of SiC_xN_y films. In fact, nitrogen and carbon, both, are required to be increases in the film, which can be achieved by the decrease of the hydrogen content in the film layer. One of the reasons for the low possibility of carbon to bridge between silicon and nitrogen is the incorporation of a high number of CH_3 species into the growing layer (CH and CH_2 are less probable due to different sticking coefficients).

Among all carbon sources used in PECVD techniques, CH_4 is the most stable one, the dissociation rates of acetylene (C_2H_2) and ethylene (C_2H_4) are higher and are in the range of SiH_4. The use of C_2H_2 gas and higher deposition temperatures guarantees a lower hydrogen content in the growing layer, which can provide the opportunity for more carbon to form bonds with nitrogen and silicon. In addition, to have a better understanding of these process parameters and type of the species during the actual deposition, it is suggested to use an OES tool that already has been calibrated for the ECR PECVD system.

Device Fabrication The information of the film composition and structure has been comprehensively established in this work. One or two complementary experiments are still required to evaluate the functionality of these thin films for the device applications. As an example, a combination of the luminescence studies presented here and some further hardness measurements along with electrical measurements open new pathways for sensors and detectors with high thermal and chemical stability.

We have performed some preliminary measurements on the hardness and Young's modulus (identifying the tendency of the material for the deformation) using tribology tests. A consistent trend was observed for both carbon varying samples and samples grown using different substrate temperatures. With increasing carbon content and deposition temperature, the hardness and elasticity of the layer increased. The study of mechanical properties of these films would be pursued by nanoscratch test that seemed to be a powerful technique to study the adhesion properties on different substrates for the optical coating designs.

Primarily Al and ITO alloying has been performed and current-voltage (IV) measurements confirmed that the addition of nitrogen to the silicon carbide structure increased the current density. Capacitance-voltage (CV) and IV measurements are necessary for any electroluminescent devices, where the adjustments of the carbon to nitrogen ratio will give a wide parameter space for SiC_xN_y structures offering perspective applications for UV sensors.

Bibliography

[1] D. Thomson, A. Zilkie, J. E. Bowers, T. Komljenovic, G. T. Reed, L. Vivien, D. Marris-Morini, E. Cassan, L. Virot, J.-M. Fédéli, J.-M. Hartmann, J. H. Schmid, D.-X. Xu, F. Boeuf, P. O'Brien, G. Z. Mashanovich, and M. Nedeljkovic, "Roadmap on silicon photonics," *Journal of Optics*, vol. 18, no. 7, p. 073003 (20pp), 2016.

[2] J. D. Plummer, M. D. Deal, and P. B. Griffin, *Silicon VLSI Technology: Fundamentals, Practice and Modeling*. Prentice Hall electronics and VLSI series, Prentice Hall, 2000.

[3] F. Priolo, T. Gregorkiewicz, M. Galli, and T. F. Krauss, "Silicon nanostructures for photonics and photovoltaics," *Nature nanotechnology*, vol. 9, no. 1, pp. 19–32, 2014.

[4] K. Wada, D. H. Ahn, D. R. Lim, J. Michel, and L. C. Kimerling, "Si microphotonics for optical interconnection," *Thin Solid Films*, vol. 508, pp. 418–421, 2006.

[5] L. C. Kimerling, "Silicon microphotonics," *Applied Surface Science*, vol. 159, pp. 8–13, 2000.

[6] L. Chrostowski and M. Hochberg, *Silicon Photonics Design: From Devices to Systems*. Cambridge: Cambridge University Press, 2015.

[7] D. Liang, G. Roelkens, R. Baets, and J. E. Bowers, "Hybrid integrated platforms for silicon photonics," *Materials*, vol. 3, pp. 1782–1802, 2010.

[8] D. A. B. Miller, "Device requirements for optical interconnects to silicon chips," *Proceedings of the IEEE*, vol. 97, no. 7, pp. 1166–1185, 2009.

[9] M. Lipson, "Guiding, modulating, and emitting light on silicon-challenges and opportunities," *Journal of Lightwave Technology,*, vol. 23, no. 12, pp. 4222–4238, 2005.

[10] L. Pavesi, "Routes toward silicon-based lasers," *Materials Today*, vol. 8, no. January, pp. 18–25, 2005.

[11] Z. Zhou, B. Yin, and J. Michel, "On-chip light sources for silicon photonics," *Light: Science and Application*, no. August, pp. 1–13, 2015.

[12] N. Daldosso and L. Pavesi, "Nanosilicon photonics," *Laser and Photonics Reviews*, vol. 3, no. 6, pp. 508–534, 2009.

[13] A. Anopchenko, A. Prokofiev, I. Yassievich, S. Ossicini, L. Tsybeskov, D. Lockwood, S. Saeed, T. Gregorkiewicz, M. Wojdak, J. Liu, and A. Meldrum, "Silicon-Based Light Sources," in *Handbook of Silicon Photonics*, Series in Optics and Optoelectronics, pp. 333–438, Taylor & Francis, apr 2013.

[14] L. Pavesi, "Will silicon be the photonic material of the third millenium?," *Journal of Physics: Condensed Matter*, vol. 15, no. 26, pp. R1169–R1196, 2003.

[15] O. Boyraz and B. Jalali, "Demonstration of a silicon Raman laser," *Optics express*, vol. 12, no. 21, pp. 5269–5273, 2004.

[16] H. Rong, R. Jones, A. Liu, O. Cohen, D. Hak, A. Fang, and M. Paniccia, "A continuous-wave Raman silicon laser," *Nature*, vol. 433, pp. 725–728, feb 2005.

[17] D. Timmerman, J. Valenta, K. Dohnalová, W. D. A. M. de Boer, and T. Gregorkiewicz, "Step-like enhancement of luminescence quantum yield of silicon nanocrystals," *Nature Nanotechnology*, vol. 6, no. 11, pp. 710–713, 2011.

[18] J. J. Gooding, E. Bakker, S. Kelley, Y. Long, M. Merkx, M. Sailor, N. Tao, and A. Mazur, "August 2017: Two Years of Submissions," *ACS Sensors*, vol. 2, no. 8, pp. 1068–1069, 2017.

[19] S. O. Kelley, "What Are Clinically Relevant Levels of Cellular and Biomolecular Analytes?," *ACS Sensors*, vol. 2, no. 2, pp. 193–197, 2017.

[20] F. Sangghaleh, I. Sychugov, Z. Yang, J. G. C. Veinot, and J. Linnros, "Near-Unity Internal Quantum E ffi ciency of Luminescent Silicon Nanocrystals with Ligand Passivation," *ACS AuthorChoice*, no. 7, pp. 7097–7104, 2015.

[21] Z. Bisadi, M. Mancinelli, S. Manna, S. Tondini, M. Bernard, A. Samusenko, M. Ghulinyan, G. Fontana, P. Bettotti, F. Ramiro-Manzano, G. Pucker, and L. Pavesi, "Silicon nanocrystals for nonlinear optics and secure communications," *Physica Status Solidi (a)*, vol. 2671, no. 12, pp. 2659–2671, 2015.

[22] B. Jalali and S. Fathpour, "Silicon photonics," *Lightwave Technology, Journal of*, vol. 24, no. 12, pp. 4600–4615, 2006.

[23] M. Estevez, M. Alvarez, and L. Lechuga, "Integrated optical devices for lab-on-a-chip biosensing applications," *Laser & Photonics Reviews*, vol. 6, no. 4, pp. 463–487, 2012.

[24] A. Badzian, T. Badzian, W. D. Drawl, and R. Roy, "Silicon carbonitride: A rival to cubic boron nitride," *Diamond and Related Materials*, vol. 7, no. 10, pp. 1519–1525, 1998.

[25] R. Riedel, A. Kienzle, W. Dressler, L. Ruwisch, J. Bill, and F. Aldinger, "A silicoboron carbonitride ceramic stable to 2,000C," 1996.

[26] L. C. Chen, C. K. Chen, and S. L. Wei, "Crystalline silicon carbon nitride : A wide band gap semiconductor," *Applied Physics Letters*, vol. 72, no. 19, pp. 2463–2465, 1998.

[27] V. M. Ng, M. Xu, S. Y. Huang, J. D. Long, and S. Xu, "Assembly and photoluminescence of SiCN nanoparticles," *Thin Solid Films*, vol. 506-507, pp. 283–287, 2006.

[28] R. Ctvrtlik, M. S. Al-Haik, and V. Kulikovsky, "Mechanical properties of amorphous silicon carbonitride thin films at elevated temperatures," *Journal of Materials Science*, vol. 50, no. 4, pp. 1553–1564, 2015.

[29] J. A. Silva, S. Quoizola, E. Hernandez, L. Thomas, and F. Massines, "Silicon carbon nitride films as passivation and antireflective coatings for silicon solar cells," *Surface and Coatings Technology*, vol. 242, pp. 157–163, 2014.

[30] K. Dunn, E. Chelomentsev, P. Wilson, T. Roschuk, J. Wojcik, and P. Mascher, "Luminescent SiC x N y Thin Films Deposited by ICP-CVD," *Vacuum*, pp. 359–364, 2010.

[31] T. R. Roschuk, *A study of luminescent Si-based materials through X-ray spectroscopies*. PhD thesis, McMaster University, 2009.

[32] P. Wilson, *Study of Luminescent Silicon-Rich Silicon Nitride and Cerium and Terbium Doped Silicon Oxide Thin Films*. PhD thesis, McMaster University, 2012.

[33] J. J. Quinn and K. S. Yi, *Solid State Physics: Principles and Modern Applications*. Springer Science & Business Media, 2009.

[34] G. Parker, *Introductory semiconductor device physics*. CRC Press, 1st ed., 2004.

[35] C. Kittel, *Introduction to Solid State Physics, 8th Edition*. Wiley, 2005.

[36] H. S. Nalwa, *Handbook of Nanostructured Materials and Nanotechnology, Five-Volume Set*, vol. 3. Academic Press, 1999.

[37] W. de Boer, D. Timmerman, K. Dohnalová, I. N. Yassievich, H. Zhang, W. J. Buma, and T. Gregorkiewicz, "Red spectral shift and enhanced quantum efficiency in phonon-free photoluminescence from silicon nanocrystals," *Nature nanotechnology*, vol. 5, no. 12, pp. 878–884, 2010.

[38] D. Liang and J. E. Bowers, "Recent progress in lasers on silicon," *Nature Photonics*, vol. 4, p. 511, jul 2010.

[39] S. Ossicini, L. Pavesi, and F. Priolo, *Light emitting silicon for microphotonics*. No. 194, Springer Science & Business Media, 1st ed., 2003.

[40] P. T. Landsberg and M. J. Adams, "Radiative and Auger processes in semiconductors," *Journal of Luminescence*, vol. 7, pp. 3–34, 1973.

[41] P. Bhattacharya, R. Fornari, and H. Kamimura, *Comprehensive Semiconductor Science and Technology, Six-Volume Set: Online version*, vol. 1. Newnes, 2011.

[42] N. Koshida, *Device Applications of Silicon Nanocrystals and Nanostructures*. Nanostructure Science and Technology, Springer US, 2008.

[43] P. Jonsson, H. Bleichner, M. Isberg, and E. Nordlander, "The ambipolar Auger coefficient : Measured temperature dependence in electron irradiated and highly injected n-type silicon," *American Institute of Physics*, vol. 81, no. November 1996, 1997.

[44] P. M. Fauchet, "Light emission from Si quantum dots," *Materials Today*, vol. 8, no. 1, pp. 26–33, 2005.

[45] M. A. Green, J. Zhao, A. Wang, P. J. Reece, and M. Gal, "Efficient silicon light-emitting diodes," *Nature*, vol. 412, no. August, pp. 2–5, 2001.

[46] L. Pavesi and D. J. Lockwood, *Silicon photonics*, vol. 1. Springer Science {&} Business Media, 2004.

[47] W. L. Ng, M. a. Lourenço, R. M. Gwilliam, S. Ledain, G. Shao, and K. P. Homewood, "An efficient room-temperature silicon-based light-emitting diode," *Nature*, vol. 410, no. 6825, pp. 192–4, 2001.

[48] H. S. Han, S. Y. Seo, and J. H. Shin, "Optical gain at 1.54 μm in erbium-doped silicon nanocluster sensitized waveguide," *Applied physics letters*, vol. 79, no. 27, pp. 4568–4570, 2001.

[49] L. T. Canham, "Silicon quantum wire array fabrication by electrochemical and chemical dissolution of wafers," *Applied Physics Letters*, vol. 57, no. 10, 1990.

[50] S. Furukawa and T. Miyasato, "Three-dimensional quantum well effects in ultrafine silicon particles," *Japanese Journal of Applied Physics, Part 1: Regular Papers and Short Notes and Review Papers*, vol. 27, no. 11, pp. 2207–2209, 1988.

[51] M. Zacharias, J. Bläsing, P. Veit, L. Tsybeskov, K. Hirschman, and P. M. Fauchet, "Thermal crystallization of amorphous Si/SiO2 superlattices," *Applied Physics Letters*, vol. 74, no. 18, pp. 2614–2616, 1999.

[52] L. Khriachtchev, *Silicon Nanophotonics: Basic Principles, Current Status and Perspectives*. Pan Stanford, illustrate ed., 2009.

[53] L. Pavesi, L. Dal Negro, C. Mazzoleni, G. Franzo, and F. Priolo, "Optical gain in silicon nanocrystals," *Nature*, vol. 408, pp. 440–444, nov 2000.

[54] G. D. Scholes and G. Rumbles, "Excitons in nanoscale systems," *Nature materials*, vol. 5, no. 9, pp. 683–696, 2006.

[55] S. W. Koch, M. Kira, G. Khitrova, and H. M. Gibbs, "Semiconductor excitons in new light," *Nature materials*, vol. 5, no. 7, pp. 523–531, 2006.

[56] G. T. Einevoll, "Confinement of excitons in quantum dots," *Physical Review B*, vol. 45, no. 7, pp. 3410–3417, 1992.

[57] J. Pickworth Glusker and K. N. Trueblood, *Crystal Structure Analysis: A Primer*. Oxford University Press, third edit ed., 1998.

[58] I. Filikhin, S. G. Matinyan, and B. Vlahovic, "Quantum mechanics of semiconductor quantum dots and rings," *Low Dimension Systems and Gauge principle*, no. September, 2011.

[59] C. d. M. Donegá, "Synthesis and properties of colloidal heteronanocrystals," *Chem. Soc. Rev.*, vol. 40, no. 3, pp. 1512–1546, 2011.

[60] K. S. Min, K. V. Shcheglov, C. M. Yang, H. A. Atwater, M. L. Brongersma, and A. Polman, "Defect-related versus excitonic visible light emission from ion beam synthesized Si nanocrystals in SiO2," *Applied Physics Letters*, vol. 69, no. 14, pp. 2033–2035, 1996.

[61] Y. U. Peter and M. Cardona, *Fundamentals of semiconductors: physics and materials properties*. Springer Science & Business Media, 2010.

[62] L. E. Brus, "Electronelectron and electron-hole interactions in small semiconductor crystallites: The size dependence of the lowest excited electronic state," *The Journal of Chemical Physics*, vol. 80, no. 9, p. 4403, 1984.

[63] Y. Kayanuma, "Quantum-size effects of interacting electrons and holes in semiconductor microcrystals with spherical shape," *Physical Review B*, vol. 38, no. 14, pp. 9797–9805, 1988.

[64] A. D. Yoffe, "Semiconductor quantum dots and related systems: Electronic, optical, luminescence and related properties of low dimensional systems," *Advances in Physics*, pp. 1–208, 2010.

[65] T. Takagahara and K. Takeda, "Theory of the quantum confinement effect on excitons in quantum dots of indirect-gap materials," *Physical Review B*, vol. 46, no. 23, pp. 15578–15581, 1992.

[66] Z. Gaburro, *Nanostructured silicon for photonics: from materials to devices*, vol. 27. Trans Tech Pubn, 2005.

[67] S. Zhang, *Nanostructured Thin Films and Coatings: Functional Properties*. Handbook of Nanostructured Thin Films and Coatings, Taylor & Francis, 2010.

[68] C. Delerue, G. Allan, and M. Lannoo, "Theoretical aspects of the luminescence of porous silicon," *Physical Review B*, vol. 48, no. 15, pp. 11024–11036, 1993.

[69] D. O. Debieu, *Optical characterization of luminescent silicon nanocrystals embedded in glass matrices*. PhD thesis, Friedrich Schiller University Jena., 2008.

[70] B. Garrido Fernandez, M. López, C. García, A. Pérez-Rodríguez, J. R. Morante, C. Bonafos, M. Carrada, and A. Claverie, "Influence of average size and interface passivation on the spectral emission of Si nanocrystals embedded in SiO2," *Journal of Applied Physics*, vol. 91, no. 2, pp. 798–807, 2002.

[71] P. D. Nguyen, D. M. Kepaptsoglou, Q. M. Ramasse, and A. Olsen, "Direct observation of quantum confinement of Si nanocrystals in Si-rich nitrides," *Physical Review B - Condensed Matter and Materials Physics*, vol. 85, no. 8, pp. 1–8, 2012.

[72] M. V. Wolkin, J. Jorne, P. M. Fauchet, G. Allan, and C. Delerue, "Electronic States and Luminescence in Porous Silicon Quantum Dots: The Role of Oxygen," *Physical Review Letters*, vol. 82, no. 1, pp. 197–200, 1999.

[73] Jan Valenta and Salvo Mirabella, *Nanotechnology and Photovoltaic*. Pan Stanford Publishing Pte. Ltd., 2010.

[74] R. B. Wehrspohn, J. N. Chazalviel, F. Ozanam, and I. Solomon, "Spatial versus quantum confinement in porous amorphous silicon nanostructures," *European Physical Journal B*, vol. 8, no. 2, pp. 179–193, 1999.

[75] D. Kovalev, H. Heckler, M. Ben-Chorin, G. Polisski, M. Schwartzkopff, and F. Koch, "Breakdown of the k-Conservation Rule in Si Nanocrystals," *Physical Review Letters*, vol. 81, no. 13, pp. 2803–2806, 1998.

[76] L. Pavesi and R. Turan, *Silicon nanocrystals: fundamentals, synthesis and applications*. John Wiley & Sons, 2010.

[77] Y.-N. Xu and W. Y. Ching, "Electronic structure and optical properties of α and β phases of silicon nitride, silicon oxynitride, and with comparison to silicon dioxide," *Physical Review B*, vol. 51, no. 24, pp. 17379–17389, 1995.

[78] R. D. Carson and S. E. Schnatterly, "Valence-band electronic structure of silicon nitride studied with the use of soft-x-ray emission," *Physical Review B*, vol. 33, no. 4, pp. 2432–2438, 1986.

[79] J. B. Casady and R. W. Johnson, "Status of silicon carbide (SiC) as a wide-bandgap semiconductor for high-temperature applications: A review," *Solid-State Electronics*, vol. 39, no. 10, pp. 1409–1422, 1996.

[80] a. a. Konakov and V. a. Burdov, "Optical gap of silicon crystallites embedded in various wide-band amorphous matrices: role of environment.," *Journal of*

physics. Condensed matter : an Institute of Physics journal, vol. 22, no. 21, p. 215301, 2010.

[81] S. Godefroo, M. Hayne, M. Jivanescu, A. Stesmans, M. Zacharias, O. I. Lebedev, G. Van Tendeloo, and V. V. Moshchalkov, "Classification and control of the origin of photoluminescence from Si nanocrystals," *Nature Nanotechnology*, vol. 3, no. 3, pp. 174–178, 2008.

[82] R. N. Pereira, D. J. Rowe, R. J. Anthony, and U. Kortshagen, "Oxidation of freestanding silicon nanocrystals probed with electron spin resonance of interfacial dangling bonds," *Physical Review B - Condensed Matter and Materials Physics*, vol. 83, no. 15, pp. 1–9, 2011.

[83] N. Wyrsch, G. Choong, C. Miazza, and C. Ballif, "Performance and transient behavior of vertically integrated thin-film silicon sensors," *Sensors*, vol. 8, no. 8, pp. 4656–4668, 2008.

[84] B. D. Fahlman, *Materials Chemistry*. Springer Netherlands, 2011.

[85] W. H. Zachariasen, "The Atomic Arrangement in Glass," *Journal of the American Chemical Society*, vol. 54, no. 10, pp. 3841–3851, 1932.

[86] R. A. Street, *Hydrogenated Amorphous Silicon*. Cambridge University Press, 2005.

[87] N. F. Mott and E. A. Davis, *Electronic processes in non-crystalline materials*. International series of monographs on physics, Clarendon Press, 1971.

[88] A. R. Forouhi and I. Bloomer, "Optical dispersion relations for amorphous semiconductors and amorphous dielectrics," *Physical Review B*, vol. 34, no. 10, pp. 7018–7026, 1986.

[89] R. Swanepoel, "Determination of the thickness and optical constants of amorphous silicon," *Journal of Physics E: Scientific Instruments*, vol. 16, no. 12, pp. 1214–1222, 2000.

[90] A. R. Zanatta and I. Chambouleyron, "Absorption edge, band tails, and disorder of amorphous semiconductors," *Physical Review B*, vol. 53, no. 7, pp. 3833–3836, 1996.

[91] G. D. Cody, T. Tiedje, B. Abeles, B. Brooks, and Y. Goldstein, "Disorder and the optical-absorption edge of hydrogenated amorphous silicon," *Physical Review Letters*, vol. 47, no. 20, pp. 1480–1483, 1981.

[92] J. J. Tauc, *Amorphous and Liquid Semiconductors, Plenum, London*. Springer US, 1 ed., 1974.

[93] D. Gon and W. M. Frenken, "Internal Photoemission of Holes and the Mobility Gap of Hydrogenated Amorphous Silicon," *Physical Review Letters*, vol. 59, no. 23, pp. 2678–2681, 1987.

[94] D. Kovalev, "Silicon photonics: Moving into the red," *Nature Nanotechnology*, vol. 5, no. 12, pp. 827–828, 2010.

[95] J. W. Luo, S. S. Li, I. Sychugov, F. Pevere, J. Linnros, and A. Zunger, "Absence of redshift in the direct bandgap of silicon nanocrystals with reduced size," *Nature Nanotechnology*, vol. 12, no. 10, pp. 930–932, 2017.

[96] N. M. Park, C. J. Choi, T. Y. Seong, and S. J. Park, "Quantum Confinement in Amorphous Silicon Quantum Dots Embedded in Silicon Nitride," *Physical Review Letters*, vol. 86, no. 7, pp. 1355–1357, 2001.

[97] A. Kassiba, M. Makowska-Janusik, J. Bouclé, J. Bardeau, A. Bulou, and N. Herlin-Boime, "Photoluminescence features on the Raman spectra of quasistoichiometric SiC nanoparticles: Experimental and numerical simulations," *Physical Review B*, vol. 66, no. 15, pp. 1–7, 2002.

[98] C. S. Solanki, *Solar Photovoltaics: Fundamentals, Technologies And Applications*. PHI Learning, 2015.

[99] D. Hiller, A. Zelenina, S. Gutsch, S. A. Dyakov, L. López-Conesa, J. López-Vidrier, S. Estradé, F. Peiró, B. Garrido, J. Valenta, M. Koínek, F. Trojánek, P. Malý, M. Schnabel, C. Weiss, S. Janz, and M. Zacharias, "Absence of quantum confinement effects in the photoluminescence of Si3N4 embedded Si nanocrystals," *Journal of Applied Physics*, vol. 115, no. 20, pp. 204–301, 2014.

[100] J. Y. Fan, X. L. Wu, and P. K. Chu, "Low-dimensional SiC nanostructures: Fabrication, luminescence, and electrical properties," *Progress in Materials Science*, vol. 51, no. 8, pp. 983–1031, 2006.

[101] V. Petrova-Koch, O. Sreseli, G. Polisski, D. Kovalev, T. Muschik, and F. Koch, "Luminescence enhancement by electrochemical etching of SiC(6H)," *Thin Solid Films*, vol. 255, no. 1-2, pp. 107–110, 1995.

[102] T. Y. Kim, N. M. Park, K. H. Kim, G. Y. Sung, Y. W. Ok, T. Y. Seong, and C. J. Choi, "Quantum confinement effect of silicon nanocrystals in situ grown

in silicon nitride films," *Applied Physics Letters*, vol. 85, no. 22, pp. 5355–5357, 2004.

[103] B. H. Kim, C. H. Cho, T. W. Kim, N. M. Park, G. Y. Sung, and S. J. Park, "Photoluminescence of silicon quantum dots in silicon nitride grown by NH3 and SiH4," *Applied Physics Letters*, vol. 86, no. 9, pp. 1–3, 2005.

[104] J. Kistner, X. Chen, Y. Weng, H. P. Strunk, M. B. Schubert, and J. H. Werner, "Photoluminescence from silicon nitride-no quantum effect," *Journal of Applied Physics*, vol. 110, no. 2, pp. 1–6, 2011.

[105] A. Zelenina, S. A. Dyakov, D. Hiller, S. Gutsch, V. Trouillet, M. Bruns, S. Mirabella, P. Loper, L. Lopez-Cinesa, J. Lopez-Vidrier, S. Estradé, F. Peiró, B. Garrido, J. Bläsing, A. Krost, D. M. Zhigunov, and M. Zacharias, "Nature of photoluminescence peak shift Structural and optical properties of size controlled Si nanocrystals in Si3N4 matrix : The nature of photoluminescence peak shift," *Journal of Applied Physics*, vol. 114, no. 184311, pp. 1–10, 2013.

[106] M. Zacharias, J. Heitmann, R. Scholz, U. Kahler, M. Schmidt, and J. Bläsing, "Size-controlled highly luminescent silicon nanocrystals: A SiO/SiO 2 superlattice approach," *Applied Physics Letters*, vol. 80, no. 4, pp. 661–663, 2002.

[107] J. Kujala, J. Slotte, F. Tuomisto, D. Hiller, and M. Zacharias, "Si nanocrystals and nanocrystal interfaces studied by positron annihilation," *Journal of Applied Physics*, vol. 120, no. 145302, p. 6, 2017.

[108] S. J. Tsai, C. I. Wang, H. C. Lee, C. Y. Lin, J. W. Chen, H.-w. Shiu, L.-y. Chang, H. T. Hsueh, H. Y. Chen, J. Y. Tsai, Y. H. Lu, T. C. Chang, L. W.

Tu, H. Teng, Y. C. Chen, C. H. Chen, and C. L. Wu, "Approaching Defect-free Amorphous Silicon Nitride by Plasma-assisted Atomic Beam Deposition for High Performance Gate Dielectric," *Nature Publishing Group*, no. February, pp. 1–9, 2016.

[109] S. V. Deshpande and E. Gulari, "Optical properties of silicon nltride films deposited by hot filament chemical vapor deposition," *J. App. Phys.*, vol. 77, no. 12, pp. 6534–6541, 1995.

[110] J. Robertson and M. J. Powell, "Gap states in silicon nitride," *Applied Physics Letters*, vol. 44, no. 4, pp. 415–417, 1984.

[111] S. Jou, I. C. Liaw, Y. C. Cheng, and C. H. Li, "Light emission of silicon oxynitride films prepared by reactive sputtering of silicon," *Journal of Luminescence*, vol. 134, pp. 853–857, 2013.

[112] S. Kohli, J. A. Theil, P. C. Dippo, K. M. Jones, M. M. Al-Jassim, R. K. Ahrenkiel, C. D. Rithner, and P. K. Dorhout, "Nanocrystal formation in annealed a-SiO 0.17:N 0.07:H films," *Nanotechnology*, vol. 15, no. 12, pp. 1831–1836, 2004.

[113] P. Melinon, B. Masenelli, F. Tournus, and A. Perez, "Playing with carbon and silicon at the nanoscale," *Nat Mater*, vol. 6, no. 7, pp. 479–490, 2007.

[114] N. Zheludev, "The life and times of the LED a 100-year history," *Nature Photonics*, vol. 1, no. April, pp. 189–192, 2007.

[115] X. L. Wu, J. Y. Fan, T. Qiu, X. Yang, G. G. Siu, and P. K. Chu, "Experimental evidence for the quantum confinement effect in 3C-SiC nanocrystallites," *Physical Review Letters*, vol. 94, no. 2, pp. 6–9, 2005.

[116] T. Rajagopalan, X. Wang, B. Lahlouh, C. Ramkumar, P. Dutta, and S. Gangopadhyay, "Low temperature deposition of nanocrystalline silicon carbide films by plasma enhanced chemical vapor deposition and their structural and optical characterization," *Journal of Applied Physics*, vol. 94, no. 8, pp. 5252–5260, 2003.

[117] R. Wu, K. Zhou, C. Y. Yue, J. Wei, and Y. Pan, "Recent progress in synthesis, properties and potential applications of SiC nanomaterials," *Progress in Materials Science*, vol. 72, pp. 1–60, 2015.

[118] S. Askari, A. Ul Haq, M. Macias-Montero, I. Levchenko, F. Yu, W. Zhou, K. K. Ostrikov, P. Maguire, V. Svrcek, and D. Mariotti, "Ultra-small photoluminescent silicon-carbide nanocrystals by atmospheric-pressure plasmas," *Nanoscale*, vol. 8, no. 39, pp. 17141–17149, 2016.

[119] G. Wen, X. Zeng, X. Wen, and W. Liao, "Photoluminescence properties and crystallization of silicon quantum dots in hydrogenated amorphous Si-rich silicon carbide films," *Journal of Applied Physics*, vol. 115, no. 16, 2014.

[120] F. Fuchs, V. a. Soltamov, S. Väth, P. G. Baranov, E. N. Mokhov, G. V. Astakhov, and V. Dyakonov, "Silicon carbide light-emitting diode as a prospective room temperature source for single photons.," *Scientific reports*, vol. 3, p. 1637, 2013.

[121] S. Castelletto, B. C. Johnson, V. Ivády, N. Stavrias, T. Umeda, A. Gali, and T. Ohshima, "A silicon carbide room-temperature single-photon source," *Nature Materials*, vol. 13, no. 2, pp. 151–156, 2014.

[122] A. Gali, P. Deák, E. Rauls, N. T. Son, I. G. Ivanov, F. H. C. Carlsson, E. Janzén, and W. J. Choyke, "Correlation between the antisite pair and the D1 center in SiC," *Physical Review B*, vol. 67, no. 15, pp. 155–203, 2003.

[123] W. Daves, A. Krauss, N. Behnel, V. Häublein, A. Bauer, and L. Frey, "Amorphous silicon carbide thin films (a-SiC:H) deposited by plasma-enhanced chemical vapor deposition as protective coatings for harsh environment applications," *Thin Solid Films*, vol. 519, no. 18, pp. 5892–5898, 2011.

[124] I. Vivaldo, M. Moreno, A. Torres, R. Ambrosio, P. Rosales, N. Carlos, W. Calleja, K. Monfil, and A. Benítez, "A comparative study of amorphous silicon carbide and silicon rich oxide for light emission applications," *Journal of Luminescence*, vol. 190, no. November 2016, pp. 215–220, 2017.

[125] W. Lu, Y. Ou, E. M. Fiordaliso, Y. Iwasa, V. Jokubavicius, M. Syväjärvi, S. Kamiyama, P. M. Petersen, and H. Ou, "White Light Emission from Fluorescent SiC with Porous Surface," *Scientific Reports*, vol. 7, no. 1, p. 9798, 2017.

[126] S. Gallis, V. Nikas, M. Huang, E. Eisenbraun, and A. E. Kaloyeros, "Comparative study of the effects of thermal treatment on the optical properties of hydrogenated amorphous silicon-oxycarbide," *Journal of Applied Physics*, vol. 102, no. 2, pp. 1–10, 2007.

[127] S. Gallis, V. Nikas, H. Suhag, M. Huang, and A. E. Kaloyeros, "White light emission from amorphous silicon oxycarbide (a-SiCx Oy) thin films: Role of composition and postdeposition annealing," *Applied Physics Letters*, vol. 97, no. 8, pp. 1–4, 2010.

[128] X. C. Xiao, Y. W. Li, L. X. Song, X. F. Peng, and X. F. Hu, "Structural analysis and microstructural observation of SiCxNy films prepared by reactive sputtering of SiC in N2 and Ar," *Applied Surface Science*, vol. 156, no. 1-4, pp. 155–160, 2000.

[129] Y. Liu, L. A. Liew, R. Luo, L. An, M. L. Dunn, V. M. Bright, J. W. Daily, and R. Raj, "Application of microforging to SiCN MEMS fabrication," *Sensors and Actuators, A: Physical*, vol. 95, no. 2-3, pp. 143–151, 2002.

[130] F. J. Gomez, P. Prieto, E. Elizalde, and J. Piqueras, "SiCN alloys deposited by electron cyclotron resonance plasma chemical vapor deposition," *Applied Physics Letters*, vol. 69, no. 6, pp. 773–775, 1996.

[131] X. W. Du, Y. Fu, J. Sun, and P. Yao, "The effect of annealing atmosphere on photoluminescent properties of SiCN films," *Surface and Coatings Technology*, vol. 201, pp. 5404–5407, 2007.

[132] H. Kato, N. Kashio, Y. Ohki, K. S. Seol, and T. Noma, "Band-tail photoluminescence in hydrogenated amorphous silicon oxynitride and silicon nitride films," *Journal of Applied Physics*, vol. 93, no. 1, pp. 239–244, 2003.

[133] F. Giorgis, C. Vinegoni, and L. Pavesi, "Optical absorption and photoluminescence properties of a-Si1-xNx:H films deposited by plasma-enhanced CVD," *Physical Review B*, vol. 61, no. 7, pp. 4693–4698, 2000.

[134] W. R. Chang, Y. K. Fang, S. F. Ting, Y. S. Tsair, C. N. Chang, C. Y. Lin, and S. F. Chen, "The hetero-epitaxial SiCN/Si MSM photodetector for high-temperature deep-UV detecting applications," *IEEE Electron Device Letters*, vol. 24, no. 9, pp. 565–567, 2003.

[135] C. W. Chen, M.-H. Lee, L. C. Chen, and K. H. Chen, "Structural and electronic properties of wide band gap silicon carbon nitride materialsa first-principles study," *Diamond and Related Materials*, vol. 13, no. 4-8, pp. 1158–1165, 2004.

[136] X. W. Du, Y. Fu, J. Sun, and P. Yao, "The evolution of microstructure and photoluminescence of SiCN films with annealing temperature," *Journal of Applied Physics*, vol. 99, no. 9, 2006.

[137] X. W. Du, Y. Fu, J. Sun, P. Yao, and L. Cui, "Intensive light emission from SiCN films by reactive RF magnetron sputtering," *Materials Chemistry and Physics*, vol. 103, no. 2-3, pp. 456–460, 2007.

[138] J. Huran, I. Hotový, F. Dubecký, and N. I. Balalykin, "N doped a-SiC:H films deposited by PECVD and annealed by pulse electron beam," *IEEE Semiconducting and Semi-Insulating Materials Conference, SIMC*, vol. 2005, pp. 93–97, 2005.

[139] J. Huran, M. Kučera, A. P. Kobzev, A. Valovič, N. I. Balalykin, and Š. Gaži, "Influence of substrate temperature on the photoluminescence properties of silicon carbide films prepared by ECR-PECVD," *Ispc{_}20*, no. November, pp. 2–5, 2011.

[140] A. Valovič, J. Huran, M. Kučera, A. P. Kobzev, and Š. Gaži, "Properties study of silicon carbide thin films prepared by electron cyclotron resonance plasma

technology," *The European Physical Journal Applied Physics*, vol. 56, no. 2, p. 24013, 2011.

[141] J. Huran, A. Valovic, M. Kucera, A. Kleinova, E. Kovacova, P. Bohacek, and M. Sekacova, "Hydrogenated Amorphous Silicon Carbon Nitride Films Prepared By Pecvd Technology: Properties," *Journal of Electrical Engineering-Elektrotechnicky Casopis*, vol. 63, no. 5, pp. 333–335, 2012.

[142] Z. F. Wu, B. Hong, K. Cheng, F. Zhang, C. G. Jin, T. Yu, and X. M. Wu, "Structure and photoluminescence properties of SiCN fi lms grown by dual ion beam reactive sputtering deposition," *Vaccum*, vol. 101, pp. 205–207, 2014.

[143] V. I. Ivashchenko, A. O. Kozak, O. K. Porada, L. A. Ivashchenko, O. K. Sinelnichenko, O. S. Lytvyn, T. V. Tomila, and V. J. Malakhov, "Characterization of SiCN thin films: Experimental and theoretical investigations," *Thin Solid Films*, vol. 569, no. C, pp. 57–63, 2015.

[144] V. I. Ivashchenko, O. K. Porada, L. A. Ivashchenko, I. I. Timofeeva, O. K. Sinel, O. O. Butenko, M. V. Ushakov, and L. A. Ushakova, "Characteristics of Thin Plasmachemical Silicon Carbon Nitride Films Deposited Using Hexamethyldisilane," *Powder Metallurgy and Metal Ceramics,*, vol. 48, no. 1, pp. 66–72, 2009.

[145] V. I. Ivashchenko, L. A. Ivashchenko, P. L. Srynsckyy, and L. A. Grishnova, "Ab Initio Simulations Of Liquid And Amorphous Sic And Sicn BT - Carbon Nanomaterials in Clean Energy Hydrogen Systems," *In: Baranowski B. et al.*

(eds) Carbon Nanomaterials in Clean Energy Hydrogen Systems. NATO Science for Peace and Security, no. Series C: Environmental Security. Springer, Dordrecht, pp. 857–862, 2008.

[146] O. Porada, A. Kozak, V. Ivashchenko, S. Dub, and G. Tolmacheva, "Hard plasmachemical a-SiCN coatings," *Journal of Superhard Materials*, vol. 38, no. 4, pp. 263–270, 2016.

[147] A. O. Kozak, V. I. Ivashchenko, O. K. Porada, L. A. Ivashchenko, O. K. Sinelnichenko, S. N. Dub, O. S. Lytvyn, I. I. Tymofeeva, and G. N. Tolmacheva, "Effect of the nitrogen flow on the properties of Si-C-N amorphous thin films produced by magnetron sputtering," *Journal of Superhard Materials*, vol. 37, no. 5, pp. 300–309, 2015.

[148] O. K. Porada, A. O. Kozak, V. I. Ivashchenko, S. M. Dub, and G. M. Tolmacheva, "Hard plasmachemical a-SiCN coatings," *Journal of Superhard Materials*, vol. 38, no. 4, pp. 263–270, 2016.

[149] Y. Liu, X. Zhang, C. Chen, G. Zhang, P. Xu, D. Chen, and L. Dong, "The photoluminescence of SiCN thin films prepared by C+ implantation into α-SiNx:H," *Thin Solid Films*, vol. 518, no. 15, pp. 4363–4366, 2010.

[150] S. Bulou, L. Le Brizoual, P. Miska, L. de Poucques, R. Hugon, M. Belmahi, and J. Bougdira, "The influence of CH4 addition on composition, structure and optical characteristics of SiCN thin films deposited in a CH4/N2/Ar/hexamethyldisilazane microwave plasma," *Thin Solid Films*, vol. 520, no. 1, pp. 245–250, 2011.

[151] S. Bulou, L. Le Brizoual, P. Miska, L. de Poucques, J. Bougdira, and M. Belmahi, "Wide variations of SiCxNy:H thin films optical constants deposited by H2/N2/Ar/hexamethyldisilazane microwave plasma," *Surface and Coatings Technology*, vol. 208, no. 2012, pp. 46–50, 2012.

[152] S. Bulou, L. Le Brizoual, R. Hugon, L. De Poucques, M. Belmahi, H. N. Migeon, and J. Bougdira, "Characterization of a N2/CH4 microwave plasma with a solid additive Si source used for SiCN deposition," *Plasma Processes and Polymers*, vol. 6, no. SUPPL. 1, pp. 576–581, 2009.

[153] Q. Li, Y. Wang, X. Shan, X. Wang, and W. Zhao, "Preparation and optical properties of SiCN thin films deposited by reactive magnetron sputtering," *Journal of Materials Science: Materials in Electronics*, vol. 28, no. 9, pp. 6769–6781, 2017.

[154] Y. Peng, J. Zhou, B. Zhao, X. Tan, and Z. Zhang, "Effect of annealing temperature and composition on photoluminescence properties of magnetron sputtered SiCN films," *Thin Solid Films*, vol. 519, no. 7, pp. 2083–2086, 2011.

[155] Z. Ma, J. Zhou, Z. Chen, and E. Xie, "Luminescence properties of terbium-doped SiCN thin films by rf magnetron reactive sputtering," *Diamond and Related Materials*, vol. 20, pp. 475–479, apr 2011.

[156] Y. Awad, M. A. El Khakani, M. Scarlete, C. Aktik, R. Smirani, N. Cami, M. Lessard, and J. Mouine, "Structural analysis of silicon carbon nitride films prepared by vapor transport-chemical vapor deposition," *Journal of Applied Physics*, vol. 107, no. 3, pp. 1–6, 2010.

[157] B. P. Jedrzejowski , J. Cizek , A. Amassian , J.E. Klemberg-Sapieha *, J. Vlcek , L. Martinu ab a a and AGroupe, "Mechanical and optical properties of hard SiCN coatings prepared by PECVD P.," *Thin Solid Films*, vol. 447448, pp. 201–207, 2004.

[158] B. P. Swain and N. M. Hwang, "Study of structural and electronic environments of hydrogenated amorphous silicon carbonitride (a-SiCN:H) films deposited by hot wire chemical vapor deposition," *Applied Surface Science*, vol. 254, no. 17, pp. 5319–5322, 2008.

[159] K. B. Sundaram and J. Alizadeh, "Deposition and optical studies of silicon carbide nitride thin films," *Thin Solid Films*, vol. 370, no. 1, pp. 151–154, 2000.

[160] S. Peter, S. Berntz, S. Berg, and F. Richter, "FTIR analysis of a-SiCN:H films deposited by PECVD," *Vacuum*, vol. 98, pp. 81–87, 2013.

[161] S. Peter, F. Speck, M. Lindner, and T. Seyller, "Analysis of a-SiCN:H films by X-ray photoelectron spectroscopy," *Vacuum*, vol. 138, pp. 191–198, 2017.

[162] M. M. Rahman and S. K. Hasan, "Ellipsometric, XPS and FTIR study on SiCN films deposited by hot-wire chemical vapor deposition method," *Materials Science in Semiconductor Processing*, vol. 42, pp. 373–377, 2016.

[163] b. Güne and K. Sel, "Effects of carbon content and plasma power on room temperature photoluminescence characteristics of hydrogenated amorphous silicon carbide thin films deposited by PECVD," *Thin Solid Films*, vol. 636, pp. 85–92, 2017.

[164] N.-M. Park, S. H. Kim, and G. Y. Sung, "Band gap engineering of SiCN film grown by pulsed laser deposition," *Journal of Applied Physics*, vol. 94, no. 4, p. 2725, 2003.

[165] S. Boughaba, G. Sproule, J. McCaffrey, M. Islam, and M. Graham, "Synthesis of amorphous silicon carbonitride films by pulsed laser deposition," *Thin Solid Films*, vol. 402, no. 1-2, pp. 99–110, 2002.

[166] A. E. Kaloyeros, F. A. Jové, J. Goff, and B. Arkles, "ReviewSilicon Nitride and Silicon Nitride-Rich Thin Film Technologies: Trends in Deposition Techniques and Related Applications," *ECS Journal of Solid State Science and Technology*, vol. 6, no. 10, pp. 691–714, 2017.

[167] D. H. Kuo and D. G. Yang, "Plasma-enhanced chemical vapor deposition of silicon carbonitride using hexamethyldisilazane and nitrogen," *Thin Solid Films*, vol. 374, no. 1, pp. 92–97, 2000.

[168] P. Capezzuto and A. Madan, *Plasma Deposition of Amorphous Silicon-Based Materials*. Plasma-Materials Interactions, Elsevier Science, 1995.

[169] A. Leo, S. Andronenko, I. Stiharu, and R. B. Bhat, "Characterization of thick and thin film SiCN for pressure sensing at high temperatures," *Sensors*, vol. 10, no. 2, pp. 1338–1354, 2010.

[170] R. Riedel, E. Horvath-Bordon, P. Kroll, G. Miehe, D. Dzivenko, H.-J. Kleebe, P. a. V. Aken, and S. Lauterbach, "Novel binary and ternary phases in the Si-C-N system," *Journal of the Ceramic Society of Japan*, vol. 116, no. 1354, pp. 674–680, 2008.

[171] R. Riedel, A. Kienzle, W. Dressler, L. Ruwisch, J. Bill, and F. Aldinger, "A silicoboron carbonitride ceramic stable to 2,000C," 1996.

[172] A. Badzian, "Stability of Silicon Carbonitride Phases," *Journal of the American Ceramic Society*, vol. 85, no. 1, pp. 16–20, 2004.

[173] J. Fan and P. K. Chu, *Silicon Carbide Nanostructures*. Springer Cham Heidelberg New York Dordrecht London, 2014.

[174] J. S. Levy, A. Gondarenko, M. a. Foster, A. C. Turner-Foster, A. L. Gaeta, and M. Lipson, "CMOS-compatible multiple-wavelength oscillator for on-chip optical interconnects," *Nature Photonics*, vol. 4, no. 1, pp. 37–40, 2010.

[175] G. Lehmann, P. Hess, J. J. Wu, C. T. Wu, T. S. Wong, K. H. Chen, L. C. Chen, H. Y. Lee, M. Amkreutz, and T. Frauenheim, "Structure and elastic properties of amorphous silicon carbon nitride films," *Physical Review B - Condensed Matter and Materials Physics*, vol. 64, no. 16, pp. 1653051–16530510, 2001.

[176] H. Hoche, C. Pusch, R. Riedel, C. Fasel, and A. Klein, "Properties of SiCN coatings for high temperature applications - Comparison of RF-, DC- and HPPMS-sputtering," *Surface and Coatings Technology*, vol. 205, no. SUPPL. 1, pp. S21–S27, 2010.

[177] D. Vrankovic, L. M. Reinold, R. Riedel, and M. Graczyk-Zajac, "Void-shell silicon/carbon/SiCN nanostructures: toward stable silicon-based electrodes," *Journal of Materials Science*, vol. 51, no. 12, pp. 6051–6061, 2016.

[178] E. Ermakova, K. Mogilnikov, Y. Rumyantsev, V. Kichay, E. Maximovskii, O. Semenova, and M. Kosinova, "Study of Cu diffusion behavior in carbon rich

SiCN:H films deposited from trimethylphenylsilane," *Thin Solid Films*, vol. 588, pp. 39–43, 2015.

[179] D. Shamiryan, T. Abell, F. Iacopi, and K. Maex, "Low-k dielectric materials," *Materials Today*, vol. 7, no. 1, pp. 34–39, 2004.

[180] A. Palov, T. V. Rakhimova, M. B. Krishtab, and M. R. Baklanov, "Dependence of dielectric constant of SiOCH low-k films on porosity and pore size," *Journal of Vacuum Science & Technology B, Nanotechnology and Microelectronics: Materials, Processing, Measurement, and Phenomena*, vol. 33, no. 2, p. 020603, 2015.

[181] H. E. Tu, Y. H. Chen, and J. Leu, "Low-k SiCxNy Films Prepared by Plasma-Enhanced Chemical Vapor Deposition Using 1,3,5-trimethyl-1,3,5-trivinylcyclotrisilazane Precursor," *Journal of The Electrochemical Society*, vol. 159, no. 5, p. G56, 2012.

[182] H. Tu, C. Su, U. Jeng, and J. Leu, "Effect of Porogen Incorporation on Pore Morphology of Low-k SiCxNy Films Prepared Using PECVD," *ECS Journal of Solid State Science and Technology*, vol. 4, no. 1, pp. N3015–N3022, 2014.

[183] S. Van Nguyen, S. Hosadugra, T. Haigh, Y. Yao, L. Tai, S. Cohen, T. Shaw, C. K. Hu, E. Liniger, K. Virwani, A. J. Kellock, and D. Canaperi, "Low Hydrogen Silicon Carbon Nitride Cap for High Performance Sub-10 nm Cu-Low k Interconnect," *ECS Journal of Solid State Science and Technology*, vol. 6, no. 7, pp. P429–P434, 2017.

[184] R. P. Birringer, R. Shaviv, P. R. Besser, and R. H. Dauskardt, "Environmentally assisted debonding of copper/barrier interfaces," *Acta Materialia*, vol. 60, no. 5, pp. 2219–2228, 2012.

[185] C. Huber, B. Stein, and H. Kalt, "Plasma-enhanced chemical vapor deposition of amorphous silicon carbonitride : Deposition temperature dependence of bonding structure , refractive index , mechanical stress and their aging under ambient air," *Thin Solid Films*, vol. 634, pp. 66–72, 2017.

[186] R. N. Candler, W. T. Park, M. Hopcroft, B. Kim, and T. W. Kenny, "Hydrogen diffusion and pressure control of encapsulated mems resonators," *Digest of Technical Papers - International Conference on Solid State Sensors and Actuators and Microsystems, TRANSDUCERS '05*, vol. 1, pp. 920–923, 2005.

[187] E. Vassallo, A. Cremona, F. Ghezzi, F. Dellera, L. Laguardia, G. Ambrosone, and U. Coscia, "Structural and optical properties of amorphous hydrogenated silicon carbonitride films produced by PECVD," *Applied Surface Science*, vol. 252, no. 22, pp. 7993–8000, 2006.

[188] F. Kraus, S. Cruz, and J. Müller, "Plasmapolymerized silicon organic thin films from HMDSN for capacitive humidity sensors," *Sensors and Actuators, B: Chemical*, vol. 88, no. 3, pp. 300–311, 2003.

[189] M. H. Kang, D. S. Kim, A. Ebong, B. Rounsaville, A. Rohatgi, G. Okoniewska, and J. Hong, "The Study of Silane-Free SiCxNy Film for Crystalline Silicon Solar Cells," *Journal of The Electrochemical Society*, vol. 156, no. 6, pp. H495—-H499, 2009.

[190] L. Sang, M. Liao, and M. Sumiya, "A comprehensive review of semiconductor ultraviolet photodetectors: From thin film to one-dimensional nanostructures," *Sensors (Switzerland)*, vol. 13, no. 8, pp. 10482–10518, 2013.

[191] T.-H. Chou, "A comparative study of lateral SiCN/porous silicon and vertical SiCN/porous silicon junctions for sensing ultraviolet light," *Solid-State Electronics*, vol. 114, pp. 55–59, 2015.

[192] W. R. Chang, Y. K. Fang, S. F. Ting, Y. S. Tsair, C. N. Chang, C. Y. Lin, and S. F. Chen, "The hetero-epitaxial SiCN/Si MSM photodetector for high-temperature deep-UV detecting applications," *IEEE Electron Device Letters*, vol. 24, no. 9, pp. 565–567, 2003.

[193] C. W. Chen, C. C. Huang, Y. Y. Lin, L. C. Chen, K. H. Chen, and W. F. Su, "Optical properties and photoconductivity of amorphous silicon carbon nitride thin film and its application for UV detection," *Diamond and Related Materials*, vol. 14, no. 3-7, pp. 1010–1013, 2005.

[194] T. H. Chou, Y. K. Fang, Y. T. Chiang, C. I. Lin, and C. Y. Yang, "A low cost n-SiCN/p-SiCN homojunction for high temperature and high gain ultraviolet detecting applications," *Sensors and Actuators, A: Physical*, vol. 147, no. 1, pp. 60–63, 2008.

[195] M. Boumerzoug, R. V. Kruzelecky, P. Mascher, and D. A. Thompson, "In-situ monitoring of electron cyclotron resonance plasma chemical vapour deposition of hydrogenated silicon nitride films," *Surface and Coatings Technology*, vol. 59, pp. 77–81, 1993.

[196] D. E. Blakie, O. H. Y. Zalloum, J. Wojcik, E. J. Irving, A. P. Knights, and P. Mascher, *Coupled luminescence centres in erbium-doped silicon rich silicon oxide thin films - art. no. 63433S*. Ph.d. thesis, McMaster Univeristy, 2006.

[197] R. DĄBKOWSKI, *New ECR-PECVD reactor and preliminary thin film depositions*. M.a.sc., McMaster University, 2011.

[198] H. Zhang, *Study of optimal deposition conditions for an inductively coupled plasma chemical vapour deposition (ICP-CVD) system*. PhD thesis, Thesis (M.A.Sc.) – McMaster University, 2005., 2005.

[199] H. Geng, *Semiconductor Manufacturing Handbook*. New York, NY, USA: McGraw-Hill, Inc., 1 ed., 2005.

[200] L. A. Nesbit, "ANNEALING CHARACTERISTICS OF Si-RICH SiO//2 FILMS.," *Applied Physics Letters*, vol. 46, no. 1, pp. 38–40, 1985.

[201] M. Ohring, *Materials Science of Thin Films*. Academic Press, 2nd ed., 2002.

[202] W. K. Chu, J. W. Mayer, T. M. Buck, G. Amsel, and F. Eisen, "Review Paper," *Thin Solid Films*, vol. 17, pp. 1–41, 1973.

[203] M. Mayer, ""SIMNRA User's Guide", Tech. Report IPP, 9/113," *Report IPP*, p. 9/113, 1997.

[204] A. Pélisson-Schecker, H. J. Hug, and J. Patscheider, "Charge referencing issues in XPS of insulators as evidenced in the case of Al-Si-N thin films," *Surface and Interface Analysis*, vol. 44, no. 1, pp. 29–36, 2012.

[205] O. H. Y. Zalloum, M. Flynn, T. Roschuk, J. Wojcik, E. Irving, and P. Mascher, "Laser photoluminescence spectrometer based on charge-coupled device detection for silicon-based photonics," *Review of Scientific Instruments*, vol. 77, no. 2, pp. 1–8, 2006.

[206] M. Boudreau, M. Boumerzoug, P. Mascher, and P. E. Jessop, "Electron cyclotron resonance chemical vapor deposition of silicon oxynitrides using tris(dimethylamino)silane," *Applied Physics Letters*, vol. 63, no. 22, pp. 3014–3016, 1993.

[207] Y. Wang and P. D. Townsend, "Potential problems in collection and data processing of luminescence signals," *Journal of Luminescence*, vol. 142, pp. 202–211, 2013.

[208] N. Ghobadi, "Band gap determination using absorption spectrum fitting procedure," *International Nano Letters*, vol. 3, no. 1, p. 2, 2013.

[209] E. G. Birgin, I. Chambouleyron, and J. M. Martnez, "Estimation of the Optical Constants and the Thickness of Thin Films Using Unconstrained Optimization," *Journal of Computational Physics*, vol. 151, no. 2, pp. 862–880, 1999.

[210] J. A. Woollam and P. G. Snyder, "Fundamentals and applications of variable angle spectroscopic ellipsometry," *Materials Science and Engineering B*, vol. 5, no. 2, pp. 279–283, 1990.

[211] I. J. A. Woollam Co., "CompleteEASE Data Analysis Manual," 2008.

[212] H. Fujiwara, *Spectroscopic Ellipsometry: Principles and Applications*. John Wiley & Sons, 2007, 2007.

[213] K. Laaziri, S. Kycia, S. Roorda, M. Chicoine, J. L. Robertson, J. Wang, and S. C. Moss, "High-energy x-ray diffraction study of pure amorphous silicon," *PHYSICAL REVIEW 8*, vol. 60, no. 19, pp. 520–533, 1999.

[214] M. C. Biesinger, B. P. Payne, A. P. Grosvenor, L. W. M. Lau, A. R. Gerson, and R. S. C. Smart, "Resolving surface chemical states in XPS analysis of first row transition metals, oxides and hydroxides: Cr, Mn, Fe, Co and Ni," *Applied Surface Science*, vol. 257, no. 7, pp. 2717–2730, 2011.

[215] J. L. Hueso, J. P. Espinós, A. Caballero, J. Cotrino, and A. R. González-Elipe, "XPS investigation of the reaction of carbon with NO, O2, N2 and H2O plasmas," *Carbon*, vol. 45, no. 1, pp. 89–96, 2007.

[216] S. Muhl and J. M. Méndez, "A review of the preparation of carbon nitride films," *Diamond and Related Materials*, vol. 8, no. 10, pp. 1809–1830, 1999.

[217] K. Yamamoto, Y. Koga, and S. Fujiwara, "XPS studies of amorphous SiCN thin films prepared by nitrogen ion-assisted pulsed-laser deposition of SiC target," *Diamond and Related Materials*, vol. 10, no. 9-10, pp. 1921–1926, 2001.

[218] C. Quiros, P. Prieto, A. Fernandez, E. Elizalde, C. Morant, R. Schlogl, O. Spillecke, and J. M. Sanz, "Bonding and morphology study of carbon nitride films obtained by dual ion beam sputtering," *Journal of Vacuum Science & Technology A: Vacuum, Surfaces, and Films*, vol. 18, no. 2, p. 515, 2000.

[219] B. Doucey, M. Cuniot, R. Moudni, F. Ténégal, J. E. Bourée, D. Imhoff, M. Rommeluére, and J. Dixmier, "Optical properties and local atomic order in non hydrogenated amorphous silicon carbonitride films," *Journal of Materials Science*, vol. 37, no. 13, pp. 2737–2745, 2002.

[220] Z. Khatami, P. R. J. Wilson, J. Wojcik, and P. Mascher, "The influence of carbon on the structure and photoluminescence of amorphous silicon carbonitride thin films," *Thin Solid Films*, vol. 622, pp. 1–10, 2017.

[221] C. Ronning, H. Feldermann, R. Merk, H. Hofsäss, P. Reinke, and J.-U. Thiele, "Carbon nitride deposited using energetic species: A review on XPS studies," *Physical Review B*, vol. 58, no. 4, pp. 2207–2215, 1998.

[222] W. M. Doyle, "Principles and applications of Fourier transform infrared (FTIR) process analysis.," *Technical Note AN906 Rev. C*, vol. 2, pp. 11–41, 1992.

[223] F. L. Pedrotti and L. S. Pedrotti, *Introduction to Optics*. Michigan: Prentice Hall, 2nd ed., 1993.

[224] S. Sriraman, S. Agarwal, E. S. Aydil, and D. Maroudas, "Mechanism of hydrogen-induced crystallization of amorphous silicon," *Nature*, vol. 418, no. 6893, pp. 62–65, 2002.

[225] N. B. Colthup and L. P. Powell, "Vibrational analysis of alkyl xanthates," *Spectrochimica Acta Part A: Molecular Spectroscopy*, vol. 43, no. 3, pp. 317–322, 1987.

[226] B. Hallam, B. Tjahjono, and S. Wenham, "Effect of PECVD silicon oxynitride film composition on the surface passivation of silicon wafers," *Solar Energy Materials and Solar Cells*, vol. 96, no. 1, pp. 173–179, 2012.

[227] F. Ay and A. Aydinli, "Comparative investigation of hydrogen bonding in silicon based PECVD grown dielectrics for optical waveguides," *Optical Materials*, vol. 26, no. 1, pp. 33–46, 2004.

[228] F. Giorgis, F. Giuliani, C. F. Pirri, E. Tresso, C. Summonte, R. Rizzoli, R. Galloni, A. Desalvo, and P. Rava, "Optical, structural and electrical properties of device-quality hydrogenated amorphous silicon-nitrogen films deposited by plasma-enhanced chemical vapour deposition," *Philosophical Magazine Part B*, vol. 77, no. 4, pp. 925–944, 1998.

[229] R. A. Van Swaaij, A. J. Berntsen, W. G. Van Sark, H. Herremans, J. Bezemer, and W. F. Van Der Weg, "Local structure and bonding states in a-Si1-xCx:H," *Journal of Applied Physics*, vol. 76, no. 1, pp. 251–256, 1994.

[230] S. W. King, J. Bielefeld, M. French, and W. A. Lanford, "Mass and bond density measurements for PECVD a-SiCx:H thin films using Fourier transform-infrared spectroscopy," *Journal of Non-Crystalline Solids*, vol. 357, no. 21, pp. 3602–3615, 2011.

[231] T. Kaneko, D. Nemoto, A. Horiguchi, and N. Miyakawa, "FTIR analysis of a-SiC:H films grown by plasma enhanced CVD," *Journal of Crystal Growth*, vol. 275, no. 1-2, pp. 1097–1101, 2005.

[232] I. Ferreira, E. Fortunato, P. Vilarinho, a.S. Viana, a.R. Ramos, E. Alves, and R. Martins, "Hydrogenated silicon carbon nitride films obtained by HWCVD, PA-HWCVD and PECVD techniques," *Journal of Non-Crystalline Solids*, vol. 352, no. 9-20, pp. 1361–1366, 2006.

[233] S. E. Rodil, R. Olivares, H. Arzate, and S. Muhl, "Properties of carbon films and their biocompatibility using in-vitro tests," *Diamond and Related Materials*, vol. 12, no. 3-7, pp. 931–937, 2003.

[234] Y. Gao, J. Wei, D. H. Zhang, Z. Q. Mo, P. Hing, and X. Shi, "Effects of nitrogen fraction on the structure of amorphous silicon-carbon-nitrogen alloys," *Thin Solid Films*, vol. 377-378, pp. 562–566, 2000.

[235] J. Wei, P. Hing, and Z. Q. Mo, "TEM, XPS and FTIR characterization of sputtered carbon nitride films," *Surface and Interface Analysis*, vol. 28, no. 1, pp. 208–211, 1999.

[236] Z. Khatami, P. R. Wilson, K. Dunn, J. Wojcik, and P. Mascher, "The influence of carbon on the structure and photoluminescence of amorphous silicon carbonitride thin films," *ECS Transactions*, vol. 45, no. 5, pp. 153–160, 2012.

[237] Z. Khatami, P. R. J. Wilson, J. Wojcik, P. Mascher, and E. Physics, "Photoluminescence Evolution of Silicon Carbonitride Thin Films Grown by Electron Cyclotron Resonance Plasma Enhanced Chemical Vapour Deposition," *Society of Vacuum Coaters Annual Technical Conference*, pp. 1–6, 2013.

[238] O. Taggart, *Mechanical properties of silicon-based films fabricated by pecvd*. Master thesis, McMaster University, 2013.

[239] T. Bååk, "Silicon oxynitride; a material for GRIN optics," *Applied Optics*, vol. 21, no. 6, p. 1069, 1982.

[240] M. A. Pereira, J. A. Diniz, I. Doi, and J. W. Swart, "Silicon nitride deposited by ECR-CVD at room temperature for LOCOS isolation technology," *Applied Surface Science*, vol. 212-213, no. SPEC., pp. 388–392, 2003.

[241] N. I. Fainer, A. N. Golubenko, Y. M. Rumyantsev, V. G. Kesler, B. M. Ayupov, V. I. Rakhlin, and M. G. Voronkov, "Tris(diethylamino)silaneA new precursor compound for obtaining layers of silicon carbonitride," *Glass Physics and Chemistry*, vol. 38, no. 1, pp. 15–26, 2012.

[242] S. Sitbon, "Low temperature deposition of silicon nitride films by distributed electron cyclotron resonance plasma-enhanced chemical vapor deposition," *Journal of Vacuum Science {&} Technology A: Vacuum, Surfaces, and Films*, vol. 13, no. 6, p. 2900, 1995.

[243] A. K. Sinha and E. Lugujjo, "Lorentz-Lorenz correlation for reactively plasma deposited Si-N films," *Applied Physics Letters*, vol. 32, no. 4, pp. 245–246, 1978.

[244] J. Zhou, Y. Peng, Y. Wang, and X. Tan, "Structural and optical properties of SiCxN16 (x=0, 4, 6, 8, 12) crystals by first principles calculations," *Physica E: Low-dimensional Systems and Nanostructures*, vol. 64, pp. 83–86, 2014.

[245] C. Raynaud, F. Ducroquet, G. Guillot, L. M. Porter, and R. F. Davis, "Determination of ionization energies of the nitrogen donors in 6H-SiC by admittance spectroscopy," *Journal of Applied Physics*, vol. 76, no. 3, pp. 1956–1958, 1994.

[246] P. R. J. Wilson, T. Roschuk, K. Dunn, E. N. Normand, E. Chelomentsev, O. H. Y. Zalloum, J. Wojcik, and P. Mascher, "Effect of thermal treatment on the growth, structure and luminescence of nitride-passivated silicon nanoclusters.," *Nanoscale Research Letters*, vol. 6, no. 1, p. 168, 2011.

[247] K. Ma, J. Y. Feng, and Z. J. Zhang, "Improved photoluminescence of silicon nanocrystals in silicon nitride prepared by ammonia sputtering.," *Nanotechnology*, vol. 17, no. 18, pp. 4650–4653, 2006.

[248] T. P. Smirnova, A. M. Badalian, L. V. Yakovkina, V. V. Kaichev, V. I. Bukhtiyarov, A. N. Shmakov, I. P. Asanov, V. I. Rachlin, and A. N. Fomina, "SiCN alloys obtained by remote plasma chemical vapour deposition from novel precursors," *Thin Solid Films*, vol. 429, no. 1-2, pp. 144–151, 2003.

[249] Z. Khatami, P. R. J. Wilson, O. Taggart, D. R. Frisina, J. Wojcik, and P. Mascher, "Structural and Optical Properties of Luminescent Silicon Carbonitride Thin Films," *ECS Transactions*, vol. 61, no. 5, pp. 97–103, 2014.

[250] Z. Khatami, C. Nowikow, J. Wojcik, and P. Mascher, "Annealing of silicon carbonitride nanostructured thin films: interdependency of hydrogen content, optical, and structural properties," *Journal of Materials Science*, vol. 53, no. 2, pp. 1497–1513, 2018.

[251] K. Jarolimek, R. A. De Groot, G. A. De Wijs, and M. Zeman, "Atomistic models of hydrogenated amorphous silicon nitride from first principles," *Physical Review B - Condensed Matter and Materials Physics*, vol. 82, no. 20, pp. 1–9, 2010.

[252] D. V. . Lindley, *Understanding uncertainty*. Hoboken, N.J.: Wiley-Interscience, 2006.

[253] M. Tilli, T. Motooka, V.-M. Airaksinen, S. Franssila, M. Paulasto-Krockel, and V. Lindroos, *Handbook of silicon based MEMS materials and technologies*. William Andrew, 2015.

[254] C. Ronning, H. Feldermann, R. Merk, H. Hofsäss, P. Reinke, and J.-U. Thiele, "Carbon nitride deposited using energetic species: A review on XPS studies," *Physical Review B*, vol. 58, no. 4, pp. 2207–2215, 1998.

[255] K. Yamamoto, Y. Koga, and S. Fujiwara, "Binding energies of amorphous CN and SiCN films on X-ray photoelectron spectroscopy," *Japanese Journal of Applied Physics, Part 2: Letters*, vol. 40, no. 2 A, 2001.

[256] N. Colthup, *Introduction to infrared and Raman spectroscopy*. Elsevier, 2012.

[257] A. Grill and D. A. Neumayer, "Structure of low dielectric constant to extreme low dielectric constant SiCOH films: Fourier transform infrared spectroscopy characterization," *Journal of Applied Physics*, vol. 94, no. 10, pp. 6697–6707, 2003.

[258] F. Ay and A. Aydinli, "Comparative investigation of hydrogen bonding in silicon based PECVD grown dielectrics for optical waveguides," *Optical Materials*, vol. 26, no. 1, pp. 33–46, 2004.

[259] W. M. A. Bik, R. N. H. Linssen, F. H. P. M. Habraken, W. F. van der Weg, and A. E. T. Kuiper, "Diffusion of hydrogen in lowpressure chemical vapor deposited silicon nitride films," *Applied Physics Letters*, vol. 56, no. 25, pp. 2530–2532, 1990.

[260] H. J. Stein, P. S. Peercy, and R. J. Sokel, "Post-deposition high temperature processing of silicon nitride," *Thin Solid Films*, vol. 101, no. 4, pp. 291–298, 1983.

[261] E. Vassallo, A. Cremona, F. Ghezzi, F. Dellera, L. Laguardia, G. Ambrosone, and U. Coscia, "Structural and optical properties of amorphous hydrogenated silicon carbonitride films produced by PECVD," *Applied Surface Science*, vol. 252, no. 22, pp. 7993–8000, 2006.

[262] Z. Khatami, P. R. J. Wilson, J. Wojcik, and P. Mascher, "On the Origin of White Light Emission from Nanostructured Silicon Carbonitride," *J. LUMIN*, no. 1091, pp. 0–23, 2017.

[263] Z. Khatami, P. R. J. Wilson, J. Wojcik, and P. Mascher, "XANES and XES Studies of Luminescent Silicon Carbonitride Thin Films," *ECS Transactions*, vol. 50, no. 41, pp. 49–56, 2013.

[264] Z. Chen, J. Zhou, X. Song, X. Xu, Y. Liu, J. Song, Z. Ma, and E. Xie, "The effect of annealing temperatures on morphologies and photoluminescence properties of terbium-doped SiCN films," *Optical Materials*, vol. 32, no. 9, pp. 1077–1084, 2010.

[265] L. Museur, A. Zerr, and A. Kanaev, "Photoluminescence and electronic transitions in cubic silicon nitride," *Scientific Reports*, vol. 6, no. August 2015, p. 18523, 2016.

[266] B. Rezgui, A. Sibai, T. Nychyporuk, M. Lemiti, and G. Brémond, "Photoluminescence and optical absorption properties of silicon quantum dots embedded in Si-rich silicon nitride matrices," *Journal of Luminescence*, vol. 129, no. 12, pp. 1744–1746, 2009.

[267] J.-H. Park, H.-S. Kwon, and J.-Y. Lee, "Structural and optical properties of hydrogenated amorphous silicon carbide deposited by glow discharge from C3H8-SiH4-H2 mixture," *Journal of Applied Physics*, vol. 72, no. 11, p. 5246, 1992.

[268] E. Tomasella, L. Spinelle, A. Bousquet, F. Rebib, M. Dubois, C. Eypert, J. P. Gaston, J. Cellier, and T. Sauvage, "Structural and optical investigations of

silicon carbon nitride thin films deposited by magnetron sputtering," *Plasma Processes and Polymers*, vol. 6, no. SUPPL. 1, pp. 11–16, 2009.

[269] I. Solomon and M. P. Schmidt, "Selective low-power plasma decomposition of silane-methane mixtures for the preparation of methylated amorphous silicon," *PHYSICAL REVIEW B*, vol. 38, no. 14, pp. 9895–9901, 1988.

[270] Q. Cheng, S. Xu, and K. K. Ostrikov, "Single-step, rapid low-temperature synthesis of Si quantum dots embedded in an amorphous SiC matrix in high-density reactive plasmas," *Acta Materialia*, vol. 58, no. 2, pp. 560–569, 2010.

[271] L. R. Tessler and I. Solomon, "Photoluminescence of tetrahedrally coordinated a-Si1-xCx:H," *Phys. Rev. B*, vol. 52, pp. 10962–10971, oct 1995.

[272] D. J. Dunstan, "Band-gap fluctuations in amorphous semiconductors," *Solid State Communications*, vol. 43, no. 5, pp. 341–344, 1982.

[273] M. Motohashi, K. Ashibu, Y. Hiruta, and K. Homma, "Optical emission spectroscopy of glow discharge plasma from SiH4CH4 system," *Electronics and Communications in Japan (Part II: Electronics)*, vol. 90, no. 2, pp. 9–16, 2007.

[274] Y. Zeng and X. Tu, "Plasma-catalytic hydrogenation of CO2 for the cogeneration of CO and CH4 in a dielectric barrier discharge reactor: Effect of argon addition," *Journal of Physics D: Applied Physics*, vol. 50, no. 18, 2017.

[275] N. R. Pinhão, A. Janeco, and J. B. Branco, "Influence of helium on the conversion of methane and carbon dioxide in a dielectric barrier discharge," *Plasma Chemistry and Plasma Processing*, vol. 31, no. 3, pp. 427–439, 2011.

[276] L.-H. Lai, D.-Y. Wu, H.-C. Hsueh, and S.-T. Shiue, "Kinetics of Thermal Chemical Vapor Deposition and Microstructures of Carbon Films Using Propane/Ammonia Mixtures," *ECS Journal of Solid State Science and Technology*, vol. 3, no. 8, pp. M45–M53, 2014.